

Creating and Destroying Rotational Quantum Coherence in a Trapped-Ion Coulomb
Crystal Rotor

by

Neil Glikin

A dissertation submitted in partial satisfaction of the

requirements for the degree of

Doctor of Philosophy

in

Physics

in the

Graduate Division

of the

University of California, Berkeley

Committee in charge:

Professor Hartmut Häffner, Chair
Professor Holger Müller
Assistant Professor Michael Zürch

Fall 2023

Creating and Destroying Rotational Quantum Coherence in a Trapped-Ion Coulomb
Crystal Rotor

Copyright 2023
by
Neil Glikin

Abstract

Creating and Destroying Rotational Quantum Coherence in a Trapped-Ion Coulomb
Crystal Rotor

by

Neil Glikin

Doctor of Philosophy in Physics

University of California, Berkeley

Professor Hartmut Häffner, Chair

This work presents the techniques used to create a freely rotating trapped-ion Coulomb crystal and to establish quantum coherent control over this rotational motion. This is done using a highly symmetric surface ion trap with circular trapping electrodes. We derive how a trapped-ion rotor couples to coherent laser light, including the motional transition sideband spectrum and the corresponding coupling strengths. We also show how rotational motion modifies the coupling of the usual trapped-ion vibrational motion to laser light. In our experiments, light which is coupled to the rotor's motion propagates nearly normal to the trap surface, which is thus also sensitive to vibrational motion in this direction. We thus also present the design of and benchmark the performance of a Faraday cage which has successfully protected this motion from harmful electric field noise.

A prerequisite to clean, coherent manipulation of the rotational quantum state of our rotor is preparing it in a rapidly rotating state with a small uncertainty in its angular momentum. This rotational state preparation is done with by accelerating a rotating quadrupole field via time-dependent voltages applied directly to the trap electrodes, resulting in rotation frequencies of 100's of kHz with uncertainties within 1 kHz. We show how this procedure allows for creation of superpositions of angular momentum states, and present considerations and measurements pertaining to optimizing this procedure. We find that the coherence of these superpositions is limited by angular momentum diffusion processes induced by coupling to noisy electric field gradients. Careful measurements of these rotor decoherence dynamics demonstrate close agreement with the corresponding theory for the first time.

Finally, we present a proposal to use angular momentum superpositions of our trapped ion rotor as an interferometer in which we may exchange the positions of two ions. This experiment would serve as a test of the symmetrization of their mutual quantum state, and would be sensitive to the phase of the exchange operation without requiring the two particles to coincide spatially. We interpret the physical meaning of this exchange phase measurement and present detailed considerations of potential errors.

Errata

You are reading the Anniversary Edition of Neil's thesis! The following errors have been corrected:

- The trap capacitance noted in Sec. 2.2.4 has been corrected from 22 pF to 15 pF.
- The order of magnitude of the atomic factor $\mathbf{k} \cdot \mathbf{r}$ noted in Sec. 2.3.3 has been corrected from 10^{-4} to 10^{-2} .
- A sign error in the complex exponentials in Eq. (2.25) has been corrected.
- The Q-factor of the resonator noted in Sec. 4.1.5 has been changed to the gain factor.
- Equation (7.20) has been corrected.
- The diffusion coefficient for the measurement of rotational friction with noise injected in Fig. 7.11 has been corrected from $19 \hbar^2/\text{ms}$ to $110 \hbar^2/\text{ms}$.

To my parents, whose lack of understanding of my career never presented an impediment
to their encouragement, appreciation, and pride in it.

Acknowledgments

I first need to thank my advisor and mentor, Hartmut. I joined the group interested in the cool and precise laser-based science being done in the lab, but also insecure about having no background whatsoever in AMO physics. Hartmut immediately assured me that this was not a problem at all, and that I would learn as I go along. Throughout my PhD, he has balanced my urge to dig deeply into a question with suggestions on how to make concrete steps towards actually completing a project, coupled with optimism and encouragement that those steps are feasible. In this way, he has always kept me moving forward in my graduate school work by being an encouraging mentor, and never by being a demanding boss. As is inevitable in science and especially in graduate school, I have had my fair share of setbacks during my PhD, and Hartmut has always responded to these by reiterating his confidence in my abilities as a scientist. I will be able to carry this confidence forward into my career, and therefore deserves a lifetime of thanks.

My coworkers in the lab, particularly those I worked with directly, have created a collaborative environment in which I had the pleasure of working. Börge and Erik handed to me a beautifully functional experiment which has miraculously remained under vacuum throughout my PhD. I couldn't have asked for a better postdoc to work with during my transition period from junior to senior graduate student than Sara, who simultaneously mentored me and worked alongside me in the lab, especially in the most discouraging moments of having to make yet another noise measurement. Ryan and Neha have enthusiastically shown up to help push the experiment to finally getting some new results, and to make sure the experiment lives on into the future.

My theory collaborators Ben and Klaus also deserve a front-and-center thank-you for being so central to my PhD. They graciously welcomed me during my visit to Duisburg and enthusiastically took on the project that became the primary result of my PhD thesis. Without them, my results which impressively validate their rotor decoherence theory would be little more than a confusing measurement.

Also deserving of thanks are the various visiting students who gave me a reason to step back and think about how to explain the science to someone who isn't just expressing curiosity for five minutes, and who also made real contributions to the project: Kai K., Kai E., Lorenzo, and Dana. Furthermore, Nadav, for whom the in-lab portion of his visit was cut short by the COVID-19 pandemic, and Shijia, who exceeded my expectations on every project, and whose opportunity to rejoin as a graduate student was unfairly stolen supposedly in the name of national security.

Sometimes, the setbacks encountered in doing science are overcome with the help of the heroic work done by past researchers who anticipated them. For this, I wholeheartedly thank Tony and Crystal, who before my time in graduate school, built the pieces of the Faraday cage that eventually brought my experiment from an electrical noise wild goose chase to a functioning science platform. And Ryan and Neha, who were instrumental in modifying and assembling those pieces.

Outside the lab, I was privileged to have a strong support network of friends and family. To my parents, thank you for always being proud of me, and for reminding me to look at the bigger picture and appreciate where I am and what I've accomplished. To Jazmin, thank you for being an unbelievably rock solid support and providing a sense of stability, contentment, and even joy in my most stressful times. To my siblings Andrew and Nicole, thank you for being such solid supports and welcoming me into your homes even when I had to shut myself away in a spare room to get some work done. Thank you to my graduate school friends, especially Pra and Donny who have stuck with me from the very beginning of graduate school to the very end. Thank you to my roommates Zach and Ryan for providing an understanding ear both for gushing and ranting about my work. And finally, thank you to my childhood friends, Azar and the guise, for maintaining such strong connections over the years despite the geographic distance, and for always being able to make me feel like a kid again, even when I was lost deep in the maze of trying to become Dr. Glikin.

Contents

Contents	iv
List of Figures	viii
List of Tables	x
1 Introduction	1
2 Trapping and controlling the quantum state of atomic ions	3
2.1 Motivation	3
2.2 Paul traps	3
2.2.1 Operating principle	3
2.2.2 Motion of a single ion in a Paul trap	4
2.2.3 Surface ion traps	6
2.2.4 The ring trap	7
2.3 Theory of light-atom interactions	8
2.3.1 Light	9
2.3.2 Atoms	10
2.3.3 Coupling of atoms to light	12
2.4 Light-atom interaction dynamics	16
2.4.1 Coherent interactions, excluding ion motion	16
2.4.2 Incoherent interactions, excluding ion motion	18
2.4.3 Coherent interactions, including ion motion	19
2.4.4 Incoherent interactions, including ion motion	23
2.5 The $^{40}\text{Ca}^+$ ion	24
2.5.1 Level structure	25
2.5.2 Lasers	26
2.6 Useful light-atom processes for quantum state engineering in $^{40}\text{Ca}^+$	26
2.6.1 Optical pumping	26
2.6.2 Cooling	27
2.6.3 Coherent quantum state operations	30
2.6.4 State readout	30

2.6.5	Quantum state experiments	31
3	The trapped-ion planar quantum rotor	33
3.1	Single ions with a single vibrational mode	34
3.2	N -ion crystals with $3N$ vibrational modes	34
3.2.1	Normal modes of motion	34
3.2.2	Interaction with a coherent laser field	36
3.3	2-ion crystals in a planar rigid rotor	38
3.3.1	Derivation of the modes of motion	38
3.3.2	Quantum mechanics of the planar rigid rotor mode	41
3.3.3	Coupling strengths of interaction with a coherent laser field	42
3.3.4	Rabi oscillations of rotational sideband transitions	47
3.4	N -ion crystals in a planar rigid rotor with vibrational motion	47
3.4.1	The position operator	48
3.4.2	The interaction-picture Hamiltonian	51
3.4.3	Approximations of the matrix elements in special cases	52
3.4.4	Summary	55
3.5	2-ion crystals in a planar non-rigid rotor	55
3.5.1	Centrifugal distortion	57
3.5.2	Non-rigid corrections to individual modes	58
3.5.3	Energy eigenspectrum	60
3.5.4	Corrections to experimentally relevant rotational parameters	60
4	Experimental setup	64
4.1	General instrumentation	64
4.1.1	Lasers	64
4.1.2	Acousto-optic modulator systems	65
4.1.3	Other optics	67
4.1.4	Experiment control electronics	67
4.1.5	Trapping electronics	67
4.1.6	Calcium ion production	68
4.1.7	Magnetic field	68
4.1.8	Software	69
4.2	Instrumentation for ion rotation	69
4.2.1	Electronics for ion rotation	69
4.2.2	Vertical 729 nm and 866 nm laser beams	71
4.3	Faraday cage	72
4.3.1	General philosophy	73
4.3.2	Electrical signals	73
5	Measuring and mitigating noise	76
5.1	Physics of trapped-ion motional heating	76

5.1.1	Heating of differential modes of motion	78
5.2	Measuring heating rates	79
5.2.1	Rabi method	79
5.2.2	Sideband ratio method	80
5.3	Origins of electric field noise in trapped-ion experiments	80
5.3.1	Surface noise	80
5.3.2	Technical noise	80
5.4	Relating technical noise spectrum measurements to the heating rate	81
5.4.1	Converting measured noise power to voltage spectral density	81
5.4.2	Converting voltage spectral density to electric field spectral density .	82
5.4.3	Choosing reference points for measurement	82
5.4.4	Comparing to heating rates	83
5.5	Minimizing technical noise	85
5.6	Performance of the Faraday cage	86
6	Creating superpositions of rotational states	88
6.1	Requirements for coherent operations	88
6.2	Rotational state preparation	90
6.2.1	Generating the pinning potential	92
6.2.2	Preparing the rotation frequency	94
6.2.3	Minimizing the angular momentum spread	97
6.3	The rotational spectrum	104
6.3.1	Choice of beam angle	105
6.4	Rotational Rabi experiments	106
6.4.1	Full 4-level dynamics	107
6.4.2	Approximation as 2-level systems	110
6.4.3	Effect of rotational state preparation quality	111
6.5	Rotational Ramsey experiments	112
6.5.1	Rotational Ramsey dephasing	113
6.5.2	Rotational Ramsey rephasing	115
7	Decoherence of rotational superpositions	116
7.1	Protocol for measuring coherence of rotational superpositions	116
7.1.1	The rotational coherence measurement protocol as a measure of pure superpositions of angular momentum eigenstates	118
7.1.2	The 4-level contrast oscillation effect	118
7.2	Potential sources of rotational decoherence	121
7.2.1	Electronic coherence	121
7.2.2	Slowly drifting residual static quadrupole fields	122
7.2.3	Rotational coupling to stretch and vertical rocking motion	123
7.2.4	Trap frequency instability	124
7.2.5	Angular momentum diffusion	124

7.3	Angular momentum diffusion	125
7.3.1	The ion-field interaction Hamiltonian	125
7.3.2	The diffusion coefficient	127
7.3.3	Comparison to the heating rate of rocking modes	128
7.3.4	Measurements of angular momentum diffusion	130
7.3.5	Noise injection	130
7.3.6	Rotational friction	133
7.4	Rotational decoherence due to angular momentum diffusion	134
7.4.1	Theory: Orientational decoherence	134
7.4.2	Diffusion-induced decoherence of the trapped-ion rotor	135
7.4.3	Measurements	138
7.4.4	Ways to improve rotational coherence	142
8	The trapped-ion rotational interferometer	144
8.1	Identical quantum particles and exchange symmetry	144
8.1.1	The symmetrization postulate	145
8.1.2	Interpreting the concept of “indistinguishability”	146
8.2	Making trapped ions indistinguishable in a quantum rotor	148
8.2.1	Symmetrization of a pinned two-ion crystal	149
8.2.2	Symmetrization of a two-ion rotor	152
8.2.3	The transition from distinguishable to indistinguishable	154
8.3	The measurement protocol	155
8.3.1	The intuitive picture: position space	155
8.3.2	The formal picture	156
8.4	Experimental considerations	163
8.4.1	Effects which shift rotational transition frequencies	163
8.4.2	Observing the $\Delta\theta = 2\pi$ revival	166
8.4.3	Observing the $\Delta\theta = \pi$ exchange revival	174
8.4.4	Measuring the exchange phase	175
8.4.5	On using more than two ions	179
9	Summary and outlook	182
Bibliography		184

List of Figures

2.1	Image and simulated pseudopotential of the ring trap	7
2.2	Simulated two-level Rabi oscillations	18
2.3	Simulated vibrational sideband spectra	22
2.4	Simulated thermal Rabi oscillations	23
2.5	Level structure diagram of $^{40}\text{Ca}^+$	25
3.1	Normal modes of a two-ion Coulomb crystal	36
3.2	Normal modes of a two-ion Coulomb crystal which is allowed to rotate within one plane	41
3.3	Geometry of a laser interacting with a two-ion rotor	43
3.4	Simulated sideband spectra for a rotor	46
3.5	Simulated Rabi oscillations for a rotor	48
3.6	Geometry of a laser interacting with a many-ion rotor	49
3.7	Rovibrational coupling strengths	54
4.1	Photograph of the compact AOM setups.	65
4.2	Compact AOM bandwidth measurements	66
4.3	Voltages required for trap DC electrodes	69
4.4	Image and schematic of the rotation circuit	70
4.5	Schematic of beams for 866 nm Doppler cooling	71
4.6	Photograph of the experimental setup with the Faraday cage.	72
4.7	Schematic of the electrical signals used in the experiment with respect to the Faraday cage.	74
4.8	Filter function of the cascaded low-pass filter used for the DC electrode signals.	74
5.1	Sample heating rate measurement	79
5.2	Example pairs of electrodes the the resulting electric fields	82
5.3	Measured noise spectra vs. heating rates	84
5.4	Groundings and lowering noise	85
5.5	Radiation lowering of Faraday cage	86
5.6	Noise spectra and heating rates of Faraday cage	87
6.1	Schematic of the spin-up-and-release procedure	91

6.2	Pinning voltage pattern	93
6.3	Rotation frequency vs. spin-up time	95
6.4	Simulated classical trajectories during rotational state preparation	96
6.5	Release process	97
6.6	Simulated angular momentum spread vs. release time and rocking mode temperature	99
6.7	Rotor eigenspectrum vs. pinning potential strength	100
6.8	Numerical simulation of angular momentum spread versus time during release .	101
6.9	Angular momentum spread vs. spin-up time	103
6.10	Rotational sideband spectrum	104
6.11	Rotational sideband coupling strengths vs. beam angle	106
6.12	Rotational Rabi oscillations	107
6.13	Energy levels coupled together in rotational Rabi experiments	109
6.14	Schematic spectrum for rotational sideband addressing	110
6.15	Measured rotational Rabi oscillations	111
6.16	Measured rotational Ramsey dephasing	114
7.1	Rotational decoherence measurements	117
7.2	Rotational superposition state schematic	118
7.3	Rotational Ramsey contrast oscillations	120
7.4	Electronic coherence measurement	122
7.5	Measurement of trap frequency stability	125
7.6	Noisy quadrupole fields on a two-ion rotor	129
7.7	Angular momentum diffusion measurement	130
7.8	Noise injection circuit	131
7.9	Diffusion vs. injected noise amplitude	132
7.10	Diffusion vs. injected noise frequency	133
7.11	Measurements of rotational friction	133
7.12	Rotational decoherence measurement schematic with position-space picture . . .	136
7.13	Simulated rotational decoherence due to diffusion	137
7.14	Rotational decoherence measurements	139
7.15	Rotational decoherence vs. angular momentum diffusion	140
7.16	Rotational decoherence vs. rotation frequency	141
8.1	Indistinguishable and distinguishable pairs of identical particles entering a beam-splitter	147
8.2	Exchange symmetry of the relative modes of a pinned two-ion crystal	150
8.3	Exchange symmetry of the relative modes of a freely rotating two-ion crystal .	153
8.4	Exchange symmetry of rotor potential eigenfunctions vs. pinning strength . . .	154
8.5	Position-space schematic of the exchange experiment	156
8.6	Excitation and parity signal for the 2-ion rotor interference experiment	162
8.7	Shifts to rotational transition frequencies	164

8.8	Scaled decoherence rate versus scaled diffusion coefficient	168
8.9	Coherence time to revival time vs. experimental parameters	169
8.10	Horizontal trap frequency vs. DC bias	171

List of Tables

2.1	Electronic transition selection rules	15
3.1	Normal mode structure and frequencies of a two-ion crystal	36
3.2	Relative coupling strengths of vibrational and rotational transitions	56
8.1	Rotational interference experiment free evolution phases	160

Chapter 1

Introduction

Trapped atoms have served as highly controllable realizations of quantum mechanical systems for decades. Their high degree of isolation from their environment allows quantum coherence to endure for experimentally accessible timescales, their small mass gives them resolvable quantized energy levels, and their ability to interact with visible laser light gives them a precise handle for controllably manipulating their quantum state. Trapped ions in particular furthermore make it possible to work with small numbers of atoms at a time and afford a high degree of controllability of their motion in the quantum regime. This quantum motion has proven to be a highly useful tool for fundamental tests of quantum mechanics, as well as for quantum simulation and quantum computation.

The work done in pursuit of my PhD thesis revolves around using a Coulomb crystals of trapped ions as a tool for simulating a quantum rotor. Typically, Paul traps confine each ion to a well-defined equilibrium position, about which it may vibrate with an amplitude that is much smaller than the distance between ions. In this work, on the other hand, we create a trapping potential which is highly isotropic within one plane, allowing the entire Coulomb crystal to freely rotate. This is a novel use of the motion of trapped ions, and as such, has required the development and implementation of unique tools to prepare and control the rotational motion. We have used these tools to create superpositions of the quantized angular momentum states of the rotating Coulomb crystal and to carefully study the coherence of these superpositions. Our tools furthermore hold promise for performing interesting tests of fundamental physics with the rich properties of quantum rotors; in particular, we propose to use a superposition of angular momenta to exchange a pair of ions with each other as a test of the symmetrization postulate using particles which never occupy the same space.

This document aims to provide documentation of the results and conclusions that I have reached over the course of my PhD work, as well as a guide for understanding the often-counterintuitive properties of the trapped-ion rotor within an experimentally useful framework.

The remainder of this thesis begins with an overview of general techniques for controlling the quantum state of trapped ions in Chapter 2. Here, special attention is paid to how trapped ions' usual vibrational motion interacts coherently with a laser field, as the nov-

elty of this work relies heavily on an analogous but novel understanding of how quantum rotational motion interacts with laser light. Chapter 3 continues on to actually apply these considerations to a trapped-ion rotor, demonstrating the ways in which rotational motion differs from vibrational motion in the context of interacting coherently with a laser field.

Chapter 4 describes the equipment used in the laboratory for conducting the experiments in this work. One particular piece of equipment, the Faraday cage, has proven pivotal in allowing the experiment to be functional. The considerations which informed its design and the decision to implement it are therefore expanded upon in Chapter 5, which also presents an evaluation of the Faraday cage's performance in mitigating harmful electric-field noise.

Chapter 6 discusses how the ion rotor properties established in Chapter 3 allow for coherent manipulation of rotational motion in an experimental context. It establishes the requirements for cleanly preparing rotational superpositions, the tools used to meet those requirements, and the considerations which go into optimizing the experiments. Chapter 7 details a study of the decoherence of rotational superpositions. It establishes the theory of how angular momentum diffusion leads to rotational decoherence. It also presents measurements which demonstrate that such diffusion indeed limits the rotational coherence in our experiment. These measurements are in close agreement with recently-established general theory work on rotor decoherence dynamics, constituting the first validation of this theory. Finally, Chapter 8 presents a proposal for an experiment to use rotational superpositions to test the symmetrization postulate by exchanging a pair of ions. First, an interpretation of this experiment as a test of fundamental physics is presented. This is followed by a detailing of considerations of how to bring the experiment into an operating regime which allows the exchange to be measured, possible error sources, and how to minimize them.

Chapter 2

Trapping and controlling the quantum state of atomic ions

2.1 Motivation

The experimental study of quantum mechanics requires a system which exhibits non-classical behavior that can be probed. Isolated atoms have long provided such a system, initially as beams and as gasses confined within a glass cell. The idea of electromagnetically trapping atoms provided a further step in isolating them from unwanted interactions and in controlling their motion, especially in allowing the motion to be cooled into a quantum regime [1–3]. This both improves the coherence of laser-based interactions with the atom’s electrons and allows the motion itself to be studied and used as a quantum mechanical degree of freedom. Ions in particular are especially susceptible to confinement via their charge, allowing the use of electric fields, which are straightforward to generate experimentally, as the trapping mechanism. Two different types of ion trapping mechanism are commonly used [4], the Penning trap [5], which uses a static electric field and a static magnetic field, and the Paul trap [6–8], which uses oscillating electric fields. This work uses a Paul trap.

2.2 Paul traps

2.2.1 Operating principle

An object may be trapped by means of applying a restoring force towards some equilibrium position. Speaking abstractly, this can be achieved with a potential featuring a point which is a local minimum in all directions. For trapping a charged particle, the most natural choice for creating a trapping mechanism is with electric fields. However, a static electric field \mathbf{E} must be related to a conservative potential Φ by $\mathbf{E} = -\nabla\Phi$, and in free space this potential must obey Laplace’s equation $\nabla^2\Phi = 0$. This forbids a potential minimum in any static electric field.

The Paul trap utilizes the following solution to this apparent problem: the applied electric field, rather than being static, is swept sinusoidally at a frequency ω_{RF} whose corresponding timescale is faster than the timescale of the motion of the particle. This can allow the charged particle to be trapped on time-average, while the field still obeys Laplace's equation instantaneously at all times. This is the mechanism by which we trap ions. To understand how this works, it is useful to analyze the motion of an ion in a Paul trap quantitatively.

2.2.2 Motion of a single ion in a Paul trap

In general, a Paul trap operates by applying a potential which is the sum of a sinusoidal term and a static term, each individually obeying Laplace's equation. Each of these terms should have a point at which there is always zero electric field. When a Paul trap is designed and operated properly, these null points should coincide. We define this to be the origin of our coordinate system. The leading-order terms of the electric potential around the origin can be written

$$\begin{aligned}\Phi(x, y, z, t) = & \frac{U_{\text{RF}}}{2}(\alpha x^2 + \beta y^2 + \gamma z^2) \cos(\omega_{\text{RF}} t) \\ & + \frac{U_{\text{DC}}}{2}(\alpha' x^2 + \beta' y^2 + \gamma' z^2),\end{aligned}\tag{2.1}$$

where the coefficients satisfy $\alpha + \beta + \gamma = 0$, $\alpha' + \beta' + \gamma' = 0$ by Laplace's equation. To understand the dynamics of an ion in such a potential, it suffices to consider the corresponding equation of motion for one dimension at a time. An ion with charge q and mass m in this potential will obey the following equation of motion in the x direction:

$$\ddot{x} = -\frac{q}{m} [\alpha U_{\text{RF}} \cos(\omega_{\text{RF}} t) + \alpha' U_{\text{DC}}] x,\tag{2.2a}$$

and corresponding similar equations in the other Cartesian directions. This differential equation has the form of the Mathieu equation, whose standard form is typically written

$$\frac{d^2 x}{d\xi^2} + [a_x - 2q_x \cos(2\xi)]x = 0.\tag{2.2b}$$

Equation (2.2a) takes the form (2.2b) upon making the substitutions

$$\xi = \frac{\omega_{\text{RF}} t}{2}, \quad q_x = \frac{2q\alpha U_{\text{RF}}}{m\omega_{\text{RF}}^2}, \quad a_x = \frac{4q\alpha' U_{\text{DC}}}{m\omega_{\text{RF}}^2}.\tag{2.2c}$$

q_x and a_x are dimensionless parameters describing the strength of the confinement provided by the RF and DC components of the trapping potential, respectively. We are frequently most interested in understanding which choice of trapping potential parameters results in stable trapping. Of these, those which satisfy $|a_x|, q_x^2 \ll 1$ are of most experimental interest.

A treatment of the more general case can be found in Ref. [9]. Under the condition $|a_x|, q_x^2 \ll 1$, the solution to (2.2a) takes the approximate form

$$x(t) \approx A_x \cos(\omega_x t) \left[1 - \frac{q_x}{2} \cos(\omega_{\text{RF}} t) \right], \quad (2.3)$$

where $\omega_x \equiv \frac{1}{2} \omega_{\text{RF}} \sqrt{a_x + \frac{1}{2} q_x^2}$,

where A_x is the amplitude of the motion and depends on the initial conditions. This solution has two important features, manifested in the two terms. The first is a harmonic motion at the frequency $\omega_x \ll \omega_{\text{RF}}$ (since $|a_x|, q_x^2 \ll 1$ by assumption). The frequency of this motion is set by both the strength of the RF fields and the DC fields (q_x and a_x), and is slow compared to the frequency of the driven RF field. This is known as secular motion. A few points are worth noting explicitly about the secular frequency ω_x :

- ω_x depends on the amplitudes of the RF and DC potentials, U_{RF} and U_{DC} via q_x and a_x . In particular, it depends on a_x and on the square of q_x , so that an increased magnitude of the DC potential may either increase or decrease the secular frequency depending on its sign, while on the other hand an increased magnitude of the RF potential may only increase the secular frequency, independent of its sign.
- In the special case $a_x = 0$ (no DC contribution), the secular frequency is directly proportional to the amplitude of the RF drive, and inversely proportional to the drive frequency: $\omega_x \propto U_{\text{RF}}/\omega_{\text{RF}}$. To consider scaling with the ion mass, it is practical to fix the stability parameter q_x , in which case the secular frequency is inversely proportional to the square root of the ion mass: $\omega_x \propto m^{-1/2}$.

The second term is motion whose amplitude is small (reduced by a factor of $q_x/2$) and whose frequency (ω_{RF}) is fast compared to that of the secular motion. This is known as micromotion. If both q_x and the amplitude of the motion are sufficiently small, micromotion may be ignored, and the motion of the trapped particle may be described by its secular motion alone to a good approximation. This approximation will be used for the remainder of this work.

Approximating the time-averaged potential of a Paul trap as a static pseudopotential alone, the quantum mechanical Hamiltonian for the motion of a trapped ion of mass m in the x -direction becomes simply the standard harmonic oscillator Hamiltonian

$$H_{\text{motion},x} = \frac{p_x^2}{2m} + \frac{1}{2} m \omega_x^2 x^2 = \hbar \omega_x \left(a_x^\dagger a_x + \frac{1}{2} \right), \quad (2.4)$$

where ω_x is given by (2.3), and a_x^\dagger, a_x are the usual quantum harmonic oscillator creation and annihilation operators. Extending this to three dimensions (x, y, z), each of which in general has its own secular frequency $\omega_i = \frac{1}{2} \omega_{\text{RF}} \sqrt{a_i + \frac{1}{2} q_i^2}$, the total Hamiltonian of the motion of a single ion in a Paul trap is that of a three-dimensional harmonic oscillator:

$$H_{\text{motion}} = \hbar \omega_x \left(a_x^\dagger a_x + \frac{1}{2} \right) + \hbar \omega_y \left(a_y^\dagger a_y + \frac{1}{2} \right) + \hbar \omega_z \left(a_z^\dagger a_z + \frac{1}{2} \right). \quad (2.5)$$

2.2.3 Surface ion traps

To realize a Paul trap, a set of electrodes with appropriate geometry and corresponding voltages must be designed which approximately realizes the potential (2.1). Early realizations of the Paul trap utilized hyperbolic electrodes to create the quadratic potential as precisely as possible [10]. More modern realizations use electrodes with simpler geometries for ease of production and assembly, which still create an approximately quadratic potential in a smaller but large-enough region of space around the trap origin. One popular design is the 4-rod trap [11], with 4 parallel rods in a square configuration. Two rods opposite each other receive identical RF voltages $V_{RF} \sin(\omega_{RFT})$, while the other two are held at ground potential. This provides RF confinement parallel to the rods, while DC confinement is provided by a segmented rod or with “end cap” electrodes.

Three-dimensional Paul trap designs such as the 4-rod trap described above are typically macroscopic (many millimeters) in size and provide a straightforward method of achieving basic ion trapping functionality. More recently however, the field of ion trapping has developed research interests which extend beyond that which can be provided by macroscopic ion traps. Such extended functionality can instead be provided by a *surface trap* architecture, which is defined by flat electrodes on a single surface that can be printed onto a chip. The surface trap architecture was first realized by Refs. [12, 13].

The motivations for using surface traps over macroscopic traps are many, including:

- Miniaturization, which can allow finer control over local DC fields with a larger number of smaller independent DC electrodes.
- The potential to house multiple independent Coulomb crystals at once, and in turn the potential to “shuttle” individual ions or chains of ions from one location to another. This may allow scaling to larger number of ions than would be possible with a macroscopic trap.
- Reproducible, high-precision manufacturing with the help of well-established micro-fabrication techniques.
- The ability to integrate other components into the trap chip, such as detectors and optical components.
- The ability to realize complex electrode geometries.

All of these features are invaluable for quantum information processing using trapped ions, but the finer control allowed by surface traps is also advantageous for other types of trapped-ion experiments, including those studying fundamental physics. The “ring trap” design used in this work heavily relies on being able to have circular electrodes whose fabrication precision allows for a high degree of symmetry.

The surface trap architecture has some disadvantages over macroscopic ion traps. Since their geometry results in fields which deviate more from the ideal quadrupole potential

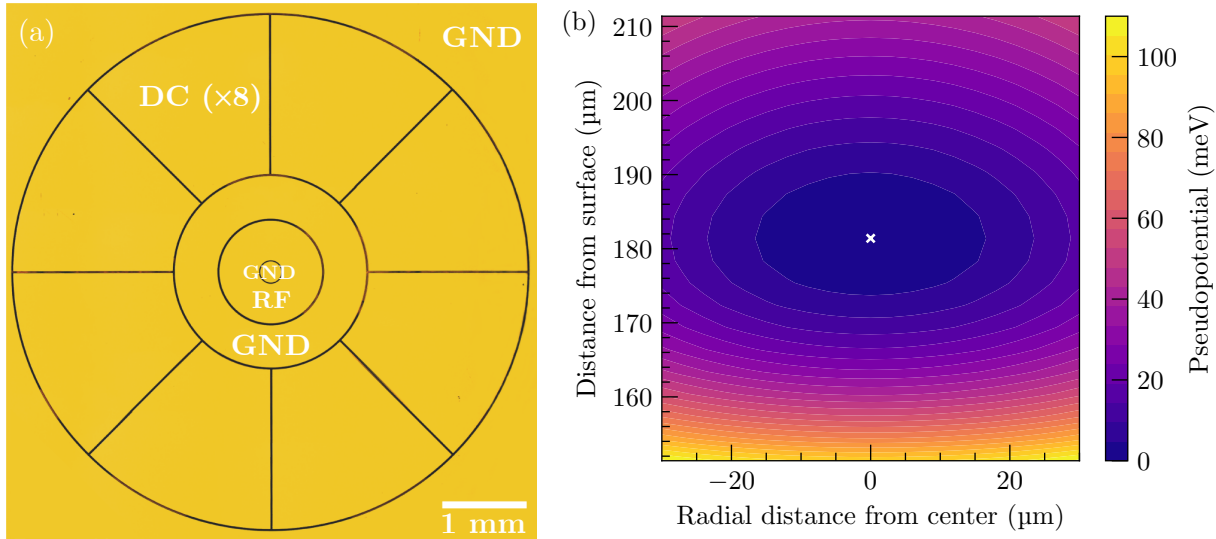


Figure 2.1: (a) Photograph of the ring trap illuminated under yellow light. Each electrode is marked by its function (RF, DC, or ground). (b) Simulated pseudopotential contour map for 21.4 MHz drive frequency and 100 V RF amplitude when applied to the second circular electrode as labeled in (a). The pseudopotential is cylindrically symmetric. The location of the potential minimum is shown by the white cross.

than those of macroscopic traps, the resulting trapping depth is significantly reduced. This problem is exacerbated by the fact that RF voltage amplitudes are typically more limited for fear of electrical breakdown between neighboring electrodes, which can be only micrometers apart from each other. The miniaturized nature of surface traps also results in small distances between the trapped ions and the nearest electrode surface, on the order of 100 μm . This makes the ion highly susceptible to electric field noise originating from the electrodes [14], which can spoil the cooling that is necessary for many applications. Finally, surface traps place limits on possible laser beam geometries.

2.2.4 The ring trap

The surface ion trap used in this work, referred to as the “ring trap”, is characterized by its circular symmetry. While most other ion traps produce an anisotropic pseudopotential such that $\omega_x \neq \omega_y \neq \omega_z$, the pseudopotential produced by the ring trap is cylindrically symmetric $\omega_x = \omega_y < \omega_z$, where here the z -direction is normal to the trap surface. This allows ion crystals in the xy -plane to freely rotate. This rotational motion is the scientific basis of all work in this thesis.

An image of the ring trap is shown in Fig. 2.1(a). The trap is fabricated from boron-doped silicon, which extrudes to a thickness of 250 μm above a glass substrate. The three circular center electrodes have outer radii of 125 μm , 600 μm , and 1100 μm . The eight outer electrodes have outer radii of 3000 μm . The trench between the center electrode and its neighbor is

$15\text{ }\mu\text{m}$ wide, and all others are $25\text{ }\mu\text{m}$ wide. The inner and outer circular electrodes are internally shorted to each other. More details about the trap design and fabrication can be found in Refs. [15, 16]. The circular “RF” electrodes create the trapping potential. This is done by applying RF voltage to the second of the three circular electrodes, and using the innermost and outermost circular electrodes as a ground reference. The circular electrodes have a capacitance of approximately 15 pF between them. The outer “DC” electrodes receive DC voltages for applying static fields, which are used to compensate stray dipole fields which otherwise result in excess micromotion [17], and to compensate stray quadrupole fields which otherwise break the cylindrical symmetry. The DC electrodes are also used to apply quadrupole fields which intentionally break the circular symmetry when desired, such as for ease of electronic state preparation and for rotating an ion crystal; see Chapter 6. It should be noted that the configuration of RF voltages discussed here and utilized in the rest of this work differs from that of Refs. [15, 16]. There, RF is applied instead to the innermost and outermost circular electrodes, with the second one held at ground. This configuration produces a different potential, with a toroidal RF null. Here, the pseudopotential has an RF null at a single point.

The pseudopotential produced by the ring trap is shown in Fig. 2.1(b). Solving for this pseudopotential is straightforwardly done by numerically computing a single integral for each RF electrode, owing to the rotational symmetry [18, 19]. The RF null is at the potential minimum at a height of $181\text{ }\mu\text{m}$ above the surface. We operate the trap at an RF drive frequency of $\omega_{\text{RF}} = 2\pi \times 21.4\text{ MHz}$. Application of 100 V amplitude at this drive frequency results in secular trap frequencies $\omega_x = \omega_y = 2\pi \times 1.45\text{ MHz}$ in the radial direction and $\omega_z = 2\pi \times 2.90\text{ MHz}$ normal to the trap surface for $^{40}\text{Ca}^+$, the ion used in this work.

A DC contribution to the trapping potential may be added by applying an offset bias to the RF drive, either by applying a DC voltage to the two grounded circular electrodes or by biasing the mean voltage of the RF drive. The lowest-order term of this contribution has the form $\Phi_{\text{DC}}(x, y, z) = U_2(2z^2 - x^2 - y^2)/2$, thus providing a stronger confinement in the radial direction and weakening the overall confinement in the z -direction, or vice-versa, depending on the sign of U_2 . Doing so does not change the equilibrium height of the ion above the surface.

Instrumentation for providing the RF and DC voltages to operate the ring trap is discussed in Chapter 4.

2.3 Theory of light-atom interactions

The primary method of controlling the quantum state of trapped atoms in general, including trapped ions, is by interaction with laser light. This can be done in a coherent manner such that the purity of the quantum state is (approximately) preserved in order to engineer useful quantum superpositions, or it can be done in an incoherent manner, involving dissipation, for the purposes of laser cooling the motion or pumping the internal state. This section will introduce the physics of such interactions, by first introducing the physics of the light

and the atoms individually, and then describing how they interact with each other, both coherently and incoherently. These interactions are the basis of all experiments conducted in this thesis.

2.3.1 Light

The classical electromagnetic fields \mathbf{E} and \mathbf{B} , in the presence of a charge density ρ and a current density \mathbf{J} , obey Maxwell's equations

$$\begin{aligned}\nabla \cdot \mathbf{E} &= \frac{\rho}{\epsilon_0} & \nabla \times \mathbf{E} &= -\frac{\partial \mathbf{B}}{\partial t} \\ \nabla \cdot \mathbf{B} &= 0 & \nabla \times \mathbf{B} &= \frac{1}{c^2} \frac{\partial \mathbf{E}}{\partial t} + \mu_0 \mathbf{J},\end{aligned}\tag{2.6}$$

where ϵ_0 and μ_0 are the permittivity and permeability of free space, and c is the speed of light. Defining the vector potential \mathbf{A} along with the scalar potential Φ such that

$$\begin{aligned}\mathbf{E} &= -\nabla\Phi - \frac{\partial \mathbf{A}}{\partial t} \\ \mathbf{B} &= \nabla \times \mathbf{A},\end{aligned}\tag{2.7}$$

and defining \mathbf{A} in the Coulomb gauge such that $\nabla \cdot \mathbf{A} = 0$, we find that \mathbf{A} obeys the wave equation

$$\nabla^2 \mathbf{A} = \frac{1}{c^2} \frac{\partial^2 \mathbf{A}}{\partial t^2}\tag{2.8}$$

in free space, i.e. when $\rho = 0$, $\mathbf{J} = 0$. Solutions appear in the form of propagating plane waves

$$\mathbf{A}(\mathbf{r}, t) = -\frac{i}{2} A [\hat{\epsilon} e^{i(\mathbf{k} \cdot \mathbf{r} - \omega t + \phi)} - \hat{\epsilon}^* e^{-i(\mathbf{k} \cdot \mathbf{r} - \omega t + \phi)}]\tag{2.9}$$

with $\omega/|\mathbf{k}| = c$ and $\hat{\epsilon} \cdot \mathbf{k} = 0$. From (2.7), the electric and magnetic fields can then be computed as

$$\mathbf{E}(\mathbf{r}, t) = \frac{1}{2} A \omega [\hat{\epsilon} e^{i(\mathbf{k} \cdot \mathbf{r} - \omega t + \phi)} + \hat{\epsilon}^* e^{-i(\mathbf{k} \cdot \mathbf{r} - \omega t + \phi)}]\tag{2.10a}$$

$$\mathbf{B}(\mathbf{r}, t) = \frac{1}{2} A [(\mathbf{k} \times \hat{\epsilon}) e^{i(\mathbf{k} \cdot \mathbf{r} - \omega t + \phi)} + (\mathbf{k} \times \hat{\epsilon}^*) e^{-i(\mathbf{k} \cdot \mathbf{r} - \omega t + \phi)}].\tag{2.10b}$$

Such plane wave solutions are a good approximation of the laser-produced light fields used in this work. Often we are interested in a few key properties of the electric field of the plane wave: the frequency ω , the amplitude $E = A\omega$, the polarization vector $\hat{\epsilon}$, the wavevector \mathbf{k} (related to the frequency by $|\mathbf{k}| = \omega/c$), and the phase ϕ .

The above is a classical description of the electromagnetic field. In general, it may also be described quantum mechanically. This thesis will not go into a quantitative description of the quantized electromagnetic field, but two important features which emerge from the

quantized picture are worth noting. The first is that from the quantized electromagnetic field emerges the concept of a photon, meaning the energy of a mode of the field with frequency ω is quantized to units of $\hbar\omega$. The second is that interactions between atoms and the quantum fluctuations of the electromagnetic field in its vacuum (zero-photon) state lead to spontaneous emission, by which an atom incoherently decays toward its ground state, a phenomenon which is not present in a purely classical EM field description.

2.3.2 Atoms

The only light-matter interactions of interest in this thesis are those of laser light with hydrogen-like atoms. Thus this section will only address the physics of isolated hydrogen-like atoms. Here, “hydrogen-like” means the atom features a single valence electron — it may have many electrons in total, but one should be significantly more weakly bound than the rest. It is useful to break the degrees of freedom into two parts: the “motional” (or “external”) degrees of freedom, and the “electronic” (or “internal”) degree of freedom. The external degrees of freedom describe the motion of the atom overall in free space. In a Paul trap, the only motional potential of interest in this thesis, the external degrees of freedom of a single trapped ion are as described in Sec. 2.2, particularly Eq. (2.5). The internal degree of freedom describes the motion of the valence electron about the nucleus and inner core of electrons.

Like any bound quantum mechanical system, a hydrogen-like atom features quantized energy eigenstates. The most important practical features of these states are the energy itself and the values of the various corresponding angular momenta, as these properties determine the properties of the light fields that are necessary to couple the atomic states together. This subsection outlines how these properties emerge from the atomic structure, namely, the behavior of the valence electron. This is done first excluding fine-structure effects and then including them. Hyperfine structure is not considered, since it is not applicable to the atoms used in this work.

Atomic structure in the electrostatic model

For the electrostatic hydrogen-like model [20], we may assume that the valence electron sees a spherically symmetric potential $U(r)$, so the Hamiltonian is

$$H_{ES} = \frac{p^2}{2m} + U(r), \quad (2.11)$$

where p is the momentum operator for the valence electron and m is the electron mass. Here, electrostatic means ignoring magnetic and radiation effects. In solving the Schrödinger equation, one finds that the eigenstates of this Hamiltonian are indexed by three numbers n, ℓ, m_ℓ , and can be split into a product of two parts, the angular wavefunction and the radial wavefunction.

- The angular eigenfunctions are the spherical harmonics $Y_{\ell m_\ell}(\theta, \phi)$ (in spherical coordinates), a result which is independent of the potential $U(r)$ (as long as it is spherically symmetric). The quantum number ℓ represents the total orbital angular momentum of the electron, and m_ℓ is the projection onto a quantization axis (usually along an applied external magnetic field).
- The radial eigenfunctions $R_{n\ell}(r)$ depend on the spherical radial coordinate only and depend on the potential $U(r)$.

The energy $E_{n\ell}$ of the eigenfunctions is independent of m_ℓ due to spherical symmetry (in the absence of an external magnetic field). Importantly, the radial eigenfunctions and energies cannot in general be solved for exactly. The hydrogen atom, with a single proton and a single electron, is an exception: its potential is $U_H(r) = -\frac{e^2}{4\pi\epsilon_0 r}$, with energy eigenvalues $E_n = -\frac{me^4}{2\hbar^2(4\pi\epsilon_0)^2 n^2} \approx \frac{-13.6 \text{ eV}}{n^2}$. For hydrogen, the energy eigenvalues are independent of ℓ , a result of the $1/r$ scaling of the potential. This is not true for other atoms, including $^{40}\text{Ca}^+$ used in this thesis, whose energies depend on ℓ . However, for most atoms which are not too heavy, this result is still instructive, as it gives an indication of the order of magnitude of energy splittings ($13.6 \text{ eV} \sim 3300 \text{ THz}$ in frequency units), as well as the scaling of energy with $-1/n^2$ which still approximately holds true.

Atomic structure with fine structure

The only correction to the electrostatic model that will be necessary to consider for this thesis is fine structure. The fine-structure correction arises from the leading order relativistic correction, and includes three terms: the kinetic term, the Darwin term, and the spin-orbit term [21]. The first two are purely “orbital” effects and depend only on the orbital angular momentum quantum number ℓ . The spin-orbit effect, however, importantly modifies the angular momentum structure relative to the spinless model.

The spin-orbit effect takes into account the spin \mathbf{S} of the electron, which in turn couples magnetically to its own angular momentum \mathbf{L} , resulting in a term in the Hamiltonian proportional to $\mathbf{S} \cdot \mathbf{L}$. This means that the total angular momentum \mathbf{J} of the system is the sum of the spin and orbital angular momenta, $\mathbf{J} = \mathbf{S} + \mathbf{L}$, and hence m_ℓ is no longer a good quantum number; instead, the magnetic quantum number should be the projection of the *total* angular momentum onto to the quantization axis, m_j . For single-electron atoms, the electron spin is always $1/2$, and therefore the spin-orbit coupling may be thought of in the following way: A state with a given ℓ value splits due to spin-orbit coupling into two states, one in which the spin and orbital angular momenta are parallel giving $j = \ell + 1/2$, and one in which they are anti-parallel giving $j = \ell - 1/2$ (the exception is $\ell = 0$, for which there is only $j = 1/2$). The energy difference between these is given by the spin-orbit term of the Hamiltonian and is roughly of order 1 THz.

In total, fine structure corrections may be regarded as a correction term H_{FS} to the electrostatic model, so that the total Hamiltonian of the atom's valence electron is

$$H_0 = \frac{p^2}{2m} + U(r) + H_{FS}, \quad (2.12)$$

which is labeled H_0 in anticipation of adding an interaction term when a light field is introduced. Including fine structure effects, the atomic eigenstates may be labelled $|n, \ell, s, j, m_j\rangle$. For hydrogen-like atoms, s is always equal to $1/2$, but it is included here for completeness.

Zeeman splitting

There are many effects which can shift the energies of the atomic eigenstates of the Hamiltonian (2.12), but the Zeeman effect is of the most relevance in this thesis. This couples a static external magnetic field \mathbf{B} to the angular momentum of the electron via its magnetic moment $\boldsymbol{\mu}$, shifting the energy of the state $|n, \ell, s, j, m_j\rangle$ by

$$\Delta E_{\text{Zeeman}} = -\boldsymbol{\mu} \cdot \mathbf{B} = -g_j \mu_B B m_j, \quad (2.13)$$

where μ_B is the Bohr magneton, B is the magnitude of the magnetic field, and the Landé g-factor g_j is given by

$$g_j = 1 + \frac{j(j+1) + s(s+1) - \ell(\ell+1)}{2j(j+1)} \quad (2.14)$$

In practice, an external magnetic field is applied to define an axis along which the angular momentum \mathbf{J} is quantized, and to split the energies of states which differ only in m_j by an amount on the order of 1 MHz per Gauss.

2.3.3 Coupling of atoms to light

The coupling of an atom to the electromagnetic field results in coupling of the atomic eigenstates $|n, \ell, s, j, m_j\rangle$ to each other. This is the mechanism by which we experimentally engineer the quantum state of the atom; by coupling otherwise stationary eigenstates together, one may induce transitions between them. It is therefore important to understand the underlying physics in order to predict what transitions are possible, the conditions under which they may occur, the strength of the coupling, and the coherence of the process. A perturbative expansion of the coupling Hamiltonian due to the light field results in a multipole expansion, giving rise to a useful categorization of transition types by leading multipole order; transitions of higher leading multipole order are suppressed by a factor of $\sim 10^4 - 10^5$ in coupling strength.

A description which excludes the motion of the atom in the trap will suffice, as the electron's motion about the nucleus takes place on very rapid time scales (transition frequencies of $\sim 10^{14}$ Hz), while the motion of the atom in the trap is comparatively slow ($\sim 10^6$ Hz). Therefore, the valence electron can respond effectively instantaneously as the nucleus moves

within the trap, so that a perfectly motionless atom is an adequate approximation for describing the dynamics of the valence electron interacting with light. The effects of atomic motion may thus be considered separately later.

The light-atom interaction Hamiltonian

In the absence of any interaction, the Hamiltonian of the atom is (2.12). Introducing the light field modifies the Hamiltonian to approximately [22]

$$H = \frac{1}{2m} [\mathbf{p} + e\mathbf{A}(\mathbf{r})]^2 + U(r) + \frac{e}{m} \mathbf{S} \cdot \mathbf{B}(\mathbf{r}) \quad (2.15)$$

where the canonical momentum \mathbf{p} has been modified to include the vector potential, $\mathbf{p} \rightarrow \mathbf{p} + e\mathbf{A}(\mathbf{r})$, and the spin \mathbf{S} of the electron may now interact with an external magnetic field \mathbf{B} .

The total Hamiltonian including this interaction is most usefully organized into three terms, $H = H_0 + H_1 + H_2$, with H_0 given by (2.12) and

$$H_1 = \frac{e}{m} [\mathbf{p} \cdot \mathbf{A}(\mathbf{r}) + \mathbf{S} \cdot \mathbf{B}(\mathbf{r})], \quad (2.16a)$$

$$H_2 = \frac{e^2}{2m} \mathbf{A}(\mathbf{r})^2. \quad (2.16b)$$

This is an expansion in the coupling of the atom to the field. If the amplitude of the field is weak compared to that seen by the electron due to the nucleus (as is the case in most applications), then H_2 is small compared to H_1 , and H_1 is small compared to H_0 . We may therefore regard H_1 as the first-order perturbation expansion, and ignore H_2 as higher order.

The multipole expansion of H_1

This atom-light perturbation Hamiltonian may couple different atomic eigenstates $|nlsjm_j\rangle$ and $|n'l's'j'm'_j\rangle$ together if $\langle n'l's'j'm'_j | H_1 | nlsjm_j \rangle \neq 0$. Computing this matrix element, or at least predicting its order of magnitude, is therefore important in understanding possible transitions between a given pair of atomic energy levels.

In the presence of a plane-wave field as in (2.9) and (2.10), the fields $\mathbf{A}(\mathbf{r})$ and $\mathbf{B}(\mathbf{r})$ have a constant amplitude, and a phase $e^{i(\mathbf{k} \cdot \mathbf{r} - \omega t)}$. The field therefore varies spatially on a length scale $\sim 1/k$; this is typically much larger than the spatial extent of the radial wavefunction of the eigenstates being considered in the matrix element, so that $\mathbf{k} \cdot \mathbf{r} \ll 1$. This allows for an expansion of H_1 in $\mathbf{k} \cdot \mathbf{r}$. Using (2.16a) for H_1 and (2.9) and (2.10) for the fields, this expansion takes the form [22]

$$\begin{aligned} H_1 = & \frac{eA}{2m} (\mathbf{p} \cdot \hat{\epsilon}) e^{-i\omega t} + h.c. \\ & + \frac{ieA}{2m} [(\mathbf{p} \cdot \hat{\epsilon})(\mathbf{k} \cdot \mathbf{r}) + \mathbf{S} \cdot (\mathbf{k} \times \hat{\epsilon})] e^{-i\omega t} + h.c. \\ & + \text{higher-order terms.} \end{aligned} \quad (2.17)$$

This is the multipole expansion: the first term is the electric dipole term, and the second is the sum of the electric quadrupole term and magnetic dipole term, which are of the same order.

A typical order of magnitude for the factor $\mathbf{k} \cdot \mathbf{r}$ is 10^{-2} (averaged over the operator \mathbf{r} along the spatial extent of the electron's wavefunction). $\mathbf{S} \cdot (\mathbf{k} \times \hat{\epsilon})$ is of the same order relative to $\mathbf{p} \cdot \hat{\epsilon}$. Therefore, in evaluating H_1 , it is often a good approximation to consider only the leading order contribution in the multipole expansion, and in turn, the leading order term for any given transition of interest has significant impact on the corresponding transition rate. For this reason, the most important classification of atomic transitions is by their leading multipole order.

The work in this thesis uses only electric dipole (E1) transitions and electric quadrupole (E2) transitions, and thus these are the only types of transitions considered here. Other trapped-ion work commonly uses magnetic dipole (M1) transitions, two-photon Raman transitions, or sometimes electric octupole (E3) transitions.

It can be shown that the electric dipole term of the light-matter interaction Hamiltonian H_1 can be written as the interaction of the electric field with the dipole moment of the atom:

$$H_1^{E1} = -\mathbf{E} \cdot e\mathbf{r}, \quad (2.18a)$$

and that the electric quadrupole term can be written as the interaction of the gradient of the electric field with the quadrupole moment $Q_{ij} = r_i r_j - \frac{1}{3}r^2 \delta_{ij}$:

$$H_1^{E2} = \frac{1}{2} \nabla_i E_j e Q_{ij}. \quad (2.18b)$$

In general, each multipole term has associated with it a spherical tensor operator in space (e.g. \mathbf{r} for E1 and Q for E2), whose rank increases as the multipole order of interest increases.

Selection rules

In classifying atomic transitions it is useful to be able to predict, without needing to carry out a full calculation, which multipole order a transition will be. Rules of symmetry via parity and angular momentum addition provide convenient shortcuts for this known as selection rules. Selection rules for E1 and E2 transitions are shown in Tab. 2.1. If a transition violates a selection rule, it guarantees that the corresponding multipole term vanishes, but the converse is not necessarily true. For example, for the special case of a $j = 0 \rightarrow j' = 0$ transition, the condition $\Delta j = 0$ holds, but E1 and E2 terms will still both vanish due to angular momentum addition rules. In general, the change in angular momentum quantum numbers is what determines the multipole order of a transition.

Driven and spontaneous atomic transitions

A coherent light field with well-defined frequency such as that from a laser will drive transitions between two eigenstates $|nlsm_j\rangle$ and $|n'l's'j'm'_j\rangle$ (or $|a\rangle$ and $|b\rangle$ for brevity) whose

Multipole order	Selection rules
E1	$\Delta\ell = \pm 1, \Delta j = 0, \pm 1, \Delta m_j = 0, \pm 1$
E2	$\Delta\ell = 0, \pm 2, \Delta j = 0, \pm 1, \pm 2, \Delta m_j = 0, \pm 1, \pm 2$

Table 2.1: Selection rules for the E1 and E2 terms of the atomic transition multipole expansion. These are necessary conditions for the corresponding terms to be nonzero.

energy difference is $\hbar\omega_{ab}$ if the light field is resonant, i.e. the light field frequency ω matches the atomic transition frequency: $\omega = \omega_{ab}$. The populations of the two states will exchange sinusoidally, at a frequency Ω known as the Rabi frequency given by

$$\Omega = \frac{\langle b|H_1|a\rangle}{\hbar} = \begin{cases} \frac{eE}{\hbar} \hat{\epsilon} \cdot \langle b|\mathbf{r}|a\rangle, & \text{E1 transitions} \\ \frac{e\nabla\mathbf{E}}{2\hbar} \hat{\epsilon}\hat{k} \langle b|Q|a\rangle, & \text{E2 transitions.} \end{cases} \quad (2.19)$$

Note that the Rabi frequency is directly proportional to the amplitude of the light field, and also depends its geometry via its polarization vector $\hat{\epsilon}$ and its wavevector \mathbf{k} . A more detailed recipe for computing these matrix elements can be found in Ref. [23].

Even in the absence of an external light field, atomic eigenstates which are not the ground state have a finite lifetime due to spontaneous emission, which occurs due to the coupling of the atom to the quantized electromagnetic field. A description of the quantized electromagnetic field is beyond the scope of this work, but the result is as follows: Letting $|b\rangle$ be the upper of the two states of interest, the spontaneous emission rate is written as Γ_b , and the lifetime is $\tau_b = 1/\Gamma_b$. The spontaneous emission rate is directly related to the atomic matrix element for the corresponding multipole order. For electric dipole transitions:

$$\Gamma_b = \frac{e^2\omega_{ab}^3}{3\pi\epsilon_0\hbar c^3} |\langle b|\mathbf{r}|a\rangle|^2, \quad (2.20a)$$

and for electric quadrupole transitions [23],

$$\Gamma_b = \frac{e^2\omega_{ab}^5}{60\pi\epsilon_0\hbar c^5} |\langle b|Q|a\rangle|^2. \quad (2.20b)$$

Both the Rabi frequency Ω and the spontaneous emission rate Γ_b are related to the matrix element $\langle b|T|a\rangle$, where T is the appropriate spherical tensor operator for the multipole order of the transition. In practice, the matrix element often cannot be computed from first principles, as it is in general not possible to solve for the radial part $R_{n\ell}(r)$ in atoms more complex than hydrogen. Instead, state lifetimes are experimentally measured directly.

Two-level transitions with a long lifetime will also have a slower Rabi frequency. As an example, we can consider the transition from the state ${}^4S_{1/2}(m=-1/2)$ to ${}^3D_{5/2}(m=-1/2)$ in ${}^{40}\text{Ca}^+$, the ion used in this thesis. This is the common spectroscopic notation for the states

which in the previous notation would be written as $|n = 4, \ell = 0, s = 1/2, j = 1/2, m_j = -1/2\rangle, |n' = 3, \ell = 2, s = 1/2, j = 5/2, m_j = -1/2\rangle$. This is an E2 transition; its wavelength is 729 nm, and its spontaneous emission rate is $\Gamma_{D_{5/2}} \approx 0.8 \text{ s}^{-1}$. A 30 mW 729 nm beam focused to a Gaussian waist 10 μm in diameter, whose polarization and wavevector are optimized for coupling to this transition, would drive it at a rate $\Omega = 2\pi \times 1 \text{ MHz}$. In comparison, if we instead consider the $^4S_{1/2}(m=-1/2)$ to $^4P_{1/2}(m=-1/2)$ E1 transition at 397 nm, the same Rabi frequency can be achieved with a laser power of merely 5 nW.

The pronounced difference makes E1 and E2 transitions useful for different processes. In summary:

- Electric dipole transitions have a short lifetime and are therefore useful for incoherent processes, in which the upper state lifetime $1/\Gamma_b$ is much shorter than the timescale of the process of interest. Here, spontaneous emission dominates and photons are quickly scattered by the atom from the laser field.
- Electric quadrupole (and other) transitions have a long lifetime and are therefore useful for coherent processes, in which $\Omega \gg \Gamma_b$. Here, spontaneous emission may be negligible, and quantum coherent effects can be engineered and measured. Driving these transitions generally requires a few orders of magnitude more laser power than E1 transitions.

The following section outlines basic dynamical processes of such coherent and incoherent light-atom interactions.

2.4 Light-atom interaction dynamics

This section will introduce the dynamics of both coherent and incoherent light-atom interactions, eventually including as well the overall motion of the ion in the Paul trap, which is also an important element in the experiments performed here. The discussion will be restricted to the case of only two atomic energy levels $|a\rangle$ and $|b\rangle$, with a single laser field (at least nearly) resonant with their transition frequency ω_{ab} .

2.4.1 Coherent interactions, excluding ion motion

In the simplest case, with two atomic energy levels where spontaneous emission can be neglected (because e.g. they are connected via an electric quadrupole transition so that the upper state exhibits a slow decay rate), it is instructive to write the atomic Hamiltonian in the absence of a light field, H_0 , in the $\{|a\rangle, |b\rangle\}$ basis:

$$H_0 = -\frac{1}{2}\hbar\omega_{ab}|a\rangle\langle a| + \frac{1}{2}\hbar\omega_{ab}|b\rangle\langle b| \quad (2.21)$$

Introducing the laser field adds H_1 (2.16a) to the Hamiltonian, coupling the two energy levels with some Rabi frequency Ω , defined by (2.19). The Hamiltonian for this interaction in the $\{|a\rangle, |b\rangle\}$ basis is

$$H_1 = (\Omega |b\rangle\langle a| + \Omega^* |a\rangle\langle b|) \cos(\omega t - \phi). \quad (2.22)$$

We may choose phases such that $\Omega = \Omega^*$ and $\phi = 0$, for convenience.

The total Hamiltonian for coherent interactions can be written as a 2×2 matrix:

$$H = H_0 + H_1 = \frac{1}{2}\hbar \begin{pmatrix} -\omega_{ab} & \Omega \cos(\omega t) \\ \Omega \cos(\omega t) & \omega_{ab} \end{pmatrix} \quad (2.23)$$

The dynamics are more easily analyzed in a “rotating frame”, defined by the unitary transformation

$$U(t) = e^{-i\frac{1}{2}\omega t(|b\rangle\langle b| - |a\rangle\langle a|)}. \quad (2.24)$$

The unitary transformation transforms the Hamiltonian as $H \rightarrow U^\dagger H U + i\hbar \dot{U}^\dagger U$, yielding the new rotating-frame Hamiltonian

$$H = \frac{1}{2}\hbar \begin{pmatrix} \omega - \omega_{ab} & \Omega(1 + e^{-2i\omega t}) \\ \Omega(1 + e^{2i\omega t}) & -(\omega - \omega_{ab}) \end{pmatrix} \quad (2.25)$$

Here we can invoke an approximation to get rid of the remaining time-dependence, the “rotating wave approximation” (RWA). This comes from the observation that the Rabi frequency (\sim kHz – MHz) is nearly always significantly slower than the laser frequency (\sim 100 THz). Therefore, on the timescale of the dynamics $\sim 1/\Omega$, the $e^{\pm 2i\omega t}$ terms will rapidly oscillate and average to zero; thus we neglect them in the RWA. Doing so gives the Hamiltonian

$$H \approx \frac{1}{2}\hbar \begin{pmatrix} \omega - \omega_{ab} & \Omega \\ \Omega & -(\omega - \omega_{ab}) \end{pmatrix} = \frac{1}{2}\hbar \begin{pmatrix} \Delta & \Omega \\ \Omega & -\Delta \end{pmatrix}, \quad (2.26)$$

where Δ is defined as the difference between the laser frequency and the transition frequency and is known as the detuning.

The most basic dynamics problem is to suppose that the system begins in the state $|a\rangle$ initially and, at time $t = 0$, begins evolving under the Hamiltonian (2.26) (due to e.g. the laser being turned on at that time). The quantity of interest is the probability that the system, after a time t , is found to have transitioned to the state $|b\rangle$ upon measurement. From the Schrödinger equation, this can be solved for exactly:

$$P_b(t) = |\langle b|e^{-iHt}|a\rangle|^2 = \frac{\Omega^2}{\Omega^2 + \Delta^2} \sin^2 \left(\frac{1}{2}\sqrt{\Omega^2 + \Delta^2} t \right). \quad (2.27)$$

The transition probability oscillates at a frequency $\sqrt{\Omega^2 + \Delta^2}$, with an amplitude $\Omega^2/(\Omega^2 + \Delta^2)$. On resonance ($\Delta = 0$), the frequency of these oscillations is equal to the Rabi frequency and the transition probability reaches unity after a time $t = \pi/\Omega$. If the

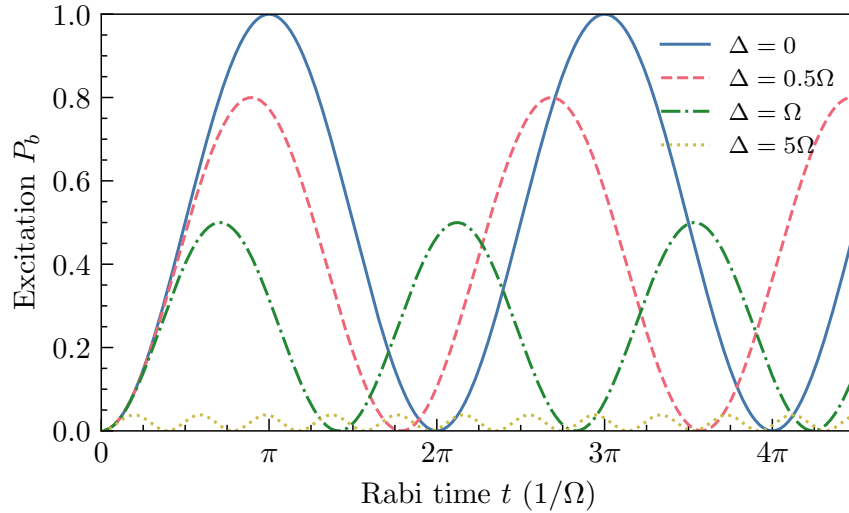


Figure 2.2: Ideal 2-level Rabi oscillations for various detunings, which are quantified in terms of the Rabi frequency.

laser frequency does not quite match the transition frequency so that $\Delta \neq 0$, the maximum transition probability falls short of unity. Quantitatively, a laser field is nearly resonant if $\Delta \ll \Omega$. Far from resonance, the transition probability is small.

In a more complete picture in which the system has more than two energy levels, off-resonant effects may need to be considered even when resonantly addressing one transition. The effect of having an off-resonant transition while addressing another should be accounted for if the detuning to the off-resonant transition is comparable to its corresponding Rabi frequency. Off-resonant effects can become important, for example, when addressing a motional sideband of an electronic transition, as the motional sideband frequencies and the electronic carrier transition Rabi frequencies can both be on the same order ~ 1 MHz.

2.4.2 Incoherent interactions, excluding ion motion

In addition to coherent dynamics, atomic states can also experience decoherence. In the two-level picture, there are two important ways in which this can occur:

- An external imperfection decays the coherence between the states $|a\rangle$ and $|b\rangle$, such as a noisy external magnetic field which randomly shifts the energies and thereby dephases the rate of coherent evolution, or a noisy laser frequency which effectively causes similar dephasing effects.
- Spontaneous emission, a fundamental effect caused by coupling of the upper state to the quantized electromagnetic field, which causes the population of the upper state to decay into the lower state and also decays the coherence between them.

It will suffice to consider these effects in terms of the spontaneous emission rate Γ_b given by (2.20), and an additional dephasing rate γ_{ab} which accounts for possible imperfections.

The Lindblad master equation which describes spontaneous emission and dephasing gives rise to a coupled set of equations for the elements of the density matrix of the system, which includes the populations ρ_{aa} , ρ_{bb} ($\rho_{aa} + \rho_{bb} = 1$) and the coherences $\rho_{ab} = \rho_{ba}^*$. These are the optical Bloch equations:

$$\dot{\rho}_{bb} = -\Gamma_b \rho_{bb} + \frac{i}{2} \Omega^* \rho_{ba} - \frac{i}{2} \Omega \rho_{ab} \quad (2.28a)$$

$$\dot{\rho}_{aa} = \Gamma_b \rho_{bb} - \frac{i}{2} \Omega^* \rho_{ba} + \frac{i}{2} \Omega \rho_{ab} \quad (2.28b)$$

$$\dot{\rho}_{ab} = -\left(\frac{\Gamma_b}{2} + \gamma_{ab}\right) \rho_{ab} - i\Delta \rho_{ab} - \frac{i}{2} \Omega^* (\rho_{bb} - \rho_{aa}) \quad (2.28c)$$

$$\dot{\rho}_{ba} = -\left(\frac{\Gamma_b}{2} + \gamma_{ab}\right) \rho_{ba} + i\Delta \rho_{ba} + \frac{i}{2} \Omega (\rho_{bb} - \rho_{aa}) \quad (2.28d)$$

In the absence of decoherence effects Γ_b and γ_{ab} , these equations reproduce the coherent 2-level light-matter interaction Hamiltonian (2.26). Dissipation from spontaneous emission can be thought of as the atom randomly emitting a photon into free space after absorbing one from the driving field, which has the effect of driving the state down from $|b\rangle$ to $|a\rangle$, damping the dynamics.

A quantity that is often of interest is the scattering rate of photons at the equilibrium state where the rate of photon absorption from the driving field is balanced by the rate of spontaneous emission. In the absence of any additional dephasing, this will be given by

$$R_{\text{scatter}} = \Gamma_b \rho_{bb} = \Gamma_b \frac{\Omega^2}{2\Omega^2 + \Gamma_b^2 + 4\Delta^2} = \frac{\Gamma_b}{2} \frac{s}{1 + s + \left(\frac{2\Delta}{\Gamma_b}\right)^2}, \quad (2.29)$$

where $s \equiv 2\Omega^2/\Gamma^2$ is known as the saturation parameter, and measures the driven transition rate due to the laser in comparison to the maximum possible driving rate, which is limited by the damping Γ_b [9]. The scattering rate is important for processes which utilize photon scattering, for example to cool the motion of the atom.

2.4.3 Coherent interactions, including ion motion

Up to here, Secs. 2.3 and 2.4 have included only a single degree of freedom, that of the valence electron moving around the nucleus. In the field of trapped ions, the quantum mechanical motion of the ion within the trap is considered equally important.

As described in Sec. 2.2, the quantum mechanical motion of a single trapped ion may be described as a three-dimensional quantum harmonic oscillator, with mode frequencies ω_x , ω_y , ω_z , and corresponding annihilation operators a_x , a_y , a_z . It will suffice to consider only one of these degrees of freedom, say the x -direction, dropping for convenience the subscript

on the creation/annihilation operators which we write as a^\dagger and a (we keep the x subscript in the mode frequency ω_x to distinguish it from the laser frequency ω).

To account for ion motion in the atom-light dynamics, we must modify the Hamiltonian (2.23) in two ways: (1) the interaction-free Hamiltonian H_0 must include the Hamiltonian of the harmonic-oscillator motion of the ion's center of mass $\hbar\omega_x(a^\dagger a + 1/2)$, and (2) the factor $\cos(\omega t)$ for the light field in the interaction Hamiltonian must now include the position-dependence, modifying it to $\cos(k_x x - \omega t)$. The Hamiltonian reads

$$\begin{aligned} H &= H_0 + H_1, \\ H_0 &= \hbar\omega_x(a^\dagger a + \frac{1}{2}) + \frac{1}{2}\hbar\omega_{ab}(|b\rangle\langle b| - |a\rangle\langle a|) \\ H_1 &= \hbar\Omega(|b\rangle\langle a| + |b\rangle\langle a|)\cos(k_x x - \omega t). \end{aligned} \quad (2.30)$$

Writing the position operator x in terms of the harmonic oscillator creation and annihilation operators,

$$\begin{aligned} k_x x &= k_x \sqrt{\frac{\hbar}{2m\omega_x}}(a + a^\dagger) = \eta(a + a^\dagger), \\ \eta &\equiv k_x \sqrt{\frac{\hbar}{2m\omega_x}}. \end{aligned} \quad (2.31)$$

Here, m now stands for the mass of the ion, rather than the mass of the electron. This defines the Lamb-Dicke parameter η , which can be regarded as the ratio between the spatial extent of the ground-state wavefunction of the ion motion and the laser wavelength divided by 2π . More precisely, it also accounts for the wavevector's projection onto the direction of the ion motion, since only the component k_x enters the definition. Often $\eta \ll 1$, making it a good expansion parameter.

It is useful to transform into the interaction picture, a rotating frame defined by the unitary transformation $U = e^{-iH_0 t/\hbar}$, where H_0 now includes both the internal and motional Hamiltonians. The transformed Hamiltonian is $H_I = U^\dagger H_1 U$. Applying this transformation, as well as a rotating wave approximation as in (2.26),

$$\begin{aligned} H_I &= \frac{1}{2}\hbar\Omega\left(|b\rangle\langle a|e^{i\eta(ae^{i\omega_x t} + a^\dagger e^{-i\omega_x t})}e^{-i\Delta t} + |a\rangle\langle b|e^{-i\eta(ae^{i\omega_x t} + a^\dagger e^{-i\omega_x t})}e^{i\Delta t}\right) \\ &= \frac{1}{2}\hbar\Omega\left(|b\rangle\langle a|e^{i\eta[\tilde{a}(t) + \tilde{a}^\dagger(t)]}e^{-i\Delta t} + |a\rangle\langle b|e^{-i\eta[\tilde{a}(t) + \tilde{a}^\dagger(t)]}e^{i\Delta t}\right), \end{aligned} \quad (2.32)$$

where $\tilde{a}(t) \equiv U^\dagger a U = ae^{i\omega_x t}$ is the annihilation operator in the interaction picture.

To analyze the implications of this Hamiltonian, we can consider a particular matrix element describing a transition from an initial state $|a, n\rangle$ to a final state $|b, n'\rangle$, where $|a\rangle$ and $|b\rangle$ are the two electronic states of interest and $|n\rangle$ and $|n'\rangle$ are Fock states of the

harmonic motion:

$$\begin{aligned}\langle b, n' | H_I | a, n \rangle &= \frac{1}{2} \hbar \Omega \langle n' | e^{i\eta[\tilde{a}(t) + \tilde{a}^\dagger(t)]} | n \rangle e^{-i\Delta t} \\ &= \frac{1}{2} \hbar \Omega \langle n' | e^{i\eta(a+a^\dagger)} | n \rangle e^{i(n-n')\omega_x t} e^{-i\Delta t} \\ &= \frac{1}{2} \hbar \Omega \langle n' | e^{i\eta(a+a^\dagger)} | n \rangle e^{-i[\Delta - (n'-n)\omega_x]t}\end{aligned}\quad (2.33)$$

We can see that resonance (vanishing time-dependence) occurs when $\Delta = (n' - n)\omega_x$; that is, the laser detuning from the electronic transition is equal to a multiple of the trap frequency ω_x that matches the difference in motional quanta between $|n'\rangle$ and $|n\rangle$. This is a manifestation of the conservation of energy; on resonance, the energy of the laser's photon is equal to the sum of the electronic energy difference $\hbar\omega_{ab}$ and the motional energy difference $(n' - n)\hbar\omega_x$.

If the trap frequency ω_x is large enough to exceed the Rabi frequency Ω , then a laser tuned to a frequency $\omega_{ab} + \Delta n \omega_x$, where Δn is an integer, incident on a trapped ion with initial internal and motional initial state $|a, n\rangle$ will drive the transition $|a, n\rangle \rightarrow |b, n + \Delta n\rangle$ in a manner equivalent to any other two-level system, as analyzed previously. The difference when considering the ion's motional degree of freedom is only that the frequency of the Rabi oscillations in this case is now $\Omega \langle n + \Delta n | e^{i\eta(a+a^\dagger)} | n \rangle$. Explicitly,

$$\langle n + \Delta n | e^{i\eta(a+a^\dagger)} | n \rangle = i^{\Delta n} e^{-\eta^2/2} \eta^{|\Delta n|} L_{\min(n,n+\Delta n)}^{(|\Delta n|)}(\eta^2) \left(\frac{n!}{(n + \Delta n)!} \right)^{\text{sign}(\Delta n)/2} \quad (2.34)$$

where $L_m^{(k)}(x)$ is the associated Laguerre polynomial. If η is small,

$$e^{i\eta(a+a^\dagger)} \approx 1 + i\eta(a + a^\dagger) - \frac{\eta^2}{2}(a + a^\dagger)^2 + \dots \quad (2.35)$$

In the Lamb-Dicke regime, where the ion is cold enough such that $\eta^2(2n + 1) \ll 1$,

$$\langle n | e^{i\eta(a+a^\dagger)} | n \rangle \approx 1 - \eta^2 \quad (2.36a)$$

$$\langle n + 1 | e^{i\eta(a+a^\dagger)} | n \rangle \approx i\eta\sqrt{n+1} \quad (2.36b)$$

$$\langle n - 1 | e^{i\eta(a+a^\dagger)} | n \rangle \approx i\eta\sqrt{n} \quad (2.36c)$$

The previous few paragraphs have broken the result (2.33) into two factors:

- The coupling strength $\Omega_{n,n'} = \Omega \langle n' | e^{i\eta(a+a^\dagger)} | n \rangle$, which determines the Rabi frequency of the particular transition. The matrix element $\langle n' | e^{i\eta(a+a^\dagger)} | n \rangle$ is given exactly by (2.34), and approximately by (2.36) in the Lamb-Dicke regime. The coupling strength depends on the laser intensity through Ω , and is independent of the laser frequency.

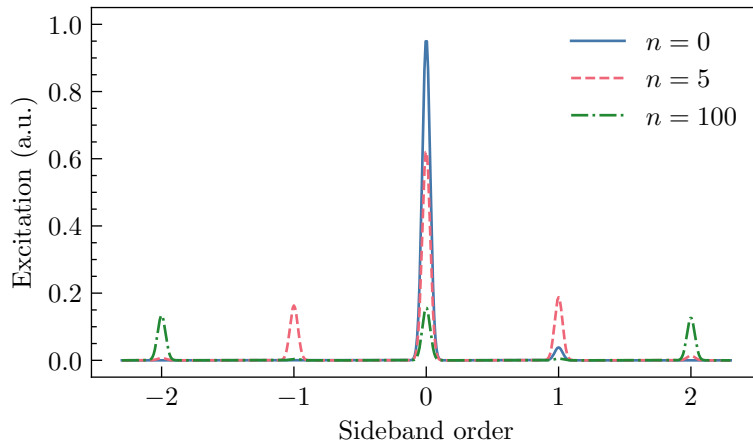


Figure 2.3: Schematic sideband spectra showing coupling strengths for different sideband orders at different starting values of the motional quantum number n , for $\eta = 0.2$. The height of the peaks shown is the square of the magnitude of the relative coupling strength (2.34). Within the Lamb-Dicke regime, sideband coupling strength falls off with sideband order, and sidebands get stronger with increasing n . $n = 100$ is beyond the Lamb-Dicke regime, and coupling strength is no longer monotonic in sideband order.

- The time-dependent phase $e^{-i[\Delta-(n'-n)\omega_x]t}$, which encodes the resonance condition, and defines the detuning with respect to the transition being considered: $\delta = \Delta - (n' - n)\omega_x$. This depends on the laser frequency through Δ , and is independent of the laser intensity. The resonance condition is related to energy conservation: on resonance, the ion's motion gains energy exactly equal to the energy from the photon $\hbar\Delta n\omega_x$ which is in excess from the electronic transition energy $\hbar\omega$ (or loses energy if $\Delta n < 0$).

Resonances which change the motional quantum number n are known as motional sidebands transitions, and the resonance which does not affect motion is known as the carrier transition. Sidebands which subtract motional quanta are known as red sidebands, and those which add motional quanta are known as blue sidebands. Experimentally, a sweep of the laser frequency about the carrier frequency reveals peaks at frequency offsets from the carrier equal to integer multiples of the trap frequency. The height of these sideband peaks is related to the corresponding matrix element. Fig. 2.3 shows some example sideband spectra.

Rather than a Fock state, which is an energy eigenstate, a more realistic initial state for the motion of the ion is a thermal state, which is a statistical mixture of many Fock states. Since the matrix element $\langle n + \Delta n | e^{i\eta(a+a^\dagger)} | n \rangle$ will differ for different values of n , the resulting dynamics will be in turn an incoherent superposition of Rabi oscillations at different frequencies. Such a thermal state may be characterized by the average Fock state

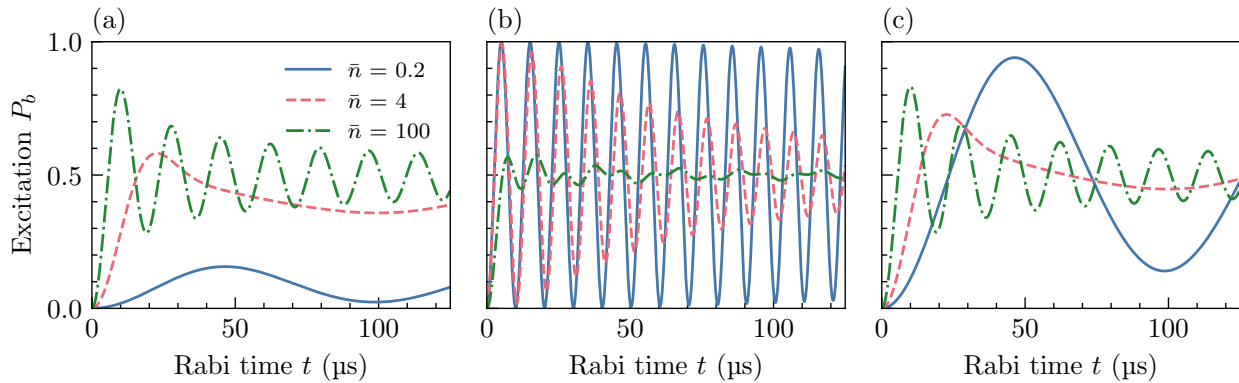


Figure 2.4: Resonant Rabi oscillations for temperatures $\bar{n} = 0.2$, 4, and 100 on (a) the first red sideband, (b) the carrier, and (c) the first blue sideband, with bare electronic Rabi frequency $\Omega = 2\pi \times 100$ kHz and Lamb-Dicke factor $\eta = 0.1$.

occupation \bar{n} . The full distribution is given by the probabilities

$$P_n = \frac{\bar{n}^n}{(\bar{n} + 1)^{n+1}}, \quad (2.37)$$

which dictates the appropriate weightings of each state $|n\rangle$ when computing the dynamics. For example, the observed Rabi oscillations will be weighted averages of those of individual Fock-state transitions, resulting in damping. The measured excitation probability for such a case on the Δn th sideband will be given by

$$P_b(t) = \sum_n P_n \frac{\Omega_{n,n+\Delta n}^2}{\Omega_{n,n+\Delta n}^2 + \delta_{\Delta n}^2} \sin^2 \left(\frac{1}{2} \sqrt{\Omega_{n,n+\Delta n}^2 + \delta_{\Delta n}^2} t \right). \quad (2.38)$$

Some thermal Rabi oscillations are shown in Fig. 2.4.

The dynamics of this section have assumed that the ion motion is harmonic-oscillator like, which is typical for trapped ions. However, much of the novelty of the work in this thesis relies on ion motion which is rotor-like, rather than oscillator-like. Chapter 3 will focus on an analogous treatment of trapped-ion motion for the case of a rotor.

2.4.4 Incoherent interactions, including ion motion

In a classical picture of trapped-ion motion, the ion oscillates sinusoidally at the trap frequency ω_x , with a period $2\pi/\omega_x \sim 10^{-6}$ s. Spontaneous emission from an electric dipole transition occurs on a much faster timescale $\sim 10^{-8}$ s; therefore, during the process of absorbing and emitting a photon from a laser field which is nearly resonant with an electric dipole transition, the ion velocity remains approximately constant. An alternative but equivalent viewpoint is one from frequency space: for electric dipole transitions and for typical trapping parameters, the rate of spontaneous emission $\sim 10^8$ Hz is much larger than the

trap frequency $\sim 10^6$ Hz, $\Gamma_b \gg \omega_x$, so that the transition is broadened in frequency space by the dissipation so much that individual sideband transitions are not resolved. This justifies the treatment of ion motion with incoherent interactions as semi-classical, where the ion's motion need not be quantized. The effect of the laser radiation on the ion's motion may be regarded as a force, which on time-average is equal to the momentum of each photon times the rate of photon absorption. For a laser whose wavevector projection onto the x -direction is k_x ,

$$F_x = m\dot{v}_x = \hbar k_x \Gamma_b \rho_{bb}, \quad (2.39)$$

where ρ_{bb} is the equilibrium excited state probability. The motion of the ion affects this equilibrium in turn via a Doppler shift, leading to a set of coupled differential equations for the ion's velocity. If the ion is moving with velocity v_x in the x -direction, the effective detuning of the laser as seen by the ion in its frame of motion shifts from Δ to $\Delta - k_x v_x$. The equilibrium excited state probability is then given by a modified version of (2.29):

$$\rho_{bb} = \frac{\Omega^2}{2\Omega^2 + \Gamma_b^2 + 4(\Delta - k_x v_x)^2}. \quad (2.40)$$

Combining these equations,

$$F_x = m\dot{v}_x = \hbar k_x \Gamma_b \frac{\Omega^2}{2\Omega^2 + \Gamma_b^2 + 4(\Delta - k_x v_x)^2}. \quad (2.41)$$

With proper choice of $\Delta < 0$, this velocity-dependent force can lead to cooling, described more in Sec 2.6. This force results from the absorption of laser photons by the ion, but at equilibrium, spontaneous emission of photons also occurs at an equal rate. Unlike the absorbed photons, the direction of the emitted photons, and hence the direction of their resulting momentum kick to the ion, is random. This leads to momentum diffusion which heats the ion, offsetting the cooling process. The random timing of the discrete absorption events from the laser also contributes to diffusion. If the ion velocity is not too large, then the rate of heating of the ion's motion due to this diffusion is given by

$$\dot{E}_h = \frac{(\hbar k)^2}{2m} \Gamma_b \rho_{bb|v=0} (1 + \xi) \quad (2.42)$$

where $\xi = 2/5$ is a geometric factor accounting for the spatial pattern of the dipole radiation [9].

2.5 The $^{40}\text{Ca}^+$ ion

The atomic ion used for the work in this thesis is $^{40}\text{Ca}^+$, singly ionized calcium with a mass of 40 amu. This atom has the hydrogen-like atomic structure described in Sec. 2.3, since neutral calcium is an alkaline earth metal with two valence electrons, leaving singly ionized calcium with only one. Beyond this highly desirable property, choosing an atomic species for ion

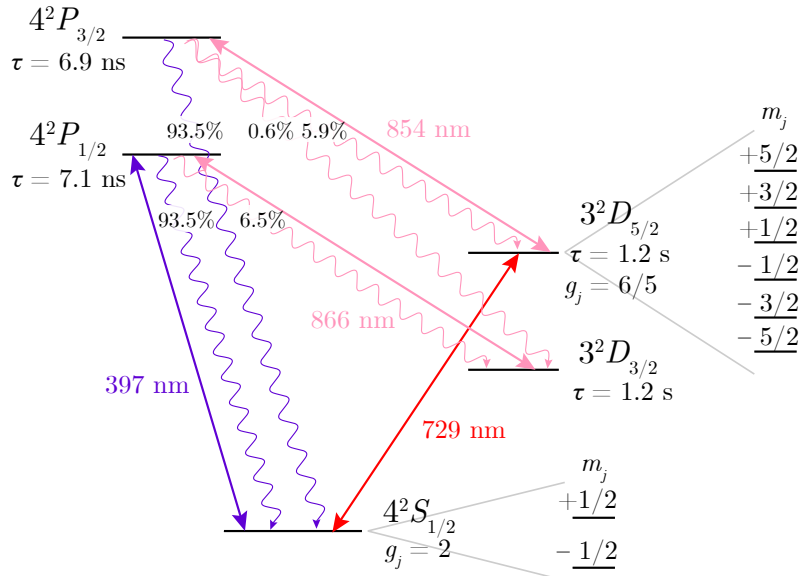


Figure 2.5: $^{40}\text{Ca}^+$ level structure. Energy levels are shown along with their lifetime. The qubit states $S_{1/2}$ and $D_{5/2}$ are additionally labeled with their Landé g-factors, and their Zeeman sublevels are also shown. Solid lines show laser transitions and are denoted with their corresponding wavelengths. Wavy lines indicate E1-allowed spontaneous decay pathways, with each labeled with the probability of decay via that pathway [24].

trapping experiments involves a number of trade-offs. Among the most desirable properties in an ion species are atomic transition frequencies whose corresponding laser wavelengths are convenient, and an energy level structure which is useful both for state preparation and for quantum coherent operations. $^{40}\text{Ca}^+$ features zero nuclear spin and therefore no hyperfine structure. This eliminates the possibility of using a pair of hyperfine levels as a qubit, but greatly simplifies the level structure. The two levels used as the qubit are connected by an electric quadrupole transition at 729 nm, a technologically convenient visible red wavelength.

2.5.1 Level structure

Fig. 2.5 shows the energy levels of $^{40}\text{Ca}^+$ which are relevant for work in this thesis. Each energy level is labelled in spectroscopic notation in terms of its quantum numbers by $n^{2s+1}[\ell]_j$, where $s = 1/2$ always and $\ell = 0, 1, 2$ is labelled S, P, D , respectively. Each splits into $2j + 1$ Zeeman sublevels with quantum numbers $m_j = -j, -j + 1, \dots + j$. The most relevant transitions, their wavelengths, energy level lifetimes, and spontaneous decay branching ratios are shown.

For experiments done in this thesis, the applied external magnetic field is of the order of a few Gauss (10^{-4} T), resulting in a Zeeman shift of all levels on the order of a few MHz. The linewidth of all E1 transitions considered here is of order 10 MHz and therefore greater than

the Zeeman shift, while the linewidth of the $S_{1/2} \leftrightarrow D_{5/2}$ transition is significantly narrower (order 100 mHz). Thus, any driven E1 transition is not selective of sublevels except for polarization considerations, but Zeeman sublevels may be easily resolved on the $S_{1/2} \leftrightarrow D_{5/2}$ transition.

The $S_{1/2}$ ground state is used as the starting point for any experiment, as well as for nearly any individual process that takes place within the experiment. It is the only truly stable level in the subspace considered here; $D_{3/2}$ and $D_{5/2}$ are only metastable, lasting for about 1 s.

2.5.2 Lasers

The transitions shown with solid arrows in Fig. 2.5 indicate transitions that we drive with lasers. There are four in total. Three of these are E1: $S_{1/2} \leftrightarrow P_{1/2}$ (397 nm), $D_{3/2} \leftrightarrow P_{1/2}$ (866 nm), and $D_{5/2} \leftrightarrow P_{3/2}$ (854 nm). The other is E2: $S_{1/2} \leftrightarrow D_{5/2}$ (729 nm). The laser power requirement for driving E1 transitions is roughly enough to reach saturation intensity, and that for driving the E2 transition is enough to have a useful Rabi frequency, of order 100 kHz. To satisfy this, assuming the beams are focused to a waist size on the order of 10 μm , we require on the order of 10 μW of power for the lasers for the E1 transitions, and on the order of 1 mW of power for the 729 nm E2 transition.

2.6 Useful light-atom processes for quantum state engineering in $^{40}\text{Ca}^+$

The light-atom interaction dynamics described in Sec. 2.4 are the building blocks for designing processes which can be used to engineer the quantum state of a trapped ion or a crystal of many trapped ions, including both their internal electronic states and the external motional states. This section describes the most basic and common of these processes: pumping, cooling, coherent manipulation, and state readout. It then describes how these are put together into full quantum state experiments.

2.6.1 Optical pumping

A typically important stage of any quantum state engineering experiment is the preparation of the electronic state into a pure energy eigenstate. The simplest and most widely used technique is known as optical pumping. Here, a laser drives population from state $|a_1\rangle$ to state $|b\rangle$, which subsequently quickly decays into either $|a_1\rangle$ or $|a_2\rangle$. The pumping depletes population from $|a_1\rangle$ and builds population in $|a_2\rangle$.

In $^{40}\text{Ca}^+$, we often want to pump the state from a mixture of the two $S_{1/2}$ sublevels (e.g. after cooling) into a pure state of one of them (e.g. for coherent operations). For optical pumping, the 729 nm laser is used since the $S_{1/2} \leftrightarrow D_{5/2}$ transition is narrow enough to resolve the two $S_{1/2}$ sublevels. However, this is a slow E2 transition, so the 854 nm laser

is additionally used to quench the transition by introducing a strong coupling from $D_{5/2}$ to $P_{3/2}$, which may quickly decay back to $S_{1/2}$. $P_{3/2}$ may also decay to $D_{3/2}$, so the 866 nm laser is also used to pump out of the $D_{3/2}$ state.

Instead of 729 nm light, one may alternatively use σ -polarized 397 nm light for optical pumping of the $S_{1/2}$ state, though this method is not used in this work. Using 397 nm σ light makes use of only an E1 transition and is thus significantly faster. However, it requires that the light is either σ^+ or σ^- polarized, which places significant restrictions on the angle between the 397 nm wavevector and the external magnetic field. Optical pumping using 729 nm light is frequency-selective and thus requires no strict polarization, making it simpler to implement and maintain. This is particularly true in this work where the applied magnetic field is created by permanent magnets rather than current-carrying coils, as magnets are not easily reconfigurable.

2.6.2 Cooling

For quantum state engineering, we wish to have clean coherent operations in order to easily prepare a quantum state of interest. A prerequisite to this is for the motion of the trapped ion to be cooled. From a semi-classical point of view, this is because the laser fields used for coherent operations have a position-dependent phase. A moving trapped ion has a time-dependent position and therefore sees a time-dependent laser phase as it moves through the laser field; if this motion is thermal, then this time-dependent phase is random, degrading the coherence of the laser-ion interaction. Two types of cooling of the motion of trapped ions are used in the work in this thesis, Doppler cooling and resolved-sideband cooling (aka simply sideband cooling) [25, 26]. These are used in stages; Doppler cooling works at high initial temperatures but is limited in its minimum final temperature, while sideband cooling requires a low initial temperature but can cool ion motion very close to its ground state. For some experiments, the ion needs only to be at a Doppler-cooled temperature, while for others, sideband cooling is necessary.

Doppler cooling

Doppler cooling exploits the Doppler effect in a laser-ion interaction where spontaneous emission is present, in which the effective frequency of the light as seen by the ion is shifted by its velocity, as in (2.40). For sufficiently small velocities, the expression for the resulting force (2.41) can be linearized around $v_x = 0$. In terms of the saturation parameter s ,

$$F_x \approx F_{x|v=0} + \frac{4\hbar k_x^2 \Delta}{\Gamma} \frac{s}{[1 + s + (2\Delta/\Gamma_b)^2]^2} v_x. \quad (2.43)$$

If $\Delta < 0$, the coefficient of the linear term will be negative, so that this force provides a viscous drag. The rate of energy loss due to this force, averaged over many harmonic

oscillation periods, is given by

$$\dot{E}_{\text{dc}} = \langle F_x v_x \rangle = \frac{4\hbar k_x^2 \Delta}{\Gamma} \frac{s}{[1 + s + (2\Delta/\Gamma_b)^2]^2} \langle v_x^2 \rangle \quad (2.44)$$

since $\langle v_x \rangle = 0$ but $\langle v_x^2 \rangle \neq 0$. When this cooling rate is balanced with the heating rate due to diffusion (2.42), a steady-state temperature can be computed [9]:

$$k_B T = m \langle v_x^2 \rangle = \frac{\hbar \Gamma_b}{8} (1 + \xi) \left[(1 + s) \frac{\Gamma_b}{2\Delta} + \frac{2\Delta}{\Gamma_b} \right]. \quad (2.45)$$

This temperature is minimum when the detuning is set to $\Delta = -\Gamma_b \sqrt{1+s}/2$:

$$k_B T_{\text{Doppler}} = \frac{\hbar \Gamma_b \sqrt{1+s}}{4} (1 + \xi), \quad (2.46a)$$

$$\bar{n}_{\text{Doppler}} = \frac{\Gamma_b \sqrt{1+s}}{4\omega_x} (1 + \xi), \quad (2.46b)$$

where $\xi = 2/5$. Note that the saturation parameter s remains a variable; the final temperature may be minimized by using as little laser power as possible, but this comes at the cost of a slower cooling rate and therefore a longer Doppler cooling duration. In practice one will often choose the minimum laser power necessary to achieve the Doppler limit within a desired time frame.

In $^{40}\text{Ca}^+$, Doppler cooling is most easily performed on the $S_{1/2} \leftrightarrow P_{1/2}$ transition at 397 nm. The $P_{1/2}$ state is the lowest-lying level above $S_{1/2}$ with an E1 transition connecting it to $S_{1/2}$. The $P_{1/2}$ state is not guaranteed to decay back into $S_{1/2}$, but rather may also decay into the long-lived $D_{3/2}$ state with probability 0.065. Thus during cooling, an additional laser at 866 nm is used to pump population out of the $D_{3/2}$ state so that it remains in the $S_{1/2} \leftrightarrow P_{1/2}$ cycle for cooling.

866 nm Doppler cooling in $^{40}\text{Ca}^+$

This work also makes use of cases where Doppler cooling is performed with the roles of the 397 nm and 866 nm lasers reversed, with the 866 nm photons providing cooling and the 397 nm laser repumping population into the $D_{3/2} \leftrightarrow P_{1/2}$ cooling transition. This scheme allows for cooling of the ion motion normal to the trap surface while avoiding directing dangerous low-wavelength 397 nm light directly onto the trap surface by directing 866 nm light onto the surface instead, with the 397 nm light parallel to it. However, it presents two main additional challenges:

1. The cooling power is reduced by about a factor of 30 in comparison to cooling with 397 nm light. Scattering on the $D_{3/2} \leftrightarrow P_{1/2}$ transition occurs at 1/14 the rate of the $S_{1/2} \leftrightarrow P_{3/2}$, and momentum kicks from 866 nm photons are a factor of 2.2 weaker than those from 397 nm photons. This raises the minimum achievable Doppler temperature.

2. The $D_{3/2} \leftrightarrow P_{1/2}$ has 6 allowed transitions between Zeeman sublevels, in comparison to 4 in the $S_{1/2} \leftrightarrow P_{3/2}$. This makes it more challenging to find an optimal detuning for cooling.

Sideband cooling

Doppler cooling is fundamentally limited by the linewidth of the cooling transition used (2.46). For cooling on the $S_{1/2} \leftrightarrow P_{1/2}$ transition with linewidth 23 MHz and at typical trap frequency of 1 MHz, Doppler cooling leaves the ion motion a thermal state of $\bar{n}_{\text{Doppler}} = 8$ at minimum. Therefore, getting the motion near the ground state ($\bar{n} < 1$ or even $\bar{n} \ll 1$) requires additional cooling by a different technique.

Sideband cooling requires *resolved sidebands*. If the linewidth of the cooling transition is smaller than the motional trap frequency, then each motional sideband can be spectrally resolved. To achieve resolved sidebands in $^{40}\text{Ca}^+$, the 729 nm $S_{1/2} \leftrightarrow D_{5/2}$ E2 transition is used. We tune the 729 nm laser to the first red sideband of the mode we are interested in cooling, $\Delta = -\omega_j$, where ω_j labels the frequency of the mode to be cooled, with Rabi frequency Ω_{cool} . We simultaneously turn on the 854 nm as an auxiliary laser, which drives $D_{5/2} \leftrightarrow P_{3/2}$ with Rabi frequency Ω_{aux} , effectively quenching the lifetime of the otherwise long-lived $D_{5/2}$ state. One may consider this quenching effect to be effectively amplifying the linewidth of the 729 nm cooling transition from Γ_{cool} to

$$\tilde{\Gamma}_{\text{cool}} = \frac{\Omega_{\text{aux}}^2}{(\Gamma_{\text{aux}} + \Gamma_{\text{cool}})^2 + 4\Delta_{\text{aux}}^2} \Gamma_{\text{aux}}, \quad (2.47)$$

where Δ_{aux} is the detuning of the 854 nm laser and Γ_{aux} is the linewidth of the $D_{5/2} \leftrightarrow P_{3/2}$ transition. Since the red sideband is being driven, each cooling cycle removes one motional quantum, which in principle continues until the ground state is reached. Importantly, the spontaneous decay back into the ground state is one which does not change the motional quantum number with high probability, as long as the ion begins in the Lamb-Dicke regime. The probability of such decays which do change the motional quantum number is of order η_{aux}^2 , where η_{aux} is the Lamb-Dicke factor with respect to the auxiliary transition. The sideband cooling process is fundamentally limited by two heating effects of the same order: off-resonant excitation of the carrier followed by decay on the blue sideband transition, and off-resonant excitation of the blue sideband followed by decay on the carrier transition. The limiting temperature for sideband cooling is [9]

$$\bar{n}_{\text{sideband}} = \frac{\tilde{\Gamma}_{\text{cool}}^2}{4\omega_j^2} \left(\frac{\eta_{\text{aux}}^2}{\eta_{\text{cool}}^2} + \frac{1}{4} \right), \quad (2.48)$$

where η_{cool} is the Lamb-Dicke factor with respect to the cooling transition. While this gives the fundamental temperature limit of sideband cooling, there will often be a higher practical limit due to other unwanted heating processes which compete with the cooling process.

In $^{40}\text{Ca}^+$, the sideband cooling cycle ideally returns population to the same $S_{1/2}$ sublevel in which we began, allowing for continuous cooling while the cooling and auxiliary lasers are on.

To maximize the probability of this occurring, the 729 nm laser is tuned to drive population from the $S_{1/2}(m = -1/2)$ state to the stretched $D_{5/2}(m = -5/2)$ state, to guarantee by E1 selection rules that the 854 nm laser then drives population to the stretched $P_{3/2}(m = -3/2)$ state, from which it must decay back to the $S_{1/2}(m = -1/2)$ state. However, in the event of a decay of $P_{3/2}$ to $D_{3/2}$ or $D_{5/2}$ instead, repumping by the 866 or 854 nm lasers may change the magnetic quantum number and allow for subsequent decay into $S_{1/2}(m = +1/2)$. Thus sideband cooling effectively slowly pumps population from $S_{1/2}(m = -1/2)$ to $S_{1/2}(m = +1/2)$. This necessitates sideband cooling in stages rather than fully continuously: After about 1 ms, sideband cooling is paused for optical pumping back to $S_{1/2}(m = -1/2)$, after which sideband cooling is resumed.

2.6.3 Coherent quantum state operations

Generally, the coherent portion of a quantum state experiment is the one of the most scientific interest, while other processes serve to prepare the ion for coherent manipulation and to measure the result. In this work, coherent operations are carried out on the $S_{1/2} \leftrightarrow D_{5/2}$ transition, where in particular any pair of Zeeman sublevels of these energy levels may be chosen, as long as they obey $|\Delta m_j| \leq 2$ so that the transition is electric-quadrupole allowed. In general, the motion of the ion will be included in the consideration of this process, which is described by the Hamiltonian (2.30), which upon transformation into the interaction picture becomes (2.32).

On the carrier transition, appropriate choice of laser pulse durations and phases can prepare an arbitrary superposition of the two electronic states. Labeling the kets corresponding to the states $S_{1/2}$ and $D_{5/2}$ as $|S\rangle$ and $|D\rangle$, respectively, an arbitrary superposition may be written as $\alpha|S\rangle + \beta|D\rangle$, with arbitrary normalized complex coefficients α and β . On motional sidebands, one can similarly manipulate the bosonic Hilbert space of the ion's harmonic oscillator motion. As a simple example, a $\pi/2$ -pulse on the blue sideband ($\Delta = \omega_x$, duration $\pi/(2\eta\Omega)$) beginning from the ground state results in the state $\frac{1}{\sqrt{2}}(|S, 0\rangle + |D, 1\rangle)$, where the two harmonic oscillator Fock states $|0\rangle$ and $|1\rangle$ are entangled with the ion's electronic state. Using such interactions as building blocks, one can prepare highly non-classical states of both the ion's internal and external degrees of freedom. Furthermore, with multiple ions, one can use similar techniques to entangle the ions together, as in the Mølmer-Sørensen interaction [27], though this is not done in this work.

2.6.4 State readout

We measure the quantum state of $^{40}\text{Ca}^+$ by applying 397 nm light, which is resonant with the $S_{1/2} \leftrightarrow P_{1/2}$ transition but off-resonant with respect to any transition from $D_{5/2}$, whereupon ion collapses into $S_{1/2}$ or $D_{5/2}$. If the ion collapses to $S_{1/2}$, then the laser light is scattered off the resonant $S_{1/2} \leftrightarrow P_{1/2}$ transition and can be measured as bright by a camera or photomultiplier tube. If the ion collapses to $D_{5/2}$, the ion scatters no light and is observed to be dark.

A superposition $\alpha |S\rangle + \beta |D\rangle$ collapses into $|S\rangle$ with probability $|\alpha|^2$ and into $|D\rangle$ with probability $|\beta|^2$. More generally, the observed probabilities correspond to diagonal elements of the reduced density matrix in the 2-dimensional electronic Hilbert space. This reduced density matrix may be mixed due to decoherence, or due to entanglement between the electronic state and the motional state. Measurement of the electronic state can thus be used to infer information about the motional state. For example, in an experiment which excites the first blue motional sideband from the ground state, one can infer addition of a motional quantum from excitation of the electronic state. This is useful because the motional degree of freedom is generally not directly measurable; the linewidth of the readout transition is 23 MHz, while the motional frequency is order 1 MHz, making individual motional energy levels unresolvable by this measurement.

When multiple ions are used, simultaneous readout of their electronic states using a photomultiplier tube yields only information about the total number of bright ions. We typically use this information to compute the average probability of excitation to the $|D\rangle$ state, which for N ions is given by

$$P_D = \frac{\sum_{n=0}^N n(1-p_n)}{N}, \quad (2.49)$$

where p_n is the probability of finding n ions bright.

2.6.5 Quantum state experiments

A full experiment in which we engineer and measure the quantum state of trapped ions combines the individual processes outlined above. A representative example sequence used in an experiment in $^{40}\text{Ca}^+$ is as follows:

1. **State initialization** (1 – 10 μs) We wish to begin with population in the $S_{1/2}$ ground state, but some population may be trapped in the long-lived $D_{3/2}$ or $D_{5/2}$ states from the previous experiment cycle. We thus apply the 854 and 866 nm lasers to pump out of the D states.
2. **Doppler cooling** (1 – 6 ms) The 397 nm laser is applied, with detuning and power optimized to minimize the ion temperature within a given cooling window. Spontaneous emission may occur from the $P_{1/2}$ to the $D_{3/2}$ state, so the 866 nm laser is also applied to pump out of $D_{3/2}$ and back into the cooling cycle.
3. **Optical pumping** (0.5 – 2 ms) Doppler cooling leaves the ion in an incoherent mixture of the two $S_{1/2}$ ground states, so optical pumping with the 729 and 854 nm lasers is used to prepare the population into purely the $m = -1/2$ sublevel. The 866 nm laser will also be on to pump out stray population decay into the $D_{3/2}$ state.
4. **Sideband cooling stages, each followed by optical pumping** ($6 \times (1 - 2 \text{ ms} + 0.5 - 1 \text{ ms})$) Each sideband cooling stage requires the 729 nm laser to be detuned to

the first red sideband of the mode being cooled. Additional stages can be introduced with different detunings in order to cool multiple motional modes. The 854 nm laser is also used, with a power optimized for the quenching process. The 866 nm is present for repumping.

5. **Coherent state manipulation** (1 μ s – 10 ms) At this stage, the ion motion has been cooled and its internal state is pure. The 729 nm laser couples the $S_{1/2}(m = -1/2)$ state to the $D_{5/2}(m = -1/2)$ state on either the carrier or a motional sideband for some prescribed sequence of pulses, resulting in some superposition of $S_{1/2}(m = -1/2)$ and $D_{5/2}(m = -1/2)$, which may include motional degrees of freedom if motional sidebands are addressed.
6. **State readout** (1 – 10 ms) The 397 nm laser is applied, along with the 866 nm laser for repumping. The quantum state of each ion collapses into either $S_{1/2}$ or $D_{5/2}$ with probability determined by the state prepared in the previous step. The amplitude of the 397 nm laser is optimized to maximize the scattering rate to read out as quickly as possible.

To actually estimate the probabilities of excitation, the experiment is repeated for typically 100 repetitions. We may then change one parameter, such as the time where the 729 nm laser is on for coherent state manipulation, and repeat. This measures the state probabilities as a function of this parameter.

Chapter 3

The trapped-ion planar quantum rotor

When multiple ions are trapped together in the same Paul-trap potential and are sufficiently cold, they form a Coulomb crystal, in which their motion finds an equilibrium balanced between the external potential from the Paul trap and the ions' mutual repulsion of each other. In a typical Coulomb crystal, the ions organize themselves into well-defined static equilibrium positions. Ion motion is restricted to small deviations from these equilibrium positions, and analysis of this motion involves breaking the motion into normal modes. Each of these modes involves the motion of multiple ions, but with an appropriate change of coordinates, each mode can be regarded as a single quantum harmonic oscillator with a characteristic oscillation frequency. Paul-trapped ion crystal motion thus represents an experimental manifestation of the quantum harmonic oscillator, a textbook quantum system. It also enables trapped ions' usefulness as a quantum computing platform by mediating entangling operations between ions. As a result, the vibrational motion of trapped ion crystals is a fundamental part of the field of trapped-ion quantum dynamics.

The work in this thesis explores a type of Paul-trapped ion Coulomb crystal which fundamentally differs from this typical picture. Rather than the ions having well-defined static equilibrium positions, the crystal is instead free to rotate in one plane. This results in one normal mode which is not a quantum harmonic oscillator, but is instead a quantum rotor. This chapter details the physics of such a Coulomb crystal rotor and how it interacts with laser light, and in particular how it differs from the trapped-ion Coulomb crystal harmonic oscillator. It begins with the well-established physics of static Paul-trapped ion crystals, the typical system featuring only vibrational modes, before similarly analyzing freely rotating ion crystals. The results are then summarized in Tab. 3.2.

Most sections in this chapter have the following structure: An analysis of the classical motion and its normal modes, followed by quantization of the motion, and finally an analysis of the quantum mechanics of a coherent laser field interacting with this quantized motion, in particular computing the coupling strength between motional states induced by the laser. In all cases considered, the laser interacts with the ion motion via motional sidebands of a

coherent (electric-dipole forbidden) electronic transition between two electronic eigenstates $|a\rangle$ and $|b\rangle$, with Rabi frequency Ω . In our experimental work, this is done on the 729 nm $S_{1/2} \leftrightarrow D_{5/2}$ transition of $^{40}\text{Ca}^+$.

3.1 Single ions with a single vibrational mode

This is the simplest case, already analyzed in Sec. 2.4.3. In summary: In the pseudopotential approximation, the ion motion is a three-dimensional harmonic oscillator with characteristic oscillation frequencies $\omega_x, \omega_y, \omega_z$, which can be quantized and described by the Hamiltonian (2.5). In the presence of a laser field near resonance with an electric dipole-forbidden transition of the ion's valence electron, the Hamiltonian (considering only one mode ω_x) is given by (2.30), which in the interaction picture is (2.32). The coupling strengths between energy eigenstates of the motion (Fock states) in the presence of this laser field are given by (2.34), which are well-approximated by (2.36) in the Lamb-Dicke regime $\eta^2(2n + 1) \ll 1$.

These results were derived by the following formulation:

1. Write the Hamiltonian in the Schrödinger picture.
2. Rewrite the operator $e^{i\mathbf{k}\cdot\mathbf{r}}$ (which comes from the plane-wave form of the laser field) in terms of ladder operators for the ion's motion (which in this case are a, a^\dagger).
3. Transform into the interaction picture.
4. Compute the matrix element between an arbitrary pair of motional eigenstates.

This procedure is followed in the following sections to derive corresponding coupling strengths for the case of multiple ions, and in the case of a freely rotating Coulomb crystal.

3.2 N -ion crystals with $3N$ vibrational modes

This section generalizes the previous section in two ways: by considering an arbitrary number of ions trapped together, and by accounting for all $3N$ of their motional degrees of freedom. For Coulomb crystals composed of many trapped ions, the results of the previous section extend to a set of $3N$ harmonic oscillators in total, each with its own characteristic vibrational frequency and Lamb-Dicke factor. The primary difference is these oscillators describe the motion of *normal modes* of the crystal, which can involve the motion of multiple ions, due to their mutual Coulomb interaction.

3.2.1 Normal modes of motion

An ion Coulomb crystal is formed when N trapped ions find their equilibrium positions which minimize the potential energy of the entire system. Contributions to this potential energy

are the external potential created by the Paul trap and the ions' mutual Coulomb repulsion. The external potential is characterized by the three center-of-mass secular frequencies ω_x , ω_y , ω_z . The N ions have $3N$ motional degrees of freedom in total, which couple to each other through the Coulomb interaction. If the crystal is sufficiently cold, the motion of the ions about their respective equilibrium positions will be small enough that the potential energy of the crystal can be adequately described using a Taylor expansion about the equilibrium position (x_i^0, y_i^0, z_i^0) of each ion i . This expansion describes harmonic motion if taken only to second order. Diagonalizing this potential energy function in the motional coordinates leads to $3N$ normal modes [28]. Each mode j has a characteristic frequency ω_j and coordinate ξ_j , which is a linear combination of the ions' real-space coordinates δx_i , δy_i , δz_i describing their deviation from their equilibrium positions. The normal mode coordinates can be related to the real-space coordinates by the $N \times 3N$ matrices

$$\delta x_i = \sum_{j=1}^{3N} X_{ij} \xi_j, \quad \delta y_i = \sum_{j=1}^{3N} Y_{ij} \xi_j, \quad \delta z_i = \sum_{j=1}^{3N} Z_{ij} \xi_j. \quad (3.1)$$

Quantizing the motion of the normal modes yields corresponding creation and annihilation operators a_j^\dagger , a_j , related to the coordinate by

$$\xi_j = \sqrt{\frac{\hbar}{2m\omega_j}} (a_j + a_j^\dagger). \quad (3.2)$$

This thesis defines $\omega_x < \omega_y < \omega_z$, contrary to some conventions where ω_z is taken to be the smallest trap frequency. This is because for the ring trap it is convenient to define the symmetry axis as the z -direction, but the confinement along this axis is the strongest. Hence here ω_z is defined to always be the axis of highest trap frequency, so that the usual anisotropic case $\omega_x < \omega_y < \omega_z$ smoothly connects with the relevant planar isotropic case $\omega_x = \omega_y < \omega_z$ as $\omega_y \rightarrow \omega_x$.

As a simple example, consider a two-ion Coulomb crystal. The equilibrium positions can be solved for analytically in this case:

$$\begin{aligned} \mathbf{r}_1^0 &= \left(\left[\frac{e^2}{16\pi\epsilon_0 m \omega_x^2} \right]^{1/3}, 0, 0 \right) \\ \mathbf{r}_2^0 &= \left(- \left[\frac{e^2}{16\pi\epsilon_0 m \omega_x^2} \right]^{1/3}, 0, 0 \right). \end{aligned} \quad (3.3)$$

There are 6 total normal modes: three center-of-mass (COM) modes with both ions oscillating in phase at the same frequency of the corresponding single ion mode, a “stretch” mode in which the ions oscillate out of phase towards and away from each other, and two “rocking” modes in which the ions oscillate out of phase normal to the ion-ion axis. The eigenfrequencies and eigenvectors of these modes are tabulated in Tab. 3.1, and shown in Fig. 3.1.

Mode	COM x	COM y	COM z	Stretch	Rocking y	Rocking z
Frequency	ω_x	ω_y	ω_z	$\sqrt{3}\omega_x$	$\sqrt{\omega_y^2 - \omega_x^2}$	$\sqrt{\omega_z^2 - \omega_x^2}$
X_j	$\frac{1}{\sqrt{2}}(\begin{smallmatrix} 1 \\ 1 \end{smallmatrix})$	$(\begin{smallmatrix} 0 \\ 0 \end{smallmatrix})$	$(\begin{smallmatrix} 0 \\ 0 \end{smallmatrix})$	$\frac{1}{\sqrt{2}}(\begin{smallmatrix} -1 \\ -1 \end{smallmatrix})$	$(\begin{smallmatrix} 0 \\ 0 \end{smallmatrix})$	$(\begin{smallmatrix} 0 \\ 0 \end{smallmatrix})$
Y_j	$(\begin{smallmatrix} 0 \\ 0 \end{smallmatrix})$	$\frac{1}{\sqrt{2}}(\begin{smallmatrix} 1 \\ 1 \end{smallmatrix})$	$(\begin{smallmatrix} 0 \\ 0 \end{smallmatrix})$	$(\begin{smallmatrix} 0 \\ 0 \end{smallmatrix})$	$\frac{1}{\sqrt{2}}(\begin{smallmatrix} 1 \\ -1 \end{smallmatrix})$	$(\begin{smallmatrix} 0 \\ 0 \end{smallmatrix})$
Z_j	$(\begin{smallmatrix} 0 \\ 0 \end{smallmatrix})$	$(\begin{smallmatrix} 0 \\ 0 \end{smallmatrix})$	$\frac{1}{\sqrt{2}}(\begin{smallmatrix} 1 \\ 1 \end{smallmatrix})$	$(\begin{smallmatrix} 0 \\ 0 \end{smallmatrix})$	$(\begin{smallmatrix} 0 \\ 0 \end{smallmatrix})$	$\frac{1}{\sqrt{2}}(\begin{smallmatrix} 1 \\ -1 \end{smallmatrix})$

Table 3.1: Mode frequencies and structure of all normal modes of a 2-ion Coulomb crystal in an anisotropic potential. Here the mode matrices X , Y , Z are shown in terms of the column that corresponds to each mode, with each element of the column corresponding to each ion. The full 2×6 matrices are constructed by concatenating the columns for each mode along each row of the table.

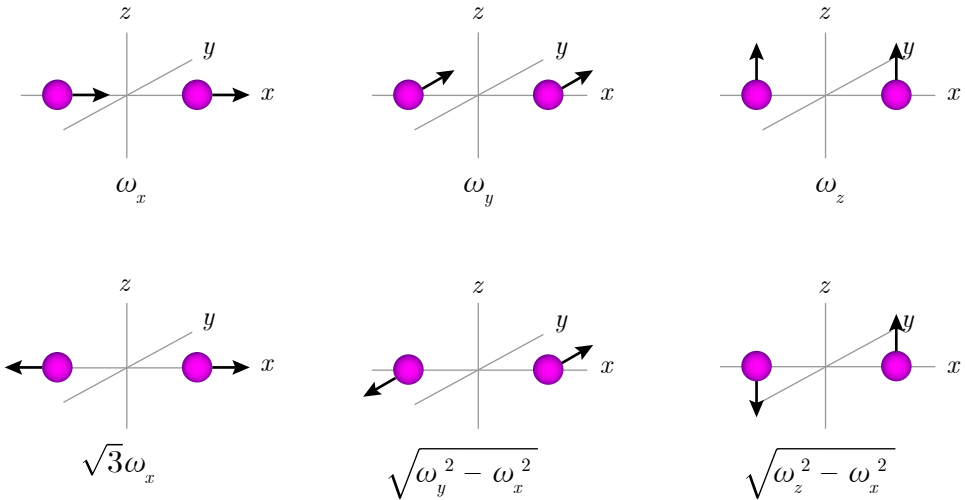


Figure 3.1: Normal modes of a 2-ion Coulomb crystal oriented along the x -direction. Each is shown with its corresponding eigenfrequency.

3.2.2 Interaction with a coherent laser field

To analyze the physics of a coherent laser field interacting with a trapped-ion Coulomb crystal with many motional modes, we can first generalize the Hamiltonian (2.30) to include multiple ions and many modes:

$$\begin{aligned}
 H &= H_0 + H_1, \\
 H_0 &= \sum_{j=1}^{3N} \hbar\omega_j (a_j^\dagger a_j + \frac{1}{2}) + \sum_{i=1}^N \frac{1}{2} \hbar\omega_{ab} (|b_i\rangle\langle b_i| - |a_i\rangle\langle a_i|) \\
 H_1 &= \sum_{i=1}^N \frac{1}{2} \hbar\Omega_i (|b_i\rangle\langle a_i| + |b_i\rangle\langle a_i|) [e^{i(\mathbf{k}\cdot\mathbf{r}_i - \omega t)} + e^{-i(\mathbf{k}\cdot\mathbf{r}_i - \omega t)}].
 \end{aligned} \tag{3.4}$$

The electronic-transition Rabi frequency Ω_i is given by the laser field's matrix element between the electronic states $|a\rangle$ and $|b\rangle$, e.g. (2.19). Hereafter we will not be concerned with computing the Rabi frequency, but instead take as a given that it takes on some value proportional to the laser field amplitude. In practice, we directly measure the Rabi frequency by observing Rabi oscillations. In general, the Rabi frequency of each ion i may differ if the laser intensity at the ions' positions differs.

Rewriting the operator $\mathbf{k} \cdot \mathbf{r}_i$ in terms of normal modes using (3.1) and (3.2),

$$\begin{aligned}\mathbf{k} \cdot \mathbf{r}_i &= \mathbf{k} \cdot (\mathbf{r}_i^0 + \delta\mathbf{r}_i) \\ &= \mathbf{k} \cdot \mathbf{r}_i^0 + k_x \sum_j X_{ij} \xi_j + k_y \sum_j Y_{ij} \xi_j + k_z \sum_j Z_{ij} \xi_j \\ &= \mathbf{k} \cdot \mathbf{r}_i^0 + \sum_j (k_x X_{ij} + k_y Y_{ij} + k_z Z_{ij}) \sqrt{\frac{\hbar}{2m\omega_j}} (a_j + a_j^\dagger) \\ &= \mathbf{k} \cdot \mathbf{r}_i^0 + \sum_j \eta_{ij} (a_j + a_j^\dagger),\end{aligned}\tag{3.5}$$

where the Lamb-Dicke factor for the i th ion and j th mode is defined as

$$\eta_{ij} \equiv (k_x X_{ij} + k_y Y_{ij} + k_z Z_{ij}) \sqrt{\frac{\hbar}{2m\omega_j}}.\tag{3.6}$$

In terms of the normal modes, the interaction-picture Hamiltonian in the RWA becomes

$$H_I = \frac{1}{2} \hbar \sum_i \Omega_i |b_i\rangle\langle a_i| \prod_j e^{i\eta_{ij}[\tilde{a}_j(t)+\tilde{a}_j^\dagger(t)]} e^{-i\Delta t} + h.c.\tag{3.7}$$

The term $\mathbf{k} \cdot \mathbf{r}_i^0$ containing the equilibrium positions becomes a constant phase factor $e^{i\mathbf{k} \cdot \mathbf{r}_i^0}$ which may be neglected, e.g. by being absorbed into the definition of Ω_i . The coupling strength for the i th ion for an arbitrary transition between motional eigenstates is

$$\langle b_i, \mathbf{n} + \Delta\mathbf{n} | H_I | a_i, \mathbf{n} \rangle = \frac{1}{2} \hbar \Omega_i \prod_j e^{i\delta_{\Delta\mathbf{n}} t},\tag{3.8a}$$

where

$$\Omega_i | \mathbf{n}, \mathbf{n} + \Delta\mathbf{n} \rangle \equiv \Omega_i \prod_j \langle n_j + \Delta n_j | e^{\eta_{ij}(a_j + a_j^\dagger)} | n_j \rangle\tag{3.8b}$$

$$\delta_{\Delta\mathbf{n}} \equiv \Delta - \sum_j \Delta n_j \omega_j\tag{3.8c}$$

This may be compared to the case of a single ion with a single mode:

- $\delta_{\Delta\mathbf{n}}$ is equal to the detuning of the laser frequency from the transition frequency of $|a, \mathbf{n}\rangle \leftrightarrow |b, \mathbf{n} + \Delta\mathbf{n}\rangle$. The resonance condition $\delta_{\Delta\mathbf{n}} = 0$ may be understood as conservation of energy for the given transition. In this case, each mode independently may change its energy by an integer number of its respective quantum $\hbar\omega_j$.
- The amplitude $\Omega_{i, \mathbf{n}, \mathbf{n} + \Delta\mathbf{n}}$ is the coupling strength for the transition, and will be equal to the Rabi frequency of transitions between $|a, \mathbf{n}\rangle$ and $|b, \mathbf{n} + \Delta\mathbf{n}\rangle$. This total coupling strength can be understood as the product of all coupling strengths of each mode individually. Thus the coupling to each mode is independent of coupling to the other modes. Each may be evaluated independently from (2.34), or (2.36) if the Lamb-Dicke approximation holds.

3.3 2-ion crystals in a planar rigid rotor

The previous sections assumed that the Paul trap potential was anisotropic, so that the three characteristic secular frequencies of the Paul trap potential $\omega_x, \omega_y, \omega_z$ were distinct. Here, we now consider the case of planar isotropy, $\omega_x = \omega_y < \omega_z$, in which we will find that the motion of ion crystals can differ quite drastically from the typical case considered previously. In particular, they exhibit rotational motion, rather than only vibrational. The smallest Coulomb crystal to exhibit this behavior consists of 2 ions, so we begin by considering this case. While the results of the previous sections of this chapter are well-established, the trapped-ion rotor is a novel system and thus the results of this section are also novel.

In the previous section, it was possible to move directly from the expression for the potential energy of the Coulomb crystal to the description of the normal modes. Deriving the normal modes for a Coulomb crystal which is allowed to rotate requires some more care, so this section will go through the derivation. Note in particular that, for the 2-ion anisotropic case, the eigenmodes and their frequencies are given in Tab. 3.1. For the present case of $\omega_x = \omega_y$, we will find that 5 of these 6 modes remain unchanged (the COM modes, stretch, and rocking z modes), while the rocking y mode is modified, as the vibrational description is no longer valid. Indeed, we can see that if it were, its frequency $\sqrt{\omega_y^2 - \omega_x^2}$ would go to zero as ω_y approached ω_x . This mode instead becomes the rotational mode of the trapped-ion rotor.

3.3.1 Derivation of the modes of motion

The full Hamiltonian of the crystal's motion in terms of the real-space positions and momenta of the two ions $\mathbf{r}_{1,2}, \mathbf{p}_{1,2}$ is

$$H = \frac{p_1^2}{2m} + \frac{p_2^2}{2m} + \frac{1}{2}m\omega_x^2(x_1^2 + y_1^2 + x_2^2 + y_2^2) + \frac{1}{2}m\omega_z^2(z_1^2 + z_2^2) + \frac{e^2}{4\pi\epsilon_0|\mathbf{r}_1 - \mathbf{r}_2|}, \quad (3.9)$$

where $p_{1,2} = |\mathbf{p}_{1,2}|$. This system has 6 degrees of freedom in total. As usual in a two-body problem, it is convenient do define new coordinates, the center-of-mass position and

momentum \mathbf{R}, \mathbf{P} and the relative position and momentum \mathbf{r}, \mathbf{p} , defined by

$$\begin{aligned}\mathbf{R} &= \frac{\mathbf{r}_1 + \mathbf{r}_2}{2}, & \mathbf{P} &= \mathbf{p}_1 + \mathbf{p}_2 \\ \mathbf{r} &= \mathbf{r}_1 - \mathbf{r}_2, & \mathbf{p} &= \frac{\mathbf{p}_1 - \mathbf{p}_2}{2}.\end{aligned}\tag{3.10}$$

Substituting this into (3.9), we find that the Hamiltonian is written as a sum two terms, one containing only center-of-mass coordinates, and one containing only relative coordinates. The center-of-mass Hamiltonian is a 3-dimensional harmonic oscillator with two isotropic directions at frequency ω_x and one at ω_z ; precisely the same as for a single ion in the same potential. The center-of-mass motion therefore exhibits the usual three vibrational normal modes.

For the three degrees of freedom for the “relative” motion, we move to cylindrical coordinates, ρ, θ, z , defined by $\rho \cos \theta = x, \rho \sin \theta = y$. The potential energy term of the relative motion in cylindrical coordinates is

$$U(\mathbf{r}) = \frac{1}{2}\mu(\omega_x^2\rho^2 + \omega_z^2z^2) + \frac{e^2}{4\pi\epsilon_0}\frac{1}{\sqrt{\rho^2 + z^2}},\tag{3.11}$$

where $\mu = m/2$ is the reduced mass. Here the rigid rotor assumption is introduced, to be clarified and justified later in this section: *The centrifugal potential has negligible effect on this potential.* We will find that this condition is equivalent to the condition that the rotation frequency ω_{rot} of the ion crystal must be small compared to the in-plane secular frequency ω_x . Under this assumption, we may proceed by finding the minimum of this potential and expand about it, without considering rotational effects. The minimum is at $z = 0$ and $\rho = \rho_e$, where

$$\rho_e = \left(\frac{e^2}{4\pi\epsilon_0\mu\omega_x^2}\right)^{1/3}.\tag{3.12}$$

Expanding the potential about $\rho = \rho_e, z = 0$, the lowest-order remaining terms are

$$U(\mathbf{r}) \approx \frac{3}{2}\mu\omega_x^2(\rho - \rho_e)^2 + \frac{1}{2}\mu(\omega_z^2 - \omega_x^2)z^2.\tag{3.13}$$

Here we've found two more normal modes, the stretch mode in which ρ oscillates about ρ_e at frequency $\sqrt{3}\omega_x$, and the rocking z mode in which z oscillates about at frequency $\sqrt{\omega_z^2 - \omega_x^2}$, precisely the same as the anisotropic case as in Tab. 3.1. To find the description of the remaining degree of freedom, the angular coordinate θ which will describe the rotational motion, it is most useful to turn to the Schrödinger equation. It will be necessary to include the radial coordinate ρ in this description.

We seek the eigenfunctions and energies from the time-independent Schrödinger equation. As is the typical technique, we assume that the eigenfunctions for the two coordinates ρ, θ factor and write them as $\psi(\rho, \theta) = R(\rho)Y(\theta)$. The time-independent Schrödinger equation

in cylindrical coordinates then reads

$$H\psi = E\psi$$

$$-\frac{\hbar^2}{2\mu} \left(\frac{\partial^2}{\partial\rho^2} + \frac{1}{\rho} \frac{\partial}{\partial\rho} + \frac{1}{\rho^2} \frac{\partial^2}{\partial\theta^2} \right) R(\rho)Y(\theta) + \frac{3}{2}\mu\omega_x^2(\rho - \rho_e)^2 R(\rho)Y(\theta) = ER(\rho)Y(\theta), \quad (3.14)$$

With some massaging, this becomes

$$\underbrace{\left[\frac{\rho^2}{R} \frac{d^2R}{d\rho^2} + \frac{\rho}{R} \frac{dR}{d\rho} - \frac{2\mu r^2}{\hbar^2} \left(\frac{3}{2}\mu\omega_x^2(\rho - \rho_e)^2 - E \right) R \right]}_{\ell^2} + \underbrace{\left[\frac{1}{Y} \frac{d^2Y}{d\theta^2} \right]}_{-\ell^2} = 0. \quad (3.15)$$

With the coordinates separated, each of the two bracketed terms must be equal to a constant, which we call $\pm\ell^2$ in anticipation of ℓ becoming the angular momentum quantum number. Indeed, the angular eigenfunctions are

$$Y_\ell(\theta) = \frac{1}{\sqrt{2\pi}} e^{i\ell\theta}. \quad (3.16)$$

Continuity of Y_ℓ requires ℓ to be an integer. For the remaining radial part of the Schrödinger equation, we define $u(\rho) = \sqrt{\rho}R(\rho)$; the radial Schrödinger equation can then be written (with some further massaging) as

$$-\frac{\hbar^2}{2\mu} \frac{d^2u}{d\rho^2} + \left[\frac{3}{2}\mu\omega_x^2(\rho - \rho_e)^2 + \frac{\hbar^2}{2\mu} \frac{\ell^2 - \frac{1}{4}}{\rho^2} \right] u = Eu. \quad (3.17)$$

We now have a typical 1-dimensional Schrödinger equation in the coordinate ρ , with a potential consisting of two terms: One is the stretch mode's harmonic potential, and the other is a centrifugal term. As previously stated, the rigid-rotor approximation neglects the modification of the centrifugal term to the harmonic one. One way to quantify this is to compute the fractional change in the equilibrium radial coordinate due to the centrifugal term, $\delta\rho_e$. The centrifugal effect can then be neglected if $\delta\rho_e/\rho_e \ll 1$. In terms of the parameters of (3.17), this condition turns out to be

$$\frac{\delta\rho_e(\ell)}{\rho_e} = \frac{\hbar^2\ell^2}{3\mu^2\rho_e^4\omega_x^2} \ll 1. \quad (3.18)$$

With typical experimental parameters, this ratio is of the order $10^{-3} - 10^{-2}$, quantifying the degree to which the rigid rotor approximation is justified. This approximation will be taken throughout the majority of this work, but Sec. 3.5 will also look more quantitatively at the implications of non-rigid effects, where also the above rigidity condition (3.18) will be shown.

In the rigid rotor approximation, we can thus set $\rho = \rho_e$ in the centrifugal term. We can also ignore the $-1/4$ term, which is justified since (1) in practice, we consider states

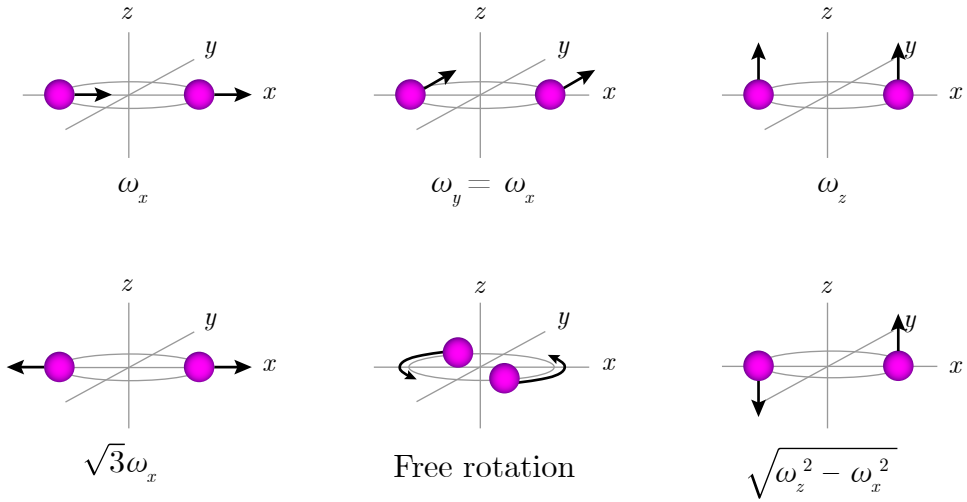


Figure 3.2: Normal modes of a 2-ion crystal which may rotate. The differences between this case and Fig. 3.1 are that here, the x and y COM frequencies are the same, and the horizontal rocking mode is replaced by the rotational mode.

where $\ell \gg 1$ (but not so large that the rigid rotor approximation is broken), and (2) if the rigid rotor approximation is already taken, the $-1/4$ term represents a constant energy offset anyway. Then the Schrödinger equation is

$$-\frac{\hbar^2}{2\mu} \frac{d^2 u}{d\rho^2} + \left[\frac{3}{2} \mu \omega_x^2 (\rho - \rho_e)^2 + \frac{\hbar^2 \ell^2}{2\mu \rho_e^2} \right] u = Eu. \quad (3.19)$$

This fully separates the stretch mode (in coordinate ρ) from the rotor mode (in coordinate θ). We can now consider the rotor mode as independent from all 5 other degrees of freedom.

3.3.2 Quantum mechanics of the planar rigid rotor mode

As found from the Schrödinger equation, the rigid rotor mode has eigenfunctions $Y_\ell(\theta) \propto e^{i\ell\theta}$ and energy $E_\ell = \hbar^2 \ell^2 / 2\mu \rho_e^2$, where ℓ is quantized to integer values. It is convenient to rewrite this now in terms of laboratory-frame parameters rather than 2-body problem parameters, $m = 2\mu$, $r = \rho_e/2$, where r is the radius of the 2-ion rotor. (We can now drop the subscript e for equilibrium from the radius for the rest of this section, since the rotor is rigid by assumption, such that it is understood that for the rigid rotor, r is a constant and not a coordinate.)

$$E_\ell = \frac{\hbar^2 \ell^2}{4mr^2} = \hbar \omega_r \ell^2, \quad (3.20)$$

where $\omega_r \equiv \hbar/4mr^2$ is the rotational constant, defining the energy scale of the rotor's energy states. In the context of molecules, this constant is sometimes called B [29]. With typical

experimental parameters in this work, the rotational constant is of the order $2\pi \times 10$ Hz. We can also rewrite the rotor radius (3.11) in terms of laboratory-frame parameters:

$$r = \left(\frac{e^2}{16\pi\epsilon_0 m \omega_x^2} \right)^{1/3}. \quad (3.21)$$

Note that this radius matches the ion equilibrium positions in the case of a 2-ion crystal in a typical anisotropic potential, (3.3). With typical experimental parameters, this is a few μm .

It is worth noting that we could also derive the eigenfunctions and energies of this rigid rotor mode directly from assuming it to be a quantum planar rotor. Such a system has only one degree of freedom, the angular position θ , whose conjugate momentum is the z -component of angular momentum L_z . The potential is constant in θ , so the Hamiltonian consists of only a kinetic energy term, $H = L_z^2/2I$, where I is the moment of inertia. For the 2-ion crystal, $I = 2mr^2$, but in general, all parameters of the planar quantum rotor can be written in terms of $I = \sum_i m_i r_i^2$, providing a more general formulation which is agnostic to the rotor's constituent particles and will become useful in the following section. In particular, the rotational constant is given in general by

$$\omega_r = \frac{\hbar}{2I}. \quad (3.22)$$

The Hamiltonian $L_z^2/2I$ manifestly commutes with the angular momentum L_z , which is found to be quantized in integer multiples of \hbar , so that the simultaneous eigenfunctions of angular momentum and the Hamiltonian, $|\ell\rangle$, satisfy $L_z |\ell\rangle = \hbar\ell |\ell\rangle$ and $H |\ell\rangle = \hbar^2\ell^2/2I |\ell\rangle = \hbar\omega_r \ell^2 |\ell\rangle$. This is the same result as (3.20).

Furthermore, from the classical relation between angular momentum and angular velocity $L = I\omega_{\text{rot}}$, we can identify angular momentum eigenstates $|\ell\rangle$ with classical angular velocities by $\hbar\ell = I\omega_{\text{rot}}$, so that

$$\omega_{\text{rot}} = \frac{\hbar\ell}{I} = 2\ell\omega_r \quad (3.23)$$

This provides an alternative interpretation of the rotational constant ω_r : The quantum of angular momentum, \hbar , has a corresponding quantum of angular velocity of $2\omega_r$, equal to twice the rotational constant.

As with harmonic oscillator modes, we are interested in how the motion of the rigid rotor mode affects a coherent electronic transition of the ions; in particular, at what frequencies motional sidebands appear, and what their coupling strengths are.

3.3.3 Coupling strengths of interaction with a coherent laser field

Here we will consider the interaction of a coherent laser field with a 2-ion crystal that exhibits *only* planar rotational motion; consider the case of including other modes is considered in Sec. 3.4.

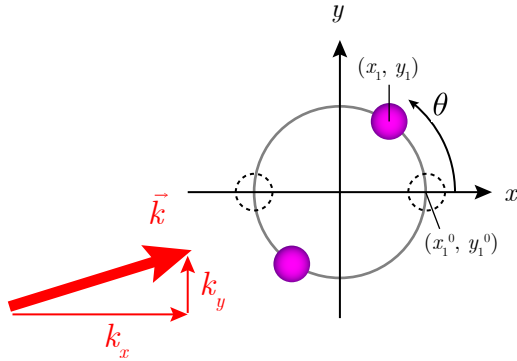


Figure 3.3: Two ions in a planar rotor illuminated by a laser field with wavevector \mathbf{k} . The coordinate θ defines the angle of rotation of the full crystal relative to a reference orientation where the ion positions are (x_i^0, y_i^0) .

The appropriate Hamiltonian, including the 2 electronic states of interest of the 2 ions and the rotational motion, interacting with a laser field at frequency ω with wavevector \mathbf{k} as usual, is

$$\begin{aligned} H &= H_0 + H_1, \\ H_0 &= \frac{L_z^2}{2I} + \sum_{i=1}^2 \frac{1}{2} \hbar \omega_{ab} (|b_i\rangle\langle b_i| - |a_i\rangle\langle a_i|) \\ H_1 &= \sum_{i=1}^2 \frac{1}{2} \hbar \Omega (|b_i\rangle\langle a_i| + |b_i\rangle\langle a_i|) [e^{i(\mathbf{k}\cdot\mathbf{r}_i - \omega t)} + e^{-i(\mathbf{k}\cdot\mathbf{r}_i - \omega t)}]. \end{aligned} \quad (3.24)$$

In this case, the ions are no longer localized to well-defined positions, so assigning a Rabi frequency Ω_i to each due to its position in the laser field is no longer meaningful. For simplicity, it is assumed that the light field uniformly illuminates the crystal, with electronic Rabi frequency Ω .

The position operator

We can first transform the operator $\mathbf{k} \cdot \mathbf{r}_i$ to be in terms of angular momentum raising and lowering operators L_{\pm} , analogous to rewriting $\mathbf{k} \cdot \mathbf{r}$ as $\eta(a + a^\dagger)$ in vibrational modes. This can be done by recognizing the angular momentum raising and lowering operators in position space as $e^{\pm i\theta}$, since $L_{\pm} |\ell\rangle = e^{\pm i\theta} \frac{1}{\sqrt{2\pi}} e^{i\ell\theta} = \frac{1}{\sqrt{2\pi}} e^{i(\ell\pm 1)\theta} = |\ell \pm 1\rangle$. The position of ion 1 is

$(x_1, y_1, z_1) = (r \cos \theta, r \sin \theta, 0)$, so

$$\begin{aligned} \mathbf{k} \cdot \mathbf{r}_1 &= k_x r \cos \theta + k_y r \sin \theta \\ &= k_x r \frac{e^{i\theta} + e^{-i\theta}}{2} + k_y r \frac{e^{i\theta} - e^{-i\theta}}{2i} \\ &= \frac{1}{2}(k_x - ik_y)rL_+ + \frac{1}{2}(k_x + ik_y)rL_- \\ &= \frac{1}{2}\zeta_1 L_+ + \frac{1}{2}\zeta_1^* L_- , \end{aligned} \quad (3.25a)$$

where

$$\zeta_1 \equiv (k_x - ik_y)r. \quad (3.25b)$$

ζ_1 (whose subscript specifies the ion number) is a dimensionless, complex parameter, effectively quantifying the ratio between the rotor radius and the laser wavelength. This is generally much larger than a typical Lamb-Dicke parameter η for a vibrational mode, since the relevant length scale is an ion-ion distance, rather than the size of a single ion's wavepacket. As an example, consider $^{40}\text{Ca}^+$ in a trap with secular frequency in the x -direction of 1 MHz interacting with 729 nm light directed along the x -direction. A single ion's vibrational mode will have a Lamb-Dicke factor of $\eta = 0.097$, while a pair of ions in a planar isotropic trap of the same secular frequency will have a rotor radius $r = 2.8 \mu\text{m}$ which gives $\zeta = 24$. The position of ion 2 is $\mathbf{r}_2 = -\mathbf{r}_1$ since we have a rigid rotor centered at the origin, so evaluating $\mathbf{k} \cdot \mathbf{r}_2$ gives $\frac{1}{2}\zeta_2 L_+ + \frac{1}{2}\zeta_2^* L_-$ where $\zeta_2 = -\zeta_1$. More generally,

$$\mathbf{k} \cdot \mathbf{r}_i = \frac{1}{2}(\zeta_i L_+ + \zeta_i^* L_-), \quad \text{where} \quad (3.26a)$$

$$\zeta_i \equiv (k_x - ik_y)(x_i^0 + iy_i^0). \quad (3.26b)$$

(x_i^0, y_i^0) is the equilibrium position of ion i in the rotor plane at $\theta = 0$. The overall phase of all ζ_i is arbitrary, depending on the choice of the directions of the x and y axes, but the relative phases between ζ_i for different ions encode information about the angles between the different ions' equilibrium positions.

The interaction picture Hamiltonian

We can now transform as usual into the interaction picture given by $H_I = U^\dagger H_1 U$, $U = e^{-iH_0 t/\hbar}$.

$$H_I = \frac{1}{2}\hbar \sum_{i=1}^2 \Omega |b_i\rangle\langle a_i| e^{i\frac{1}{2}[\zeta_i \tilde{L}_+(t) + \zeta_i^* \tilde{L}_-(t)]} e^{-i\Delta t} + h.c. \quad (3.27)$$

where

$$\tilde{L}_+(t) = \sum_{\ell} e^{i(2\ell+1)\omega_r t} |\ell+1\rangle\langle\ell| \quad (3.28)$$

is the interaction-picture angular momentum raising operator. From here we can compute matrix elements between energy eigenstates, analogous to (2.33):

$$\begin{aligned}\langle b_i, \ell' | H_I | a_i, \ell \rangle &= \frac{1}{2} \hbar \Omega e^{-i\Delta t} \langle \ell' | e^{i\frac{1}{2}[\zeta_i \tilde{L}_+(t) + \zeta_i^* \tilde{L}_-(t)]} | \ell \rangle \\ &= \frac{1}{2} \hbar \Omega e^{-i[\Delta - (\ell'^2 - \ell^2)\omega_r]t} \langle \ell' | e^{i\frac{1}{2}(\zeta_i L_+ + \zeta_i^* L_-)} | \ell \rangle\end{aligned}\quad (3.29)$$

Here, we find that resonance occurs when $\Delta = (\ell'^2 - \ell^2)\omega_r$, or when the detuning from the carrier electronic transition is equal to the transition frequency between the states $|\ell\rangle$ and $|\ell'\rangle$, $(E_{\ell'} - E_\ell)/\hbar = (\ell'^2 - \ell^2)\omega_r$.

Rotational transition coupling strengths

The coupling strengths of rotational sidebands are calculated by evaluating the remaining matrix element. To do this, it is useful to rewrite ℓ' as $\ell + \Delta\ell$. The matrix element can be computed by writing everything in position space and evaluating the appropriate integral:

$$\begin{aligned}\langle \ell + \Delta\ell | e^{i\frac{1}{2}[\zeta L_+ + \zeta^* L_-]} | \ell \rangle &= \int_0^{2\pi} d\theta \frac{1}{\sqrt{2\pi}} e^{-i(\ell + \Delta\ell)\theta} e^{i\frac{1}{2}(\zeta e^{i\theta} + \zeta^* e^{-i\theta})} \frac{1}{\sqrt{2\pi}} e^{i\ell\theta} \\ &= \frac{1}{2\pi} \int_0^{2\pi} e^{i\frac{1}{2}(\zeta e^{i\theta} + \zeta^* e^{-i\theta}) - i\Delta\ell\theta} \\ &= e^{i\Delta\ell[\arg(\zeta) + \pi/2]} J_{\Delta\ell}(|\zeta|).\end{aligned}\quad (3.30)$$

The magnitude of this matrix element is the $\Delta\ell$ th order Bessel function of the first kind evaluated at $|\zeta|$. Note that this expression holds even for transitions which lower the angular momentum quantum number, using the Bessel function identity $J_{-n}(x) = (-1)^n J_n(x)$. In total then, we have

$$\langle b_i, \ell + \Delta\ell | H_I | a_i, \ell \rangle = \frac{1}{2} \hbar \Omega_{\Delta\ell} e^{-i\delta_{\ell, \ell+\Delta\ell} t}, \quad (3.31a)$$

where

$$\Omega_{\Delta\ell} \equiv \Omega J_{\Delta\ell}(|\zeta_i|) e^{i\Delta\ell[\arg(\zeta_i) + \pi/2]} \quad (3.31b)$$

$$\delta_{\ell, \ell+\Delta\ell} \equiv \Delta - (2\ell\Delta\ell + \Delta\ell^2)\omega_r. \quad (3.31c)$$

This result for rotor-mode laser-ion coupling can be compared to that of vibrational-mode laser-ion coupling (3.8). A few points in particular are worth making:

- Resonance occurs at a detuning of $\Delta = (2\ell\Delta\ell + \Delta\ell^2)\omega_r$, which is the transition frequency between the states $|\ell\rangle$ and $|\ell + \Delta\ell\rangle$. Unlike the harmonic oscillator, because the rotor is nonlinear, this transition frequency depends on the starting state $|\ell\rangle$, not just on the number of quanta being added or subtracted.

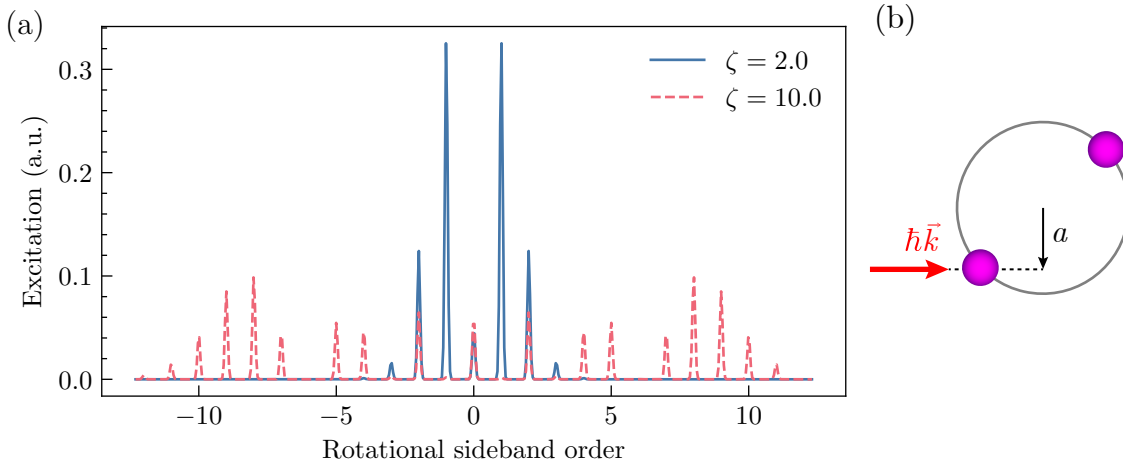


Figure 3.4: (a) Schematic sideband spectra for rigid rotor sideband transitions. The height of the peaks shown is the square of the magnitude of the relative coupling strength $J_{\Delta\ell}(|\zeta|)$. Typical values of $|\zeta|$ are greater than 1, so unlike a vibrational mode in the Lamb-Dicke-regime, the rotational coupling strengths do not fall monotonically with sideband order. (b) Semi-classical picture of the rotor absorbing a photon carrying linear momentum $\hbar k$ at a perpendicular distance a away from the axis of rotation, thus imparting angular momentum $L = \hbar k a$.

- If $\ell \gg \Delta\ell$, then the sideband frequency is approximately $2\ell\Delta\omega_r = \Delta\ell \omega_{\text{rot}}$, which is $\Delta\ell$ times the classical rotation frequency that corresponds to the angular momentum $\ell\hbar$. Thus, in this limit, motional sidebands are found at integer multiples of the classical rotation frequency. This agrees with a classical expectation of finding modulation sidebands at the frequency of the motion.
- The magnitude of the coupling strength, $J_{\Delta\ell}(|\zeta_i|)$, is independent of the starting state $|\ell\rangle$, and depends only on the order of the sideband transition, unlike the harmonic oscillator.

In summary, rotational sidebands occur at frequencies which are (approximately) integer multiples of the rotation frequency, with coupling strengths that are independent of the state $|\ell\rangle$ and depend only on $\Delta\ell$. In particular, their magnitude is given by $J_{\Delta\ell}(|\zeta|)$, where $|\zeta|$ is a dimensionless parameter equal to the product of the rotor radius and the laser wavevector projected onto the rotor plane.

We can compare this result to a semi-classical interpretation, shown schematically in Fig. 3.4(b): A single photon, approximated as a hard point-sized sphere carrying linear momentum $\hbar k$ (when projected onto the rotor plane), collides with the rotor at some position a distance a away from the center. This adds an angular momentum of $\hbar k a$ to the rotor. If the laser is fully illuminating the rotor, then a photon may collide with the rotor at any distance a where $-r < a < r$, with some probability. Thus the maximum possible angular

momentum transfer is $\hbar kr = \hbar\zeta$, so if the angular momentum is quantized, then $\Delta\ell$ is bound between $-\zeta$ and ζ . The true coupling strength $J_{\Delta\ell}(|\zeta|)$ indeed falls off rapidly with increasing $\Delta\ell$ beyond the point where $|\Delta\ell| > |\zeta|$, as can be seen from Fig. 3.4(a).

3.3.4 Rabi oscillations of rotational sideband transitions

The transition frequencies and coupling strengths of transitions which change the rotational state of a trapped-ion rotor derived above inform the shape of measured Rabi oscillations. As with vibrational sidebands, if the initial state is not an energy eigenstate, then the observed result will be a weighted average over the initial state (Eq. (2.38)). In contrast to vibrational sideband transitions, which exhibit different Rabi frequencies for different n due to their different coupling strengths, rotational sideband transitions have the same coupling strength for different ℓ but have different detunings. A typical initial state for the rotor in this work is one where the initial state is close to Gaussian-distributed in angular momentum space, with a mean $\bar{\ell}$ large compared to its standard deviation, σ_ℓ . As described in more detail in Chapter 6, this allows us to spectrally resolve sidebands by their transition order $\Delta\ell$. For an initial state of the rotor given by some probability P_ℓ , Rabi oscillations on the $\Delta\ell$ sideband take the form

$$P_b(t) = \sum_\ell P_\ell \frac{\Omega_{\Delta\ell}^2}{\Omega_{\Delta\ell}^2 + \delta_{\ell,\ell+\Delta\ell}^2} \sin^2 \left(\frac{1}{2} \sqrt{\Omega_{\Delta\ell}^2 + \delta_{\ell,\ell+\Delta\ell}^2} t \right). \quad (3.32)$$

Here dephasing of the oscillations comes from the contributions of different detunings. Figure 3.5 shows some Rabi oscillations for an angular momentum distribution which is Gaussian-distributed with standard deviation σ_ℓ . Note that the relation (3.32) strictly holds for only a single ion in a rotor; for a rotor with two ions, both may be excited, and the result is slightly modified, though negligibly so in most cases of experimental interest. Sec 6.4 quantifies this discrepancy.

3.4 N -ion crystals in a planar rigid rotor with vibrational motion

This section generalizes the results of the previous section to a Coulomb crystal which may exhibit vibrational motion in addition to the rotational motion. This is straightforwardly furthermore generalized to a crystal which contains an arbitrary number of constituent ions. This section makes both of these generalizations together.

Here, the rotational motion fundamentally alters the way that a laser field interacts with vibrational modes, in contrast to a static Coulomb crystal whose vibrational modes may be considered independent of each other. We assume here that the rotor is still rigid in the sense that the ions' equilibrium positions do not change with the rotational state from centrifugal effects, though they may vibrate about those equilibrium positions. We further assume that

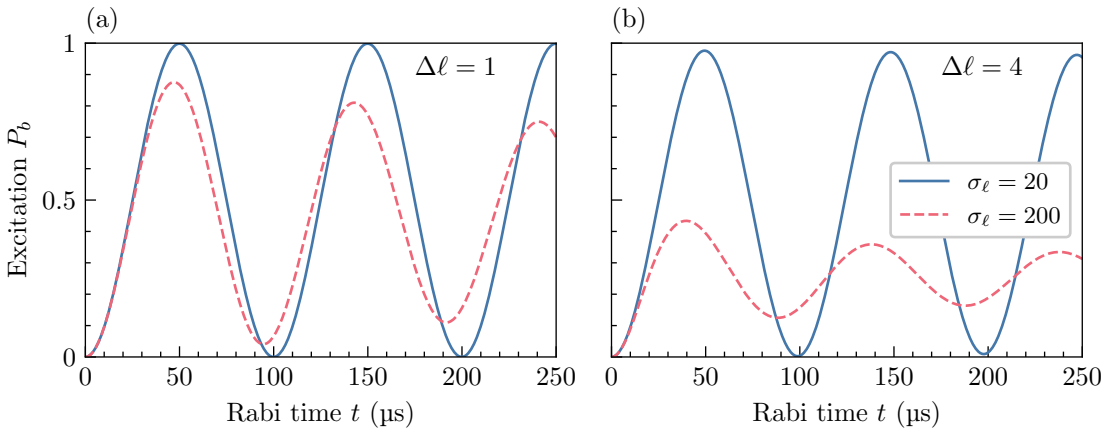


Figure 3.5: Simulated Rabi oscillations on rotational sidebands for different angular momentum distribution widths σ_ℓ for $\Delta\ell = 1, 4$. Different values of $\Delta\ell$ result in different detunings $\delta_{\ell,\ell+\Delta\ell}$. In both cases, the coupling strength $\Omega_{\Delta\ell}$ is set to $2\pi \times 10$ kHz.

the Coulomb crystal is at most 2-dimensional so that ions' equilibrium positions all lie within the xy -plane.

3.4.1 The position operator

When considering the vibrational normal modes of the N -ion crystal in addition to the rigid rotor mode, the Hamiltonian (3.24) generalizes to

$$\begin{aligned} H &= H_0 + H_1, \\ H_0 &= \frac{L_z^2}{2I} + \sum_j \hbar\omega_j (a_j^\dagger a_j + \tfrac{1}{2}) + \sum_i \frac{1}{2} \hbar\omega_{ab} (|b_i\rangle\langle b_i| - |a_i\rangle\langle a_i|) \\ H_1 &= \sum_i \frac{1}{2} \hbar\Omega (|b_i\rangle\langle a_i| + |b_i\rangle\langle a_i|) [e^{i(\mathbf{k}\cdot\mathbf{r}_i - \omega t)} + e^{-i(\mathbf{k}\cdot\mathbf{r}_i - \omega t)}], \end{aligned} \quad (3.33)$$

where the index i runs over the N ions and the index j runs over the $3N - 1$ vibrational modes. As usual, we will rewrite the ion positions \mathbf{r}_i in terms of normal mode coordinates, but here, unlike the case of an anisotropic potential, the ions do not have unique equilibrium positions. Instead, they are unique only up to the overall orientation of the crystal, θ . We define a reference ‘‘equilibrium’’ position \mathbf{r}_i^0 as the equilibrium position of ion i at $\theta = 0$.

To illustrate this concretely, consider the ion positions of a 2-ion crystal at orientation $\theta = 0$, plus some finite excitation of the stretch mode only. The equilibrium positions match the anisotropic case given in (3.3), and similarly the eigenvector of the stretch mode matches Tab. 3.1, so that for a stretch mode coordinate ξ_{stretch} ,

$$\begin{aligned} \mathbf{r}_1^{\theta=0} &= (r + \frac{1}{\sqrt{2}}\xi_{\text{stretch}}, 0, 0) \\ \mathbf{r}_2^{\theta=0} &= (-r - \frac{1}{\sqrt{2}}\xi_{\text{stretch}}, 0, 0). \end{aligned} \quad (3.34)$$

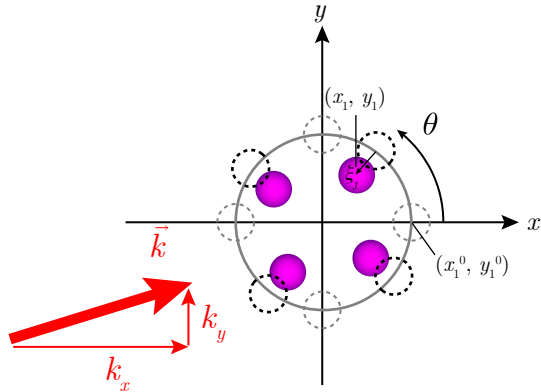


Figure 3.6: Four ions in a planar rotor illuminated by a laser field with wavevector \mathbf{k} . The ions may rotate about the origin, described by the angle coordinate θ , and may also vibrate. In total there are $2N - 1 = 7$ vibrational modes within the xy -plane. One of them, the breathing motion, is shown, with coordinate ξ_j . Grey dotted circles show the ions' reference positions when all coordinates are zero, and black dotted circles show the ions' positions when only the angular coordinate θ is nonzero.

If on the other hand $\theta \neq 0$, the entire crystal is reoriented, which can be quantified by applying a rotation matrix:

$$\mathbf{r}_i = \begin{pmatrix} \cos \theta & -\sin \theta & 0 \\ \sin \theta & \cos \theta & 0 \\ 0 & 0 & 1 \end{pmatrix} \mathbf{r}_i^{\theta=0} \quad (3.35)$$

The effect is to rotate not only the “equilibrium” positions of the ions, but to also reorient the vibrational normal modes. In the example of the 2-ion crystal where we consider the contribution of the stretch mode only, finite θ results in new positions

$$\begin{aligned} \mathbf{r}_1 &= \left(\cos \theta [r + \frac{1}{\sqrt{2}}\xi_{\text{stretch}}], \sin \theta [r + \frac{1}{\sqrt{2}}\xi_{\text{stretch}}], 0 \right) \\ \mathbf{r}_2 &= \left(\cos \theta [-r - \frac{1}{\sqrt{2}}\xi_{\text{stretch}}], \sin \theta [-r - \frac{1}{\sqrt{2}}\xi_{\text{stretch}}], 0 \right). \end{aligned} \quad (3.36)$$

Since the direction of the vibrational normal modes depends on the orientation θ , it is convenient to define the normal mode matrices (X_{ij}, Y_{ij}, Z_{ij}) describing the contribution of mode j to ion i) at the reference orientation $\theta = 0$. Generalizing to all modes, the position

of ion i in terms of normal mode coordinates is given by

$$\mathbf{r}_i = \left(\begin{array}{l} \cos \theta \left[x_i^0 + \sum_j X_{ij} \xi_j \right] - \sin \theta \left[y_i^0 + \sum_j Y_{ij} \xi_j \right], \\ \sin \theta \left[x_i^0 + \sum_j X_{ij} \xi_j \right] + \cos \theta \left[y_i^0 + \sum_j Y_{ij} \xi_j \right], \\ \sum_j Z_{ij} \xi_j \end{array} \right). \quad (3.37)$$

Since the rotation is confined to the xy -plane, the orientation has no effect on the equilibrium position or normal modes in the z -direction. All normal modes of a 2D ion crystal will either be entirely in the plane ($Z_{ij} = 0$) or entirely out of the plane ($X_{ij} = Y_{ij} = 0$), categories which we label “horizontal” and “vertical” modes. For an anisotropic (planar isotropic) N -ion crystal, there are exactly $2N$ ($2N - 1$) horizontal vibrational modes, and N vertical vibrational modes. This distinction is useful in the case of the rotor, since the rotor mode affects the horizontal modes, but not the vertical modes.

We can now rewrite (3.37) with the mode coordinates $\theta, \{\xi_j\}$ written in terms of operators. The result, when dot-multiplied with the laser wavevector \mathbf{k} , is

$$\mathbf{k} \cdot \mathbf{r}_i = \frac{1}{2} (\zeta_i L_+ + \zeta_i^* L_-) + \sum_{j \in \text{horiz. modes}} \frac{1}{2} (\tilde{\eta}_{ij} L_+ + \tilde{\eta}_{ij}^* L_-) (a_j + a_j^\dagger) + \sum_{j \in \text{vert. modes}} \eta_{ij} (a_j + a_j^\dagger), \quad (3.38)$$

where

$$\tilde{\eta}_{ij} \equiv (k_x - ik_y)(X_{ij} + iY_{ij}) \sqrt{\frac{\hbar}{2m\omega_j}}, \quad (3.39)$$

and ζ_i and η_{ij} are already defined by (3.26b) and (3.6), respectively. $\tilde{\eta}_{ij}$ can be interpreted as a sort of modified Lamb-Dicke factor. (Note that here, the tilde in $\tilde{\eta}$ indicates a complex number, not an interaction-picture operator.) It is useful to compare this result to the corresponding results for crystals when only vibrational motion is present (3.5), and for planar-isotropic crystals whose rotational motion is considered alone (3.26). To summarize some noteworthy points about this comparison:

- $\mathbf{k} \cdot \mathbf{r}_i$ is a sum of three terms: one corresponding to the rotational motion, one to the vibrational motion in the plane of rotation, and one to the vibrational motion out of the plane of rotation. The first is precisely the same as (3.26) (rotational motion only), and the last is precisely the same as (3.5) (vibrational motion only) up to a constant term. The remaining term is a modified version of (3.5), where the real-valued Lamb-Dicke factor η_{ij} is instead replaced by a Hermitian operator $\frac{1}{2}(\tilde{\eta}_{ij} L_+ + \tilde{\eta}_{ij}^* L_-)$, an operator in the rotational Hilbert space. Therefore, unlike the case of a typical Coulomb crystal which exhibits only vibrational motion, the motional modes of motion of a planar

isotropic crystal do not fully separate for the purposes of laser interaction with those modes, even in the rigid rotor approximation; rather, the rotational degree of freedom fundamentally modifies the coupling of the horizontal vibrational modes to the laser.

- In a purely vibrational crystal, $\mathbf{k} \cdot \mathbf{r}_i$ is given by (3.5), which contains a constant term $\mathbf{k} \cdot \mathbf{r}_i^0$ for the equilibrium position of ion i . When exponentiated, this constant term becomes a phase factor which may be ignored. In the rotational case, on the other hand, it is precisely this term which instead turns into the rotational term $\frac{1}{2}(\zeta_i L_+ + \zeta_i^* L_-)$ in (3.38).
- The complex dimensionless factor $\tilde{\eta}_{ij}$ is a modified version of the real Lamb-Dicke factor η_{ij} . Comparing to (3.6), we find that the real part of $\tilde{\eta}_{ij}$ is precisely η_{ij} , and the imaginary part is what the Lamb-Dicke factor would be if the mode were rotated by 90 degrees (up to a sign). We can think of the rotational degree of freedom as eliminating any concept of a well-defined angle between the laser wavevector and the direction of mode j .
- Under the rigid rotor assumption, rotational operators L_\pm and vibrational operators a_j, a_j^\dagger commute; this assumption was made in deriving the result.

3.4.2 The interaction-picture Hamiltonian

With (3.38) as an expression for $\mathbf{k} \cdot \mathbf{r}_i$ in terms of operators, we can transform (3.33) into the interaction picture. For simplicity, we can ignore the vertical modes for this step; their contribution to the laser coupling is unchanged from what they would be in case of an anisotropic case, which has already been analyzed.

$$H_I = \frac{1}{2}\hbar \sum_i \Omega |b_i\rangle\langle a_i| \prod_j e^{i\frac{1}{2}[\zeta_i \tilde{L}_+(t) + \zeta_i^* \tilde{L}_-(t)]} e^{i\frac{1}{2}[\tilde{\eta}_{ij} \tilde{L}_+(t) + \tilde{\eta}_{ij}^* \tilde{L}_-(t)][\tilde{a}_j(t) + \tilde{a}_j^\dagger(t)]} e^{-i\Delta t} + h.c. \quad (3.40)$$

Here the index j runs over horizontal modes only. To find the coupling strength for a transition between eigenstates for ion i , we seek matrix elements of the form $\langle b_i, \ell + \Delta\ell, \mathbf{n} + \Delta\mathbf{n} | H_I | a_i, \ell, \mathbf{n} \rangle$, where now \mathbf{n} stands for the state of all $2N - 1$ horizontal vibrational modes. Note that, unlike (3.7) for N -ion crystals with only vibrational motion, (3.40) is not simply a product of terms for each mode, so we cannot simply compute the matrix element of the full Hamiltonian as a product of matrix elements for each mode. Instead, the rotational and vibrational motion each affect the nature of the other's interaction with the laser field. As a result, a simple closed-form expression for the matrix elements of H_I is not in general possible for rovibrational transitions. However, we can write the expression for the matrix elements in a form which is easier to interpret, after which we may gain some insight by looking at some special cases. Taking the matrix element, inserting a

resolution of the identity, and pulling out the time-dependence, we find

$$\begin{aligned} & \langle b_i, \ell + \Delta\ell, \mathbf{n} + \Delta\mathbf{n} | H_I | a_i, \ell, n \rangle \\ &= \frac{1}{2} \hbar \Omega \sum_{\ell'} \langle \ell + \Delta\ell | e^{i\frac{1}{2}(\zeta_i L_+ + \zeta_i^* L_-)} | \ell' \rangle \prod_j \langle \ell', \mathbf{n} + \Delta\mathbf{n} | e^{i\frac{1}{2}(\tilde{\eta}_{ij} L_+ + \tilde{\eta}_{ij}^* L_-)(a_j + a_j^\dagger)} | \ell, \mathbf{n} \rangle \quad (3.41) \\ & \times e^{-i[\Delta - ((\ell + \Delta\ell)^2 - \ell^2)\omega_r + \sum_j \Delta n_j \omega_j]t} + h.c. \end{aligned}$$

Two notes to interpret this result are as follows:

- As usual, we are able to express the matrix elements in terms of matrix elements of time-independent Schrödinger picture operators. The time dependence from the interaction-picture operators becomes a phase factor representing the resonance condition. In this case, the resonance is at the sum of detunings due to the rotational $\ell \rightarrow \ell + \Delta\ell$ transition and the vibrational $n_j \rightarrow n_j + \Delta n_j$ transitions. This is as expected from conservation of energy.
- The matrix element has been broken into a product of more manageable matrix elements, at the cost of introducing an infinite sum over rotational states ℓ' from a resolution of the identity.

3.4.3 Approximations of the matrix elements in special cases

To further analyze these matrix elements, we must make some assumptions, so only a few special cases of interest will be considered. We consider only one vibrational mode for simplicity, so that for the calculation the ion and mode indices i and j may be dropped. The matrix element (3.41) in this case is written

$$\begin{aligned} \Omega_{\ell, n, \ell + \Delta\ell, n + \Delta n} &= \langle b, \ell + \Delta\ell, n + \Delta n | H_I | a, \ell, n \rangle \\ &= \frac{1}{2} \hbar \Omega \sum_{\ell'} \langle \ell + \Delta\ell | e^{i\frac{1}{2}(\zeta L_+ + \zeta^* L_-)} | \ell' \rangle \langle \ell', n + \Delta n | e^{i\frac{1}{2}(\tilde{\eta} L_+ + \tilde{\eta}^* L_-)(a + a^\dagger)} | \ell, n \rangle. \quad (3.42) \end{aligned}$$

We further make the Lamb-Dicke approximation, which here means $|\tilde{\eta}_{ij}|^2(2n_j + 1) \ll 1$. In this case,

$$e^{i\frac{1}{2}(\tilde{\eta} L_+ + \tilde{\eta}^* L_-)(a + a^\dagger)} = 1 + \frac{i}{2}(\tilde{\eta} L_+ + \tilde{\eta}^* L_-)(a + a^\dagger) + \mathcal{O}(|\tilde{\eta}|^2). \quad (3.43)$$

Some special cases to consider are the following:

1. Transitions of the form $\ell \rightarrow \ell + \Delta\ell$, $n \rightarrow n$

To first order, only the carrier term of (3.43) contributes, as that is the only term which will not change the vibrational quantum number.

$$\begin{aligned}
 \Omega_{\ell,n,\ell+\Delta\ell,n+\Delta n} &= \sum_{\ell'} \langle \ell + \Delta\ell | e^{i\frac{1}{2}(\zeta L_+ + \zeta^* L_-)} | \ell' \rangle \langle \ell', n | e^{i\frac{1}{2}(\tilde{\eta} L_+ + \tilde{\eta}^* L_-)(a+a^\dagger)} | \ell, n \rangle \\
 &\approx \sum_{\ell'} \langle \ell + \Delta\ell | e^{i\frac{1}{2}(\zeta L_+ + \zeta^* L_-)} | \ell' \rangle \langle \ell', n | \ell, n \rangle \\
 &= \langle \ell + \Delta\ell | e^{i\frac{1}{2}(\zeta L_+ + \zeta^* L_-)} | \ell \rangle \\
 &= e^{i\Delta\ell[\arg(\zeta)+\pi/2]} J_{\Delta\ell}(|\zeta|),
 \end{aligned} \tag{3.44}$$

precisely as found in (3.31).

2. Transitions of the form $\ell \rightarrow \ell, n \rightarrow n + 1$

Here, only terms of (3.43) containing a^\dagger will contribute.

$$\begin{aligned}
 \Omega_{\ell,n,\ell+\Delta\ell,n+\Delta n} &= \sum_{\ell'} \langle \ell | e^{i\frac{1}{2}(\zeta L_+ + \zeta^* L_-)} | \ell' \rangle \langle \ell', n + 1 | e^{i\frac{1}{2}(\tilde{\eta} L_+ + \tilde{\eta}^* L_-)(a+a^\dagger)} | \ell, n \rangle \\
 &\approx \sum_{\ell'} \langle \ell | e^{i\frac{1}{2}(\zeta L_+ + \zeta^* L_-)} | \ell' \rangle \langle \ell', n + 1 | \frac{i}{2}(\tilde{\eta} L_+ + \tilde{\eta}^* L_-) a^\dagger | \ell, n \rangle \\
 &= -|\tilde{\eta}| \sqrt{n+1} J_1(|\zeta|) \operatorname{Re}(e^{i[\arg(\tilde{\eta})-\arg(\zeta)]})
 \end{aligned} \tag{3.45}$$

To interpret this result, we may compare to the case of a static Coulomb crystal. In that case, the magnitude of the equivalent matrix element (i.e. where the motional quantum number increases by 1) is $\eta\sqrt{n+1}$, (2.36b). The above result for a crystal which is allowed to rotate is similar, but with $|\tilde{\eta}|$ replacing η , and multiplied by two additional factors:

- The first factor is $J_1(|\zeta|)$. This is also the magnitude of the matrix element for a $|\ell\rangle \rightarrow |\ell+1\rangle$ transition. We can interpret this from the structure of (3.42), which contains a product of two matrix elements: One for the rotational part alone, and one for the vibrational part which necessarily also contains rotational operators. This may be interpreted as two energy-conserving processes. In the Lamb-Dicke expansion (3.43), we see that a change in vibrational quantum number must come with a change in rotational quantum number. Thus in order to change only the vibrational quantum number, one of these processes must change the rotational quantum number by 1 (with magnitude $\sim |\tilde{\eta}|\sqrt{n+1}$), and the other must change it back (with magnitude $\sim J_1(|\zeta|)$).
- The second factor is $\operatorname{Re}(e^{i[\arg(\tilde{\eta})-\arg(\zeta)]})$, which arises from the interference of the $\ell \pm 1$ terms that contribute. This factor effectively measures the relative phase between the rotational and vibrational parameters ζ and $\tilde{\eta}$. This relative phase encodes how “radial” the mode j is for ion i ; if the ion’s motion due to mode j

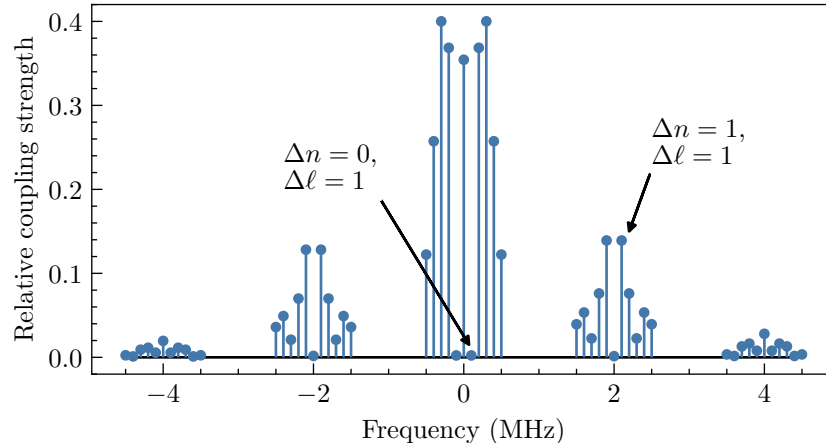


Figure 3.7: Sample spectrum showing the coupling strengths of rovibrational transitions. The y -axis is the magnitude of the matrix elements of the operator (3.43). The vibrational mode has a frequency of 2 MHz and the rotation frequency is set to 100 kHz, so that rotational transitions are grouped within the separated vibrational sidebands. The vibrational Lamb-Dicke parameter is $\eta = 0.2$, and $\zeta = 3.86$. Because ζ is near a zero of J_1 , the coupling strength of the $\Delta\ell = 1$ transition nearly vanishes, but on the $\Delta n = 1$ vibrational sideband, the $\Delta\ell = 1$ transition is allowed.

is outward from the crystal's axis of rotation, then the relative phase is zero and this matrix element is maximum. If the ion's motion due to mode j is tangent to the crystal's rotation, then the relative phase is $\pi/2$ and this matrix element vanishes.

This result demonstrates that, even when addressing a purely vibrational sideband (i.e. with no rotational transition, $\Delta\ell = 0$), the coupling strength is affected by the presence of a rotational degree of freedom. This is to be contrasted with the case of a purely vibrational ion crystal, where each mode of motion acts independently of the others. In special cases, the first vibrational sideband can vanish entirely, independent of the state of the vibrational motion. It will vanish exactly for a mode with components only in the angular direction, and will also vanish to first order in $|\tilde{\eta}|$ for a wavevector such that $|\zeta|$ is a zero of the Bessel function J_1 , as shown in Fig. 3.7.

3. Transitions of the form $\ell \rightarrow \ell + \Delta\ell, n \rightarrow n + 1$

This is the generalization of the previous case, where we now allow the angular mo-

mentum quantum number to change as well.

$$\begin{aligned} & \sum_{\ell'} \langle \ell + \Delta\ell | e^{i\frac{1}{2}(\zeta L_+ + \zeta^* L_-)} | \ell' \rangle \langle \ell', n + 1 | e^{i\frac{1}{2}(\tilde{\eta} L_+ + \tilde{\eta}^* L_-)(a + a^\dagger)} | \ell, n \rangle \\ & \approx |\tilde{\eta}| \sqrt{n+1} \frac{1}{2} [e^{i[\arg(\tilde{\eta}) - \arg(\zeta)]} J_{\Delta\ell-1}(|\zeta|) - e^{-i[\arg(\tilde{\eta}) - \arg(\zeta)]} J_{\Delta\ell+1}(|\zeta|)] e^{i\Delta\ell[\arg(\zeta) + \pi/2]} \end{aligned} \quad (3.46)$$

Unlike the previous case, we have two terms which contain Bessel functions of different orders, and thus do not in general vanish in special cases. It is clear that this matrix element is not a simple product of the two matrix elements for the individual transitions $|\ell\rangle \rightarrow |\ell + \Delta\ell\rangle$ and $|n\rangle \rightarrow |n + 1\rangle$, unlike the (3.8b), where the transition of each vibrational mode contributes an independent factor to the overall matrix element.

In cases 2 and 3 considered above, the result is the same if we instead consider the red vibrational sideband $|n\rangle \rightarrow |n - 1\rangle$, except with the factor $\sqrt{n+1}$ replaced by \sqrt{n} .

3.4.4 Summary

Table 3.2 summarizes the coupling strengths computed for vibrational and rotational transitions.

Measurements of pure rotational sideband coupling strengths have been done in this work, but not rovibrational sidebands. Measuring a rovibrational spectrum would be challenging, as we use a nearly vertical beam to measure rotational sidebands, which significantly suppresses coupling to in-plane vibrational modes.

3.5 2-ion crystals in a planar non-rigid rotor

This section outlines some modifications to the results of the previous section which occur when the rigid rotor assumption is relaxed, and centrifugal effects are considered. This is done perturbatively to first order only. Only the energy eigenspectrum is considered; laser-ion interaction coupling strengths are not. Practically, a modification to the energy spectrum of the order 10^{-2} could be significant, but a modification of the same order to coupling strengths will not. This section also considers only a 2-ion crystal, the simplest case.

The rigid rotor condition was defined previously by (3.18). It is useful to rewrite the rotor rigidity condition as $\epsilon_\ell \ll 1$, defining the small parameter ϵ_ℓ which can be written in several equivalent ways:

$$\epsilon_\ell \equiv \frac{r_\ell - r_0}{r_0} = \frac{\hbar^2 \ell^2}{3I_0^2 \omega_x^2} = \frac{D\ell^2}{\omega_{r0}} = \frac{4\omega_{r0}^2 \ell^2}{3\omega_x^2} \approx \left(\frac{\omega_\ell^{\text{rot}}}{\omega_{\text{stretch}}} \right)^2. \quad (3.47)$$

Case	Transition form	Relative coupling strength	Approximations in special cases
1 ion, 1 vib. mode	$ n\rangle \rightarrow n + \Delta n\rangle$	$\begin{aligned} & e^{-\eta^2/2} \eta^{ \Delta n } \\ & \times L_{\min(n, n+\Delta n)}^{(\Delta n)}(\eta^2) \\ & \times \left(\frac{n!}{(n+\Delta n)!} \right)^{\text{sign}(\Delta n)/2} \end{aligned} \quad (2.34)$	Lamb-Dicke regime: $\Delta n = 0 \quad 1 - \eta^2 \quad (2.36)$ $\Delta n = 1 \quad \eta \sqrt{n+1}$
N ions, $3N$ vib. modes	$ \mathbf{n}\rangle \rightarrow \mathbf{n} + \Delta \mathbf{n}\rangle$	$\begin{aligned} & \prod_j e^{-\eta_j^2/2} \eta_j^{ \Delta n_j } \\ & \times L_{\min(n_j, n_j+\Delta n_j)}^{(\Delta n_j)}(\eta_j^2) \\ & \times \left(\frac{n_j!}{(n_j+\Delta n_j)!} \right)^{\text{sign}(\Delta n_j)/2} \end{aligned} \quad (3.8)$	(products of above cell)
2 ions, 1 rot. mode	$ \ell\rangle \rightarrow \ell + \Delta \ell\rangle$	$J_{\Delta \ell}(\zeta) \quad (3.30)$	(none necessary)
N ions, 1 rot. mode + $2N - 1$ in-plane vib. modes	$ \ell, \mathbf{n}\rangle \rightarrow \ell + \Delta \ell, \mathbf{n} + \Delta \mathbf{n}\rangle$	No closed-form expression; Written in terms of matrix elements in (3.41)	Lamb-Dicke regime, 1 vib. mode only: $\Delta n = 0 \quad J_{\Delta \ell}(\zeta) \quad (3.44)$ $\Delta n = 1 \quad \begin{aligned} & \frac{1}{2} \tilde{\eta} \sqrt{n+1} \\ & \times [e^{i\alpha} J_{\Delta \ell-1}(\zeta) \\ & - e^{-i\alpha} J_{\Delta \ell+1}(\zeta)], \end{aligned} \quad (3.46)$ where $\alpha = \arg(\tilde{\eta}) - \arg(\zeta)$

Table 3.2: Summary of relative coupling strengths for motional transitions. Relative coupling strength refers to the coupling strength of the transition divided by the bare electronic Rabi frequency Ω . Each expression for a coupling strength includes a reference to the corresponding equation in the text. Here, overall phase factors are omitted.

The quantity D , defined as

$$D \equiv \frac{4\omega_{r0}^3}{\omega_{\text{stretch}}^2} = \frac{4\omega_{r0}^3}{3\omega_x^2}, \quad (3.48)$$

is the centrifugal distortion constant commonly used in the context of diatomic molecules [29].

Definitions of new symbols used in (3.47) are as follows:

- r_ℓ is the centrifugally distorted equilibrium radius when the angular momentum quantum number is equal to ℓ , and r_0 is the equilibrium radius in the absence of centrifugal effects.
- ω_{r0} is the same rotation constant defined by (3.22), but with an extra subscript 0 to indicate that this is the value in the absence of centrifugal effects, in anticipation that we will find that the effective rotation constant changes due to centrifugal distortion (see Sec. 3.5.4).
- I_0 is similarly the moment of inertia in the absence of centrifugal effects.
- ω_ℓ^{rot} is the rotation frequency at angular momentum quantum number ℓ , with a subscript ℓ to make the ℓ -dependence explicit. In the absence of centrifugal effects, this is given by (3.23).
- ω_{stretch} is the stretch mode frequency.

In the final equality of (3.47), we use the relationship between the angular momentum and classical rotation frequency, $\omega_\ell^{\text{rot}} = 2\omega_{r0}\ell$. This is only approximately true since the relationship between rotation frequency and angular momentum quantum number depends on the moment of inertia, which itself also changes due to centrifugal effects; see Sec. 3.5.4. However, it is the most practically useful relation, as it is written in terms of 2 measurable quantities, the rotation frequency and the stretch mode frequency. When the rotation frequency is large enough such that it is comparable to the stretch motion frequency, the rigid rotor approximation no longer holds. In this section, only leading-order corrections to the rigid rotor approximation are considered, i.e. when the quantity ϵ_ℓ is not negligible, but still small enough that second-order corrections may be ignored. An example of typical experimental parameters is $\omega_r = 2\pi \times 10 \text{ Hz}$, $\omega_{\text{stretch}} = 2\pi \times 2 \text{ MHz}$, and $\omega_{\bar{\ell}}^{\text{rot}} = 2\pi \times 150 \text{ kHz}$ (where $\bar{\ell}$ is the mean of the rotational state, which in general has some distribution over angular momenta). In this case, $D = 2\pi \times 1 \text{ nHz}$ and $\epsilon_{\bar{\ell}} = 6 \times 10^{-3}$.

3.5.1 Centrifugal distortion

Sec. 3.3 derives the normal modes of motion for a 2-ion rotor. The final step in this process before invoking the rigid rotor approximation was writing the potential energy of the motion of the relative coordinate, (3.11). The following step was to solve for the equilibrium positions expand the potential about that point. If the rotor is not rigid, then the rotational motion will

create a centrifugal potential and thus modify the equilibrium positions. Thus we must first find the new equilibrium position in the non-rigid case. Including the centrifugal potential term, (3.11) is modified to

$$U_\ell(\mathbf{r}) = \frac{1}{2}\mu(\omega_x^2\rho^2 + \omega_z^2z^2) + \frac{e^2}{4\pi\epsilon_0} \frac{1}{\sqrt{\rho^2 + z^2}} + \frac{\hbar^2\ell^2}{2\mu\rho^2}. \quad (3.49)$$

It will be convenient here to shift into laboratory-frame coordinates, using the physical radius of the rotor $r = \rho/2$ as well as the true mass of each ion $m = 2\mu$:

$$U_\ell(r, z) = m(\omega_x^2 r^2 + \frac{1}{4}\omega_z^2 z^2) + \frac{e^2}{4\pi\epsilon_0} \frac{1}{\sqrt{4r^2 + z^2}} + \frac{\hbar^2\ell^2}{4mr^2}. \quad (3.50)$$

To solve for the radius r which minimizes this potential, we set $z = 0$ and solve $\partial U_\ell / \partial r = 0$. We write $r = r_0 + \delta r$ and expand perturbatively:

$$\begin{aligned} U_\ell(r) &= m\omega_x^2 r^2 + \frac{e^2}{8\pi\epsilon_0 r} + \frac{\hbar^2\ell^2}{4mr^2} \\ &= m\omega_x^2(r_0 + \delta r)^2 + \frac{e^2}{8\pi\epsilon_0(r_0 + \delta r)} + \frac{\hbar^2\ell^2}{4m(r_0 + \delta r)^2}. \end{aligned} \quad (3.51)$$

Setting $\partial U_\ell / \partial r = \partial U_\ell / \partial \delta r = 0$ and solving for δr , we find, to first order in $\delta r/r_0$,

$$\frac{\delta r_\ell}{r_0} = \frac{\hbar^2\ell^2}{12m^2r_0^4\omega_x^2} = \epsilon_\ell. \quad (3.52)$$

The subscript ℓ in δr_ℓ indicates that this is the solution for angular momentum quantum number ℓ . This is the same quantity from (3.18), rewritten in laboratory-frame coordinates. This justifies the claim from Sec. 3.3 that the rigidity condition should be defined by the condition (3.18), which we later define as ϵ_ℓ in (3.47). The radius of a non-rigid rotor is therefore approximately $r_\ell = r_0(1 + \epsilon_\ell)$.

3.5.2 Non-rigid corrections to individual modes

In the presence of centrifugal distortion, the potential of all three “relative motion” degrees of freedom of a 2-ion crystal is modified: the vertical rocking motion, the stretch motion, and the rotational motion. All of these modifications arise from the centrifugal distortion increasing the distance between the ions, which in turn modifies the respective motional frequencies.

Vertical rocking mode

To analyze the vertical rocking mode, we first expand the potential (3.50) about $z = 0$:

$$U_\ell(r, z) \approx m(\omega_x^2 r^2 + \frac{1}{4}\omega_z^2 z^2) + \frac{e^2}{4\pi\epsilon_0} \left(\frac{1}{2r} - \frac{z^2}{16r^3} \right) + \frac{\hbar^2\ell^2}{4mr^2}. \quad (3.53)$$

We are interested in the coordinate z , so we can set the radius r of the rotor to be equal to the centrifugally distorted radius at rotational quantum number ℓ , $r_\ell = r_0(1 + \epsilon_\ell)$ and perturbatively expand:

$$\begin{aligned} U_\ell(r_\ell, z) &\approx \frac{1}{4}m\omega_z^2 z^4 - \frac{e^2}{64\pi\epsilon_0 r_0^3 (1 + \epsilon_\ell)^3} z^2 + (\text{constant terms}) \\ &= \frac{1}{4}m \left[\omega_z^2 - \frac{\omega_x^2}{(1 + \epsilon_\ell)^3} \right] z^2 \\ &\approx \frac{1}{4}m \left[\sqrt{\omega_z^2 - \omega_x^2} \left(1 + \frac{3\omega_x^2}{2(\omega_z^2 - \omega_x^2)} \epsilon_\ell \right) \right]^2 z^2. \end{aligned} \quad (3.54)$$

Therefore, the vertical rocking mode frequency, to first order due to centrifugal effects, is

$$\omega_{\text{vert rock}} = \omega_{vr} \approx \sqrt{\omega_z^2 - \omega_x^2} \left(1 + \frac{3\omega_x^2}{2(\omega_z^2 - \omega_x^2)} \epsilon_\ell \right) \quad (3.55)$$

Centrifugal distortion increases this frequency by a factor of $1 + [3\omega_x^2/2(\omega_z^2 - \omega_x^2)]\epsilon_\ell$. The correction term is half the square of the ratio of the stretch mode frequency to the rocking mode frequency (in the absence of distortion). Typically in the work done in this thesis, $\omega_z \approx 2\omega_x$, in which case this correction term is approximately $\epsilon_\ell/2$.

Stretch and rotational modes

These two modes take place within the horizontal plane, so we begin by taking the potential (3.50) and setting $z = 0$. We will need to expand the coordinate r about its equilibrium position r_ℓ , which depends on the angular momentum quantum number. It will be convenient to write the coordinate r as $r = r_0(1 + \epsilon_\ell + a)$. The explicit expansion of r_ℓ into $r_0(1 + \epsilon_\ell)$ makes it clear where the quantity ϵ_ℓ shows up, which is convenient since it is our expansion parameter. This defines a dimensionless coordinate $a = (r - r_\ell)/r_0$, which rescales $r - r_\ell$, the deviation of r from its equilibrium point, in units of r_0 . Rewriting (3.50) in these terms with $z = 0$,

$$\begin{aligned} U_\ell(a, 0) &= m\omega_x^2 r_0^2 (1 + \epsilon_\ell + a)^2 + \frac{e^2}{4\pi\epsilon_0 r_0} \frac{1}{(1 + \epsilon_\ell + a)} + \frac{\hbar^2 \ell^2}{4mr_0^2} \frac{1}{(1 + \epsilon_\ell + a)^2} \\ &= m\omega_x^2 r_0^2 (1 + \epsilon_\ell + a)^2 + 2m\omega_x^2 r_0^2 \frac{1}{(1 + \epsilon_\ell + a)} + \hbar\omega_{r0} \ell^2 \frac{1}{(1 + \epsilon_\ell + a)^2} \end{aligned} \quad (3.56)$$

We expand this potential to second order in a to recover a harmonic potential. We also keep terms only to first order in ϵ_ℓ .

$$\begin{aligned} U_\ell(r) &\approx 3m\omega_x^2 (r - r_\ell)^2 (1 + \epsilon_\ell) + \hbar\omega_{r0} \ell^2 (1 - \epsilon_\ell) \\ &\approx m \left[\sqrt{3}\omega_x (1 + \frac{1}{2}\epsilon_\ell) \right]^2 (r - r_\ell)^2 + \hbar\omega_{r0} \ell^2 (1 - \epsilon_\ell) \end{aligned} \quad (3.57)$$

The stretch mode frequency to first order due to centrifugal effects is thus

$$\omega_{\text{stretch}} = \omega_s = \sqrt{3}\omega_x \left(1 + \frac{1}{2}\epsilon_\ell\right) \quad (3.58)$$

The final term, the rotational energy, may be written as

$$E_\ell^{\text{rot}} = \hbar(\omega_{r0}\ell^2 - D\ell^4), \quad (3.59)$$

where D is the distortion constant defined in (3.48). This lowers the energy of a given angular momentum state compared with the rigid case. The physical reason for this is that centrifugal distortion expands the size of the rotor, increasing its moment of inertia, and thus decreasing its classical angular velocity for a given angular momentum.

3.5.3 Energy eigenspectrum

The energy eigenspectrum of the vertical rocking, stretch, and rotational motion will be given by

$$E(n_{vr}, n_s, \ell) = \hbar\omega_{vr}(n_{vr} + \frac{1}{2}) + \hbar\omega_s(n_s + \frac{1}{2}) + E_\ell^{\text{rot}} \quad (3.60)$$

where the final term is given by (3.59). In the presence of centrifugal distortion, the energy eigenspectrum of the three modes is not separable, since now the rocking and stretch mode frequencies, given by (3.55) and (3.58) respectively, depend on the rotational quantum number ℓ via ϵ_ℓ . To make this explicit, we can write ϵ_ℓ as $D\ell^2/\omega_{r0}$:

$$\begin{aligned} E(n_{vr}, n_s, \ell) &= \hbar\sqrt{\omega_z^2 - \omega_x^2} \left[1 + \frac{3\omega_x^2 D}{2(\omega_z^2 - \omega_x^2)\omega_{r0}} \ell^2 \right] (n_{vr} + \frac{1}{2}) \\ &\quad + \hbar\sqrt{3}\omega_x \left(1 + \frac{D}{2\omega_{r0}} \ell^2 \right) (n_s + \frac{1}{2}) \\ &\quad + \hbar(\omega_{r0}\ell^2 - D\ell^4) \end{aligned} \quad (3.61)$$

The transition frequency for a unit increase in the vibrational mode quantum numbers depends on ℓ and is already given by (3.55) and (3.58). The transition frequency for a unit increase in the rotational quantum number ℓ , $E(n_{vr}, n_s, \ell + 1) - E(n_{vr}, n_s, \ell)$, also now depends on the values of n_{vr} and n_s . With typical experimental parameters, these corrections are very small unless $n \gtrsim 10^3$, at which point they become only corrections to the non-rigid correction term.

3.5.4 Corrections to experimentally relevant rotational parameters

In general, the state of the rotational degree of freedom may be a distribution of angular momenta, in which case corrections to relevant quantities such as the energy spectrum of the stretch mode will also have some spread. As mentioned in Sec. 3.3.4, a typical state of

our trapped-ion rotor is one whose angular momentum is large and well-localized, $\bar{\ell} \gg \sigma_\ell$. The small spread makes it convenient to characterize the non-rigid correction factor by only the mean value of the distribution, such that $\epsilon_{\bar{\ell}}$ alone approximately fully characterizes non-rigid correction quantities. One way to manifest this approximation is to define an effective rotational constant $\omega_{r,\ell}$, and substitute its value at $\bar{\ell}$, $\omega_{r,\bar{\ell}}$, in for the rotational constant. Due to the nonlinearity of the corrections, the appropriate effective rotational constant will depend on the quantity of interest.

Rotational energy spectrum

Equation (3.59) gives the non-rigid energy spectrum, which may be rewritten as

$$E_\ell = \hbar\ell^2(\omega_{r0} - D\ell^2) = \hbar\omega_{r0}\ell^2(1 - \epsilon_\ell). \quad (3.62)$$

Defining the “effective” rotational constant as $\omega_{r,\bar{\ell}} = \omega_{r0}(1 - D\bar{\ell}^2) = \omega_{r0}(1 - \epsilon_{\bar{\ell}})$, the energy may be written as approximately

$$E_\ell \approx \hbar\omega_{r,\bar{\ell}}\ell^2, \quad (3.63a)$$

where

$$\omega_{r,\bar{\ell}} = \omega_{r0}(1 - \epsilon_{\bar{\ell}}). \quad (3.63b)$$

This approximation holds only for values of ℓ near $\bar{\ell}$.

Rotation frequency and transition frequencies

The rotation frequency ω_ℓ^{rot} is in general related to the angular momentum in terms of the moment of inertia I via $L = I\omega_\ell^{\text{rot}} \implies \omega_\ell^{\text{rot}} = \hbar\ell/I$. When the rotor is not rigid, the radius depends on ℓ , and thus in turn so does the moment of inertia. To leading order,

$$\omega_\ell^{\text{rot}} = \frac{\hbar\ell}{I_\ell} = \frac{\hbar\ell}{2mr_\ell^2} = \frac{\hbar\ell}{2mr_0(1 + \epsilon_\ell)^2} \approx \frac{\hbar\ell}{I_0}(1 - 2\epsilon_\ell) = 2\omega_{r0}\ell(1 - 2\epsilon_\ell). \quad (3.64)$$

Thus with the appropriate effective rotational constant $\omega_{r,\bar{\ell}}$,

$$\omega_\ell^{\text{rot}} \approx 2\omega_{r,\bar{\ell}}\ell \quad (3.65a)$$

where

$$\omega_{r,\bar{\ell}} = \omega_{r0}(1 - 2\epsilon_{\bar{\ell}}). \quad (3.65b)$$

Note that the correction term $2\epsilon_{\bar{\ell}}$ differs by a factor of 2 from the corresponding correction term for the energy (3.63b). Again, the above approximation holds only for values of ℓ near $\bar{\ell}$.

In Sec. 3.3.3 we found the transition frequency from $|\ell\rangle$ to $|\ell + \Delta\ell\rangle$ to be approximately $\Delta\ell \omega_\ell^{\text{rot}}$, as long as $\ell \gg \Delta\ell$. This proportionality between rotation frequency and transition

frequency continues to hold for the non-rigid rotor. To see this, we compute the difference $\omega_{\ell+\Delta\ell,\ell} = (E_{\ell+\Delta\ell} - E_\ell)/\hbar$ with each term given by (3.59). The leading-order result is

$$\omega_{\ell+\Delta\ell,\ell} = \frac{E_{\ell+\Delta\ell} - E_\ell}{\hbar} \approx \Delta\ell(2\omega_{r0}\ell - 4D\ell^3) = \Delta\ell 2\omega_{r0}\ell(1 - 2\epsilon_\ell). \quad (3.66)$$

Thus if we again define $\omega_{r,\bar{\ell}} = \omega_{r0}(1 - 2\epsilon_{\bar{\ell}})$, then

$$\frac{E_{\ell+\Delta\ell} - E_\ell}{\hbar} \approx \Delta\ell 2\omega_{r,\bar{\ell}}\ell = \Delta\ell \omega_\ell^{\text{rot}} \quad (3.67)$$

as defined by (3.65a). Thus when computing non-rigid-corrected transition frequencies, the appropriate effective rotational constant is $\omega_{r,\bar{\ell}} = \omega_{r0}(1 - 2\epsilon_{\bar{\ell}})$, the same as for computing the non-rigid-corrected rotation frequency.

Spread in angular momentum

The angular momentum spread σ_ℓ of the state of the rotational mode is an important experimental parameter (see Chapter 6). This is measured by measuring the spread in transition frequencies of a rotational sideband of order $\Delta\ell$, which effectively leads to a broadening of the sideband. It is thus necessary to understand the relationship between the measured sideband linewidth (a spread in frequency space) and the spread of the angular momentum state. Defining the transition frequency between states $|\ell\rangle$ and $|\ell + \Delta\ell\rangle$ as $\omega_{\ell+\Delta\ell,\ell}$, we are interested in the unit change in this transition frequency: $\omega_{\ell+\Delta\ell+1,\ell+1} - \omega_{\ell+\Delta\ell,\ell}$. For a perfectly rigid rotor, this is equal to exactly $2\omega_{r0}\Delta\ell$: each increment in ℓ increases the transition frequency (of the $\Delta\ell$ -order transition) by $2\omega_{r0}\Delta\ell$. Thus if the angular momentum state has a spread σ_ℓ , the transition frequencies of transitions of order $\Delta\ell$ will have a spread of $2\omega_r\Delta\ell\sigma_\ell$. If we include non-rigid correction terms, then

$$\omega_{\ell+\Delta\ell+1,\ell+1} - \omega_{\ell+\Delta\ell,\ell} = \frac{E_{\ell+\Delta\ell+1} - E_{\ell+1}}{\hbar} - \frac{E_{\ell+\Delta\ell} - E_\ell}{\hbar} \approx (2\omega_{r0} - 12D\ell^2)\Delta\ell. \quad (3.68)$$

We thus recover the original expression for the transition frequency difference if we define the effective rotational constant

$$\omega_{r,\bar{\ell}} = \omega_{r0}(1 - 6\epsilon_{\bar{\ell}}), \quad (3.69)$$

whereupon we may write the rotational sideband linewidth as $2\omega_{r,\bar{\ell}}\Delta\ell\sigma_\ell$. Note that the correction term for the effective rotational constant is $6\epsilon_{\bar{\ell}}$, which differs from the appropriate correction term when computing energies ($\epsilon_{\bar{\ell}}$) and transition frequencies ($2\epsilon_{\bar{\ell}}$).

Computing the correction factor itself

All non-rigid corrections in this section have been given in terms of the small parameter ϵ_ℓ , which depends on the angular momentum quantum number. In practice, we measure

rotation frequency rather than angular momentum quantum number. This poses an apparent complication since the relationship between rotation frequency and angular momentum itself depends on ϵ_ℓ and thus on angular momentum. In fact, the corresponding correction is second order and thus negligible. To show this, we can use the relations $\epsilon_\ell = 4\omega_{r0}^2\ell^2/3\omega_x^2$ from (3.47) and $\omega_\ell^{\text{rot}} = 2\omega_{r0}\ell(1 - 2\epsilon_\ell)$ from (3.64):

$$\epsilon_\ell = \frac{4\omega_{r0}^2\ell^2}{3\omega_x^2} \approx \frac{(\omega_\ell^{\text{rot}})^2(1 + 4\epsilon_\ell)}{3\omega_x^2}. \quad (3.70)$$

This is an implicit expression for ϵ_ℓ . Solving it,

$$\epsilon_\ell = \frac{\frac{(\omega_\ell^{\text{rot}})^2}{3\omega_x^2}}{1 - 4\frac{(\omega_\ell^{\text{rot}})^2}{3\omega_x^2}} \approx \frac{(\omega_\ell^{\text{rot}})^2}{3\omega_x^2} + 4 \left[\frac{(\omega_\ell^{\text{rot}})^2}{3\omega_x^2} \right]^2. \quad (3.71)$$

We have already assumed that the ratio $\omega_\ell^{\text{rot}}/3\omega_x^2$ is small, so the second term of the above equation is higher order in the very same parameter. Thus it suffices to write our correction parameter ϵ_ℓ as being equal to $\omega_\ell^{\text{rot}}/3\omega_x^2$. It is for this reason that the final equality of (3.47) is only approximately true, though it is correct to first order, which is the level of approximation we are interested in.

Chapter 4

Experimental setup

At the center of the experimental setup is an ultra-high vacuum chamber, held at a pressure below 10^{-11} Torr. Internal to the chamber is the ion-trap chip and calcium source. External to the chamber are sources of electrical signals which are routed into the chamber, laser light sources and their respective control systems, optics and electronics for ion detection, and magnets. The chamber is surrounded by a Faraday cage to prevent electrical noise.

4.1 General instrumentation

4.1.1 Lasers

A total of six lasers are used for our experiments with $^{40}\text{Ca}^+$. Four of the lasers correspond to the wavelengths shown in Fig. 2.5 for driving electronic state transitions in $^{40}\text{Ca}^+$: 397 nm for $S_{1/2} \leftrightarrow P_{1/2}$, 866 nm for $D_{3/2} \leftrightarrow P_{1/2}$, 854 nm for $D_{5/2} \leftrightarrow P_{3/2}$, and 729 nm for $S_{1/2} \leftrightarrow D_{5/2}$. Two additional lasers are used for photoionization of neutral Ca to create Ca^+ . This photoionization is done with a two-photon process: 423 nm light drives a transition from $S_{1/2}$ to $P_{1/2}$ in neutral Ca, and 375 nm light promotes the $P_{1/2}$ population to the continuum, completing the ionization process.

All lasers used are diode lasers. The 854 nm and 866 nm light beams are generated directly by their respective laser diodes, and are frequency-stabilized by Pound–Drever–Hall locking to external cavities. The 397 nm light is derived from 794 nm light generated by a diode laser, then frequency doubled via second-harmonic generation to 397 nm. The 397 nm light is stabilized by locking the 794 nm light to an external cavity. The 423 nm and 375 nm lasers are generated from diodes and are left free-running with no external cavity locking. Finally, the 729 nm laser light is stabilized by locking to a high-finesse cavity. This light is then amplified with two stages of injection locking, followed by two stages of tapered amplifiers. Locking the 854, 866, and 397 nm lasers to their respective cavities yields linewidths of order 10 MHz. Locking to the high-finesse 729 nm cavity yields a linewidth of less than 1 kHz, as required to coherently drive the $S_{1/2} \leftrightarrow D_{5/2}$ electric quadrupole transition in $^{40}\text{Ca}^+$.

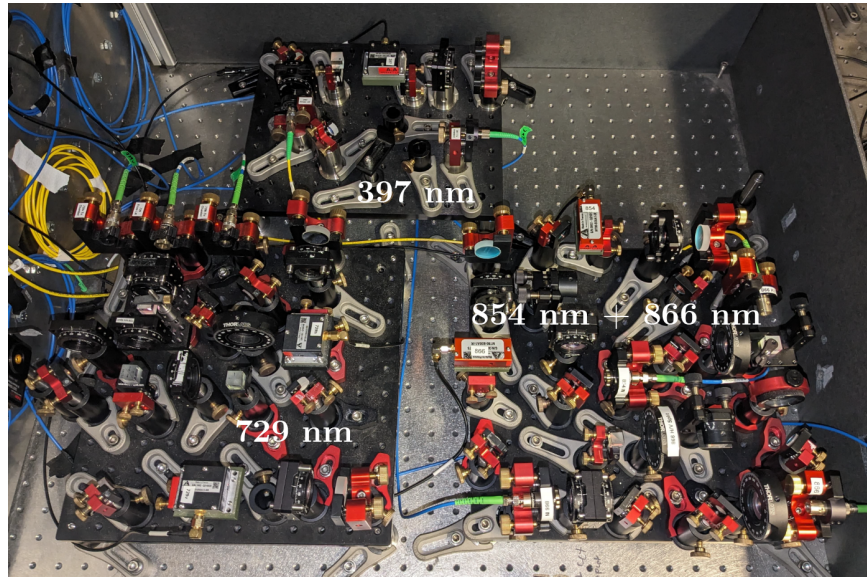


Figure 4.1: Photograph of the compact AOM setups.

Each of the laser wavelengths is generated in a room separated from the vacuum chamber and delivered to the experiment via optical fibers. These fibers output $500\text{ }\mu\text{W} - 2\text{ mW}$ of light for the 397, 866, 854, 423, and 375 nm lasers. The fiber for the 729 nm laser outputs approximately 20 mW.

The 397, 866, 854, and 729 nm light used for running experiments with trapped $^{40}\text{Ca}^+$ is passed through acousto-optic modulator optical systems before delivery to the vacuum chamber (where the ions reside). The AOMs provide control over these beams at the chamber (see Sec. 4.1.2). The 423 nm and 375 nm photoionizing beams are delivered directly to the chamber by the fibers from the laser room, with a simple mechanical shutter for binary control.

4.1.2 Acousto-optic modulator systems

Timing, frequency, and amplitude control of the lasers are achieved with acousto-optic modulators (AOMs). Each of the AOM systems in this experimental setup use AOMs in the double-pass configuration, where the light is passed through the same AOM twice in order to mitigate effects of the diffracted beam angles changing with RF drive frequency by canceling their first-order dependency. The full optical systems for the AOMs include optics to focus the beam into the center of the piezoelectric crystal, separate out the +1 or -1 order diffracted beam, reflect and re-focus it back into the AOM for the second pass, and finally deliver it to an optical fiber which in turn delivers it to the vacuum chamber.

While the double-pass configuration cancels first-order sensitivities of diffracted beam angle with AOM drive frequency, there still remains some dependence. This presents a problem since the position of the beam at the output of the AOM system, and thus in turn

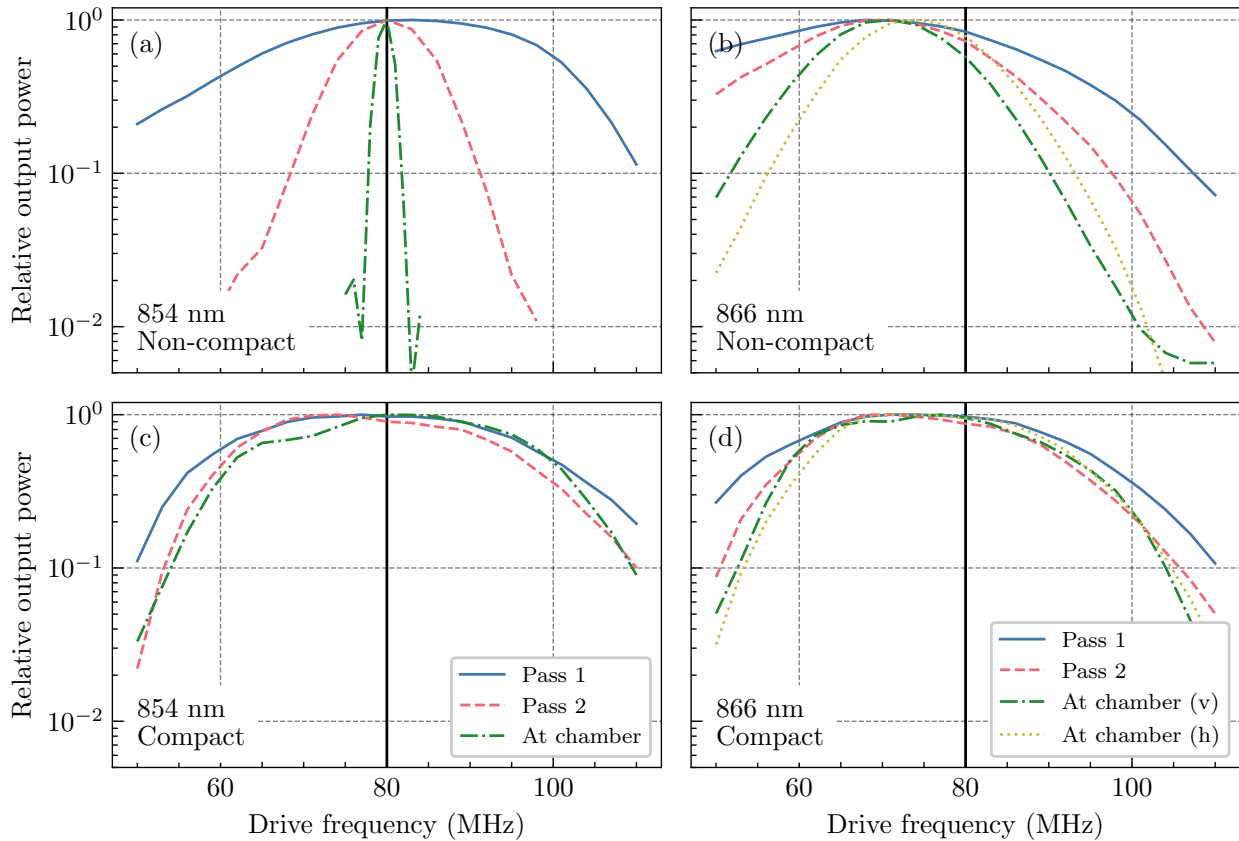


Figure 4.2: Measurements of the bandwidth of the 854 and 866 nm AOM setups, before and after switching to the compact design. Power is measured at the location indicated by the legend and plotted relative to the maximum measured value. In all cases, the target center frequency is 80 MHz. The 866 nm setup has two output fibers, one to address the ions vertically (v) and one to address them horizontally (h).

the efficiency of the coupling to the optical fiber, will depend on the drive frequency. This can limit the practical bandwidth of the AOM system. The AOM systems in this setup, shown in Fig. 4.1, are designed to be as compact as possible to minimize the optical path length. The design choices made to this end include using small components (e.g. 1/2 inch diameter mirrors), and focusing the beam into the first AOM pass using the collimator from the input fiber to the system, and into the second pass using a curved mirror. This obviates the need for additional focusing lenses. In addition, the AOM systems are built onto their own small optical breadboards for modularity. The 854 and 866 nm laser AOM systems are built onto the same board so that they may share an output fiber. The 729 nm laser AOM system contains two AOMs, each with its own output fiber: one to address the ions parallel to the trap surface, and one to address them normal to the trap surface.

Prior to the compact AOM systems, all AOM systems used in this experiment had comparatively long optical path lengths. A comparison of the performance of the non-

compact and compact versions of the AOM systems for the 854 and 866 nm lasers can be seen in Fig. 4.2. The performance after the first pass through the AOM indicates the intrinsic bandwidth of the AOM device itself, while that at more downstream locations indicates losses due to changes in beam angle along the optical path. After switching to compact AOM setups, the bandwidth of both setups was improved. The efficiency at the optimal AOM frequency remained approximately the same.

4.1.3 Other optics

Ions are imaged by an objective lens which resides immediately outside the vacuum chamber. The objective is bichromatic for 397 nm and 729 nm light. 397 nm photons which are fluoresced by ions are focused by the objective onto an image plane, after which the image light is split with a pellicle beamsplitter onto a photo-multiplier tube (PMT) and an Andor Luca EMCCD camera. The PMT provides photon counts for detection of ions, as well as for state discrimination at the readout stage of an experiment between the bright ($S_{1/2}$) and dark ($D_{5/2}$) qubit states. The camera is also used for ion detection and for beam alignment.

4.1.4 Experiment control electronics

Electrical RF signals to control the AOMs, as well as simple binary transistor-transistor logic (TTL) signals for other devices such as switches, are provided by a piece of custom hardware named the pulse sequencer, or pulser [30]. The pulser contains direct digital synthesizer (DDS) boards to generate the RF signals for driving the AOMs and several TTL channels. Sequences of pulses of these DDS and TTL channels can be programmed onto an FPGA. The timing is controlled with the aid of an external clock, which is provided by a 800 MHz signal generated by a function generator. The pulser also records the photon counts generated by the PMT for the purposes of state readout.

4.1.5 Trapping electronics

RF Drive

The RF voltage to provide the Paul-trapping potential is sourced by a Rhode & Schwarz SMB 100A signal generator, typically operated at an output power between 18 and 24 dBm. This RF signal is passed through an inductive transformer, known as the resonator, made of copper wire wound about a toroidal iron core. When loaded by the 22 pF capacitive load provided by the trap's RF electrodes, the resonator has a resonance frequency of 21.4 MHz. When properly grounded, the resonator provides voltage amplification with a gain factor of about 29.

DC Voltages

DC voltages are applied to DC electrodes to provide compensating electric fields at the location of the ions. These fields compensate stray dipole and quadrupole fields. The voltages are sourced from a custom-built digital-to-analog converter (DAC) system, which can provide up to ± 10 V DC.

4.1.6 Calcium ion production

Calcium ions are produced by an oven, composed of a tube of high-purity calcium granules and a wire to pass current through it. When a current is passed through the granules, they heat up and sublime, creating a stream of gaseous neutral calcium directed above the trap surface. The 423 and 375 nm photoionizing lasers illuminate the trapping location, as do the 397 nm and 866 nm cooling lasers. When a passing calcium atom is ionized near the center of the trapping potential and has little enough kinetic energy, it becomes trapped. It then scatters 397 nm photons off of the $S_{1/2} \leftrightarrow P_{1/2}$ transition, producing fluorescence which may be detected by the PMT or camera.

4.1.7 Magnetic field

An applied magnetic field is necessary for the purposes of inducing a Zeeman splitting, particularly for the $S_{1/2} \leftrightarrow D_{5/2}$ transition so that Zeeman sublevels may be spectrally resolved by the 729nm laser. This is applied by small highly temperature-stable permanent magnets held by a 3D-printed holder, mounted near the vacuum chamber. This provides a magnetic field of 3 – 5 Gauss at the location of the ions, providing a Zeeman splitting of a few MHz between neighboring $S_{1/2} \leftrightarrow D_{5/2}$ lines, and spanning about 20 MHz total. This splitting is large enough that motional sidebands of different $S_{1/2} \leftrightarrow D_{5/2}$ transitions can be resolved, but small enough that the AOM (center frequency 220 MHz) can span the full range of Zeeman transitions.

The choice of permanent magnets over coils of wire is primarily for stability of the magnetic field. This comes at the cost of making it difficult to change the magnetic field, as magnets need to be manually added or removed. It is particularly difficult to tune the magnetic field to a precise desired value or direction, as there is no precise way to predict the field resulting from a particular arrangement of magnets other than to use a trapped ion to measure it after making each manual change. This choice is thus only appropriate for cases where it is not important for the magnetic field to be precisely tuned, which is the case in this work. We set the direction of the magnetic field only roughly such that it is close to optimizing the coupling strength of the $\Delta m = 0$ electronic $S_{1/2} \leftrightarrow D_{5/2}$ when the 729 nm laser addresses the ions normal to the trap surface, which is done when the ions are rotating (see Chapter 6).

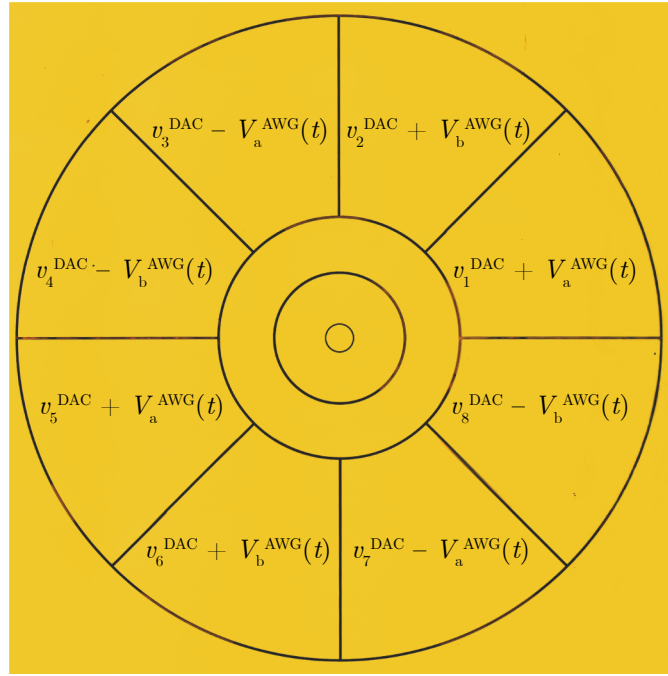


Figure 4.3: Voltage pattern required on the trap DC electrodes to allow simultaneously for stray field compensation and ion rotation.

4.1.8 Software

Control of the experiment, which primarily includes programming timed sequences of DDS and TTL pulses onto the pulser, reading photon counts from the PMT, and handling data flow, is handled by LabRAD [31]. This is instantiated in Python, and provides a server-client architecture which allows for asynchronous independent control of different devices relevant to the experiment, such as the pulser and the DAC.

4.2 Instrumentation for ion rotation

The instrumentation which is unique for this experimental setup is centered around ion rotation. This includes electronics for enabling the rotation, and lasers for cooling and addressing the ion crystal normal to the trap surface. The ion trap itself is discussed in Sec. 2.2.4.

4.2.1 Electronics for ion rotation

As discussed in more detail in Sec. 6.2, rotating a Coulomb crystal of ions is done by applying a rotating quadrupole potential. This can be achieved by sourcing only two unique voltages and applying them in the appropriate pattern to the eight DC electrodes of the trap, with

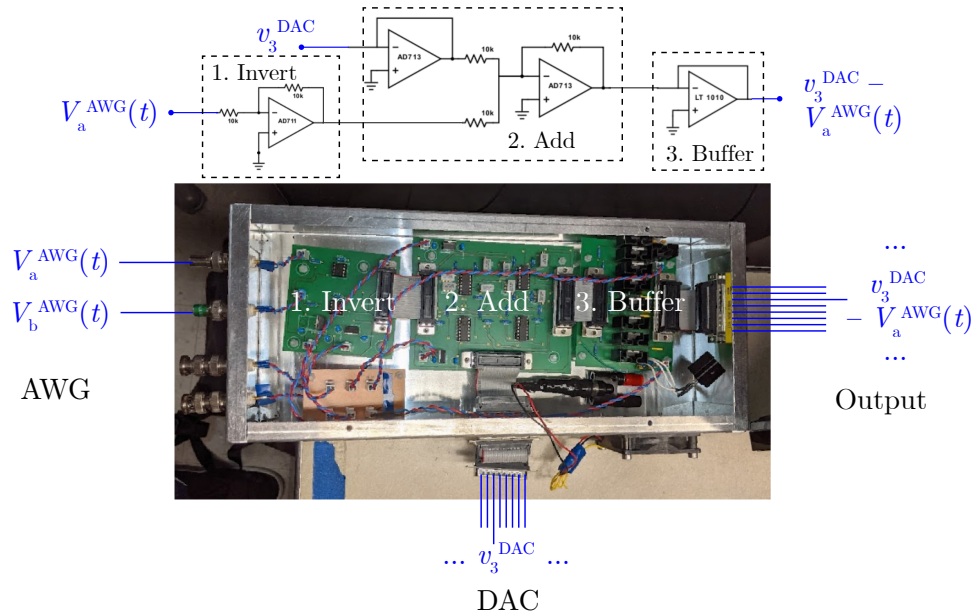


Figure 4.4: Image of the rotation circuit, with a schematic for one of the eight output channels.

some of the signals inverted. This is in principle straightforwardly achieved by using a two-channel arbitrary waveform generator (AWG), duplicating the outputs, and inverting some of the duplicates using an inverting op-amp to produce voltages $\pm V_a^{\text{AWG}}(t)$ and $\pm V_b^{\text{AWG}}(t)$, where $V_{a,b}^{\text{AWG}}(t)$ are the outputs of the two channels of the AWG. However, we additionally require that the DC electrodes still serve the purpose of compensating stray dipole and quadrupole electric fields. This in general requires each to have a unique static offset v_i^{DAC} , which is provided by the DAC. These two purposes, ion rotation and field compensation, can be served simultaneously by adding the respective required voltages. The resulting required voltage on the DC electrodes is shown in Fig. 4.3. Producing these voltages is done using a custom-built circuit, the rotation circuit.

The rotation circuit

The rotation circuit serves three main purposes: (1) to invert the AWG voltage (where necessary), (2) to add together voltages from the DAC for field compensation and from the AWG for ion rotation, and (3) to provide current buffering to enable driving the DC electrodes, which are RC low-pass filtered, at frequencies on the order of 100 kHz. An image of the rotation circuit is shown in Fig. 4.4. Above, a schematic is also shown for one of the eight output channels. Inversion and addition is provided by op-amps, and a high-current buffer provides additional current output capabilities, which is required to be roughly 100 mA. For channels where the AWG voltages should be added to the DAC voltage rather than subtracted, the inversion step is omitted. More details about the rotation circuit

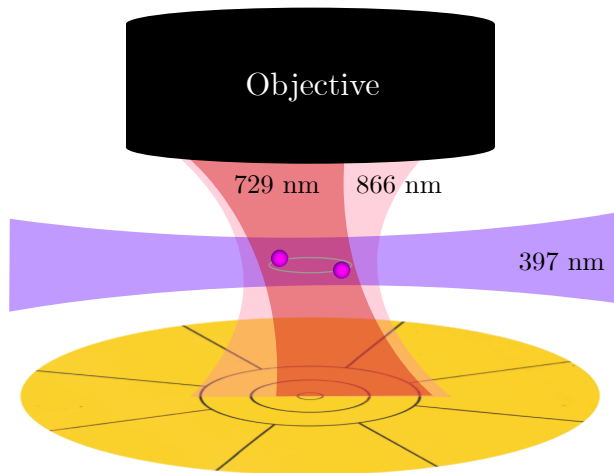


Figure 4.5: Schematic of beam orientations for 866 nm Doppler cooling of the vertical direction. The 866 nm laser provides cooling, and 397 nm laser repumps the ions without being directed toward the trap surface. This cooling allows the vertically oriented 729 nm beam to coherently address the ions.

can be found in Ref. [16].

The arbitrary waveform generator

The AWG used is a Keysight 33500B, which provides 1 million waveform points at a sample rate of up to 250 megasamples per second. We interface with it via a custom LabRAD server that allows for programming arbitrary waveforms within the same interface that controls the rest of the experiment.

4.2.2 Vertical 729 nm and 866 nm laser beams

As discussed in Chapter 6, it is best to address a rotating ion crystal with a 729 nm laser beam which is oriented nearly normal to the plane of rotation. Doing so coherently requires that the vibrational motion of the crystal in the normal direction is cold, and thus we also require cooling lasers to be oriented along the rotor normal. This is an atypical requirement; nearly all surface ion traps are concerned only with ion motion within the plane parallel to the surface. Doppler cooling is typically performed with the 397 nm laser, but blue or UV laser light directed at the trap surface risks photo-electric charging of and damage to the trap. Thus instead, we direct a beam of 866 nm laser light, which is typically used only for repumping during Doppler cooling, vertically to provide Doppler cooling. In this scheme, a 397 nm beam oriented parallel to the trap surface provides the repumping. This presents additional challenges in Doppler cooling (see Sec. 2.6.2). Sideband cooling is provided by the same vertically oriented 729 nm beam used for coherent addressing. To achieve verti-

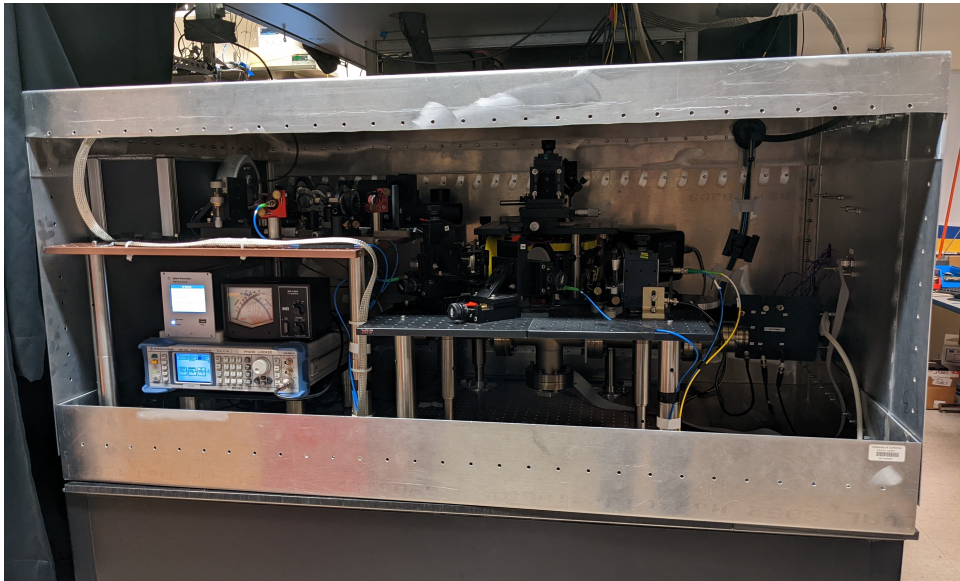


Figure 4.6: Photograph of the experimental setup with the Faraday cage.

cally oriented beams, both the 729 nm and the 866 nm beams are focused through the same objective used to collect ion fluorescence. This scheme is shown in Fig. 4.5. There is also a horizontally oriented counterpart for each. The 729 nm laser in particular has its own AOM control for the horizontal and vertical beams to allow for sideband cooling and state preparation in either direction independently.

4.3 Faraday cage

The experimental setup is surrounded by a Faraday cage, constructed from five sheets of aluminum, with one side of the setup left open for access. The experiment is constructed on top of the bottom sheet, which lays separated from the metal surface of the optical table by an insulating layer. All electrical signals which enter the Faraday cage are first filtered at the outer surface. The motivation for constructing the cage was to reduce electrical noise which had previously been resulting in ion motional heating, particularly in the direction normal to the trap surface. This had prevented sideband cooling in this direction. The source(s) of the noise had proven difficult to identify. The relationship between electrical noise and trapped-ion motional heating, as well as evaluation of the performance of the Faraday cage, are considered in Chapter 5. In short, ion motional heating is caused by electrical noise whose frequency is resonant with the ion motion, which is in the hundreds of kilohertz to megahertz regime. This section describes the design of the Faraday cage, whose main function is to filter electric field noise at ion motional frequencies. Much of the design and construction of the Faraday cage is credited to graduate student Ryan Tollefsen and postdoc Neha Yadav.

4.3.1 General philosophy

The Faraday cage is intended to both prevent noisy radiation and to filter intentionally incoming electrical signals. A few goals of the design of the Faraday cage for minimizing noise as much as possible are as follows:

- All electrical signals which enter the Faraday cage are filtered at the entrance, with the exterior of the cage as the ground reference for the filters. This allows for the exterior surface of the cage to conduct away noisy currents while shielding the interior surface from the noise.
- To prevent ground loops, there is only a single reference for AC power, which in turn provides the earth reference for the entire system within the Faraday cage.
- The Faraday cage and the components inside of it are isolated from all other electrical systems, especially the pulser, the optical table, and the wall ground aside from the single reference point.

4.3.2 Electrical signals

All electrical signals which are used for the experiment but which are generated outside of the Faraday cage are low-pass filtered at its external surface. These include the voltages for the DC electrodes, other DC signals, and 60 Hz AC wall power.

Trap DC electrode voltages

To allow for ion rotation, discussed in Chapter 6, AC voltages at hundreds of kilohertz must be allowed to be applied to the trap DC electrodes while filtering as much as possible at motional frequencies ($\gtrsim 1 \text{ MHz}$). Furthermore, because voltages applied directly to the trap electrodes are those which are in the most danger of causing ion heating, they are additionally filtered at the entrance of the vacuum chamber to eliminate noise as downstream in the signals' paths as possible. The design of a filter for these signals is constrained by a 10 nF capacitor to ground for each DC electrode inside the vacuum chamber.

Figure 4.7 shows the filter used for the signals to the DC electrodes, which originate from the rotation circuit. At the entrance of the cage, they are filtered by a 4-stage cascaded low-pass filter. Inside the cage, at the entrance of the vacuum chamber, there is an additional low-pass filter consisting of the internal 10 nF capacitor and an external resistor. The resulting filter function is shown in Fig. 4.8. The total filtering inside the chamber becomes higher order starting at about 1 MHz due to the cascaded filter outside the cage. Inside the Faraday cage but outside the vacuum chamber, there is still $> 20 \text{ dB}$ filtering to minimize noise inside the Faraday cage while still ensuring that the filter at the chamber is able to eliminate any noise which may have originated inside the cage. The filtering at frequencies within the regime intended to be used for ion rotation is between 10 and 20 dB, which we find is little

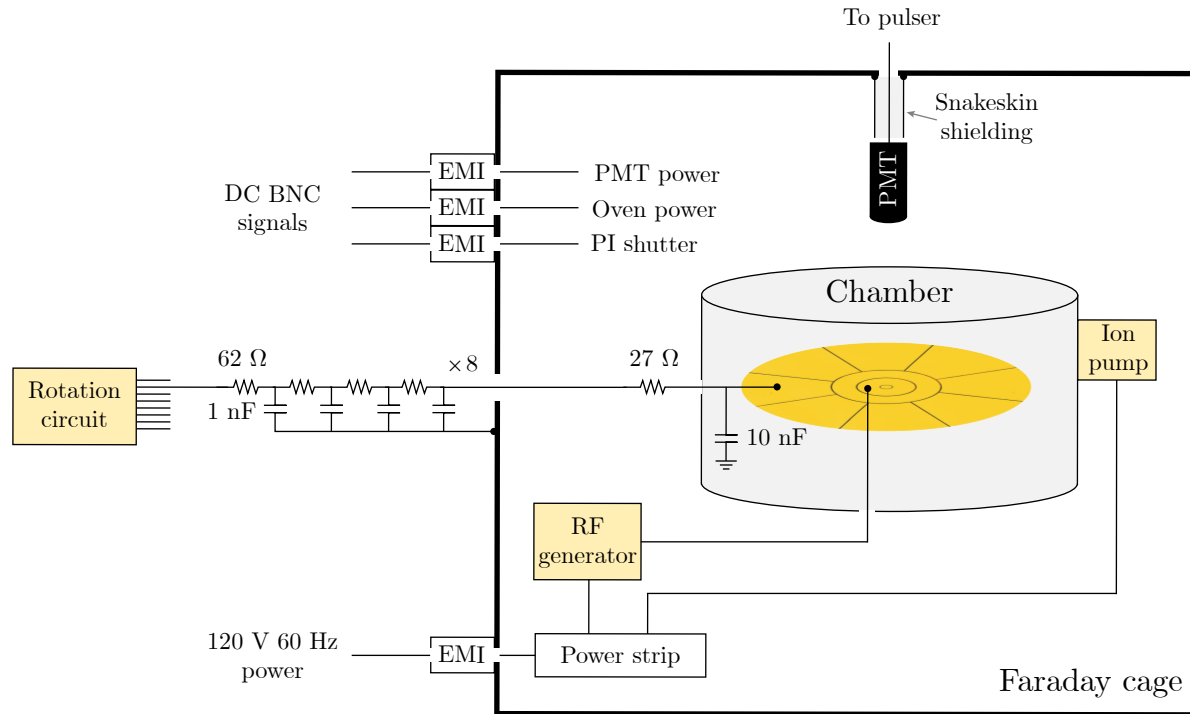


Figure 4.7: Schematic of the electrical signals used in the experiment with respect to the Faraday cage.

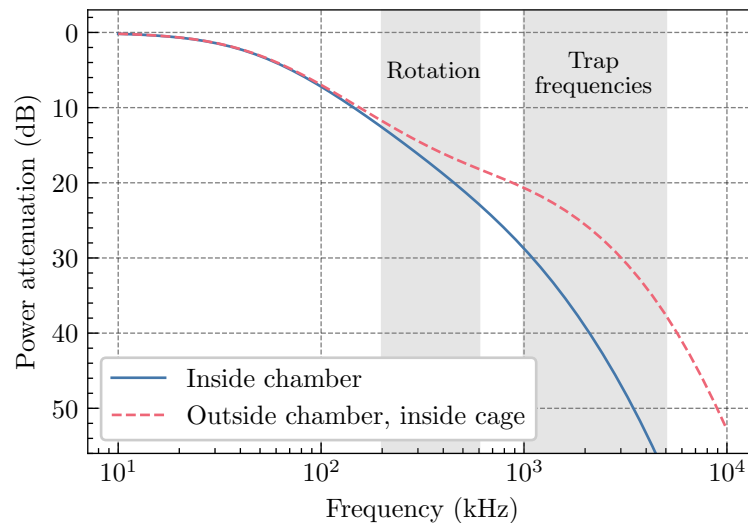


Figure 4.8: Filter function of the cascaded low-pass filter used for the DC electrode signals.

enough to still allow for applying voltages for ion rotation. Above 1 MHz, the filters provide > 30 dB suppression.

The low-pass filters do not use precision capacitors or resistors, so there may be some concern about whether the filtering of the eight DC electrode channels is the same. The quality of the rotational potential created by the rotation circuit can be compromised if not. The actual variation of the total capacitance of the filters across the eight channels is only 0.6%, and the variation of the resistances is within 0.2%. Furthermore, measurements of the actual attenuation due to each channel's respective filter at 200 kHz show that there is no correlation across channels between attenuation factor and capacitance for the filters external to the cage, suggesting that the small variation which is present does not limit the uniformity of the channels' attenuation.

Other DC signals

A few signals which must enter the cage but are not used directly for trapping include the power for the PMT, the oven, and the control for the PI laser shutter. These are passed through Schaffner EMC FN2010N1-6-06 EMI filters, which provide > 50 dB filtering in the range 1 – 10 MHz.

AC power

To prevent ground loops as much as possible, all instruments which are inside the Faraday cage, require AC power, and whose grounds connect to the vacuum chamber or the trap chip share a single AC power strip. The power cable for this is passed through the same type of EMI filter as those for the other DC signals. This provides the single ground reference for the entire Faraday cage system via the connection of the shielding of the EMI filter to the outside of the cage, to which the ground of the input power line also connects. The RF generator and ion pump receive power in this way.

PMT signal

The PMT which reads photons emitted by the ions is inside of the Faraday cage. It sends signals to the pulser with pulses on the nanosecond timescale, and thus cannot be easily filtered. Instead, it is shielded from the rest of the Faraday cage by a metal snakeskin shielding wrapping around the signal line which is connected to the interior of the cage.

Chapter 5

Measuring and mitigating noise

Over the course of maintaining operational conditions for this experiment, much time was spent attempting to lower the heating rate of the ion motion in the vertical direction, i.e. normal to the trap surface plane. This heating rate had been higher than the cooling rate afforded by sideband cooling, thus precluding cooling of the vertical motion to its ground state. This in turn prevented clean diagnostics of and coherent operations with rotational motion, discussed in Chapter 6. Construction of the Faraday cage ultimately solved this problem. This solution was effective enough to be successfully implemented without a true diagnosis of the origin of the heating problem. Nevertheless, this chapter discusses some of the techniques used in attempting to diagnose the problem prior to the Faraday cage. Measurements of the cage's performance are also presented.

5.1 Physics of trapped-ion motional heating

While trapped ions' charge enables the trapping mechanism, it also makes them susceptible to unwanted electric fields. In particular, it is often important in experiments for the motion of trapped ions to be in a well-defined state. Uncontrolled electric fields can couple to the motion and thus present a problem in trapped-ion experiments.

To show the effect of electric field noise on trapped ion motion, consider a single trapped ion. It will suffice to consider a single direction of motion $r_j \in \{x, y, z\}$ so that the Hamiltonian of the ion's motion in that direction is $H_0 = \hbar\omega_j(a_j^\dagger a_j + \frac{1}{2})$. The unwanted component of the electric field can be written in terms of an electric potential $\Phi(\mathbf{r}, t)$. The physical origin of this field is always much further away from the ion than the distance scale of its motion, so the field changes on a length scale much larger than that of the ion's motion. This allows the potential to be expanded into multipoles as

$$\Phi(\mathbf{r}, t) = \Phi(0, t) - \mathbf{r} \cdot \mathbf{E}(0, t) - \frac{1}{2} \sum_{j,j'} r_j r_{j'} \frac{\partial E_j}{\partial r_{j'}}(0, t) + \dots \quad (5.1)$$

where $\mathbf{E} = -\nabla\Phi$. The origin is set at the center of the ion's motional potential. The three terms shown are a spatially constant potential (which does not affect the motion), the electric field, and the gradient of the electric field. Since the magnitude of these terms falls off as long as the multipole expansion holds, the electric field term dominates. For a single ion moving in the r_j direction, the Hamiltonian for interaction with the electric field is

$$H_E(t) = e\Phi(r_j, t) = -er_j E_j(t) = -e\sqrt{\frac{\hbar}{2m\omega_j}}(a_j + a_j^\dagger)E_j(t) = -\mu_j(a_j + a_j^\dagger)E_j(t). \quad (5.2)$$

for a singly positively charged ion with charge e , where $E_j(t) = E_j(0, t)$, the electric field at the origin where the ion resides.

$$\mu_j = e\sqrt{\frac{\hbar}{2m\omega_j}} \quad (5.3)$$

is the ion's dipole moment for motion in the j -direction. The total Hamiltonian is $H(t) = H_0 + H_I(t)$. Transforming into the interaction picture with respect to H_0 ,

$$H_I = -\mu_j \left(a_j e^{i\omega_j t} + a_j^\dagger e^{-i\omega_j t} \right) E_j(t). \quad (5.4)$$

The creation and annihilation operators will induce transitions between Fock states of the motion. A noisy electric field will be stochastic, so that the total effect is an incoherent average over many realizations of $E_j(t)$. This final result is a tendency towards a thermal distribution, with the average Fock state occupation \bar{n} increasing linearly at a rate Γ_h , known as the heating rate. One way to compute this is to suppose the system begins in the ground state $|n=0\rangle$, and compute the probability of transitioning to state $|n=1\rangle$ within a small time window Δt . Following Ref. [32], from the Schrödinger equation, the probability amplitude of the state $|1\rangle$ evolves as

$$\dot{c}_1 = \frac{1}{i\hbar} \langle 1 | H_I | 0 \rangle = i\frac{\mu_j}{\hbar} E_j(t) e^{-i\omega_j t}. \quad (5.5)$$

The transition probability after time Δt over many realizations is

$$P_1(\Delta t) = \langle |c_1(\Delta t)|^2 \rangle = \left\langle \left| \int_0^{\Delta t} \dot{c}_1(t) dt \right|^2 \right\rangle = \frac{\mu_j^2}{\hbar^2} \left\langle \left| \int_0^{\Delta t} E_j(t) e^{-i\omega_j t} dt \right|^2 \right\rangle. \quad (5.6)$$

It can be shown that this is equivalent to

$$P_1(\Delta t) = \frac{\mu_j^2}{2\hbar^2} \Delta t \int_{-\infty}^{\infty} d\tau 2 \langle E_j(t) E_j(t + \tau) \rangle e^{-i\omega_j t} \quad (5.7)$$

under the following assumptions:

- The correlation time of the electric field is much shorter than the integration time Δt .

- The integration time Δt is much longer than the oscillation period $2\pi/\omega_j$.
- The electric field is weak enough so that the transition rate is much smaller than the harmonic oscillation rate ω_j .

The integral in (5.7) is the Fourier transform of the autocorrelation function of the electric field, at frequency ω_j , and is precisely equal to the power spectral density of the electric field in the j -direction, $S_{E_j}(\omega_j)$. The heating rate is thus

$$\Gamma_h = \frac{P_1(\Delta t)}{\Delta t} = \frac{\mu_j^2}{2\hbar^2} S_{E_j}(\omega_j) = \frac{e^2}{4\hbar m \omega_j} S_{E_j}(\omega_j). \quad (5.8)$$

Under heating, the mean Fock state occupation \bar{n} of the mode being considered increases at the rate Γ_h : $\dot{\bar{n}} = \Gamma_h$.

Because this mechanism is a resonant effect, the heating rate is dependent only on the spectral density of electric field noise at precisely the motional frequency. In an intuitive picture, we may think of motional heating as occurring when an unwanted electric field resonantly excites the motion, but does so with a random phase so that the process is incoherent.

5.1.1 Heating of differential modes of motion

For multiple ions in a crystal, the electric-field term contribution of the expansion (5.1) vanishes for modes of motion other than the center-of-mass mode. The heating rate is then instead dominated by the next nonvanishing term, which in the simplest case is the electric-field gradient. Here, rather than the heating rate being proportional to a dipole moment squared times the power spectral density of the electric field, it is proportional to a quadrupole moment squared times the power spectral density of the electric field gradient:

$$\Gamma_h \propto Q_j^2 S_{\nabla E}(\omega_j). \quad (5.9)$$

Equation (5.3) shows that for center-of-mass heating, the relevant length scale for the dipole moment is the size of the motional ground-state wavepacket. For differential mode heating of a typical vibrational ion crystal, the two length scales for the quadrupole moment are the ground state wavepacket size and the ion-ion distance $2r$, so that $Q \sim \mu r$. Meanwhile, the magnitude of the electric field gradient is roughly that of the electric field divided by the ion-surface distance h , so its spectral density is the square of this relationship: $S_{\nabla E} \sim h^{-2} S_E$. Therefore, the heating rate for a differential mode is reduced as compared to that of a comparable center-of-mass mode by $(r/h)^2$, the ratio of the ion-ion distance to the ion-surface distance. This ratio is typically $10^{-2} - 10^{-1}$, so that differential modes tend to heat at rates $10^2 - 10^4$ times slower than center-of-mass modes.

Rotational ion crystal motion is also a differential mode of motion, insensitive to electric fields but sensitive to their gradients. The nature of this interaction differs in some ways from vibrational motion, however; see Sec. 7.3.

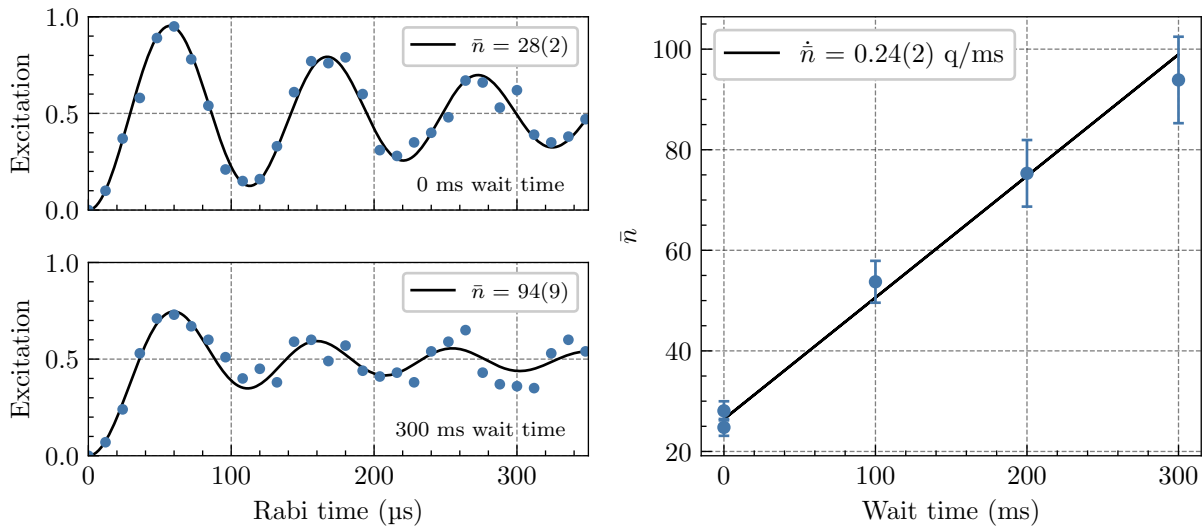


Figure 5.1: Heating rate measurement of the z -direction using a single ion at mode frequency $\omega_z = 2\pi \times 1.96$ MHz. For each wait time, a Rabi oscillation on the carrier is measured and fit for \bar{n} . The heating rate is quantified as the number of motional quanta added to the mode per millisecond (q/ms).

5.2 Measuring heating rates

To measure the heating rate, we measure the average Fock state occupation \bar{n} as a function of time in between cooling and measurement. The slope of \bar{n} versus time is the heating rate. We employ two methods to measure \bar{n} , the Rabi method and the sideband method. Under typical experimental parameters, the Rabi method is most appropriate for \bar{n} ranging from 1 to 1000, and the sideband method is most appropriate for $\bar{n} < 1$. For $\bar{n} \gtrsim 1000$, there is so little motional coherence that laser-based measurements are of little use, and alternative thermometry methods are required.

5.2.1 Rabi method

Using the Rabi method, we infer the ion's motional temperature from Rabi oscillations [33]. As seen in Fig. 2.4, the form of Rabi oscillations is dictated by the temperature. The carrier transition is most often used, which is typically most appropriate for values of \bar{n} between 3 and 1000. If $\bar{n} \lesssim 3$, the carrier oscillations decay slowly, and using a sideband instead may provide some greater discrimination between possible values of \bar{n} . We fit to a function of the form (2.38) parameterized by \bar{n} through (2.37). For higher heating rates, it is usually appropriate to begin at a Doppler-cooled temperature and use the Rabi method for measurements. Figure 5.1 shows a sample heating rate measured using the Rabi method.

5.2.2 Sideband ratio method

When \bar{n} is small enough, $\lesssim 1$, a direct comparison of red and blue sideband heights for a given pulse duration yields the most information about the temperature. It can be shown that if the motional state is thermal, then the ratio between the red and blue sideband heights is $\bar{n}/(\bar{n} + 1)$ [25]. However it should be noted that the motional distribution after sideband cooling is in fact typically not thermal, and the sideband ratio method can systematically underestimate \bar{n} [34], and in turn underestimate the heating rate. The sideband ratio method is most appropriate for low heating rates because it is highly sensitive to small changes in \bar{n} if one initially sidebands cools.

5.3 Origins of electric field noise in trapped-ion experiments

An ion trapped within a surface Paul trap is typically 10s to hundreds of micrometers away from the trap surface, and significantly further away from any other object. The dominant source of electric field noise at the location of a trapped ion crystal is thus almost always voltage fluctuations on the surface of the trap. The physical origin of these fluctuations can be broken into two broad categories: surface noise and technical noise.

5.3.1 Surface noise

Surface noise refers to voltage fluctuations arising from physical processes due to the trap surface being a material at a finite temperature with some composition, morphology, and possibly defects and contamination. Surface noise is thus related to the properties of the surface. In many trapped-ion experiments, the magnitude of surface noise is high enough to be a limiting factor in their respective figures of merit, such as two-qubit gate fidelities [27, 35]. The physical origins of surface noise in trapped-ion experiments is unknown, and is several orders of magnitude higher than what would be expected from basic considerations such as blackbody radiation and Johnson noise [32, 36]. For this reason, motional heating due to surface noise is sometimes referred to as “anomalous motional heating.”

5.3.2 Technical noise

Technical noise refers to electric field noise due to voltage fluctuations not related to the trap surface. These most frequently are small stray voltages unintentionally applied to the trap surface via channels which are intended to apply voltages related to trapping, such as the RF confining voltages or voltages for stray field compensation. The consequences of technical noise differ from those of surface noise in a few key ways:

- Technical voltage noise is fully spatially correlated across the entire electrode experiencing the noisy voltage. Surface noise, on the other hand, may have smaller spatial

correlations or practically none at all. This can give technical electric field noise a preferred direction with respect to the trap surface.

- The power spectral density of technical noise is often complex and inconsistent over time because it arises from uncontrolled sources. Surface noise, on the other hand, often follows a smooth power law in the spectral density as a function of noise frequency.

5.4 Relating technical noise spectrum measurements to the heating rate

If ion motional heating is limited by technical noise, then reducing it amounts to identifying and removing the source of the noise, weakening its effect, or making the system insensitive to the noise. This typically involves isolating or removing electrical devices from the system, or changing grounding connections to remove or redirect noisy currents. Because the goal of lowering electric-field noise is to lower the motional heating rate, the heating rate itself is the ultimate figure of merit. Such measurements can be slow however, taking at least several minutes to estimate a heating rate at a single motional frequency, making it difficult to iterate between electrical configurations. An alternative method is to use a spectrum analyzer measurement as a proxy. This directly yields a power spectrum of voltage between two reference points. If we can estimate a heating rate using this information, then spectrum analyzer measurements can provide a useful benchmark as a proxy measurement. To do this, we must estimate the electric field spectral density at the location of the ion from the spectrum analyzer measurement, from which we can estimate the heating rate using (5.8).

5.4.1 Converting measured noise power to voltage spectral density

A spectrum analyzer will typically provide a measurement in terms of noise power, in dBm, as a function of frequency. To estimate noise levels, however, we need to know the spectral density of the noise. The measured power is the spectral density integrated over frequency window, typically referred to as the resolution bandwidth. The spectral density can thus be estimated by dividing the measured power by the resolution bandwidth. This is done on a log scale for measurements in dB. For example, a measured noise power of -90 dBm using a 30 kHz resolution bandwidth corresponds to an average spectral density of $-90 - 10 \log_{10}(30 \times 10^3) = -135 \text{ dBm/Hz}$ over the integration window. This is equivalent to $1 \text{ mW/Hz} \times 10^{-135/10} = 3.2 \times 10^{-17} \text{ W/Hz}$ in absolute power. We further convert this to a voltage spectral density using the known impedance of the spectrum analyzer: $3.2 \times 10^{-17} \text{ W/Hz} \times 50 \Omega = 1.6 \times 10^{-15} \text{ V}^2/\text{Hz}$.

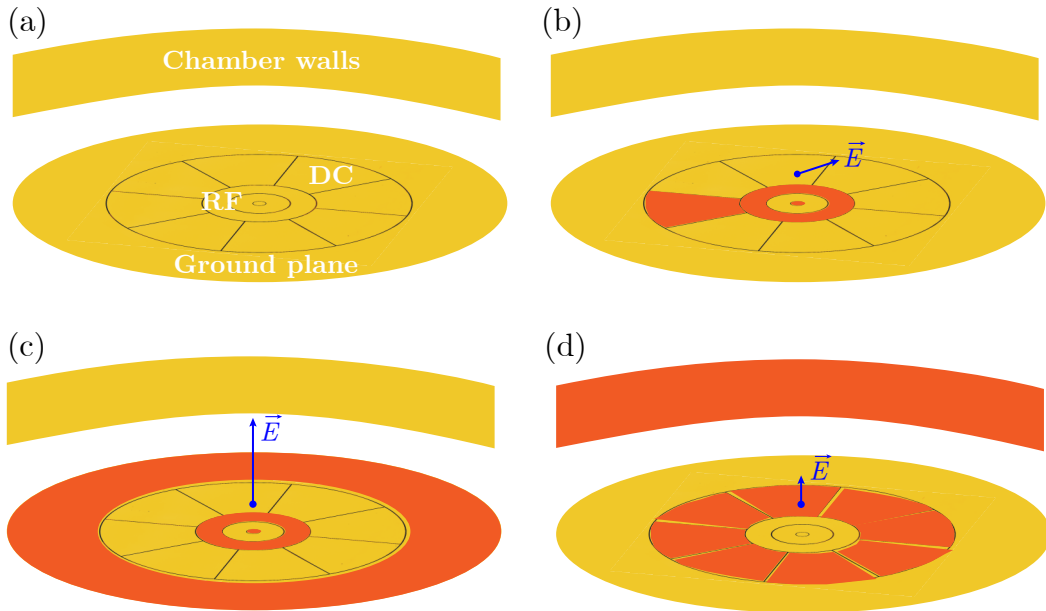


Figure 5.2: Examples of pairs of electrodes which may experience a potential difference, and a qualitative representation of the electric field produced.

5.4.2 Converting voltage spectral density to electric field spectral density

Converting voltage to electric field is a matter of electrostatics and geometry. The two reference points being measured will correspond to electrodes on the trap, and given the geometry, one can in principle solve the corresponding electrostatics problem to determine how a given potential difference between the two electrodes translates into an electric field. It sometimes suffices to roughly estimate the appropriate length scale d such that potential difference ΔV gives an electric field of magnitude E : $E = \Delta V/d$. As a reference it is useful to keep in mind that two parallel infinite planar surfaces separated by a distance d will have a corresponding length scale equal to exactly d , and any other geometry will be less efficient and thus have a larger such length scale. Continuing the previous example, if the appropriate length scale is 1 cm, then the electric field spectral density is $1.6 \times 10^{-15} \text{ V}^2/\text{Hz}/d^2 = 1.6 \times 10^{-11}(\text{V}/\text{m})^2/\text{Hz}$.

5.4.3 Choosing reference points for measurement

Equation (5.8) can be used to convert an electric field spectral density into a heating rate. If $S_E = 1.6 \times 10^{-11}(\text{V}/\text{m})^2/\text{Hz}$ at a frequency of 1 MHz, then from (5.8), a single $^{40}\text{Ca}^+$ ion will be heated at a rate of 2.3 quanta/ms. In general, the total electric field seen by the ion is the sum of the contributions from all pairs of electrodes. It is therefore useful to estimate which

pairs are most likely to contribute to electric field noise to inform where to make spectrum analyzer measurements.

In our case, prior to construction of the Faraday cage, heating rates in the vertical direction were measured to be consistently at least several quanta/ms, while those in the horizontal direction were consistently below 0.05 q/ms. This indicates that the geometry of the technical noise was such that the noisy fields were primarily in the direction normal to the trap surface.

Figure 5.2 shows a few different example pairs of electrodes of the ring trap, and the electric fields which arise from a potential difference between them. The geometry of the electrode pair being considered influences both the direction and the magnitude of the field produced. For the purposes of these considerations, the vacuum chamber itself is able to act as an electrode. For example, a potential difference between one of the DC electrodes and the grounded RF electrodes would produce a tilted electric field (b). A potential difference between the grounded RF electrodes and the surrounding ground plane, on the other hand, has cylindrical symmetry, so that the electric field points entirely in the vertical direction (c). Spatially correlated noise on all eight DC electrodes with respect to the vacuum chamber also yields the right symmetry for a vertical electric field, but because all of these electrodes are further from the ion, the field is smaller for a given potential difference (d). The first and third ring RF electrodes are shorted to each other inside of the chamber, so they share the same potential.

In our spectrum analyzer measurements, we chose to measure two pairs of points: the surface of the chamber and the ground pin of the DC voltage cable (which connects to the ground plane surrounding the trap), and the surface of the chamber and the grounded RF electrodes (which also connects to the ground plane). It was suspected that the center electrode in particular was the most likely to contribute to the measured noise, as it the closest electrode to the ions, and also has the right cylindrically symmetric geometry to produce vertical fields.

5.4.4 Comparing to heating rates

Figure 5.3(a) shows spectrum analyzer measurements taken between two different reference points. Each shows a range of noise powers, showing the minimum and maximum of several different measurements spanning several days. Each measurement is with the same grounding configuration, and was taken before construction of the Faraday cage.

To compare the measured noise spectra with heating rates, we convert the measured power to voltage spectral density. Furthermore, because the heating rate is also inversely proportional to frequency from (5.8), we divide the result by frequency. In other words, for a given noise spectral density, the heating rate will be lower at higher frequency because the ion is more tightly confined and thus has a smaller dipole moment to interact with the noise. The result is now directly proportional to the heating rate that would result from the noise measured. Whether this relationship actually holds in reality is contingent on the heating rate being limited by the measured noise, as opposed to by noise from some other

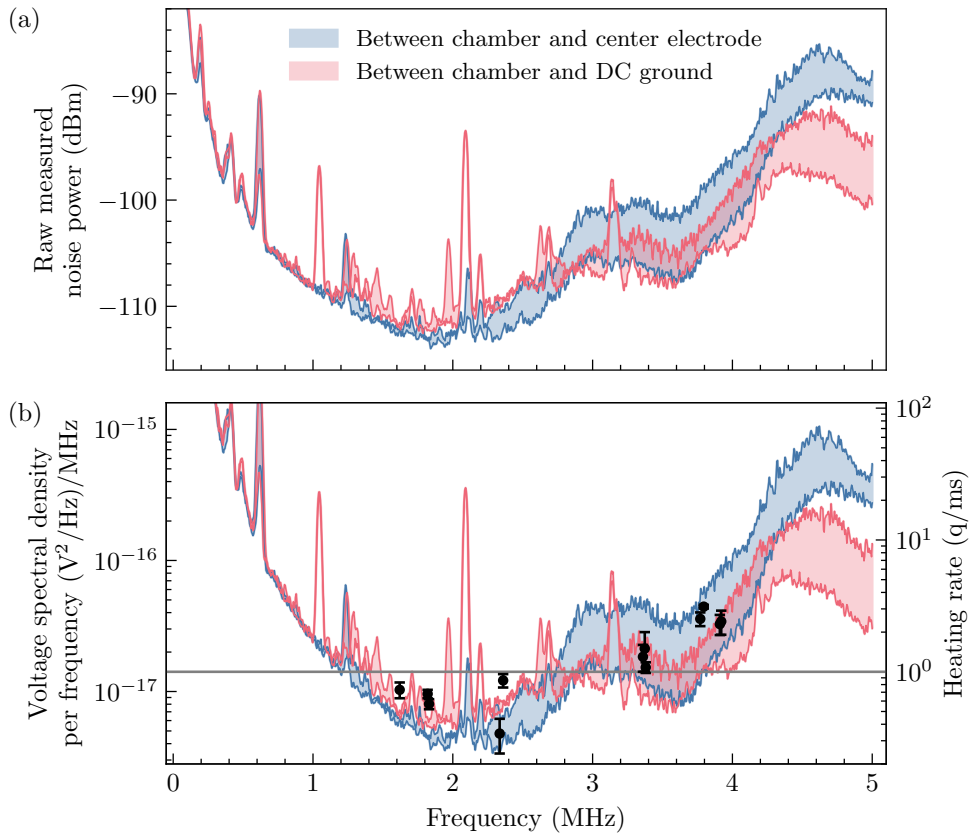


Figure 5.3: (a) Raw measured noise spectra between two pairs of reference points, shown as a range of measured noise powers over several different measurements. These measurements were taken with a spectrum analyzer using a resolution bandwidth of 30 kHz. (b) The same data converted to voltage spectral density and scaled by frequency, compared with measurements of vertical heating rates. The horizontal line at 1 q/ms is a rough benchmark for the heating rate threshold needed to allow for sideband cooling.

unmeasured pair of reference points. Figure 5.3(b) plots this scaled noise on one axis, and measured vertical heating rates on the other. The heating rates were measured within the time interval of the spectrum analyzer measurements. We do not attempt to convert voltage spectral density to electric field spectral density here, but the noise and heating rate scales are set proportionally to each other. We find in this case some agreement between the scaled noise level and the heating rates, contributing evidence that the heating rates may be limited by noise across the measured points. It should be noted however that the measured noise spectra have a large variation, greater than 5 dB (a factor of 3) over much of the spectrum, making it easier to artificially induce agreement between noise spectrum and heating rate measurements.

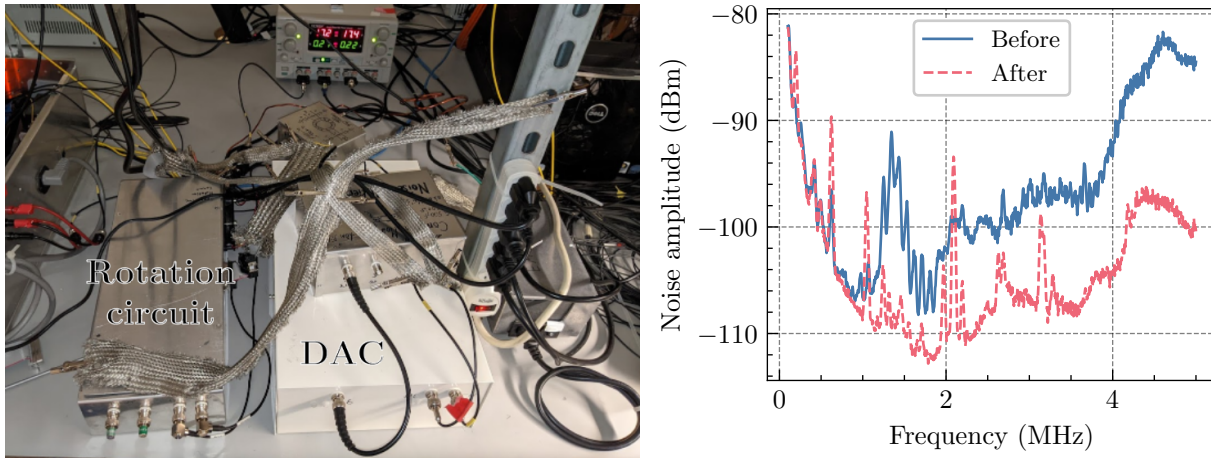


Figure 5.4: Left: Photo of a subset of the grounding connections made during one attempt to reduce the noise spectrum. Right: The measured noise spectrum before and after adding the connections shown on the left. The measurement was made between the chamber surface and the DC ground pin, using a resolution bandwidth of 30 kHz.

5.5 Minimizing technical noise

Prior to construction of the Faraday cage, we attempted to lower the measured noise spectra by changing grounding configurations. This was successful in lowering the noise spectrum somewhat, but was not successful in lowering vertical heating rates reliably and consistently below the threshold required for sideband cooling of the vertical motion. This is shown in Fig. 5.4. Nonetheless, we list some of the general strategies used in choosing grounding configurations which were likely to lower the noise spectrum. The list is not comprehensive, nor even self-consistent.

- Use as few independent connections to wall power ground as possible. Ideally, only a single reference to wall ground is made. All other devices which produce voltages which will ultimately go to the trap should be isolated from the wall ground and connected instead directly to each other.
- Isolate the system of all devices, active or passive, which contribute to trap electrode voltages from all other electrical systems. Within this system, ideally all grounded points are connected to each other at a single point of intersection, a “star ground”, to prevent loops of current (“ground loops”).
- Spectrum analyzer measurements should be made with the spectrum analyzer isolated from wall ground, and instead referenced to some point on the system being measured.
- For making electrical connections between points, large contact surface areas are preferred over high-conductivity material; e.g. snakeskin tubing is preferred over a thin

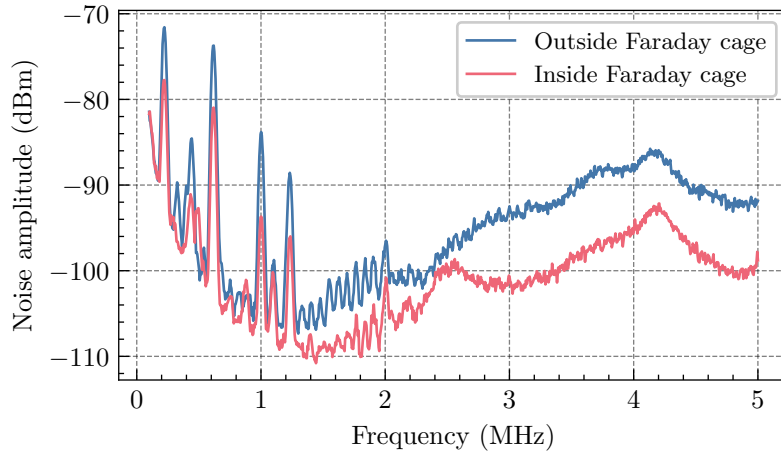


Figure 5.5: Spectrum analyzer measurements of radiation pickup using a loop of wire, inside vs. immediately outside the Faraday cage.

copper wire. One can measure a noise spectrum just across the connecting cable to test its efficacy at making electrical connections at the frequencies of interest.

- For identifying a single source of noise, it is best to disconnect all devices and reconnect one at a time.
- After using carefully establishing a starting point for connection with all necessary devices in place, one may still find that additional grounding connections between devices helps lower the noise spectrum.

Our best efforts of finding an optimal grounding configuration lowered the noise spectrum by approximately 1 order of magnitude in the frequency range of interest, about 2 – 5 MHz.

5.6 Performance of the Faraday cage

We benchmark the performance of the Faraday cage in three ways: reduction of radiation, reduction of the noise spectrum as measured between the chamber surface and RF ground pin, and reduction of the vertical heating rate. The latter is the most important.

Measurements of the radiation pickup are presented in Fig. 5.5. The spectrum analyzer was connected to a loop of copper wire about 10 cm in diameter, and placed immediately outside the Faraday cage, and then again inside the Faraday cage. The measured radiation pickup was reduced by about 1 order of magnitude inside the cage at 3 MHz and above.

Voltage noise spectra measured directly on the system are presented together with measurements of the vertical heating rate in Fig. 5.6. The two noise spectra shown are with and without the Faraday cage, measured at across the same two points: the surface of the chamber, and the RF pin which connects to the center electrode. In reality, many such noise

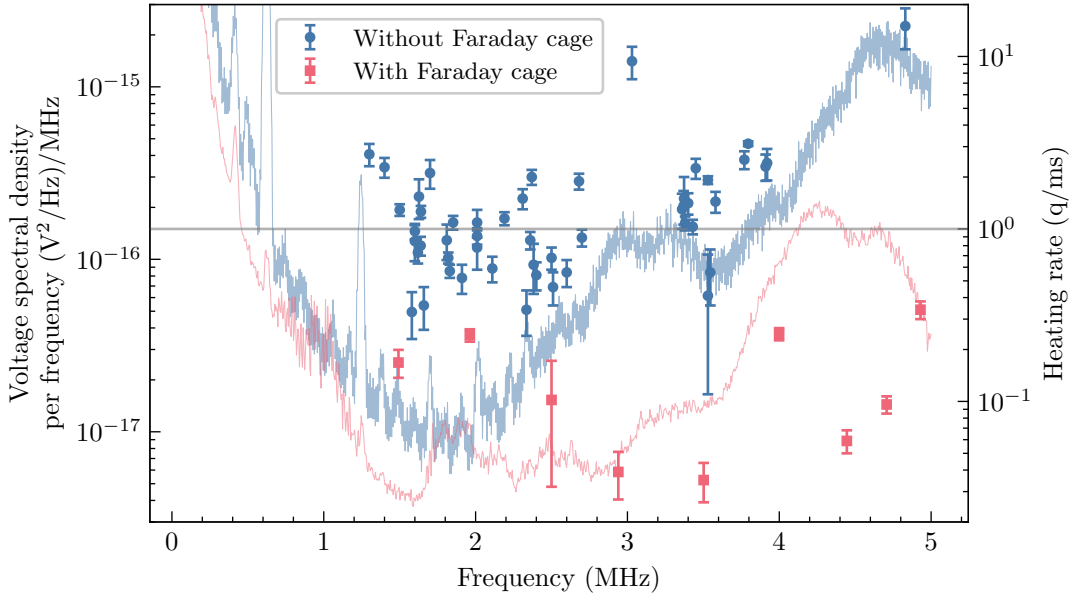


Figure 5.6: Voltage noise spectra and vertical heating rates, comparing before and after installation of the Faraday cage. Noise spectra are measured between the chamber surface and pin connecting to the center electrode. The blue trace is the lowest measured noise spectrum prior to installation of the Faraday cage, and the red trace is the noise spectrum after its installation. Points with error bars are vertical heating rate measurements. Heating rates before the Faraday cage (blue circles) are an aggregate of many different grounding configurations. The grey horizontal line is at 1 q/ms heating rate as a reference point. The two y -axes are scaled to be proportional to each other, but their ratio is chosen arbitrarily.

spectra were measured prior to the installation of the Faraday cage; the one shown is the one with the lowest measured amplitude of all grounding configurations. The cage appears to improve the noise amplitude by one order of magnitude at 3 MHz and above, except for a small range near 4 MHz.

The heating rates shown in Fig. 5.6 labelled “Without Faraday cage” are an aggregate of measurements made with many grounding configurations. Prior to the Faraday cage, heating rates varied significantly and were often larger than 1 q/ms. With the Faraday cage, the vertical heating rate was lowered by 1–2 orders of magnitude, and was consistently below 0.4 q/ms, low enough to reliably allow for sideband cooling. We also see that the heating rate does not appear to follow a simple power law scaling as a function of frequency, and thus is likely still limited by technical noise. Finally, we see generally poor agreement in this case between the noise spectra (scaled by frequency) and the heating rates. These measurements were taken with one side of the Faraday cage open, and have demonstrated this configuration to be sufficient. We have therefore decided to not fully enclose the Faraday cage, which could risk complications such as trapping heat emitted by the enclosed electronics.

Chapter 6

Creating superpositions of rotational states

For many quantum systems, all features which make them interesting from an experimental point of view can be linked to the prospect of using them to create interesting non-classical states. In the case of trapped ions, this applies not only to the internal electronic degree of freedom, but also to the external motional degree of freedom of the Coulomb crystal as a whole. Several decades ago, the creation of highly non-classical states of trapped-ion harmonic motion was in itself a high-profile research endeavour [37, 38], and interest in this pursuit has persisted into recent years [39, 40].

In this work, we create non-classical superposition states of our quantum rotor. In particular, we create superpositions of two different angular momenta, i.e. states of the form $|\ell\rangle + |\ell + \Delta\ell\rangle$. This chapter details the experimental requirements and procedures used for doing so, and presents measurements of the results.

6.1 Requirements for coherent operations

Coherent manipulation of trapped-ion vibrational motion is typically done by addressing motional sidebands of a coherent electronic transition. Classically, we may think of these sidebands as arising from modulation of the laser (or microwave) field in this ion's frame of reference due to its motion. Quantum mechanically, we may identify the sidebands as being allowed transitions which conserve energy. A vibrational mode with frequency ω_j has a single transition frequency between all neighboring vibrational states, ω_j itself. All motional sidebands are therefore at integer multiples of ω_j : $(E_{n_j+\Delta n_j} - E_{n_j})/\hbar = \Delta n_j \omega_j$. A valuable feature of this transition spectrum is that transition orders Δn_j are resolved, as they are separated from one another by ω_j , which is typically of order MHz.

In the case of a rotational mode, as discussed in Chapter 3, one similarly finds sidebands at the motional transition frequencies. However, unlike the harmonic oscillator, the rotor's energy eigenspectrum is nonlinear and therefore features a significantly more complex transi-

tion spectrum. The eigenenergies are $E_\ell = \hbar\omega_r\ell^2$ (3.20), and thus the transition frequencies are

$$\frac{E_{\ell+\Delta\ell} - E_\ell}{\hbar} = \omega_r(2\ell\Delta\ell + \Delta\ell^2), . \quad (6.1)$$

where ω_r is the rotational constant $\hbar/2I$ with I being the moment of inertia. Suppose the rotor is in a thermal state. Since the ground state is $\ell = 0$, a thermal state will have occupation in the vicinity of $\ell = 0$. Such a state will have population at values of ℓ which are small. We find two problems with addressing sidebands in this case:

- The transition frequencies are small, near ω_r which is of order 10 Hz.
- Transitions of different orders $\Delta\ell$ have significant overlap with each other.

Both of these effects make it prohibitively difficult to address transitions of a well-defined order $\Delta\ell$.

A solution to this problem is to instead prepare the rotor into a rapidly rotating state, with a mean angular momentum $\bar{\ell}$ which is large compared to 1 and compared to its width σ_ℓ . In this case, when considering transition orders which are small (in practice, $\Delta\ell = 6$ or smaller), then $\ell \gg \Delta\ell$, so that the transition frequencies approximately obey

$$\frac{E_{\ell+\Delta\ell} - E_\ell}{\hbar} \approx 2\omega_r\ell\Delta\ell. \quad (6.2)$$

Here, transition orders $\Delta\ell$ are separated from each other by $2\omega_r\ell$, which is equal to the rotation frequency corresponding to angular momentum $\hbar\ell$. This matches a classical expectation of finding modulation sidebands at integer multiples of the rotation frequency. To create resolved rotational sidebands, we therefore prepare the rotor into a rapidly rotating state to separate the $\Delta\ell$ sidebands from each other. To avoid strong centrifugal effects, this rotation frequency should also be chosen such that it is not too close to the stretch mode frequency (see Sec. 3.5), which is typically a few MHz. We therefore choose rotation frequencies of $100 - 300$ kHz. This corresponds to angular momenta on the order of $10^3 - 10^4 \hbar$.

In practice, we do not prepare an angular momentum eigenstate, i.e. a state with well-defined rotation frequency. Instead, the state always has some spread in angular momentum. This finite angular momentum width has the effect of broadening the $\Delta\ell$ rotational transition sidebands. If the width of the rotational state in angular momentum space is $\hbar\sigma_\ell$, then the $\Delta\ell$ -order sideband will span in frequency space from $2\omega_r(\ell - \sigma_\ell)\Delta\ell$ to $2\omega_r(\ell + \sigma_\ell)\Delta\ell$, giving it a linewidth of

$$\gamma_{\Delta\ell} = 4\omega_r\sigma_\ell\Delta\ell. \quad (6.3)$$

In total, to produce resolved rotational sidebands, have three requirements:

- The mean rotation frequency $\omega_{\bar{\ell}}^{\text{rot}} = 2\omega_r\bar{\ell}$ must be small compared to the stretch mode frequency ω_{stretch} to avoid strong centrifugal effects.
- The mean rotation frequency must be larger than the Rabi frequency of the neighboring sidebands $\Omega_{\Delta\ell\pm 1}$ being addressed to avoid off-resonant coupling.

- The Rabi frequency of the sideband being addressed $\Omega_{\Delta\ell}$ must be larger than its linewidth $4\omega_r\sigma_\ell\Delta\ell$, so that the operations are coherent.

The Rabi frequencies $\Omega_{\Delta\ell}$ are proportional to $J_{\Delta\ell}(|\zeta|)$ (3.31b), where ζ is a dimensionless parameter given by (3.26b). It will suffice here to assume that ζ is a modest value such that the Rabi frequencies of the transition orders of interest are all of the same order, so that $\Omega_{\Delta\ell\pm 1} \sim \Omega_{\Delta\ell}$. Then we can summarize our requirements as follows:

$$\omega_{\text{stretch}} \gg \omega_{\text{rot}} \gg \Omega_{\Delta\ell} \gg \gamma_{\Delta\ell}. \quad (6.4)$$

In practice, the stretch mode frequency ω_{stretch} is of order 1 MHz, the rotation frequency $\omega_{\ell}^{\text{rot}} = 2\omega_r\bar{\ell}$ is of order 100 kHz, the rotational sideband Rabi frequency $\Omega_{\Delta\ell}$ is of order 10 kHz, and the sideband linewidth $\gamma_{\Delta\ell} = 4\omega_r\sigma_\ell\Delta\ell$ is of order 1 kHz.

The rotational constant ω_r is an important parameter in most measurements pertaining to the ion rotor. Using two ions, it is calculated as $\hbar/4mr^2$, where the radius r is always inferred by measuring the horizontal secular trap frequency and using (3.21) to compute r . If necessary, non-rigid corrections may be included according to either (3.65b) or (3.69) as appropriate (see Sec. 3.5). Over the course of the work done in this thesis, we have used rotor radii spanning between 2.1 μm and 3.2 μm , corresponding to rotational constants ranging from $2\pi \times 14$ Hz to $2\pi \times 6$ Hz.

6.2 Rotational state preparation

All experimental work related to rotational motion in this thesis is done with a two-ion crystal. The technique used to produce a rapidly rotating state of the rotational mode of the two-ion crystal can be summarized by the following procedure:

- The in-plane rotational symmetry is broken by the application of a “pinning” quadrupole potential via the DC compensation electrodes of the trap, aligning the ion crystal along a chosen in-plane axis.
- Electronic state preparation and Doppler cooling are performed, after which the horizontal rocking mode, which later becomes the rotational mode, is sideband cooled. The vertical COM and rocking modes are also sideband cooled, though this is for the purposes of helping to later coherently address the rotational motion rather than preparing it (see Sec. 6.3).
- The ion crystal is spun up to a chosen rotation frequency by rotating the orientation of the pinning potential with a constant acceleration until the desired rotation frequency is reached.
- The amplitude of the pinning potential is lowered linearly until it reaches zero, while the rotation frequency is kept constant. This restores the in-plane rotational symmetry

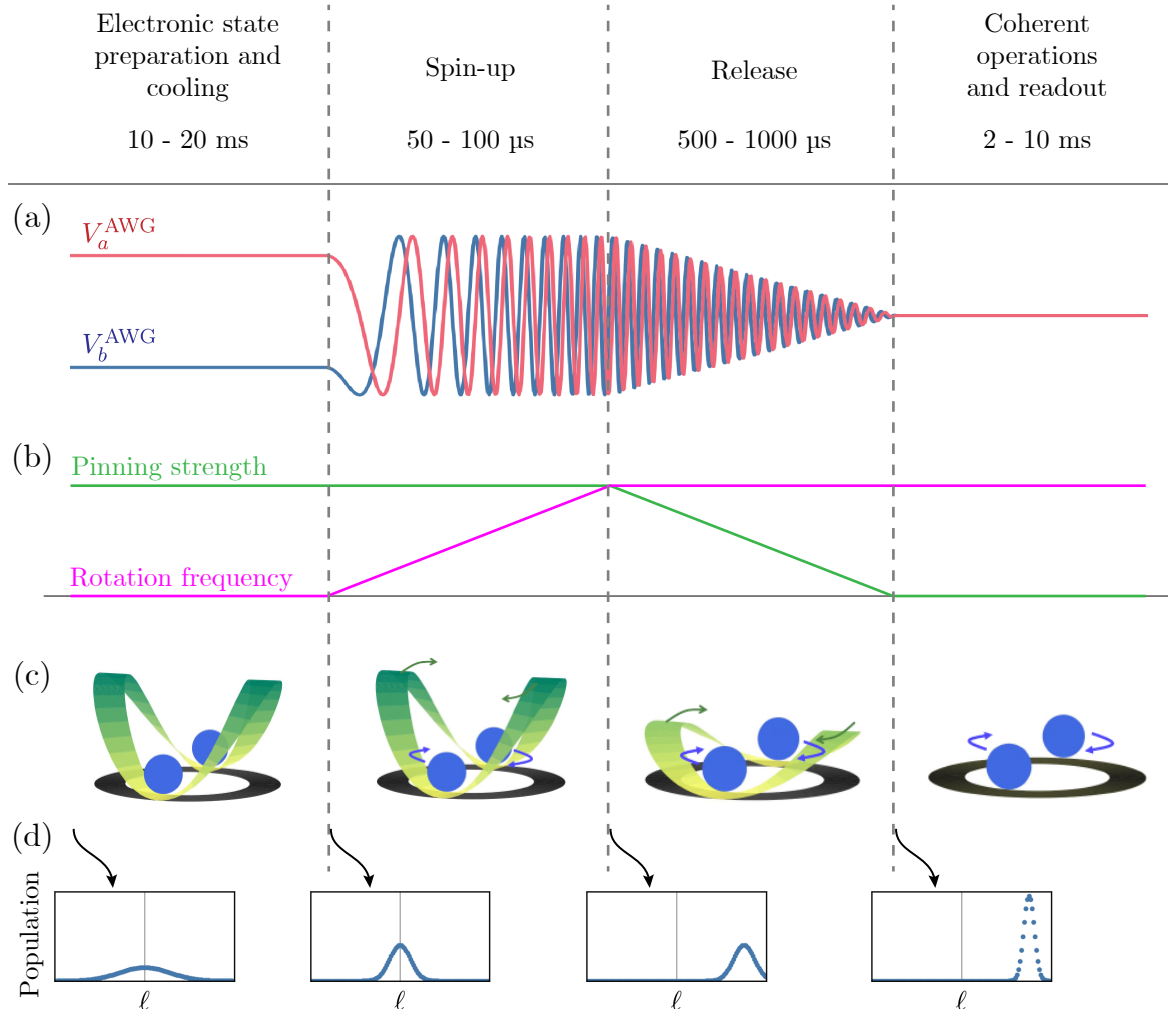


Figure 6.1: Schematic of the spin-up-and-release procedure used for rotational state preparation. (a) The voltages used on the two channels of the AWG to generate the pinning potential as a function of time, defined in (6.8). (b) Pinning strength and rotation frequency of the pinning potential as a function of time. (c) The potential of the two ions in the well at each stage. Arrows indicate rotation. (d) Population of the rotor's state in angular momentum space at the beginning of each stage.

allowing the rotor to freely rotate. The rotor continues to rotate at the previously chosen rotation frequency due to conservation of angular momentum.

This procedure is illustrated in Fig. 6.1. Most importantly, Fig. 6.1(d) shows the angular momentum space population of the rotor at the beginning of each stage of the procedure. The ions begin strongly pinned and stationary, and thus have a large spread of angular momentum centered at zero. Sideband cooling of the horizontal rocking motion narrows the distribution. Then, spin-up displaces the distribution to some large mean angular momentum

$\bar{\ell}$. Finally, release allows the rotor wavefunction to spread in position space and thus further narrow in angular momentum space. The angular momentum wavefunction then remains stationary. The angular momentum state at the end is centered at $\bar{\ell} \simeq \omega_{\text{rot}}/2\omega_r \sim 10^3 - 10^4 \hbar$ with a spread of $\hbar\sigma_\ell \sim 10^1 - 10^2 \hbar$.

We consider rotational state preparation to be successful if the following two conditions are satisfied:

1. The mean rotational frequency of the final angular momentum state ω_{rot} is near the target rotation frequency, e.g. within a few kHz.
2. The spread of the final angular momentum state σ_ℓ is as small as possible. For addressing the $\Delta\ell$ -order sideband, its linewidth $4\omega_r\sigma_\ell\Delta\ell$ must be small compared to the Rabi frequency, which itself must be small compared to ω_{rot} (6.4).

In practice, successful rotational state preparation is sensitively dependent on the choice of parameters in the spin-up-and-release procedure. In particular, there is a strong dependence of the choice of spin-up time and release time, which we choose to be approximately $50 - 100 \mu\text{s}$ and $500 - 1000 \mu\text{s}$, respectively. Numerical simulations of the dynamics of the procedure can provide some insight into the observed results, though we find there remain unexplained phenomena. No general formulation for predicting successful rotational state preparation parameters *a priori* has as of yet been developed.

The following subsections discuss how the pinning potential is provided and how parameters for the spin-up-and-release procedure are chosen to maximize the likelihood of successful rotational state preparation.

6.2.1 Generating the pinning potential

The pinning quadrupole potential is produced by applying voltages to the DC compensation electrodes of the trap as shown in Fig. 6.2. This pattern of voltages has two free parameters, the amplitude V_{pin} and the phase φ_{pin} . The resulting pinning quadrupole potential takes the form

$$\Phi_{\text{pin}}(x, y) = U_{\text{pin}} \left[\frac{y^2 - x^2}{2} \cos(2\varphi_{\text{pin}}) - xy \sin(2\varphi_{\text{pin}}) \right], \quad (6.5)$$

where the quadrupole strength U_{pin} is proportional to the voltage amplitude V_{pin} . (Note that Φ_{pin} is a potential energy, not an electric potential.) Thus the orientation of the pinning potential is set by φ_{pin} , and the amplitude is set by V_{pin} . It can be shown that the application of the pinning potential results in two distinct secular trap frequencies in the plane given by

$$\omega_{1,2} = \sqrt{\omega_{xy}^2 \pm \frac{U_{\text{pin}}}{m}}, \quad (6.6)$$

where ω_{xy} is the isotropic in-plane secular trap frequency in the absence of the pinning potential. (The two in-plane secular frequencies are referred to as ω_x and ω_y in Chapter 3,

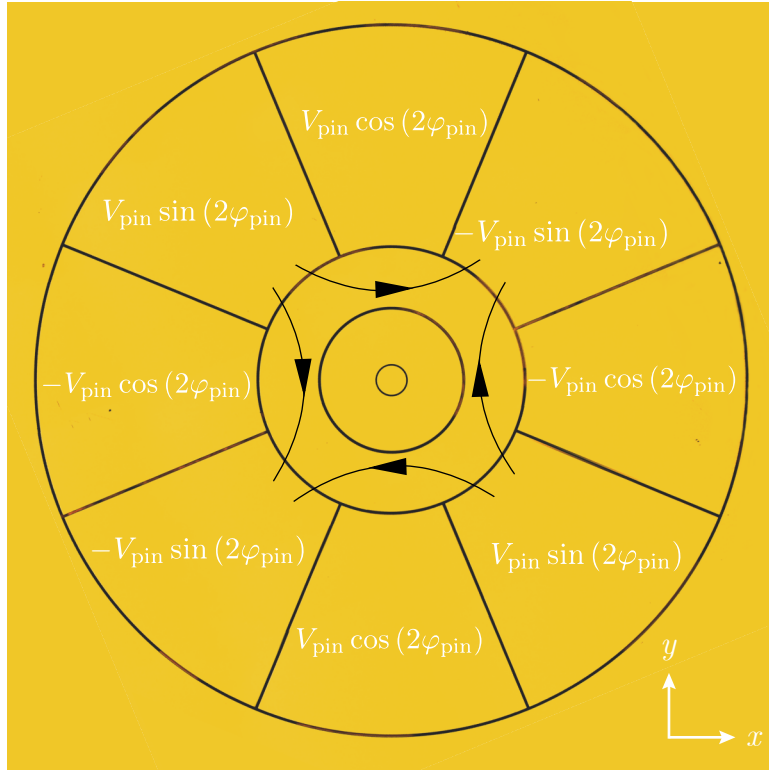


Figure 6.2: Voltages applied to the outer DC electrodes to produce the pinning quadrupole potential. An example quadrupole field is shown in black lines, whose orientation corresponds to $\varphi_{\text{pin}} = \pi/4$ or $5\pi/4$.

but here we use ω_1 and ω_2 to emphasize that the pinning potential may orient the eigenmodes arbitrarily.) Experimentally, the strength of the pinning is most readily characterized by the frequency of the horizontal rocking mode, given by

$$\omega_{\text{horiz rock}} = \omega_{hr} = \sqrt{\omega_2^2 - \omega_1^2} = \sqrt{\frac{2U_{\text{pin}}}{m}} \propto \sqrt{V_{\text{pin}}}. \quad (6.7)$$

The proportionality is determined by the trap geometry. In practice we choose $V_{\text{pin}} = 5 \text{ V}$ which gives $\omega_{hr} = 2\pi \times 280 \text{ kHz}$.

Creating the pinning potential requires four distinct voltages, $\pm V_{\text{pin}} \cos(2\varphi_{\text{pin}})$ and $\pm V_{\text{pin}} \sin(2\varphi_{\text{pin}})$. Since these come in two pairs of opposite sign, this may be achieved by sourcing only two distinct voltages and inverting them where appropriate. The pinning potential must also be dynamic in order to provide the spin-up-and-release sequence used to prepare the rotor state. We therefore source the pinning voltages from a two-channel arbitrary waveform generator, with the two channels a and b producing the voltages

$$\begin{aligned} V_a^{\text{AWG}}(t) &= V_{\text{pin}}(t) \cos[2\varphi_{\text{pin}}(t)] \\ V_b^{\text{AWG}}(t) &= V_{\text{pin}}(t) \sin[2\varphi_{\text{pin}}(t)]. \end{aligned} \quad (6.8)$$

We pass these through the rotation circuit (Sec. 4.2.1) to apply them to the appropriate electrodes, while still maintaining the DC offset necessary for stray static field compensation. The spin-up-and-release procedure is implemented by choosing waveforms such that V_{pin} and φ_{pin} vary with time as follows:

- For electronic state preparation and cooling, the ions are statically pinned at the maximum values of V_{pin} at an orientation which is convenient given the directions of the cooling lasers.
- Spin-up is performed by linearly accelerating φ_{pin} until $\dot{\varphi}_{\text{pin}}$ is equal to the target rotation frequency $\omega_{\text{rot}}^{\text{target}}$.
- Release is performed by linearly lowering V_{pin} until it reaches zero, while $\dot{\varphi}_{\text{pin}}$ is maintained at $\omega_{\text{rot}}^{\text{target}}$.

The functional form of these waveforms is schematically illustrated in Fig. 6.1(a).

In reality, due to the low-pass filtering of the DC electrode voltages, the pinning potential weakens as the orientation is accelerated, even before the amplitude of the voltage from the AWG is lowered.

6.2.2 Preparing the rotation frequency

As discussed above, the two important figures of merit for successful rotation preparation are the mean rotation frequency and the angular momentum spread. Of these two, the mean rotation frequency is the more reliably prepared to an acceptable value. However, we still find that there is significant variation in the mean rotation frequency, which is often roughly 5% of the target rotation frequency, e.g. 5 – 10 kHz variation when the target rotation frequency is 150 kHz. In particular, a strong dependence on the spin-up time is often observed. Figure 6.3 exemplifies this dependence. For target rotation frequencies of 100 kHz and 150 kHz, the actual prepared rotation frequency may differ from the target by up to 5 – 10 kHz in either direction.

Classical dynamics simulations

Numerical simulations can provide some insight into the spin-up-and-release process, and we find that indeed some dependence of mean rotation frequency on spin-up time is to be expected. Classical simulations are preferable over quantum mechanical simulations for tracking the mean rotation frequency during the spin-up process, since the mean angular momentum changes from 0 to at least $10^3 \hbar$, thus requiring a prohibitively large Hilbert space for faithful quantum simulations. However, as long as the acceleration of the pinning potential is not too fast, the wavefunction remains near the bottom of the well during spin-up, so that the dynamics of the mean rotation frequency follow the classical dynamics. This has been confirmed with quantum simulations using mock parameters to allow for a smaller

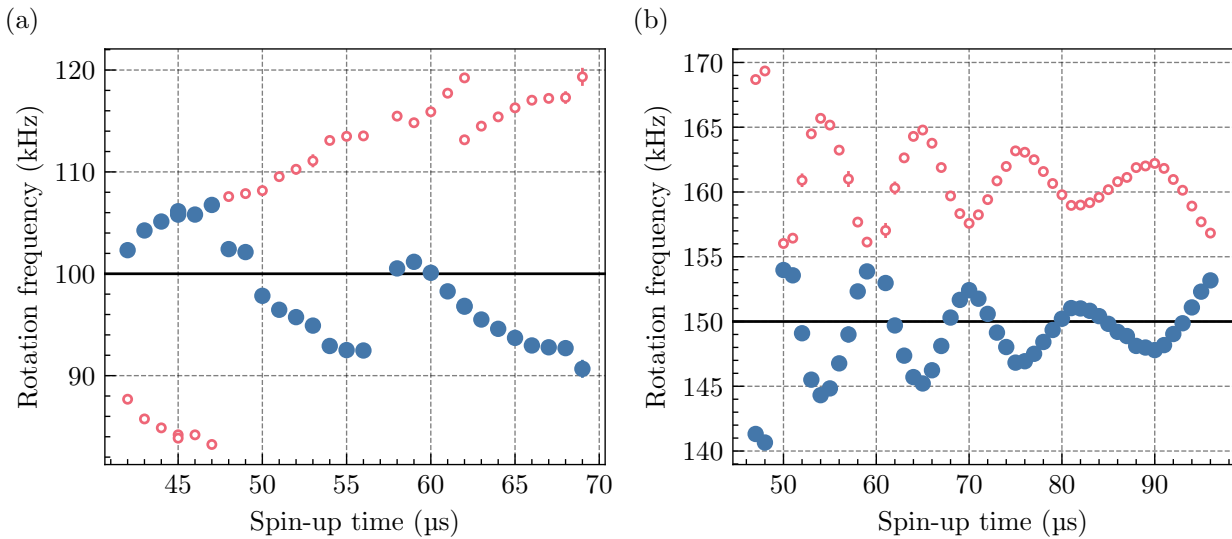


Figure 6.3: Actual rotation frequencies as a function of spin-up time for target rotation frequencies of 100 kHz (a) and 150 kHz (b). The solid horizontal line indicates the target rotation frequency. In these measurements, the rotation frequency is inferred from the frequency of Ramsey fringes (see Sec. 6.5). These indicate the detuning of the rotational sideband from the laser pulse frequency, but do not indicate the sign. Thus for each measurement there are two possible rotation frequencies which could give the same result. It is assumed that the more likely of the two possibilities is always the one which is closest to the target rotation frequency, which is marked in the solid blue markers, but for completeness the other possible result is also plotted in open red markers.

Hilbert space. Quantitatively, the requirement to be satisfied is $\alpha/\omega_{hr}^2 \ll 1$, where α is the rate of angular acceleration of the pinning potential. Given that for a linear spin-up, $\alpha = \omega_{\text{rot}}^{\text{target}}/t_{\text{spinup}}$, this is equivalent to $t_{\text{spinup}} \gg \omega_{\text{rot}}^{\text{target}}/\omega_{hr}^2$. For typical parameters, this requirement is easily satisfied.

We take the orientation θ of the rotor as the only degree of freedom. The rotor radius is assumed to be constant, though this is not strictly true experimentally: the radius is a function of the smallest secular frequency via (3.21), which in turn is a function of the pinning strength U_{pin} via (6.6)¹. The radius will thus change as U_{pin} is lowered during release, but this change is only approximately 1%. Along the circle of radius r in the xy -plane, the pinning potential (6.5) is a double well with the form

$$\Phi_{\text{pin}}(\theta) = U_{\text{pin}}r^2 \sin^2(\theta - \varphi_{\text{pin}}) = \Phi_{\text{pin}}^0 \sin^2(\theta - \varphi_{\text{pin}}). \quad (6.9)$$

Note that, from (6.7), the horizontal rocking mode frequency may be directly related to the

¹Here, ω_x in (3.21) should be replaced by ω_1 , which is given by the smaller of (6.6).

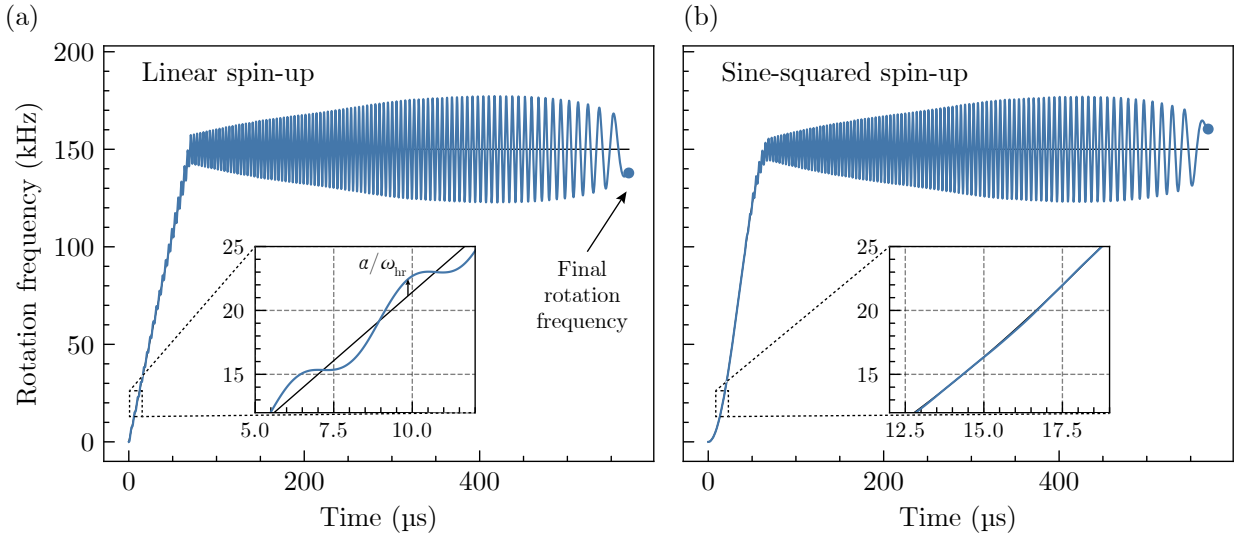


Figure 6.4: Simulated spin-up-and-release using classical dynamics for linear spin-up (left) and sine-squared spin-up (right). In both cases, the spin-up phase lasts 70 μs , and the release phase lasts 500 μs . The blue line shows the simulated trajectory of the rotor, and the black line shows the rotation rate of the underlying potential.

amplitude of the pinning potential Φ_{pin}^0 by

$$\omega_{hr} = \sqrt{\frac{2\Phi_{\text{pin}}^0}{mr^2}} = 2\sqrt{\omega_r \frac{\Phi_{\text{pin}}^0}{\hbar}}. \quad (6.10)$$

The classical dynamics may thus be described by the Lagrangian

$$\mathcal{L}(\theta, \dot{\theta}, t) = \frac{1}{2}I\dot{\theta}^2 - \Phi_{\text{pin}}^0(t) \sin^2 [\theta - \varphi_{\text{pin}}(t)]. \quad (6.11)$$

Figure 6.4 shows a classical simulation of the spin-up-and-release process for typical experimental parameters: 70 μs spin-up time, 500 μs release time, and 150 kHz target final rotation frequency. The rotor begins at rest in one of the potential minima. Figure 6.4(a) shows a linear spin-up function, which is used in all experiments. Initially, the rotor oscillates within the potential due to the sudden acceleration. These oscillations occur at the horizontal rocking mode frequency $\omega_{hr} = 278$ kHz, and initially have an amplitude of $\alpha/\omega_{hr} = 2\pi \times 1.2$ kHz from the instantaneous rotation frequency of the potential. The oscillation amplitude then grows gradually, possibly due to anharmonic contributions of the potential. The oscillations then abruptly grow significantly after completion of spin-up. During release, the rotor becomes allowed to oscillate with still greater amplitude as the potential becomes shallower. The oscillations also correspondingly decrease in frequency as the rocking frequency is lowered. The final rotation frequency at the completion of rotational state preparation is therefore highly sensitive to the phase of these oscillations at the moment of completion. Replacing

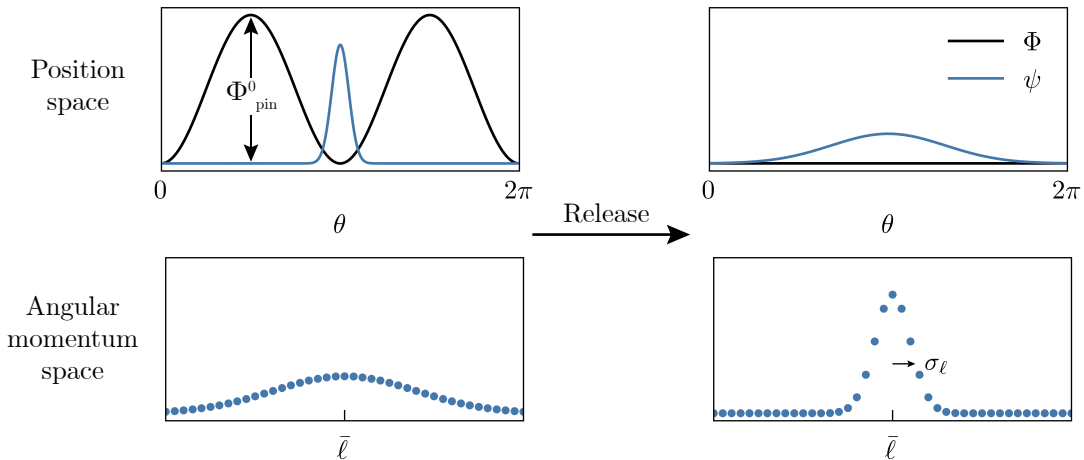


Figure 6.5: The release process in position space (shown in a rotating frame) and in angular momentum space. Initially, the rotor is pinned and the wavepacket is localized in position and spread in angular momentum. As the pinning potential is lowered, the position space wavepacket spreads and the angular momentum space wavefunction narrows.

the spin-up process with a smoother sine-squared function (Fig. 6.4(b)) does not help to eliminate this strong effect. The initial oscillations are nearly eliminated, but they begin to appear as the spin-up acceleration slows, and still become significantly amplified at the onset of release. These simulations do not account for weakened pinning during spin-up due to filtering.

6.2.3 Minimizing the angular momentum spread

The spread in angular momentum is best modeled quantum mechanically. At the beginning of the spin-up-and-release process, the initial state is inside a deep potential well. This localizes the wavepacket in position to $4 - 10 \times 10^{-3}$ radians, which thus has a large uncertainty in momentum of $50 - 120 \hbar$ when in the ground state of the horizontal rocking mode, and larger if in an excited state. The spin-up process displaces the center of this wavepacket $\langle L_z \rangle$ from 0 to close to $I\omega_{\text{rot}}^{\text{target}}$, but does not affect the spread. The release process then lowers the pinning potential, allowing the position-space wavepacket to spread more, which in turn narrows the angular momentum space distribution, as desired. The angular momentum spread after rotational state preparation is thus most directly affected by the release process.

We find that the final angular momentum spread depends on four main factors:

- The initial state of the horizontal rocking mode. The colder the horizontal rocking mode, the more localized it is in angular momentum to begin with, and the more localized it is after spin-up-and-release. This is observed both in experiment and in simulations.

- The release time. This is related to the adiabaticity of the release process: In the limit of a perfectly adiabatically release, an eigenstate of the initial Hamiltonian (e.g. the ground state of the horizontal rocking mode) gets mapped onto an eigenstate of the final Hamiltonian (i.e. an angular momentum eigenstate). A slower rate keeps the release process in the adiabatic regime for longer, allowing the angular momentum wavefunction to narrow more. This has been explored in simulations to inform the choice of release time, but has not been explored thoroughly in experiment.
- Residual quadrupole fields which may remain uncompensated in the absence of an intentionally applied pinning potential. We find experimentally that the angular momentum spread suffers if these are not compensated precisely. This dependence has not been thoroughly studied in simulations.
- The spin-up time. This dependence is observed only experimentally, and remains unexplained.

Effects of initial temperature and rate of release

The effects of both initial temperature and release rate may be modeled using quantum mechanical simulations under the Hamiltonian

$$H(t) = \frac{L_z^2}{2I} + \Phi_{\text{pin}}^0(t) \sin^2 \theta. \quad (6.12)$$

Here, only the release process is modeled, and is done in a rotating frame. Despite the empirical observation that the spin-up time affects the final angular momentum distribution, full quantum mechanical simulations which include the spin-up process do not indicate any affect of spin-up on the angular momentum spread. It thus suffices in these idealized simulations to model release only.

It may be noted that Hamiltonian used (6.12) ignores the rotation of the potential, but this does not affect the dynamics of the release process. This is justified as follows: In the lab frame, the Hamiltonian is

$$H_{\text{labframe}}(t) = \frac{L_z^2}{2I} + \Phi_{\text{pin}}^0(t) \sin^2(\theta - \omega_{\text{rot}}^{\text{target}} t). \quad (6.13)$$

To transform into the rotating frame, we may apply the unitary $U = e^{-i\omega_{\text{rot}}^{\text{target}} t L_z / \hbar}$, yielding an effective Hamiltonian

$$H_{\text{rotframe}}(t) = \frac{L_z^2}{2I} + \Phi_{\text{pin}}^0(t) \sin^2(\theta) - \omega_{\text{rot}}^{\text{target}} L_z. \quad (6.14)$$

This differs from the Hamiltonian actually used (6.12) only by the term $-\omega_{\text{rot}}^{\text{target}} L_z$. This term serves only to make the angular momentum state which matches the potential's rotation, $\ell \approx I\omega_{\text{rot}}^{\text{target}}/\hbar$, the new ground state. It otherwise does not qualitatively change the energy

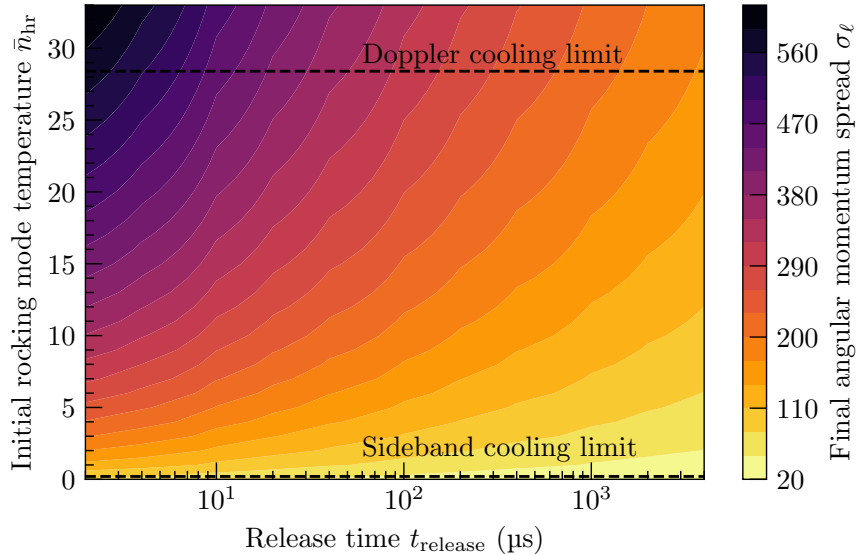


Figure 6.6: Final angular momentum spread as a function of initial rocking mode temperature and release time, as determined from a collection of quantum mechanical simulations of the release process. For these simulations, $r = 3 \mu\text{m}$, or equivalently, $\omega_r = 2\pi \times 7.0 \text{ Hz}$.

eigenspectrum. It therefore suffices to model the potential and the state as both not rotating as in (6.12), which is preferable for simplicity.

The temperature of the horizontal rocking mode dictates the choice of initial state in the simulation, and the release time determines the slope of the linear ramp of the pinning strength $\Phi_{\text{pin}}^0(t)$ from its initial value down to zero. Figure 6.6 shows the simulated angular momentum spread as a function of initial rocking mode temperature and release time. We see that sideband cooling the horizontal rocking mode lowers σ_ℓ by 1–2 orders of magnitude over just Doppler cooling. This pronounced difference is also seen experimentally. The horizontal rocking mode is always sideband cooled prior to rotational state preparation for this reason. Once the initial state is as cold as it can be however, releasing for longer than 100’s of μs provides little added benefit.

We find in practice that the optimal angular momentum spread, when other factors are optimized to the best of our ability, is approximately a factor of 2 greater than those predicted in Fig. 6.6. We also find that release times longer than 1 ms result in a much larger angular momentum spread, for unknown reasons.

Adiabaticity of release

We find from simulations which begin in the ground state of the rocking mode that the release process may be well-approximated as an initially adiabatic narrowing of the angular momentum distribution, followed by an abrupt transition after which the narrowing stops nearly entirely once the adiabaticity condition is violated. From the adiabatic theorem, the

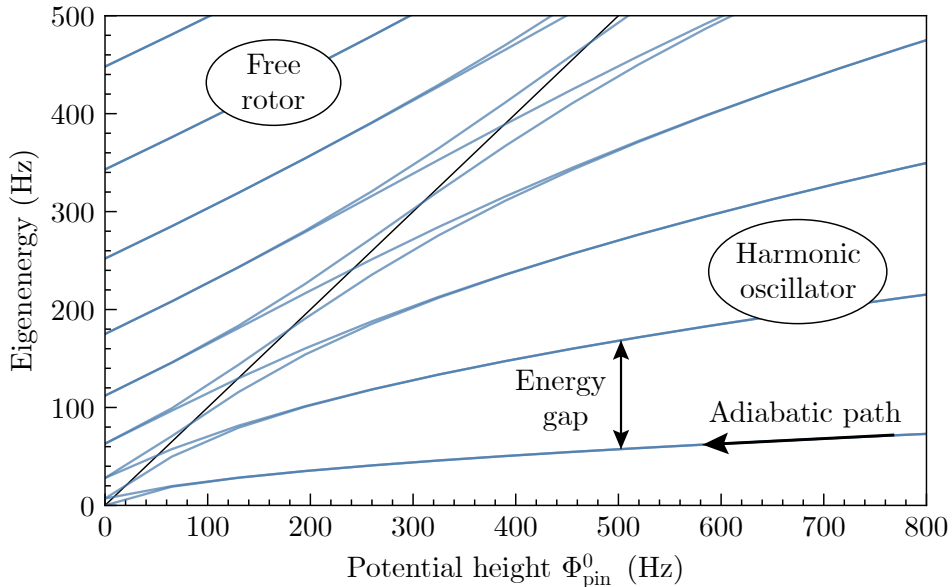


Figure 6.7: Eigenspectrum of the Hamiltonian (6.12) as a function of the potential height for $\omega_r = 2\pi \times 7 \text{ Hz}$. The plot is zoomed in to energies which are much smaller than those which are experimentally relevant in order to resolve the individual eigenenergies. Along the black line, the x and y coordinates are equal. Above it, the eigenspectrum is approximately that of a free rotor, and below it, it is approximately that of a harmonic oscillator. A system which begins at large Φ_{pin}^0 in the ground state will follow the lowest energy curve adiabatically as Φ_{pin}^0 is reduced until the energy gap becomes small enough to violate the adiabaticity condition.

condition for adiabatic evolution is

$$\frac{\dot{\omega}_{hr}}{\omega_{hr}} \ll \omega_{hr} \implies \frac{1}{2} \frac{\dot{\Phi}_{\text{pin}}^0}{\Phi_{\text{pin}}^0} \ll \omega_{hr}. \quad (6.15)$$

At the beginning of the release process, the system is in the ground state of the Hamiltonian (6.12), which is approximately a harmonic oscillator. The energy gap is thus the horizontal rocking mode frequency ω_{hr} . As the potential height is lowered, this gap becomes smaller. The energy gap is initially very large compared to its rate of change, but eventually the gap becomes small enough that the adiabaticity condition is violated. The angular momentum spread at the time of adiabaticity violation determines the final spread.

For a linear release, $\Phi_{\text{pin}}^0(t) = \Phi_{\text{pin}}^0(t=0) \times (1 - t/t_{\text{release}})$. Substituting this into the condition (6.15), the release is adiabatic for times t which satisfy

$$\left(1 - \frac{t}{t_{\text{release}}}\right)^{3/2} \gg \frac{1}{2t_{\text{release}}\omega_{hr}(t=0)}. \quad (6.16)$$

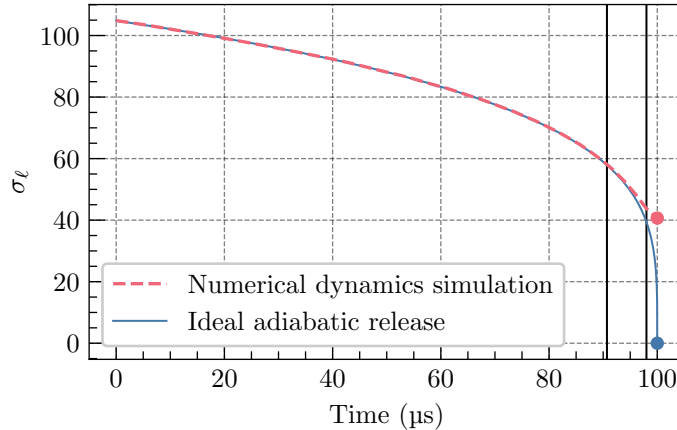


Figure 6.8: Time series of a numerical simulation of the release process for a $100\text{ }\mu\text{s}$ release time, beginning from the ground state of the horizontal rocking mode, for $\omega_r = 2\pi \times 7\text{ Hz}$. The solid curve shows the angular momentum spread for an ideal adiabatic trajectory, given by (6.18). Vertical lines show where the energy gap exceeds its relative rate of change (i.e. the inequality (6.16)) by a factor of 10 (left) and where they are equal (right).

Linear release begins deeply in the adiabatic regime, with the left-hand side of (6.16) exceeding the right-hand side by more than 3 orders of magnitude. One may roughly estimate that adiabaticity is violated when the energy gap exceeds the relative rate of change of the Hamiltonian by less than one order of magnitude. For a $500\text{ }\mu\text{s}$ release time, this suggests from (6.16) that the adiabaticity condition is violated when $t = 0.97t_{\text{release}}$, so that only the final few microseconds are nonadiabatic. We thus expect the angular momentum spread here to be determined by the angular momentum spread when $\Phi_{\text{pin}}^0 = 0.03\Phi_{\text{pin}}^0(t=0)$, which for $\omega_r = 2\pi \times 7\text{ Hz}$ is $17\hbar$. Extending the release time by an order of magnitude to 5 ms would make the adiabaticity last until $t = 0.993t_{\text{release}}$, at which point the angular momentum spread is expected to be $8.4\hbar$, only a factor of 2 smaller. This estimate somewhat agrees with the simulations from Fig. 6.6, underestimating them by approximately a factor of 2.

As an example, Fig. 6.8 shows the time series result of one of the simulated releases shown in Fig. 6.6: starting in the ground state and releasing for $100\text{ }\mu\text{s}$. The dashed curve shows the simulated angular momentum spread during the release process, while the solid curve shows the angular momentum spread if the state were to follow a perfect adiabatic trajectory, i.e. always remaining in the ground state. The simulated spread closely follows the adiabatic trajectory up until the final few microseconds, where the adiabaticity condition is violated. A perfectly adiabatic release would bring σ_ℓ down to 0, since at the end of release, the energy eigenstates are exactly angular momentum eigenstates. However, the true process limits the angular momentum spread σ_ℓ to 41 in this simulation. Maintaining adiabaticity all the way down to the level where the energy gap is on the order of ω_r using a linear ramp would require a ramp time on the order of 10's of days.

Such a dramatic jump from adiabatic to diabatic suggests that when releasing linearly,

time is wasted at the beginning of the release process by releasing so slowly. It is possible that there exists a wiser choice of release function. Using (6.15), one way to define such a function is such that the ratio $\omega_{hr}/\omega_{hr}^2$ remains approximately constant. Imposing this condition results in the release function

$$\Phi_{\text{pin}}^0(t) = \frac{\Phi_{\text{pin},i}^0}{(1 + \omega_{hr,i}t)^2}. \quad (6.17)$$

where $\Phi_{\text{pin},i}$ and $\omega_{hr,i}$ are the initial values of Φ_{pin} and ω_{hr} at $t = 0$. Using this function, it would take only approximately 10 ms for the energy gap to adiabatically go down to roughly ω_r . It should be noted however that most of the time is spent at very small potential heights of under 1 kHz. If such shallow potentials are required, other limitations will become relevant. One such limitation is the resolution of the AWG which generates the pinning potential. In general, the ground state of the rotor in a quadrupole potential with height Φ_{pin}^0 has angular momentum uncertainty

$$\sigma_\ell = \frac{1}{\sqrt{2}} \left(\frac{\Phi_{\text{pin}}^0/\hbar}{\omega_r} \right)^{1/4}. \quad (6.18)$$

This is the absolute minimum angular momentum spread possible in the presence of a quadrupole potential rotating along with the rotor (unless some other highly precise diabatic process were to be employed). The AWG currently used for rotational state preparation has a resolution of 16 bits, so that the minimum possible nonzero pinning voltage is can apply is $\Phi_{\text{pin}}^0 = h \times 15 \text{ kHz}$. This limits the angular momentum spread to $4\hbar$ before the pinning voltage is lowered abruptly to zero. Additionally, any residual static quadrupole in the absence of an intentionally applied pinning potential will also inhibit narrowing of the angular momentum distribution.

Effect of residual quadrupoles

The width of the angular momentum distribution after rotational state preparation is empirically found to be very sensitive to the presence of static residual quadrupole fields. Compensation of these fields is done by measuring the frequency of the horizontal rocking mode in the absence of an applied pinning potential, and adjusting the compensating quadrupole values via the DC electrode voltage contributions from the DAC such that the mode frequency is minimized. A typical minimally achievable rocking mode frequency is 20 kHz. It should be noted therefore that the experiments carried out in this work are done in the presence of an underlying quadrupole potential. However, referring back to Fig. 6.7, the Hamiltonian is still approximately that of a free rotor as long as the rotational kinetic energy is large compared to the residual potential height. In terms of the residual horizontal rocking mode frequency $\omega_{hr,\text{resid}}$, this condition is equivalent to $\omega_{\text{rot}}^2 \gg \omega_{hr,\text{resid}}^2$.

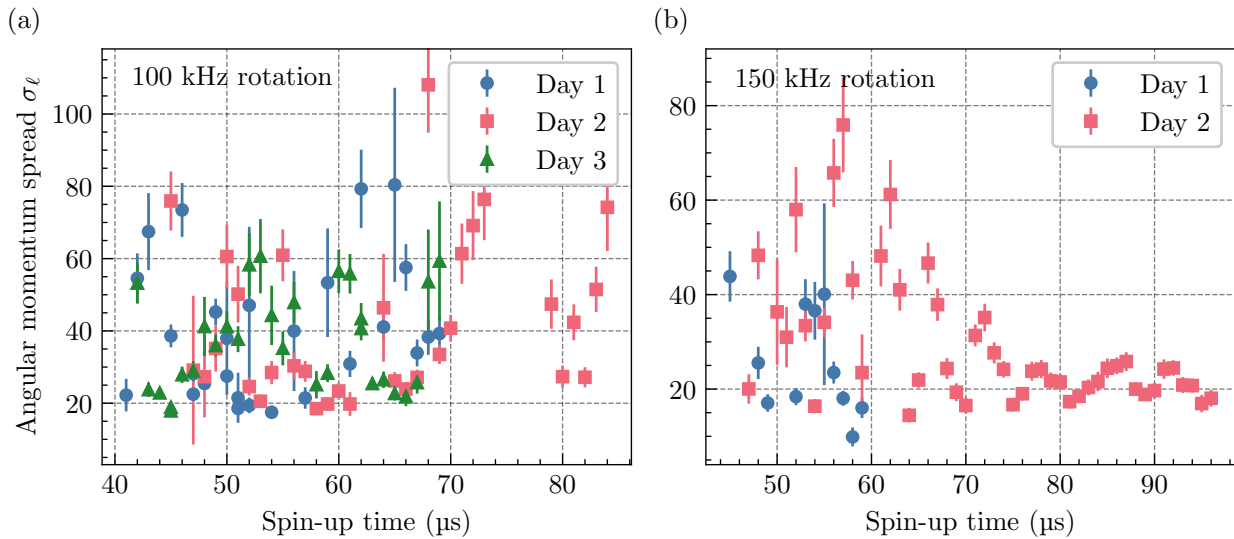


Figure 6.9: Measured angular momentum spread as a function of spin-up time for 100 kHz rotation (a) and 150 kHz rotation (b). Different datasets have been taken on different days. Here, $r = 2.2 \mu\text{m}$, or equivalently, $\omega_r = 2\pi \times 13 \text{ Hz}$.

Effect of spin-up time

In practice, the final angular momentum spread is a strong function of the spin-up time. The dependence is commonly reproducible on a given day, but rarely reproducible between days. Figure 6.9 exemplifies this dependence. Some of these data correspond to the same measurements as those shown in Fig. 6.3. If one plots angular momentum spread against rotation frequency for these data points, no correlation is apparent.

No mechanism by which such a strong dependence may exist is known. However, preliminary work from visiting student Shijia Sun has suggested that there may be a resonance mechanism which occurs in the presence of a residual static quadrupole field. The resonance occurs when the horizontal rocking mode frequency equals the rotation frequency, which occurs during release if the target rotation frequency is smaller than the initial rocking mode frequency. In the frame rotating with the potential, the static quadrupole is then resonant with the rocking mode, which could possibly cause heating. Such a mechanism would likely be sensitive to the phase of the wavepacket's oscillation within the potential at the moment of this resonance, which would indeed be affected by the spin-up time on the microsecond scale.

The distribution of angular momentum

In most of this work, the angular momentum wavefunction is assumed to be Gaussian-distributed about its center $\bar{\ell}$. Two different ways of estimating the distribution lead to this assumption:

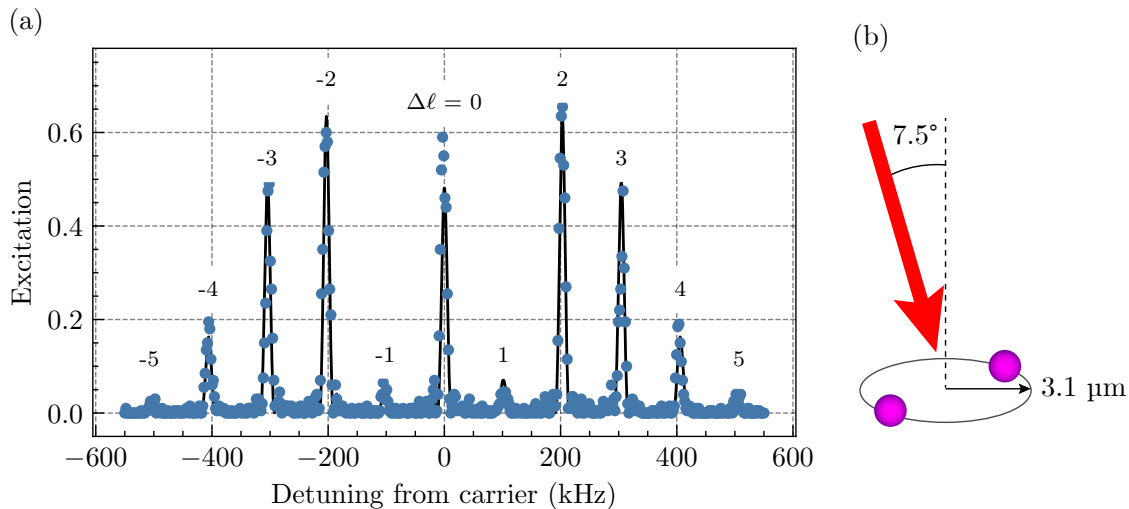


Figure 6.10: (a) Spectrum of sidebands of the 729 nm transition of a 2-ion crystal freely rotating at 101.5 kHz. The solid curve is a fit for angle of the 729 nm addressing laser relative to the rotor, and yields 7.5° relative to the normal of the rotor plane. Each sideband is labelled with its rotational transition order $\Delta\ell$. This data has been published in Ref. [41]. (b) Schematic of the geometry of the 729 nm laser beam relative to the rotor as inferred from the coupling strengths seen in the data.

- The state at the beginning of rotational state preparation, which is the ground state of the horizontal rocking mode if it is sideband cooled, is Gaussian-distributed in both position and angular momentum. Quantum mechanical simulations of the spin-up-and-release process indicate that spin-up changes only the mean of the distribution and release changes only the width, but that the Gaussian shape is maintained throughout.
- A thermal state of the rotor is Gaussian-distributed, as follows from the Boltzmann distribution $P_\ell \sim e^{-E_\ell/k_B T} = e^{-\hbar\omega_r \ell^2/k_B T}$. Thus even if some process tends to thermalize the rotational state, it will still tend towards a Gaussian distribution, albeit an incoherent one.

The exact distribution, and even its coherence, is largely inconsequential for the work done in this thesis. We assume always that the angular momentum wavefunction is localized and characterized by some width σ_ℓ , but major results such as those in Chaps. 7 and 8 do not rely on precise knowledge of the distribution.

6.3 The rotational spectrum

Successful rotational state preparation results in a state whose angular momentum is centered near $I\omega_{\text{rot}}^{\text{target}}$ and spread minimally, ideally such that the sideband linewidth $4\omega_r\sigma_\ell\Delta\ell$ is on the

order of 1 kHz. In this case, rotational sidebands of different orders $\Delta\ell$ become spectrally resolved. A scan of the 729 nm laser frequency around the carrier electronic transition between the $S_{1/2}$ and $D_{5/2}$ states reveals sidebands at detunings equal to integer multiples of the rotation frequency. Figure 6.10(a) shows a measured rotational sideband spectrum. Here, the target rotation frequency was 100 kHz, and sidebands are found at integer multiples of 101.5 kHz. The height of the sidebands encodes their relative coupling strengths. From (3.31b), the relative coupling strength of the $\Delta\ell$ -order sideband is

$$\Omega_{\Delta\ell} \propto J_{\Delta\ell}(\zeta). \quad (6.19)$$

Here the dimensionless parameter ζ , defined in (3.26b), may be taken to be real without loss of generality. Note that while in principle, ζ_i may take on a different value for each ion in a rotating ion crystal, each ion in our 2-ion crystal case has the same radius and thus has the same magnitude of ζ_i . Defining relative phases such that ζ is real gives a more practical expression for our 2-ion case:

$$\zeta = k_{\parallel} r = kr \sin \theta_k, \quad (6.20)$$

where $k_{\parallel} = \sqrt{k_x^2 + k_y^2}$ is the projection of laser wavevector onto the rotor plane, and θ_k is the angle of the wavevector relative to the normal of the rotor plane. The solid curve in Fig. 6.10(a) is a fit to all coupling strengths together, using ζ as the only free parameter. The relative coupling strengths seen in the data agree well with $\zeta = 3.5$. Using $k = 2\pi/(729 \text{ nm})$ and $r = 3.1 \mu\text{m}$, we thus infer the beam angle θ_k to be 7.5° from the rotor normal.

6.3.1 Choice of beam angle

For a rotor of radius 3 μm , ζ may range between 0 and $kr = 26$, depending on the choice of beam angle. As shown in Fig. 6.11, as the beam is tilted from vertical towards horizontal, the coupling strengths become spread out across more transition orders. It is important to choose a beam angle such that ζ is not too large, for a few reasons:

- A rotational spectrum with many sideband orders will be dense and span several MHz, risking spectral overlap between sidebands of different modes, or even a neighboring carrier Δm of the $|S\rangle \leftrightarrow |D\rangle$ electronic transition. Fewer sideband orders keeps the spectrum clean and easy to manage and interpret.
- The value of ζ which optimizes the $\Delta\ell$ -order sideband coupling strength is very roughly $\zeta \sim \Delta\ell$. For example, as seen in Fig. 6.10, $\zeta = 3.5$ works well for addressing $\Delta\ell \leq 4$. A large ζ would thus be optimal for addressing high-order rotational transitions, but doing so is generally not preferred. There are two reasons for this:
 - The optimal possible coupling strength for a given sideband order falls as the order decreases, as can be seen from Fig. 6.11.
 - The linewidth of the $\Delta\ell$ sideband increases proportionally with $\Delta\ell$.

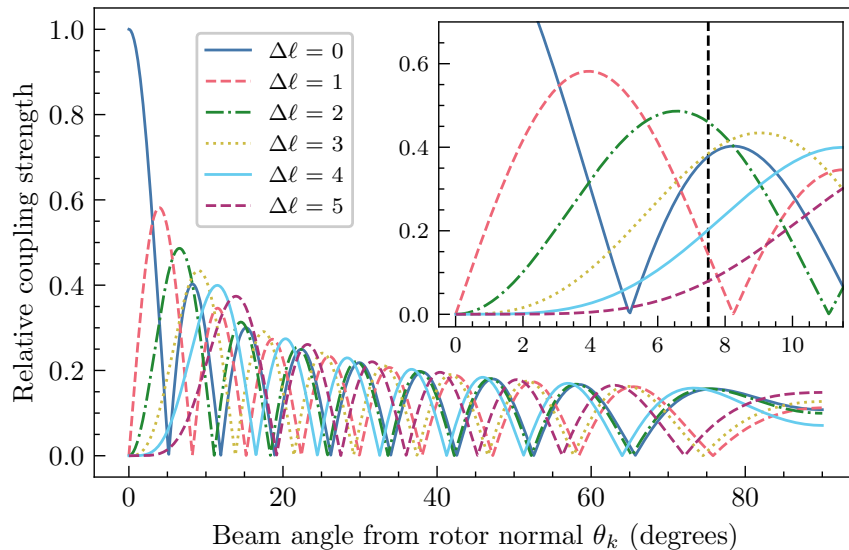


Figure 6.11: Relative rotational sideband coupling strength as a function of beam angle as given by (6.20), for a rotor radius $r = 3.1 \mu\text{m}$. The inset is a zoom-in of the same plot. The vertical line in the inset is at 7.5° . The relative coupling strengths at this point are those seen in Fig. 6.10.

Both of these effects serve to degrade the quality of operations on higher-order rotational sidebands. It is thus better to instead optimize for sideband orders which do not exceed ~ 6 .

For this reason, a nearly vertical beam is used to address rotational sideband transitions. An additional benefit of using an addressing beam that is normal to the rotor plane is avoiding the effects of heavy excess micromotion which occurs in the radial direction, due to the ions being displaced by several micrometers from the RF null at the center of the trapping potential. Addressing the ions vertically necessitates sideband cooling of the vertical COM and rocking modes prior to rotational operations in order to facilitate coherent operations on rotational sidebands. This requirement is what necessitates mitigation of technical electric field noise in the vertical direction.

6.4 Rotational Rabi experiments

With resolved rotational sidebands, a particular transition order $\Delta\ell$ may be spectroscopically chosen for coherent addressing. Figure 6.12 shows Rabi oscillations of the first three rotational sideband orders, spectrally separated from each other by 150 kHz. These Rabi oscillations are very clean due to high-quality rotational state preparation, but in general, the shape of the rotational sideband Rabi oscillations depends strongly on the quality of rotational state preparation.

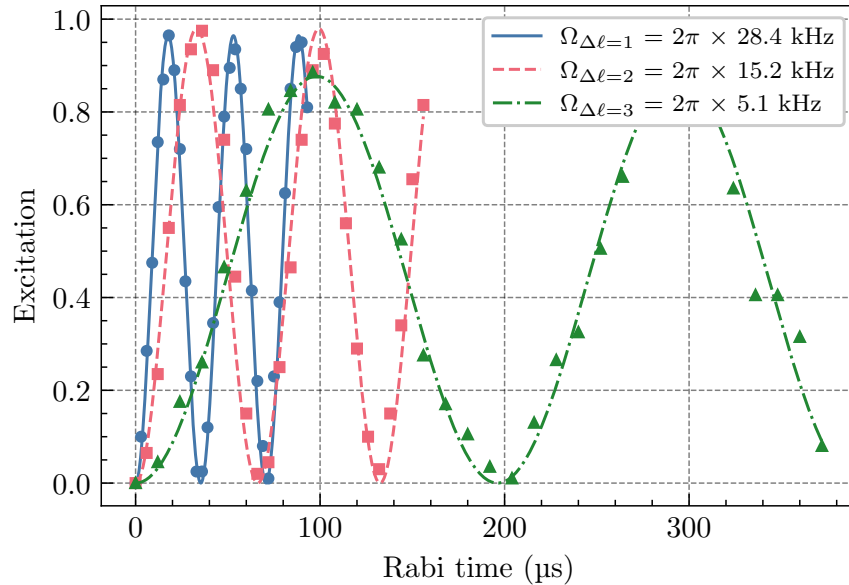


Figure 6.12: Rabi oscillations on 1st, 2nd, and 3rd order rotational sidebands when rotating at 150 kHz. The coupling strengths are given directly by the frequency of the Rabi oscillations, and their relative values are consistent with $\zeta = 1.85$. This data was taken using a different rotor radius and beam angle from that in Fig. 6.10.

6.4.1 Full 4-level dynamics

A more thorough description of the Rabi oscillation dynamics can be deduced beginning with the Hamiltonian (3.24). It is convenient to divide through by \hbar so that the Hamiltonian is written in frequency units. It then may be written

$$\begin{aligned}
 H = & \omega_r \left(\frac{L_z}{\hbar} \right)^2 + \sum_{i=1}^2 \frac{1}{2} \omega_{SD} (|D_i\rangle\langle D_i| - |S_i\rangle\langle S_i|) \\
 & + \frac{1}{2} \left[\Omega |D_1\rangle\langle S_1| e^{i\frac{1}{2}\zeta(L_+ + L_-) - i\omega t} + h.c. \right] \\
 & + \frac{1}{2} \left[\Omega |D_2\rangle\langle S_2| e^{-i\frac{1}{2}\zeta(L_+ + L_-) - i\omega t} + h.c. \right], \tag{6.21}
 \end{aligned}$$

where ω is the laser frequency and ω_{SD} is the $|S\rangle \leftrightarrow |D\rangle$ transition frequency. Here we have used the fact that for a 2-ion crystal, $\zeta_2 = -\zeta_1$, so we define $\zeta \equiv \zeta_1$. We also define ζ to be real. Unlike in (3.24), here the Rabi frequency Ω is allowed in general to be complex. This is a useful generalization for Ramsey experiments (see Sec. 6.5), where the phase of the final pulse may differ from that of the initial pulse.

From (3.30), we may expand the operators $e^{\pm i\frac{1}{2}\zeta(L_++L_-)}$ as

$$\begin{aligned} e^{i\frac{1}{2}\zeta(L_++L_-)} &= \sum_{\ell,\Delta\ell} e^{i\pi\Delta\ell/2} J_{\Delta\ell}(\zeta) |\ell + \Delta\ell\rangle\langle\ell| \\ e^{-i\frac{1}{2}\zeta(L_++L_-)} &= \sum_{\ell,\Delta\ell} e^{i\pi\Delta\ell/2+i\pi\Delta\ell} J_{\Delta\ell}(\zeta) |\ell + \Delta\ell\rangle\langle\ell| \end{aligned} \quad (6.22)$$

If the sidebands are resolved, then only one value of $\Delta\ell$ will contribute to the above sum, and the others will be off-resonant. We may furthermore shift the overall phase factor by $e^{-i\pi\Delta\ell/2}$ for convenience, so that $e^{i\pi\Delta\ell/2} \rightarrow 1$ and $e^{i\pi\Delta\ell/2+i\pi\Delta\ell} \rightarrow e^{i\pi\Delta\ell} = (-1)^{\Delta\ell}$.

$$\begin{aligned} H = \omega_r \left(\frac{L_z}{\hbar} \right)^2 + \sum_{i=1}^2 \frac{1}{2} \omega_{SD} (|D_i\rangle\langle D_i| - |S_i\rangle\langle S_i|) \\ + \frac{1}{2} \sum_{\ell} [\Omega_{\Delta\ell} |D_1, \ell + \Delta\ell\rangle\langle S_1, \ell| e^{-i\omega t} + h.c.] \\ + (-1)^{\Delta\ell} \frac{1}{2} \sum_{\ell} [\Omega_{\Delta\ell} |D_2, \ell + \Delta\ell\rangle\langle S_2, \ell| e^{-i\omega t} + h.c.], \end{aligned} \quad (6.23)$$

where $\Omega_{\Delta\ell} = \Omega J_{\Delta\ell}(\zeta)$. The factor of $(-1)^{\Delta\ell}$ on the term for ion 2 relative to that of ion 1 may be interpreted as a phase difference of either 0 or π , arising from the fact the two ions always move in opposite directions when the crystal rotates.

To see the dynamics most clearly, we may now take two further steps, summarized as follows:

- All terms Hamiltonian should be written in the basis $\{|SS, \ell\rangle, |DS, \ell + \Delta\ell\rangle, |SD, \ell + \Delta\ell\rangle, |DD, \ell + 2\Delta\ell\rangle\}$. In doing so, we find that the Hamiltonian may be structured as a sum of non-interacting 4-level systems, one for each value of ℓ . In matrix form the Hamiltonian thus takes a block-diagonal form.
- We transform into a rotating frame which eliminates the time-dependence, defined by the unitary

$$U = \prod_{\ell} e^{i\frac{1}{2}\omega(2|DD, \ell + 2\Delta\ell\rangle\langle DD, \ell + 2\Delta\ell| - 2|SS, \ell\rangle\langle SS, \ell|)t}. \quad (6.24)$$

This is somewhat more convenient than choosing the interaction picture transformation, since the rotor nonlinearity means that each transition comes with its own unique time-dependent transition frequency in the interaction picture (see e.g. (3.28)).

The resulting effective Hamiltonian may be written $\sum_{\ell} H_{\ell}$, with each term most conveniently written in matrix form using the basis $\{|SS, \ell\rangle, |DS, \ell + \Delta\ell\rangle, |SD, \ell + \Delta\ell\rangle, |DD, \ell + 2\Delta\ell\rangle\}$:

$$H_{\ell} = \begin{pmatrix} \omega_r \ell^2 + \Delta & \frac{1}{2} \Omega_{\Delta\ell}^* & (-1)^{\Delta\ell} \frac{1}{2} \Omega_{\Delta\ell}^* & 0 \\ \frac{1}{2} \Omega_{\Delta\ell} & \omega_r (\ell + \Delta\ell)^2 & 0 & (-1)^{\Delta\ell} \frac{1}{2} \Omega_{\Delta\ell}^* \\ (-1)^{\Delta\ell} \frac{1}{2} \Omega_{\Delta\ell} & 0 & \omega_r (\ell + \Delta\ell)^2 & \frac{1}{2} \Omega_{\Delta\ell}^* \\ 0 & (-1)^{\Delta\ell} \frac{1}{2} \Omega_{\Delta\ell} & \frac{1}{2} \Omega_{\Delta\ell} & \omega_r (\ell + 2\Delta\ell)^2 - \Delta \end{pmatrix}, \quad (6.25)$$

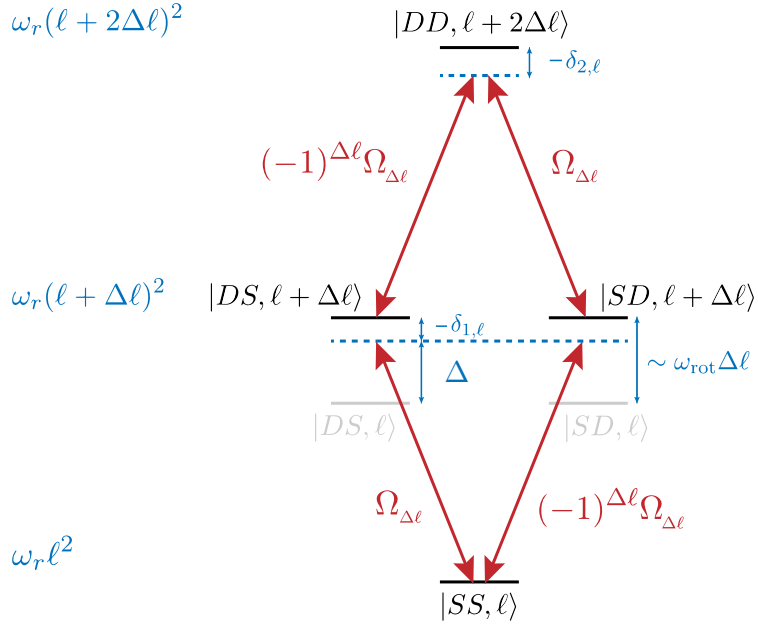


Figure 6.13: Energy level diagram for addressing the $\Delta\ell$ -order rotational sideband of a 2-ion crystal. A single laser is used, whose detuning from the carrier Δ is close to $\omega_{\text{rot}}\Delta\ell$, and is near resonance with four transitions. Energies and transition frequencies are shown in blue, and coupling strengths are shown in red. Due to the nonlinearity of the rotor, the two excitations do not have precisely the same transition frequency, so each has its own detuning, labelled $\delta_{1,\ell}$ and $\delta_{2,\ell}$. A copy of this diagram applies for each ℓ which is initially occupied.

where $\Delta \equiv \omega - \omega_{SD}$ is the detuning from the carrier transition. Finally, one further simplification may now be made by subtracting a constant $\omega_r\ell^2 + \Delta$ from each term of the Hamiltonian. This value depends on ℓ , so performing this simplification changes the relative phase between the terms H_ℓ of the Hamiltonian. It is therefore only appropriate when the coherences between the terms are irrelevant. One case in which this condition may be violated is an experiment which involves multiple pulses on different $\Delta\ell$ sidebands, though this is not done in this work. After subtracting off $\omega_r\ell^2 + \Delta$ from each term, we are left with

$$H = \sum_{\ell} H_{\ell}, \quad \text{where} \\ H_{\ell} = \begin{pmatrix} 0 & \frac{1}{2}\Omega_{\Delta\ell}^* & (-1)^{\Delta\ell}\frac{1}{2}\Omega_{\Delta\ell}^* & 0 \\ \frac{1}{2}\Omega_{\Delta\ell} & -\delta_{1,\ell} & 0 & (-1)^{\Delta\ell}\frac{1}{2}\Omega_{\Delta\ell}^* \\ (-1)^{\Delta\ell}\frac{1}{2}\Omega_{\Delta\ell} & 0 & -\delta_{1,\ell} & \frac{1}{2}\Omega_{\Delta\ell}^* \\ 0 & (-1)^{\Delta\ell}\frac{1}{2}\Omega_{\Delta\ell} & \frac{1}{2}\Omega_{\Delta\ell} & -\delta_{1,\ell} - \delta_{2,\ell} \end{pmatrix} \quad (6.26)$$

with

$$\delta_{1,\ell} \equiv \Delta - \omega_r(2\ell\Delta\ell + \Delta\ell^2) \\ \delta_{2,\ell} \equiv \Delta - \omega_r(2\ell\Delta\ell + 3\Delta\ell^2). \quad (6.27)$$

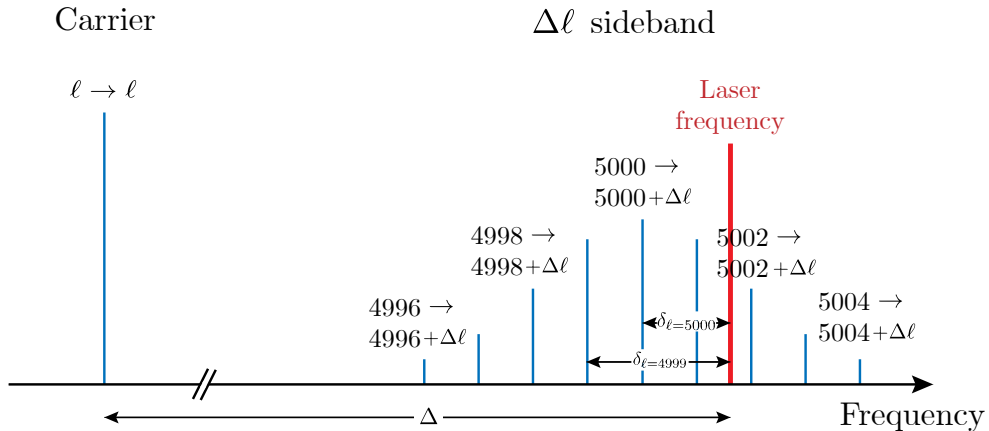


Figure 6.14: Schematic example spectrum for an angular momentum distribution centered at $\bar{\ell} = 5000$ showing how various detunings are defined. Each blue line is a transition from $\ell \rightarrow \ell + \Delta\ell$, each of which has a different detuning from the laser frequency. This schematic applies in the approximation that the two excitations of the ions $\ell \rightarrow \ell + \Delta\ell$ and $\ell + \Delta\ell \rightarrow \ell + 2\Delta\ell$ have approximately the same transition frequency.

$\delta_{1,\ell}$ and $\delta_{2,\ell}$ are the detunings from the $|\ell\rangle \rightarrow |\ell + \Delta\ell\rangle$ transition and from the $|\ell + \Delta\ell\rangle \rightarrow |\ell + 2\Delta\ell\rangle$ transition, respectively. Since the rotor energy eigenspectrum is nonlinear, these transition frequencies are not exactly the same, and differ by $2\omega_r\Delta\ell^2$. This difference is independent of ℓ .

6.4.2 Approximation as 2-level systems

In many cases, the difference between the two relevant transition frequencies $2\omega_r\Delta\ell^2$ is small and may be neglected. The dynamics will be affected by this discrepancy only at times which are not small compared to about $1/\omega_r\Delta\ell^2$. As an example with large ω_r and $\Delta\ell$, if the rotor radius is $1.8 \mu\text{m}$ so that $\omega_r = 2\pi \times 20 \text{ Hz}$, then on the $\Delta\ell = 4$ transition, the 4-level dynamics become relevant at times approaching or greater than $\sim 1 \text{ ms}$. This is longer than a typical time for a Rabi oscillation, whose Rabi frequency is typically several kHz, but can be relevant for Ramsey experiments.

In the approximation that the detunings (6.27) are equal (which we then call simply δ_ℓ), the 4-level dynamics are equivalent to the dynamics of a tensor product of two identical two-level systems, each of which has the Hamiltonian

$$H_{2\text{-level},\ell} = \frac{1}{2} \begin{pmatrix} \delta_\ell & \Omega_{\Delta\ell}^* \\ \Omega_{\Delta\ell} & -\delta_\ell \end{pmatrix}. \quad (6.28)$$

We may then interpret the dynamics as an ensemble of such 2-level systems, one for each ℓ . After rotational state preparation, the state of the rotor is approximately Gaussian-distributed with center $\bar{\ell} = I\omega_{\text{rot}}/\hbar$ and standard deviation σ_ℓ . Each value of ℓ will have

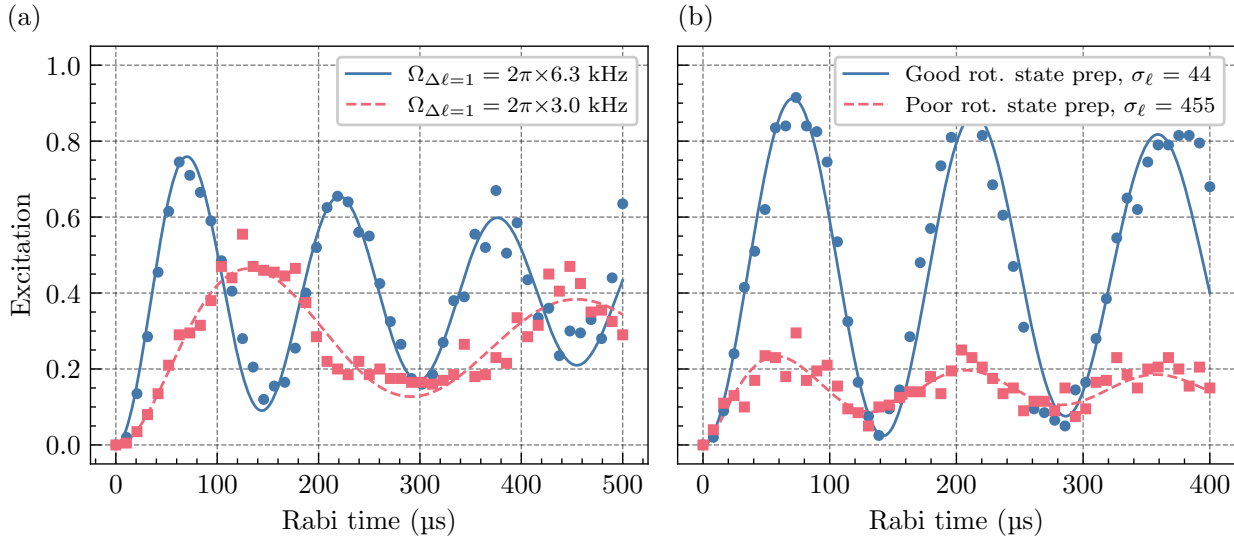


Figure 6.15: Measured Rabi oscillations of rotational sideband transitions. (a) Rabi oscillations on the $\Delta\ell = 1$ transition using the same rotational state preparation but different laser powers to change the Rabi frequency. For comparison to the measured Rabi frequencies, the sideband linewidth here is $\gamma_{\Delta\ell=1} = 2\pi \times 8$ kHz. (b) Rabi oscillations on the $\Delta\ell = 4$ transition using the same Rabi frequency but different rotational state preparation conditions.

a different detuning, which is what gives the $\Delta\ell$ -order sideband a finite linewidth. This is schematically illustrated in Fig. 6.14. The dynamics then follow (3.32), which is convenient to repeat here:

$$P_D(t) = \sum_{\ell} P_{\ell} \frac{\Omega_{\Delta\ell}^2}{\Omega_{\Delta\ell}^2 + \delta_{\ell}^2} \sin^2 \left(\frac{1}{2} \sqrt{\Omega_{\Delta\ell}^2 + \delta_{\ell}^2} t \right). \quad (6.29)$$

6.4.3 Effect of rotational state preparation quality

Importantly, the broader the angular momentum distribution, the more detuned contributions are present in the sum in (6.29), and hence the lower the overall contrast of the Rabi oscillations. In particular, the contrast depends on the ratio of the Rabi frequency $\Omega_{\Delta\ell}$ to the sideband linewidth $\gamma_{\Delta\ell} = 4\omega_r \sigma_{\ell} \Delta\ell$. The contrast of rotational sideband Rabi oscillations may therefore be used as a measure of the angular momentum distribution width. We do this by fitting a measured Rabi oscillation on a rotational sideband to (6.29), with the distribution P_{ℓ} parameterized as

$$P_{\ell}(\sigma_{\ell}) = \frac{1}{\sigma_{\ell} \sqrt{2\pi}} e^{-\frac{1}{2} \left(\frac{\ell - \bar{\ell}}{\sigma_{\ell}} \right)^2}. \quad (6.30)$$

Fig. 6.15 shows measured Rabi oscillations and their fits using these parameters. Figure 6.15(a) demonstrates the effect of the contrast of the oscillations being dependent on

the Rabi frequency. Figure 6.15(b) demonstrates the dependence of the contrast of the oscillations on the quality of rotational state preparation.

The data in Fig. 6.15 is fit to functions of the form (6.29). It should be noted, however, that this is valid only when other modes of motion may be ignored. Since our addressing beam is nearly in the vertical direction, we must in general take into account the state of the vertical vibrational modes. These are typically sideband cooled so as to not hinder rotational operations. Still in general, while the functional form of rotational Rabi oscillations depends on σ_ℓ , they are not always a good measurement of it. This is because σ_ℓ primarily influences the Rabi oscillations via the contrast, which is sensitive to other factors. These include the temperature of the vertical vibrational motion, but also include unintentional detunings from the sideband, which can occur due to AC Stark shifts or due to a discrepancy between the intended and actual rotation frequency, as in e.g. Fig. 6.3. Rotational Rabi oscillations are therefore best used only as a rough estimate of the angular momentum width. A Ramsey measurement can provide a more precise measurement of σ_ℓ .

6.5 Rotational Ramsey experiments

The previous section has shown that when the Rabi frequency of a rotational sideband transition exceeds its linewidth, all angular momentum states which have significant population are near resonance, yielding a coherent Rabi oscillation. In this case, it becomes possible to perform a $\pi/2$ pulse by turning on the laser for time $\pi/2\Omega_{\Delta\ell}$. Taking the laser phase to be zero (such that the Rabi frequency is real), this approximately performs the operation

$$\sum_\ell c_\ell |SS, \ell\rangle \xrightarrow{\text{Pulse } t_{\pi/2} = \frac{\pi}{2\Omega_{\Delta\ell}}} \frac{1}{2} \sum_\ell c_\ell [|SS, \ell\rangle - i|DS, \ell + \Delta\ell\rangle - (-1)^{\Delta\ell} i|SD, \ell + \Delta\ell\rangle - (-1)^{\Delta\ell} i|DD, \ell + 2\Delta\ell\rangle], \quad (6.31)$$

where c_ℓ is the angular momentum space wavefunction, so that $P_\ell = |c_\ell|^2$ in the case of a pure state. Using the conventions for energy offsets defined in (6.26), free evolution of this state (i.e. in the absence of laser coupling) for time T evolves each term according to

$$\begin{aligned} |SS, \ell\rangle &\rightarrow |SS, \ell\rangle \\ |DS, \ell + \Delta\ell\rangle &\rightarrow e^{-i\delta_{1,\ell}T} |DS, \ell + \Delta\ell\rangle \\ |SD, \ell + \Delta\ell\rangle &\rightarrow e^{-i\delta_{1,\ell}T} |SD, \ell + \Delta\ell\rangle \\ |DD, \ell + 2\Delta\ell\rangle &\rightarrow e^{-i(\delta_{1,\ell} + \delta_{2,\ell})T} |DD, \ell + 2\Delta\ell\rangle \end{aligned} \quad (6.32)$$

where $\delta_{1,\ell}$ and $\delta_{2,\ell}$ are given by (6.27). It is convenient to define an overall detuning of the laser from the center of the $\Delta\ell$ sideband, which is approximately $\omega_{\text{rot}}\Delta\ell \approx 2\omega_r\bar{\ell}\Delta\ell$. More precisely, there are two transition frequencies $\omega_r(2\bar{\ell}\Delta\ell + \Delta\ell^2)$ and $\omega_r(2\ell\Delta\ell + 3\Delta\ell^2)$, for

exciting the first and second ion, respectively. Defining the offset is arbitrary, but here we will choose the average of these two, so that

$$\delta \equiv \Delta - \omega_r(2\bar{\ell}\Delta\ell + 2\Delta\ell^2). \quad (6.33)$$

Equation (6.32) then becomes

$$\begin{aligned} |SS, \ell\rangle &\rightarrow |SS, \ell\rangle \\ |DS, \ell + \Delta\ell\rangle &\rightarrow e^{i\omega_r[2(\ell-\bar{\ell})\Delta\ell-\Delta\ell^2]T-i\delta T} |DS, \ell + \Delta\ell\rangle \\ |SD, \ell + \Delta\ell\rangle &\rightarrow e^{i\omega_r[2(\ell-\bar{\ell})\Delta\ell-\Delta\ell^2]T-i\delta T} |SD, \ell + \Delta\ell\rangle \\ |DD, \ell + 2\Delta\ell\rangle &\rightarrow e^{i\omega_r4(\ell-\bar{\ell})\Delta\ell T-2i\delta T} |DD, \ell + 2\Delta\ell\rangle. \end{aligned} \quad (6.34)$$

6.5.1 Rotational Ramsey dephasing

The relative phases evolve at different rates for different values of ℓ , leading to a dephasing in the electronic degree of freedom. Focusing on the phase of the $|DS, \ell + \Delta\ell\rangle$ term in (6.34), the discrepancy in phase between angular momenta ℓ_1 and ℓ_2 is $2\omega_r(\ell_2 - \ell_1)\Delta\ell T$. For an angular momentum distribution whose standard deviation is σ_ℓ , the appreciably occupied angular momentum states span roughly from $\bar{\ell} - \sigma_\ell$ to $\bar{\ell} + \sigma_\ell$, so that the spread of phases across the distribution is roughly $4\omega_r\sigma_\ell\Delta\ell T = \gamma_{\Delta\ell}T$. The timescale of the dephasing is therefore given by the reciprocal of the sideband linewidth $1/\gamma_{\Delta\ell}$. Thus for broader angular momentum distributions or for higher-order sidebands, this dephasing occurs more quickly. These dynamics may be probed with a Ramsey experiment where a second $\pi/2$ pulse is applied after free evolution for time T . Note that this dephasing comes from fully coherent dynamics, and occurs because the measurement traces the state over the rotational degree of freedom.

We may also interpret the Ramsey dephasing from a semi-classical point of view in position space. The superposition $|\ell\rangle + |\ell + \Delta\ell\rangle$ is a superposition of two angular frequencies whose difference is $2\omega_r\Delta\ell$. We interpret this as the ion crystal's orientation being in superposition, with the arms of the superposition separating at angular frequency $2\omega_r\Delta\ell$. If the angular momentum spread is σ_ℓ , then the position-space spread is $1/2\sigma_\ell$ radians by the uncertainty principle. It therefore takes a time $T = (1/2\sigma_\ell)/(2\omega_r\Delta\ell) = 1/4\omega_r\sigma_\ell\Delta\ell = 1/\gamma_{\Delta\ell}$ for the position-space wavepackets to no longer overlap each other. The separation in position space becomes manifested in the dephasing of the electronic state. It should be noted however that the true quantum evolution in position space involves dispersion of the wavepacket across the entire rotor, so the picture of two well-defined orientations in superposition is not strictly correct.

It is worth noting explicitly here that, while the results of this section (the Ramsey dephasing dynamics) and those of Sec. 6.4 (Rabi oscillations) both show that the dynamics are sensitive to the angular momentum spread, they do not assume the angular momentum wavefunction to be a pure state. The same results apply in both cases for an incoherent mixture or a pure state. This is because as long as a single $\Delta\ell$ sideband is addressed within

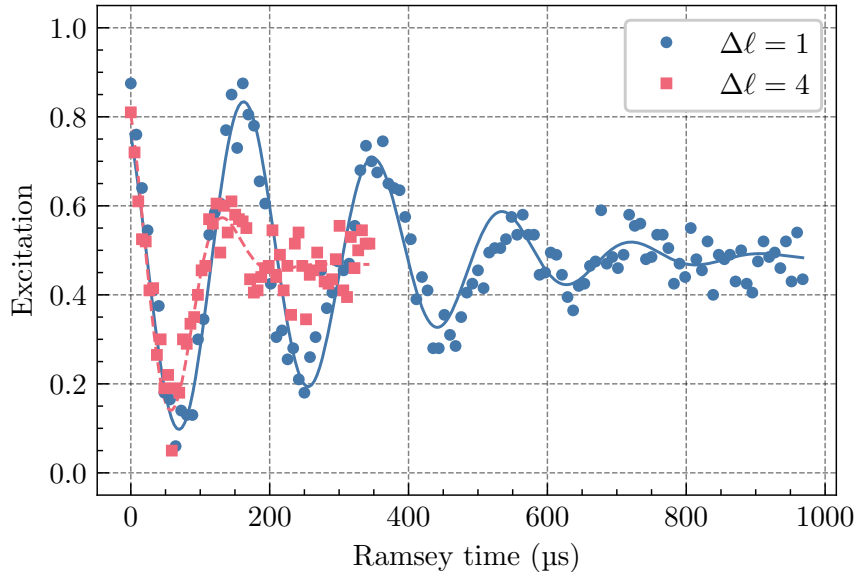


Figure 6.16: Measurements of rotational Ramsey dephasing on the $\Delta\ell = 1$ and $\Delta\ell = 4$ sidebands, using identical rotational state preparation. Here, $\omega_r = 6.2$ Hz. Both curves are fit to $\sigma_\ell = 36$. This data is published in Ref. [41], where the fitting function used was slightly different and thus yielded a slightly different value of σ_ℓ .

an experiment, the coherences between angular momentum states do not factor in. This can be traced back to the terms of the Hamiltonian (6.26) all commuting with one another: $[H_\ell, H_{\ell'}] = 0$.

Measurements and utility as a measurement of rotational state preparation quality

Fig. 6.16 shows a measurement of the Ramsey dephasing for $\Delta\ell = 1$ and $\Delta\ell = 4$ superpositions. In both cases, an overall detuning of about 6 kHz is used to see fringes. We expect the shape of the decay to be Gaussian, as it should be the Fourier transform of the underlying angular momentum distribution causing the dephasing, which we assume to be Gaussian. The data in Fig. 6.16 are fit to a function of the form

$$P_D(T) = \frac{1}{2} \left[e^{-(2\omega_r\sigma_\ell\Delta\ell T)^2/2} \cos(\delta T) + 1 \right], \quad (6.35)$$

with additional parameters to account for imperfect overall contrast and phase offsets. The shape of the measured decay is consistent with this Gaussian shape. Furthermore, the value of σ_ℓ for the two curves agree, i.e. the Ramsey contrast of the $\Delta\ell = 4$ sideband decays 4 times faster than that of the $\Delta\ell = 1$ sideband, as expected.

The rotational Ramsey decay rate makes for a reliable measurement of the angular momentum spread. The rate of dephasing is directly proportional to σ_ℓ , which is the only

unknown parameter. Factors that could be convolved with the contribution of σ_ℓ when measuring using Rabi oscillations are instead easily distinguished when measuring using Ramsey measurements: A finite temperature reduces only the overall contrast, and a detuning only changes the frequency of the fringes. Both of these are independent of the rate of dephasing which encodes σ_ℓ . This is the method by which the measurements of σ_ℓ in Fig. 6.9 were made.

6.5.2 Rotational Ramsey rephasing

At time $T = \pi/\omega_r\Delta\ell$, the phases of all terms in (6.34) differ by exactly a multiple of 2π . A rephasing should therefore be expected to occur at this time. In the semi-classical picture of a superposition of separating orientations, this time corresponds to the time it takes for the two different orientations to separate by 2π radians and thus overlap again. This experiment has not yet been performed, but considerations regarding it are the subject of Chapter 8. It has thus far been hindered by decoherence of angular momentum superpositions, which is the subject of Chapter 7.

Chapter 7

Decoherence of rotational superpositions

The utility of any non-classical superposition state is limited by its coherence time. For superpositions of angular momenta in the trapped-ion rotor, a simple Ramsey experiment does not suffice to measure coherence. This is due to the dephasing dynamics discussed in Sec. 6.5.1, which occur even with perfect unitary evolution. Instead, to measure the coherence of angular momentum superpositions, we insert a Hahn-echo π pulse at the center of the Ramsey time to reverse the free evolution. This measurement is described in more detail in Sec. 7.1. Figure 7.1 shows two sample measurements, for $\Delta\ell = 1$ and 4, of the rotational coherence. We find that the coherence lasts on the order of a few milliseconds, and decays faster for higher-order superpositions.

In the process of investigating the cause of rotational decoherence, we have considered several potential sources and estimated the magnitude of their impact. These are described in Sec. 7.2. The particular source of decoherence which has proven to be the limiting factor in our experiment, angular momentum diffusion, is expanded upon further in Secs. 7.3 and 7.4.

7.1 Protocol for measuring coherence of rotational superpositions

The full protocol for measuring rotational coherence is as follows:

- Rotational state preparation
- $\pi/2$ pulse: 729 nm laser pulse on the $\Delta\ell$ sideband for time $t_{\pi/2} = \pi/2\Omega_{\Delta\ell}$
- Wait for time $T/2$
- π pulse: 729 nm laser pulse on the $\Delta\ell$ sideband for time $t_\pi = \pi/\Omega_{\Delta\ell}$

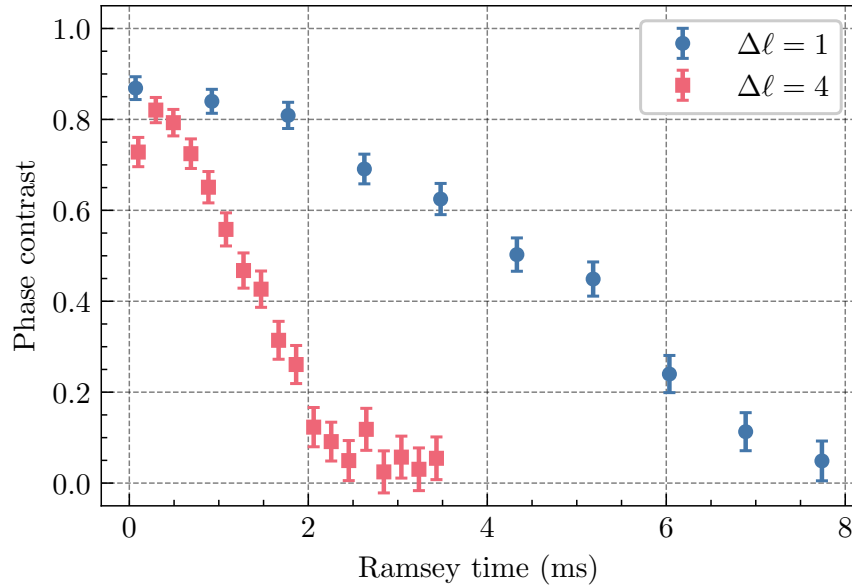


Figure 7.1: Coherence measurement of angular momentum superpositions of orders $\Delta\ell = 1$ and 4. Here the ion crystal is rotating at approximately 100 kHz and has a rotational constant of $\omega_r = 2\pi \times 6.2$ Hz.

- Wait for time $T/2$
- $\pi/2$ pulse on the $\Delta\ell$ sideband with some arbitrary phase ϕ .

For most precise measurements, we scan the phase of the final pulse from 0 to 2π before incrementing the Ramsey time T . The coherence at a given Ramsey time is quantified by the phase contrast. This way, phase shifts which occur during the experiment (but which are the same for every repetition) do not affect the results. The alternative way to see full phase contrast is to add a detuning to the pulses so that the relative phase of the final pulse oscillates as the Ramsey time is scanned, as for example in Fig. 6.16. We find that full phase scan measurements are helpful when Ramsey times exceed ~ 1 ms.

We find in our experiment that the local magnetic field drifts with the phase of the AC electrical wall power, causing dephasing of the electronic $|S\rangle \leftrightarrow |D\rangle$ transition, whose transition frequency depends on the magnetic field. The total period is $1/(60\text{ Hz}) = 16.7$ ms, and magnetic field dephasing effects become significant after $2 - 3$ ms. Thus for any experiment which lasts longer than ~ 2 ms and relies on electronic coherence, we synchronize the start of each repetition of the experiment to the wall phase to eliminate this effect.

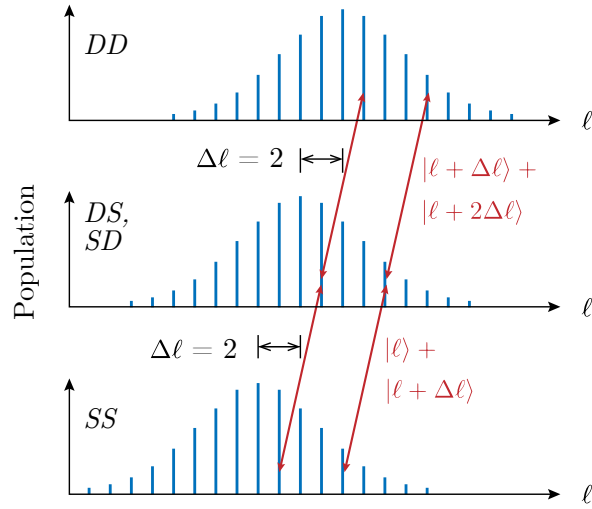


Figure 7.2: Schematic of the state of the system after the first $\pi/2$ pulse in a Ramsey experiment for $\Delta\ell = 2$. Red arrows show some of the coherences which are probed by the laser.

7.1.1 The rotational coherence measurement protocol as a measure of pure superpositions of angular momentum eigenstates

We claim that the measurement protocol outlined in this section is a measure of the coherence of pure angular momentum superpositions, i.e. $|\ell\rangle + |\ell + \Delta\ell\rangle$. This may not be immediately obvious given that the initial state of our rotor is typically spread across many values of ℓ , and that this spread ($\sim 20 - 40$) is in fact much larger than $\Delta\ell$ (1 – 4). To see this, we may recall the picture of the rotor in superposition as an ensemble of non-interacting 4-level manifolds containing states $\{|SS, \ell\rangle, |DS, \ell + \Delta\ell\rangle, |SD, \ell + \Delta\ell\rangle, |DD, \ell + 2\Delta\ell\rangle\}$, offered in Secs. 6.4 and 6.5. The $\pi/2$ and π pulses induce transitions only within these manifolds, and thus the measurement only sensitive to the coherences within them. Figure 7.2 shows this schematically, indicating that the only coherences probed by the laser are those of the fixed value $\Delta\ell$. The values of ℓ for these manifolds are spread across a range given by σ_ℓ , and are centered at $\bar{\ell} > 10^3$. Therefore, unless the nature of some decoherence source changes significantly across values of ℓ which are spread by $\sigma_\ell/\bar{\ell} \sim 1\%$, the angular momentum spread will not have any impact on its effect, and we may regard the measured decoherence as being due to a simple superposition of the form $|\ell\rangle + |\ell + \Delta\ell\rangle$.

7.1.2 The 4-level contrast oscillation effect

Ideally, the Ramsey experiment with a spin-echo pulse included would reverse all detunings, resulting in a rephasing and thus effectively applying the identity operation overall in the

absence of decoherence. This is usually approximately the case, but the small discrepancy between the transition frequencies of $|\ell\rangle \rightarrow |\ell + \Delta\ell\rangle$ and $|\ell + \Delta\ell\rangle \rightarrow |\ell + 2\Delta\ell\rangle$ results in interference of the phases acquired by these two superpositions, which in turn affects the overall phase contrast. It is important to understand this effect so that it may be differentiated from true decoherence in a measurement.

Oscillations in the excitation contrast

We may compute the full time-evolution operator of the rotational-Ramsey-with-spin-echo protocol using the Hamiltonian (6.26). At each step in the protocol we compute the corresponding time-evolution operator as $e^{-iH(\Omega_{\Delta\ell})t}$, where $t = t_{\pi/2}$ for the initial and final pulses, $t = t_\pi$ for the echo pulse, and $t = T/2$ for the Ramsey wait times. During the wait times, $\Omega_{\Delta\ell} = 0$. The final $\pi/2$ pulse has a phase ϕ relative to the first. For a simpler calculation, we may assume that the operations are perfect ($\Omega_{\Delta\ell} \gg \delta_{1,2,\ell}$) so that $\delta_{1,2,\ell} = 0$ during the pulses. The full time-evolution operator U is computed as the product of that for each step. It is easiest to do this individually for each term ℓ , so that $U = \prod_\ell U_\ell$. Explicitly,

$$U_\ell = e^{-iH_\ell(\Omega_{\Delta\ell}e^{i\phi})t_{\pi/2}}e^{-iH_\ell(0)T/2}e^{-iH_\ell(\Omega_{\Delta\ell})t_\pi}e^{-iH_\ell(0)T/2}e^{-iH_\ell(\Omega_{\Delta\ell})t_{\pi/2}}. \quad (7.1)$$

For an initial state $\sum_\ell c_\ell |SS, \ell\rangle$, we can then compute the final state probabilities:

$$\begin{aligned} P_{SS} &= \sum_\ell |c_\ell|^2 |\langle SS, \ell | U_\ell | SS, \ell \rangle|^2 = \frac{1}{4} \left[1 + 2 \cos(\phi) \cos\left(\frac{\delta_{2,\ell} - \delta_{1,\ell}}{2} T\right) + \cos^2(\phi) \right] \\ &\quad = \frac{1}{4} [1 + 2 \cos(\phi) \cos(\Delta\ell^2 \omega_r T) + \cos^2(\phi)] \\ P_{DS} &= \sum_\ell |c_\ell|^2 |\langle DS, \ell | U_\ell | SS, \ell \rangle|^2 = \frac{1}{2} \sin^2(\phi) \\ P_{SD} &= \sum_\ell |c_\ell|^2 |\langle SD, \ell | U_\ell | SS, \ell \rangle|^2 = \frac{1}{2} \sin^2(\phi) \\ P_{DD} &= \sum_\ell |c_\ell|^2 |\langle DD, \ell | U_\ell | SS, \ell \rangle|^2 = \frac{1}{4} \left[1 - 2 \cos(\phi) \cos\left(\frac{\delta_{2,\ell} - \delta_{1,\ell}}{2} T\right) + \cos^2(\phi) \right] \\ &\quad = \frac{1}{4} [1 - 2 \cos(\phi) \cos(\Delta\ell^2 \omega_r T) + \cos^2(\phi)]. \end{aligned} \quad (7.2)$$

The difference $\delta_{2,\ell} - \delta_{1,\ell}$ is equal to $2\Delta\ell^2 \omega_r$, independent of ℓ . Excitation is computed as

$$E = \frac{1}{2}(2P_{DD} + P_{DS} + P_{SD}), \quad (7.3)$$

and the excitation contrast is the difference between the minimum and maximum values of the excitation as ϕ is swept from 0 to 2π , which is given by

$$C = |\cos(\Delta\ell^2 \omega_r T)|. \quad (7.4)$$

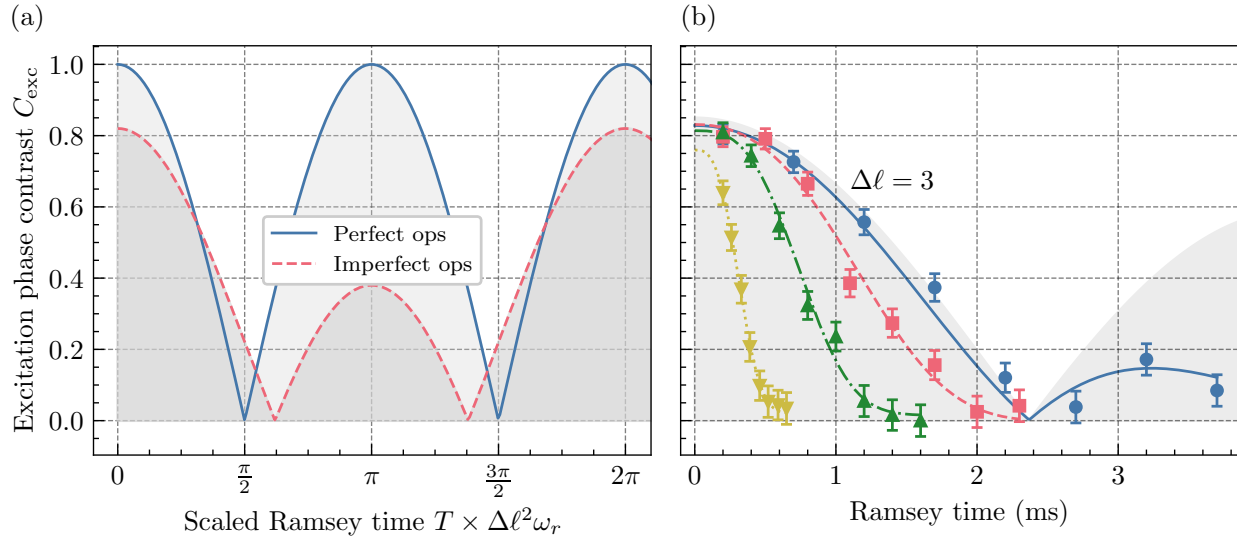


Figure 7.3: (a) Simulated excitation phase contrast in a rotational Ramsey experiment with a spin echo, for the cases of perfect and imperfect rotational sideband operations. The shaded regions show the range of possible phase contrasts which may be measured if decoherence is present. (b) Sample decoherence measurements with $\Delta\ell = 3$, with the corresponding expected contrast oscillation envelope shown. Here $\omega_r = 2\pi \times 13 \text{ Hz}$.

Thus the full phase contrast is in fact modulated at the frequency $\Delta\ell^2\omega_r$, which is equal to half the difference in transition frequencies between $|\ell\rangle \rightarrow |\ell + \Delta\ell\rangle$ and $|\ell + \Delta\ell\rangle \rightarrow |\ell + 2\Delta\ell\rangle$. This effect produces a node in the contrast at time $T = \pi/2\Delta\ell^2\omega_r$, which could be mistaken for decoherence. This effect becomes rapidly more pronounced as $\Delta\ell$ is increased: For $\omega_r = 2\pi \times 10 \text{ Hz}$, the node occurs at $T = 25 \text{ ms}$ for $\Delta\ell = 1$, and $T = 1.6 \text{ ms}$ for $\Delta\ell = 4$.

Equation (7.4) assumes perfect operations. Relaxing this assumption makes it difficult to obtain a closed-form solution, but numerical simulations suggest that the contrast oscillations are affected by the quality of operations. In particular, lowering the initial contrast increases the Ramsey time at which the first node occurs. Therefore, imperfect operations cannot be accounted for by simply multiplying (7.4) by a constant factor less than unity; numerical simulations are necessary to predict the node time. The simulations are done by implementing the time-evolution operator (7.1) without assuming the detunings to be zero during the Rabi pulses. Empirically, the numerically simulated contrast follows the form

$$C = |(a + b) + (a - b) \cos(\Delta\ell^2\omega_r T) - 1|, \quad (7.5)$$

where a and b are empirical parameters. For perfect operations, $a = 1$ and $b = 0$. As an example, Fig. 7.3(a) shows the simulated phase contrast for the case of perfect operations and for the case where $\Omega_{\Delta\ell}/\gamma_{\Delta\ell} = 1$, whose corresponding Rabi oscillations have an initial contrast of 0.81, independent of $\Delta\ell$. The simulated phase contrast for the case of imperfect contrast is well-modeled by (7.5) with $a = 0.91$ and $b = 0.31$. In this case, imperfect

operations are thus predicted to increase the time of the first node by a factor of 1.2. In the presence of decoherence, the measured phase contrast must lie somewhere within the corresponding shaded region. Figure 7.3(b) demonstrates this effect with data. A sample of measured decoherence curves for $\Delta\ell = 3$ is shown, with fits of the form $C(T) = C_0 e^{-(\gamma T)^3}$ (see Sec. 7.4 for the motivation for this choice of coherence decay function), additionally multiplied by the envelope (7.5) accounting for the imperfect operations. If the coherence time is long enough, then it is necessary to take into account the contrast oscillation effect in order to properly estimate the underlying decoherence rate γ .

The parity contrast

In principle, the contrast oscillation effect only appears to be indistinguishable from true decoherence because of the choice of excitation as the observable. One may instead choose a different observable, for example the parity, defined as

$$\Pi = P_{SS} + P_{DD} - P_{DS} - P_{SD}. \quad (7.6)$$

The parity is effectively a measure of the coherence between the $|SS, \ell\rangle$ and $|DD, \ell + 2\Delta\ell\rangle$ terms of the superposition, as opposed to between the terms which differ by only $\Delta\ell$. From (7.2), we find that the parity is simply $\cos^2(\phi)$, and therefore the parity contrast is always unity in the absence of decoherence: $C_{\text{par}} = 1$. Choosing the parity as the observable should therefore circumvent the contrast oscillation effect. However, in this work the excitation is always chosen as the observable.

7.2 Potential sources of rotational decoherence

7.2.1 Electronic coherence

The rotational coherence measurement protocol entangles the rotational state with the electronic state. Thus if the electronic state decoheres, due to for example magnetic field fluctuations or laser instability, then a loss in phase contrast will be measured. This will translate directly to decoherence in a rotational coherence measurement. Figure 7.4 shows a coherence measurement on the carrier transition using a single ion. Here, the superposition $|S_{1/2}(m = -1/2)\rangle + |D_{5/2}(m = -1/2)\rangle$ is created. This experiment uses a spin-echo π pulse in the middle of the Ramsey sequence for best comparison to the rotational coherence measurements. The coherence lasts for more than 30 ms, which is much longer than measured rotational coherence times. For minimized sensitivity to electronic decoherence due to magnetic field fluctuations, the $S_{1/2}(m = \pm 1/2) \leftrightarrow D_{5/2}(m = \pm 1/2)$ transition is always used when creating rotational superpositions.

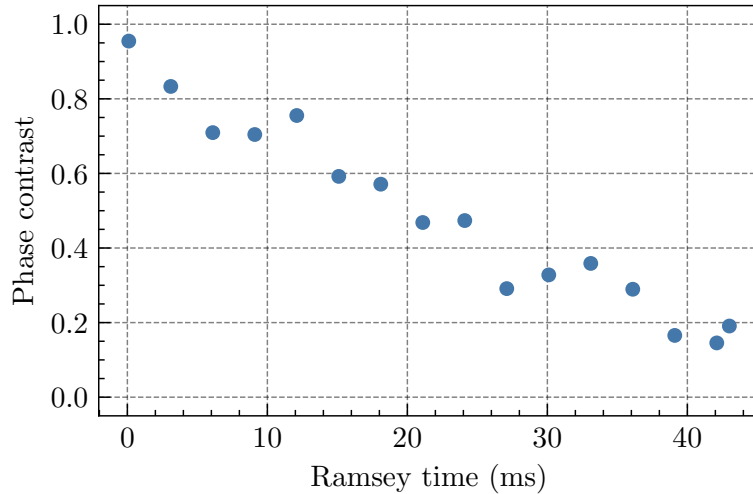


Figure 7.4: Measurement of electronic coherence with spin-echo included, using a single ion in the $|S_{1/2}(m = -1/2)\rangle + |D_{5/2}(m = -1/2)\rangle$ superposition.

7.2.2 Slowly drifting residual static quadrupole fields

Static voltages on the DC electrodes are used to compensate stray fields such that the potential landscape for the rotor is as flat as possible in the absence of an applied pinning potential. Since a stray dipole field will physically move the ions into a new potential minimum, the lowest-order multipole component of possible stray fields in the rotor potential is quadrupole fields. A stray quadrupole field in the rotor may be described by the potential

$$\Phi(\theta) = \Phi_0 \sin^2 \theta. \quad (7.7)$$

We measure the magnitude of stray quadrupoles by measuring the frequency of the horizontal rocking mode $\omega_{hr,\text{resid}}$ with no pinning potential applied, which is related to the magnitude of the stray quadrupole by

$$\omega_{hr,\text{resid}} = 2\sqrt{\frac{\Phi_0 \omega_r}{\hbar}}. \quad (7.8)$$

This relation is also given in (6.10), where the only difference is that in (6.10), the quadrupole potential is intentional.

A typical minimum achievable magnitude of stray quadrupole is such that $\omega_{hr,\text{resid}} \approx 2\pi \times 20 \text{ kHz}$. The corresponding potential height is much smaller than rotational energies when the rotor rotates at frequencies on the order of 100 kHz, so this stray quadrupole does not hinder rotation. However, it does act as a perturbation to the rotational energies. Using perturbation theory, the first-order energy perturbation of (7.7) to an otherwise free rotor is $\Phi_0/2$, independent of ℓ and thus has no effect on transition frequencies. For large ℓ (compared to 1), the second-order perturbing energy term is

$$\delta E_\ell^{(2)} = \frac{\Phi_0^2}{64\hbar\omega_r\ell^2}. \quad (7.9)$$

This is a function of ℓ and thus will affect rotational transition frequencies. We can compute that the residual quadrupole changes the transition frequency by

$$\delta\omega_{\ell,\ell+\Delta\ell} = \frac{\Phi_0^2 \Delta\ell}{32\hbar^2 \omega_r \ell^3} = \frac{\omega_{hr,\text{resid}}^4}{64\omega_{\text{rot}}^3} \Delta\ell, \quad (7.10)$$

where the second equality uses the relations (7.8) and $\omega_{\text{rot}} = 2\omega_r \ell$.

The presence of a truly static residual quadrupole field will only shift the rotational energies and transition frequencies; if these remain constant, then it will not result in decoherence. If on the other hand the magnitude of the residual quadrupole drifts, then the rotational transition frequency will change, resulting in dephasing. Assuming a fairly extreme residual quadrupole magnitude drift of 50%, the resulting drift in transition frequency is roughly $5 \text{ Hz} \times \Delta\ell$ for 100 kHz rotation frequency. This corresponds to dephasing times on the order of 100 ms (if $\Delta\ell$ is not too large), and longer if the rotation frequency is faster. This effect is therefore small in comparison to measured coherence times.

7.2.3 Rotational coupling to stretch and vertical rocking motion

Centrifugal distortion of the rotor results in coupling between the rotational motion and the stretch and vertical rocking motion, as discussed in Sec. 3.5. This in turn causes the energy eigenspectrum to be non-separable in the quantum numbers of the respective modes, given by (3.61). The rotational transition frequency then depends on the state of the stretch and rotational modes, which when in some thermal distribution would be expected to cause a spread in rotational transition frequencies and thus rotational dephasing. To estimate the magnitude of this effect, we compute the transition frequency between $|\ell\rangle$ and $|\ell + \Delta\ell\rangle$ using (3.61):

$$\omega_{\ell,\ell+\Delta\ell}(n_s, n_{vr}) \approx 2\omega_r \ell \Delta\ell \left(1 - 2\epsilon_\ell + \frac{2\omega_r n_s}{\omega_s} + \frac{2\omega_r n_{vr}}{\omega_{vr}} \right), \quad (7.11)$$

so that the contribution to the transition frequency from the stretch and rocking motion is

$$\delta\omega_{\ell,\ell+\Delta\ell} \approx 2\omega_r \ell \Delta\ell \left(\frac{2\omega_r}{\omega_s} n_s + \frac{2\omega_r}{\omega_{vr}} n_{vr} \right). \quad (7.12)$$

For both the stretch and vertical rocking modes, the fractional change in rotational transition frequency is $2\omega_r n_j / \omega_j$.

- *Stretch:* The factor $2\omega_r n_s / \omega_s$ is roughly $10^{-5} n_s$. Assuming that the stretch mode is at the Doppler temperature occupies a spread of 10^2 Fock states, the fractional change in rotational transition frequency is 10^{-3} , or an absolute spread of $100 \text{ Hz} \times \Delta\ell$ for 100 kHz rotation, yielding a dephasing time of roughly 10 ms. This has not been observed to be a limiting factor, but if it does become one, a simple solution is to sideband cool the stretch motion.

- *Vertical rocking:* The vertical rocking mode is typically sideband cooled and thus will contribute very little to this effect. It should be noted however that if the vertical and horizontal COM secular frequencies are close to each other, then this mode frequency can be small, enhancing this effect. For this to become comparable to the contribution from the stretch mode (when the stretch motion is not sideband cooled), the vertical rocking mode frequency would need to be reduced by a factor of roughly 10^2 , or down to the order of 10 kHz.

7.2.4 Trap frequency instability

The energy scale of the rotational eigenspectrum is set by the rotational constant: $E_\ell = \hbar\omega_r \ell^2$. The rotational constant is inversely proportional to the square of the rotor radius, which is set directly by the horizontal COM secular frequency. Therefore, instabilities in the horizontal trap frequency will cause rotational dephasing. Explicitly,

$$\omega_r = \left(\frac{4\pi^2 \hbar^3 \epsilon_0^2}{me^4} \right)^{1/3} \omega_x^{4/3} = (4.36 \times 10^{-8} \text{ s}^{1/3}) \omega_x^{4/3}. \quad (7.13)$$

The $\Delta\ell$ transition frequency is

$$\omega_{\ell,\ell+\Delta\ell} = 2\omega_r \ell \Delta\ell \quad (7.14)$$

for $\ell \gg \Delta\ell$ so that $\Delta\ell^2$ terms can be neglected. If the trap frequency changes by $\delta\omega_x$, this will cause a change in the rotational constant $\delta\omega_r$ according to (7.13), which shifts the rotational transition frequency according to (7.14) by

$$\delta\omega_{\ell,\ell+\Delta\ell} = \frac{4\omega_{\text{rot}}}{3\omega_x} \delta\omega_x \Delta\ell, \quad (7.15)$$

where the relation $\omega_{\text{rot}} = 2\omega_r \ell$ has been used. This directly relates the timescale of dephasing of the horizontal COM vibrational motion $1/\delta\omega_x$ to the timescale of dephasing of a rotational superposition $1/\delta\omega_{\ell,\ell+\Delta\ell}$. The former is straightforwardly measured by preparing a superposition $|0\rangle + |1\rangle$ of the horizontal COM mode and measuring its decoherence. This can be done using only a single ion. We prepare this superposition disentangled from the vibrational superposition using the pulse sequence shown in Fig. 7.5. This measurement requires ground-state cooling. The measured timescale of the decoherence is 32 ms at a trap frequency of 1.45 MHz. For a conservatively high rotation frequency of 300 kHz, this corresponds to an inferred rotational coherence time of $120 \text{ ms}/\Delta\ell$, much longer than our measured rotational coherence times.

7.2.5 Angular momentum diffusion

A mechanism which torques the rotor will result in transitions between angular momentum states. If these angular momentum kicks are random and are also equally likely to increase or decrease the angular momentum, the result is a random walk in angular momentum

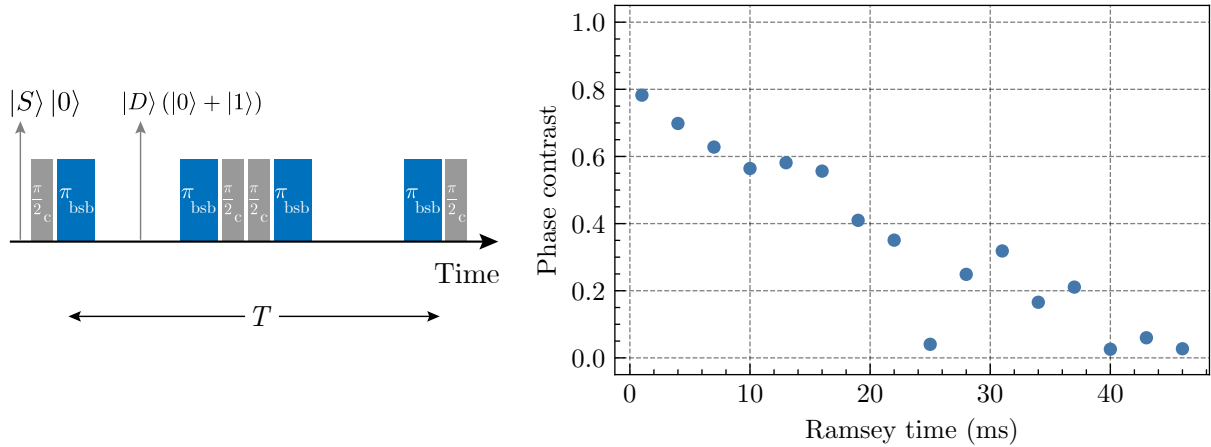


Figure 7.5: Coherence measurement of the transverse vibrational motion using a single trapped ion. Left: Pulse sequence for the measurement, using composite combinations of pulses. $\pi/2_c$ refers to a $\pi/2$ pulse on the carrier transition, and π_{bsb} refers to a π pulse on the blue sideband of the mode being measured. A composite echo pulse is included to reproduce the conditions of the rotational coherence measurements. Right: Measurement of the stability of the horizontal motion. The motional coherence lasts for approximately 32 ms.

space. Over time and averaged over many realizations, this diffuses the angular momentum state, increasing the spread σ_ℓ . The random nature of the angular momentum kicks makes the process incoherent, therefore leading to decoherence of the rotor state. Theoretical derivation of the Lindblad master equation corresponding to this situation, as well as its consequences, has taken place recently in the literature [42–44].

For the work done in this thesis, angular momentum diffusion has been the limiting factor for rotational coherence. To show this, we have performed a systematic study of diffusion-limited decoherence of our rotor. Sec. 7.3 discusses angular momentum diffusion as it pertains to the trapped-ion rotor, and Sec. 7.4 discusses the resulting decoherence.

7.3 Angular momentum diffusion

7.3.1 The ion-field interaction Hamiltonian

Angular momentum diffusion occurs in our trapped-ion rotor as a result of noisy electric fields. In order to cause angular momentum kicks, the noise must be resonant with the rotation. This is analogous to heating of the center-of-mass motion discussed in Sec. 5.1. To see this, we can begin with the multipole expansion of an arbitrary electric field interacting with the ions, as given by (5.1). Here, we have two ions, with positions \mathbf{r}_1 and \mathbf{r}_2 . The

Hamiltonian for interaction with this potential is

$$\begin{aligned} H_E(t) = e\Phi(\mathbf{r}_1, t) + e\Phi(\mathbf{r}_2, t) &= 2e\Phi(0, t) - e\mathbf{r}_1 \cdot \mathbf{E}(0, t) - \frac{e}{2} \sum_{j,j'} r_{1j} r_{1j'} \frac{\partial E_j}{\partial r_{1j'}}(0, t) + \dots \\ &\quad - e\mathbf{r}_2 \cdot \mathbf{E}(0, t) - \frac{e}{2} \sum_{j,j'} r_{2j} r_{2j'} \frac{\partial E_j}{\partial r_{2j'}}(0, t) + \dots \end{aligned} \quad (7.16)$$

In this case, we will find that we need to keep the field gradient terms. The first term is constant in space and thus does not contribute any force. It is convenient to make a coordinate transformation into center-of-mass and relative coordinates $\mathbf{R} = (\mathbf{r}_1 + \mathbf{r}_2)/2$ and $\mathbf{r} = \mathbf{r}_1 - \mathbf{r}_2$. Substituting these new coordinates into (7.16), we find that the terms fully separate into center-of-mass terms and relative terms. Since we are interested only in the rotational motion, which is a relative mode, we may ignore the center-of-mass terms. We find that the $\mathbf{r}_i \cdot \mathbf{E}$ terms contribute only to the center-of-mass terms in the new coordinates, leaving us only with the field gradient terms. The remaining terms, when expanded out for each coordinate, are

$$\begin{aligned} H_{E,\text{rel}}(t) &= -\frac{e}{4} \left(x^2 \frac{\partial E_x}{\partial x} + y^2 \frac{\partial E_y}{\partial y} + z^2 \frac{\partial E_z}{\partial z} \right) \\ &\quad - \frac{e}{2} \left(xy \frac{\partial E_x}{\partial y} + yz \frac{\partial E_y}{\partial z} + xz \frac{\partial E_z}{\partial x} \right). \end{aligned} \quad (7.17)$$

Next, we transform into cylindrical coordinates, as done in Sec. 3.3.1. The radial and angular coordinates ρ and θ replace x and y as $\rho \cos \theta = x$, $\rho \sin \theta = y$. We furthermore write all coordinates in terms of ladder operators for their respective relative modes:

$$\begin{aligned} \rho &= \rho_e + \sqrt{\frac{\hbar}{2\mu\omega_s}} (a_s + a_s^\dagger) \\ \cos \theta &= \frac{1}{2} (L_+ + L_-) \\ \sin \theta &= \frac{1}{2i} (L_+ - L_-) \\ z &= \sqrt{\frac{\hbar}{2\mu\omega_{vr}}} (a_{vr} + a_{vr}^\dagger). \end{aligned} \quad (7.18)$$

The subscripts s and vr refer to the stretch and vertical rocking modes. Since we are using relative coordinates as in Sec. 3.3.1, this has been written in terms of the relative equilibrium radius ρ_e (which is equal to twice the true radius $2r$) and in terms of the reduced mass μ (which is equal to half the mass of one ion $m/2$). Substituting into (7.17), we find that the dominant terms involving rotational operators emerge from the x^2 , y^2 , and xy terms. In

total these are

$$H_{E,\text{rot}}(t) = \frac{e\rho_e^2}{16} [\mathcal{E}(t)L_+^2 + \mathcal{E}(t)^*L_-^2] = \frac{er^2}{4} [\mathcal{E}(t)L_+^2 + \mathcal{E}(t)^*L_-^2], \quad (7.19)$$

where $\mathcal{E} = -\partial_x E_x + \partial_y E_y + 2i\partial_y E_x$. This indicates that circularly polarized electric field gradients can kick the angular momentum up or down in units of $2\hbar$. There are also terms which couple the rotational motion to the stretch and vertical rocking motion, but these are suppressed by a factor of $\sqrt{\hbar/2\mu\omega_j}/r \sim 10^{-2}$. Such rovibrational heating is considered later in Sec. 8.4.3.

7.3.2 The diffusion coefficient

The Hamiltonian (7.19) kicks the angular momentum up and down with equal coupling strength. Thus if the electric field is noisy, we expect this to lead to angular momentum diffusion. This can be expressed in terms of the diffusion coefficient D , defined by the rate of increase of the variance of the angular momentum state: $\frac{d}{dt}\langle L_z^2 \rangle = 2D$. Under diffusion, the dimensionless angular momentum standard deviation σ_ℓ will increase with time according to

$$\sigma_\ell(t) = \sqrt{\sigma_\ell(0)^2 + \frac{2Dt}{\hbar^2}}. \quad (7.20)$$

To show that the interaction (7.19) leads to angular momentum diffusion, we can perform a similar treatment to that outlined in Sec. 5.1, where we transform into the interaction picture and compute the transition rate between eigenstates. The result is angular momentum diffusion with diffusion coefficient

$$D = \left(\frac{er^2}{2}\right)^2 S_\mathcal{E}(2\omega_{\text{rot}}), \quad (7.21)$$

where $S_\mathcal{E}(2\omega_{\text{rot}}) = 2 \int_{-\infty}^{\infty} d\tau \langle \mathcal{E}(t)\mathcal{E}(t+\tau) \rangle e^{-i2\omega_{\text{rot}}t}$ is the power spectral density of the relevant circularly polarized field gradient at twice the rotation frequency. The derivation of this result can be found in [45]. To summarize some noteworthy points about the result:

- The quadrupole moment for the interaction of the rotor with the field gradient is $er^2/2$. This is large compared to the corresponding quadrupole moment for vibrational differential modes in typical trapped ion crystals by a factor of the rotor radius divided by the spatial extent of the ground state wavefunction of the vibrational mode. Thus in a sense, angular momentum diffusion occurs faster than heating of an analogous vibrational mode. Section 7.3.3 quantifies this comparison.
- Unlike a harmonic mode, the transition frequency for a rotor depends on its state. This manifests in the interaction picture transformation, where L_+ in the interaction picture is given by (3.28), repeated here for convenience:

$$\tilde{L}_+(t) = \sum_\ell e^{i(2\ell+1)\omega_r t} |\ell+1\rangle\langle\ell|. \quad (7.22)$$

It was therefore necessary to also assume the following to derive (7.21):

- The rotor state is localized in angular momentum.
- The bandwidth of the noise is larger than the spread of rotation frequencies, so that the noise power spectral density is approximately constant across this spread, allowing the diffusion coefficient to be expressed as a function of only a single spectral density.
- Resonance occurs when the noise field oscillates at twice the rotation frequency. The intuition for why this should be is as follows: The rotor has a 180° rotational symmetry, and thus effectively returns to its original orientation after half of a rotation period. The noise must therefore oscillate at twice the rotation frequency to be resonant. See also Fig. 7.6. A noise field which oscillates at the rotation frequency would always speed up the rotor during half of a rotation and slow it down during the other half, and thus would not be resonant. In general, a rotor with N -fold rotational symmetry would be sensitive to noise at frequency $N\omega_{\text{rot}}$.

Fig. 7.6 provides a visualization of resonant field gradients that can cause diffusion. In both cases, the field co-rotates with the ions, but the phase of the rotation differs in the two examples. In (a), the field direction at the location of the ions matches their direction of rotation, thus speeding the rotor up. In (b), the field direction is the opposite of the direction of rotation, slowing the rotor down. Noise (by definition) is a randomization of this phase, so the overall effect is diffusion. Note that a linearly polarized noisy field gradient may be written as a sum of two oppositely-rotating circularly polarized field gradients. Only the component which is co-rotating with the rotor will contribute to diffusion.

7.3.3 Comparison to the heating rate of rocking modes

As discussed in Sec. 5.1.1, differential modes of motion of a trapped-ion crystal (where ions move relative to each other, as opposed to center-of-mass modes) are sensitive to electric field gradients. The crystal's motion couples to these gradients via a quadrupole moment, which for a vibrational mode of motion is proportional to the ion-ion distance times the ground-state wavefunction size, $Q \sim r\sqrt{\hbar/2m\omega_j}$. The former is typically of order $1\text{ }\mu\text{m}$ and the latter is typically of order 10 nm . The resulting heating rate is proportional to the square of this quadrupole moment.

In comparison, the rotor spans a much larger region of space than the motion of a pinned ion crystal. The quadrupole moment for the rotor coupling to electric field gradient noise is proportional to r^2 , and is thus significantly larger. The rate of diffusion, D/\hbar , proportional to the square of the quadrupole moment, is therefore a factor of $\sim 10^4$ times that of a comparable differential vibrational mode of motion, e.g. the horizontal rocking mode when the crystal is pinned. Therefore, while the heating rate of a differential vibrational mode of motion is often negligible, the rate of diffusion of the rotor is not.

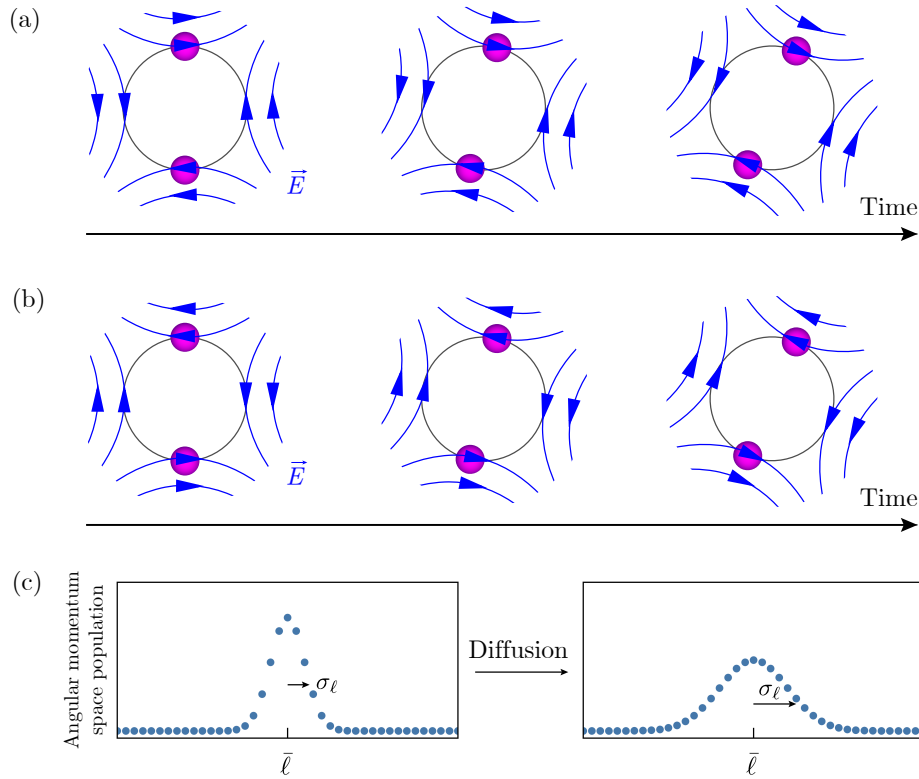


Figure 7.6: (a-b) Possible configurations of resonant electric-field gradients which may torque the rotor. The ions are shown rotating clockwise, and the field co-rotates with them, thus changing the angular momentum. (c) The effect of diffusion on the angular momentum space population. The width σ_ℓ increases according to (7.20). The center of the distribution $\bar{\ell}$ remains constant, and the shape remains Gaussian.

Using these relations, one may derive an estimate for the expected angular momentum diffusion coefficient given known heating rates. The horizontal center-of-mass motion has been measured to heat at roughly 50 q/s at a frequency of 1 MHz. We may estimate the corresponding heating rate of a comparable differential mode at the same frequency by multiplying by $(2r/h)^2 \approx 5 \times 10^{-4}$, where $2r \approx 4 \mu\text{m}$ is the ion-ion distance and $h \approx 180 \mu\text{m}$ is the height of the ion crystal above the trap surface. Multiplying by 10^4 to account for the increased quadrupole moment of the rotor and another factor of 5 assuming $1/f$ noise to scale the resonance frequency from 1 MHz down to 200 kHz, we may estimate the diffusion coefficient to be of the order $D/\hbar^2 \sim 1 \text{ ms}^{-1}$. The measurements shown in the following subsection indeed find the diffusion coefficient to be of this order of magnitude.

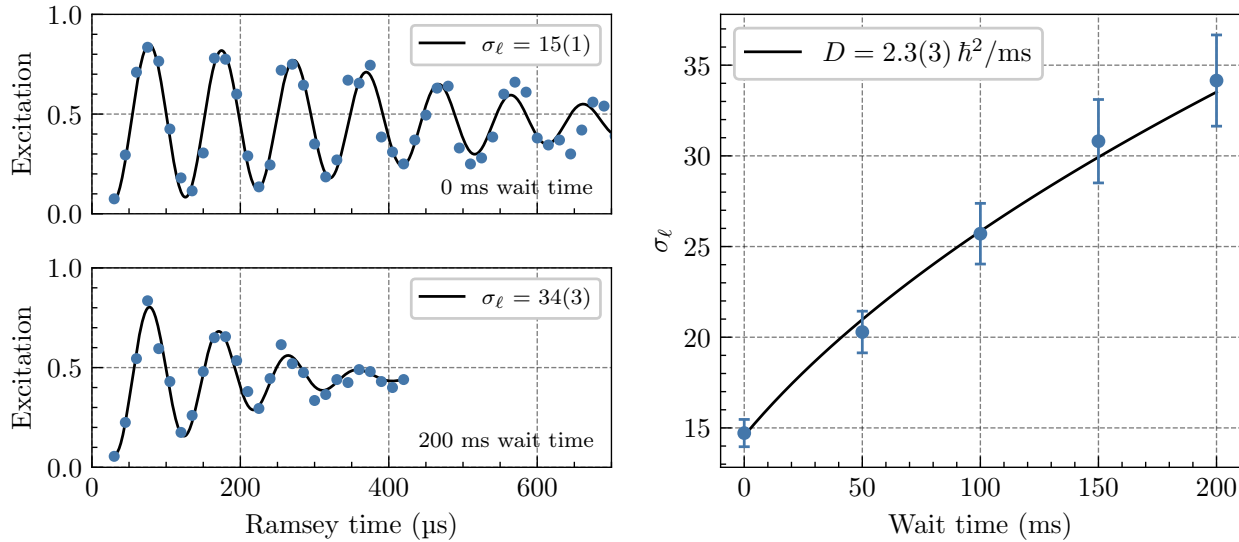


Figure 7.7: Sample diffusion coefficient measurement. Here, the ion crystal is rotating at 100 kHz and has a radius of 2.1 μm . For each wait time, a Ramsey decay curve on the $\Delta\ell = 1$ sideband is measured and fit for σ_ℓ .

7.3.4 Measurements of angular momentum diffusion

To measure angular momentum diffusion, we measure the angular momentum spread σ_ℓ as a function of wait time between rotational state preparation and measurement. This is analogous to a measurement of the heating rate of a vibrational mode, where one measures \bar{n} as a function of time after cooling (see Sec. 5.2). The measurement of σ_ℓ is most reliably done by measuring the rate of Ramsey dephasing of a $\Delta\ell = 1$ superposition, as discussed in Sec. 6.5.1. The Ramsey decay curve is fit to a function of the form (6.35) to extract σ_ℓ . During the wait time, noisy resonant electric fields diffuse the angular momentum state in accordance with (7.20), and we infer the diffusion coefficient D from the measurements of σ_ℓ as a function of wait time. Figure 7.7 shows a sample measurement of the diffusion coefficient. Here, the result is $2.3 \hbar^2/\text{ms}$. We find in general that the diffusion coefficient is inconsistent, ranging between 2 and $20 \hbar^2/\text{ms}$. This is possibly due to inconsistent levels of technical noise on the electrodes.

7.3.5 Noise injection

The diffusion coefficient measurement shown in Fig. 7.7 can be considered a measurement of the power spectral density of the electric field gradient at 200 kHz, related to the diffusion coefficient via (7.21). In the same sense as heating of a harmonic mode, this indicates the level of noise arising from either fluctuations on the trap surface or stray voltages on the trap electrodes (see Sec. 5.3). However, we can also study the relationship between noise spectral density and diffusion more thoroughly by injecting additional voltage noise onto the trap

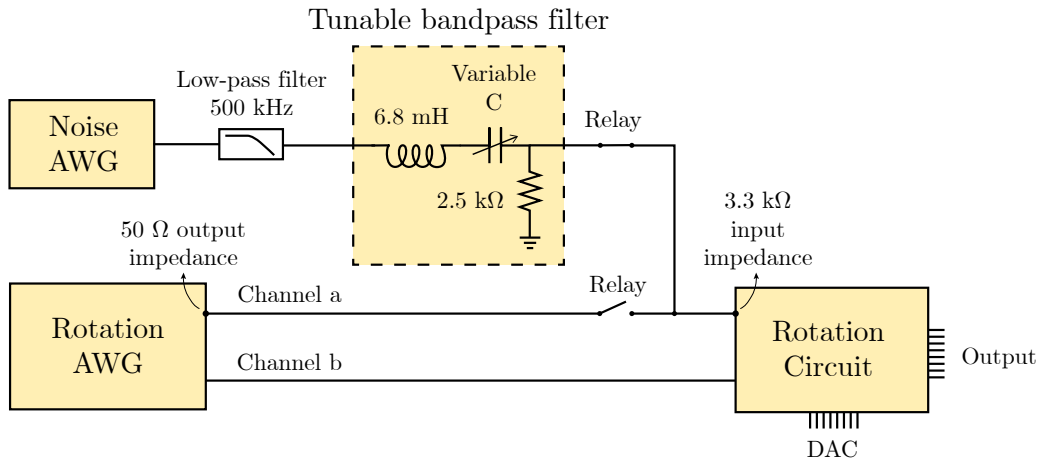


Figure 7.8: Circuit used for injecting quadrupole noise, including the rotation circuit.

electrodes. It is most convenient to do this in a way that ensures that the average electric field vanishes, $\langle E \rangle = 0$. While diffusion is insensitive to the electric field, a noisy field will cause heating of COM vibrational modes of the crystal, making measurements more difficult. We ensure that we create a noisy gradient alone by adding a noisy voltage onto one of the two AWG input channels of the rotation circuit. By design, this distributes the voltage onto the DC electrodes such that it produces only a quadrupole field, with vanishing dipole field.

Noise injection circuit

The circuit used to inject noise onto the DC electrodes for diffusion is shown in Fig. 7.8. Noise is sourced from a separate arbitrary waveform generator, which generates white noise at an arbitrary amplitude. This is passed through a tunable bandpass filter before being input into the rotation circuit. The bandpass filter is supplemented with a low-pass filter at 500 kHz because the inductor within the bandpass filter becomes capacitive at high frequencies.

The RLC bandpass filter uses a manually tuned variable capacitor to tune the center frequency, given by $1/\sqrt{LC}$. The capacitance ranges between 18 and 300 pF, which with the 6.8 mH inductor can produce center frequencies between 110 kHz and 450 kHz. The bandwidth is equal to R/L and is therefore independent of the capacitance, allowing for tuning of the center frequency while leaving the bandwidth constant. When also connected to the finite input impedance of the rotation circuit, the bandpass filter bandwidth is 19 kHz.

For switching, relay switches are chosen to physically disconnect the rotation AWG during noise injection, and to disconnect the noise circuit at all other times. This is helpful due to the relatively high input impedance of the rotation circuit ($3.3 \text{ k}\Omega$), which would significantly reduce the effectiveness of the noise injection if the noise circuit were to be also connected to a 50Ω load. The relays are Sensata Technologies Cynergy3 S2-03P reed relays, and respond within 300 μs when closing and 100 μs when opening. They are controlled by the pulser and

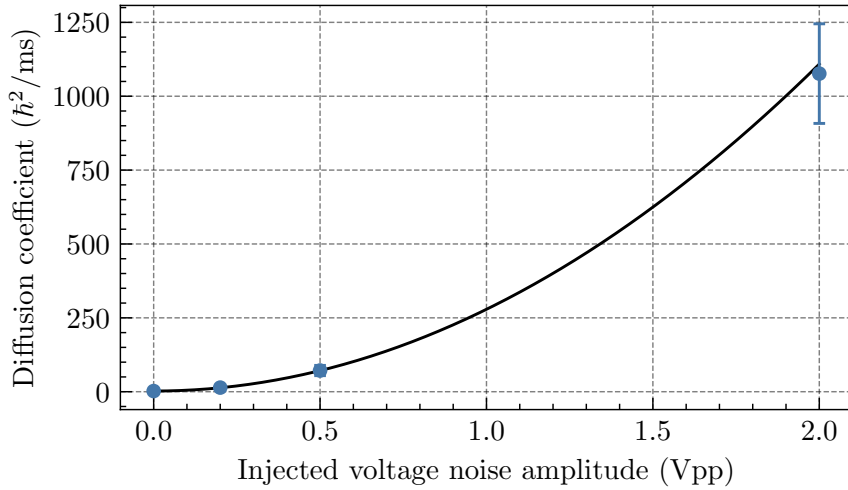


Figure 7.9: Measured diffusion coefficient with various amplitudes of noise injected. Here the ion crystal rotates at 153 kHz and has a radius of 2.1 μm .

connect the noise circuit to the rotation circuit for diffusion measurements only during the wait time between rotational state preparation and the Ramsey measurement.

Amplitude dependence

To tune the amplitude of the injected quadrupole noise, we set the amplitude of the white noise generated by the noise AWG. The amplitude of the voltage reaching the electrodes will be smaller by some factor due to filtering, but will be proportional. Since the power spectral density is proportional to the voltage amplitude squared, we expect the diffusion coefficient to go as the square of the injected noise amplitude. Figure 7.9 shows that this is the case. The fit is offset by $2.2 \hbar^2/\text{ms}$, the diffusion coefficient in the absence of noise. The noise injection circuit allows us to increase the diffusion coefficient by several orders of magnitude.

Frequency dependence

We can observe the diffusion resonance at $2\omega_{\text{rot}}$ by using the tunable bandpass filter to tune the center frequency of the noise injected while keeping its amplitude constant. We also keep the rotation frequency constant. This changes the noise spectral density at the rotation frequency: When the noise center frequency is equal to $2\omega_{\text{rot}}$, $S_E(2\omega_{\text{rot}})$ is maximized and the rotor sees the most diffusion-inducing noise, while when the noise is centered off the rotor resonance, $S_E(2\omega_{\text{rot}})$ is smaller and the diffusion coefficient is reduced. Measurements of diffusion coefficient as a function of injected noise center frequency, holding the rotation frequency and noise amplitude constant, are shown in Fig. 7.10. The rotation frequency is $144 \pm 2 \text{ kHz}$. The data agrees well with a Lorentzian centered at $2\omega_{\text{rot}}$, confirming that

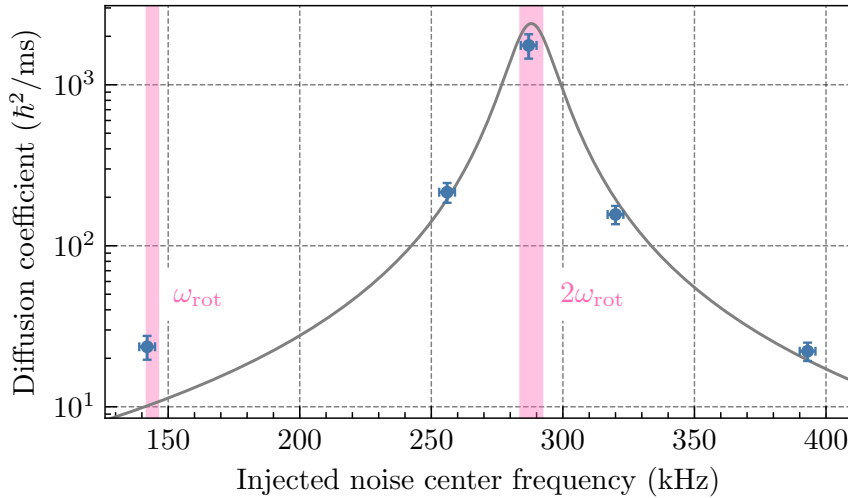


Figure 7.10: Measured diffusion coefficient with various center frequencies of injected noise, with the rotation frequency and amplitude held constant. Here the ion crystal rotates at 144 ± 2 kHz. Vertical bands indicate ω_{rot} and $2\omega_{\text{rot}}$, including variation in the rotation frequency. A Lorentzian lineshape centered at $2\omega_{\text{rot}}$ and with bandwidth equal to that of the noise injection circuit, 19 kHz, is also shown for reference.

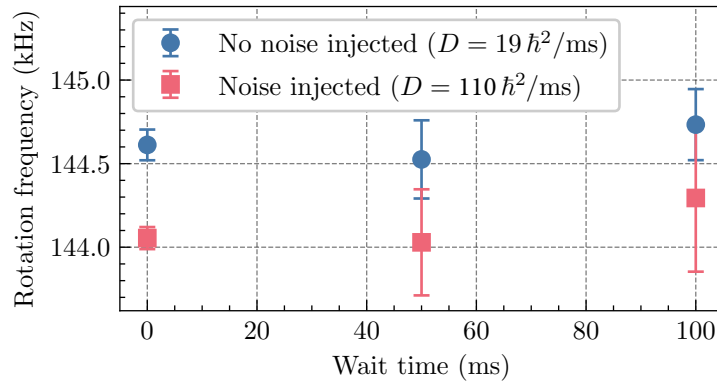


Figure 7.11: Measurements of rotational friction, with and without noise injected.

the appropriate resonance frequency for diffusion is at $2\omega_{\text{rot}}$. The lower limit of diffusion coefficient of about $20 \text{ } \hbar^2/\text{ms}$ in this measurement is possibly due to the ambient noise floor.

7.3.6 Rotational friction

By the fluctuation-dissipation theorem, diffusion may in general be accompanied by friction. When coupled to a thermal bath at temperature T , the rate of angular momentum slowing due to friction f is related to the diffusion coefficient by $D = k_B T I f$ [44], where I is the rotor's moment of inertia. Figure 7.11 shows measurements of the rotation frequency as a

function of wait time after rotational state preparation, with and without noise injection. The rotation frequency is measured by measuring the center frequency of the $\Delta\ell = 3$ sideband, and inferring ω_{rot} as 1/3 of this frequency. In both cases, no observable slowing is measured over 100 ms. These measurements bound the rate of angular momentum slowing to be less than $0.3 \hbar/\text{ms}$, a negligible rate. The noise in our system is therefore well-approximated as infinite temperature.

7.4 Rotational decoherence due to angular momentum diffusion

7.4.1 Theory: Orientational decoherence

The full quantum dynamics of a rotor under angular momentum diffusion, when induced by interaction with a Markovian environment, are best described by a Lindblad master equation. Development of the theoretical treatment of such a case began within the past decade with Ref. [46], which considered rotors undergoing random dipole-dipole interactions with an environment. Here it was shown that the corresponding Lindblad operators are proportional to $e^{i\theta}$, where θ is the operator for the rotor's orientation. Subsequent work has considered other specific microscopic models of environments such as background gas collisions, and has also shown that the resulting interactions, when weak and frequent, lead to angular momentum diffusion irrespective of the physical nature of the interaction [42, 43, 47], thus generalizing the master equations. For a general three-dimensional rotor, diffusion is described by a tensor, whose eigenvalues are the diffusion coefficients in different rotational directions. For the special case of a planar rotor, which has only a single diffusion coefficient D , the Lindblad master equation can be written

$$\dot{\rho} = -i[H_0, \rho] + \frac{D}{\hbar^2} (e^{-i\theta} \rho e^{i\theta} + e^{i\theta} \rho e^{-i\theta} - 2\rho) \quad (7.23a)$$

for dipole-dipole interaction with the environment, or

$$\dot{\rho} = -i[H_0, \rho] + \frac{D}{4\hbar^2} (e^{-2i\theta} \rho e^{2i\theta} + e^{2i\theta} \rho e^{-2i\theta} - 2\rho) \quad (7.23b)$$

for quadrupole-quadrupole interaction. Under these master equations, the angular momentum wavefunction diffuses at a rate given by D . In addition, orientational coherences decay. The density matrix element for the coherence between two orientations θ_1 and θ_2 , $\rho_{\theta_1\theta_2} = \langle \theta_1 | \rho | \theta_2 \rangle$, evolves in the interaction picture as

$$\dot{\rho}_{\theta_1\theta_2} = -\frac{4D}{\hbar^2} \sin^2 \left(\frac{\theta_1 - \theta_2}{2} \right) \rho_{\theta_1\theta_2} \quad (7.24a)$$

$$\dot{\rho}_{\theta_1\theta_2} = -\frac{D}{\hbar^2} \sin^2 (\theta_1 - \theta_2) \rho_{\theta_1\theta_2} \quad (7.24b)$$

for dipolar and quadrupolar interactions, respectively. One further generalization of this theory has included considerations of friction [44].

The form of (7.24) suggests a fundamental scaling relationship: for a superposition of orientations $|\theta_1\rangle + |\theta_2\rangle$, their coherence decays at a rate proportional to the sine-squared of half their relative angle (in the case of dipolar interaction). Indeed intuitively, we should expect that this rate is small for small angle separations, is maximum for an angle separation of π , and is periodic. For quadrupolar interaction, the rotor has 2-fold rotational symmetry, so the decoherence rate is π -periodic in the angle separation rather than 2π -periodic. The decoherence rate is also directly proportional to the diffusion coefficient. These scalings are reminiscent of well-known decoherence rate scalings for the harmonic oscillator: For a superposition of coherent states $|\alpha_1\rangle + |\alpha_2\rangle$, the coherence decays at a rate proportional to $|\alpha_1 - \alpha_2|^2$ when the oscillator is “amplitude damped” (coupled to the environment by operators a, a^\dagger) and proportional to the strength of the coupling to the environment [48, 49]. The harmonic oscillator decoherence scalings have been observed in several contexts, including photon fields and trapped ions [50–52]. The scaling laws for rotor decoherence, on the other hand, have not been experimentally observed prior to this work, though rotational decoherence has been empirically observed in the context of molecular collisions [53–55] and differential light shifts of trapped molecules [56–58]. A deeper understanding of the decoherence of rotational systems is likely to be of use to several emerging rotor-based quantum technologies. These include molecule-based quantum simulators [59–62], logical qubits [63, 64], levitated nano-rotors [65–67], and torsional opto-mechanical resonators [68].

7.4.2 Diffusion-induced decoherence of the trapped-ion rotor

It can be shown that the rotor-field interaction Hamiltonian (7.19), when averaged over many realizations, leads to the master equation (7.23b) [45]. To apply this to our experiments, we must solve for the evolution an angular momentum superposition of order $\Delta\ell$, take into account the electronic degrees of freedom, and solve for the phase contrast, which is the experimental measure of coherence. This derivation is given in Ref. [45], and the result is

$$C(T) = \exp\left(-\frac{DT}{2\hbar^2} [1 - \text{sinc}(2\Delta\ell\omega_r T)]\right). \quad (7.25)$$

This is the observable decoherence due to angular momentum diffusion. In general, the excitation phase contrast is also be multiplied by the factor (7.4), which we omit here to help conceptually separate this measurement artifact from the true decoherence factor.

This result has a direct connection to the rate of orientational decoherence (7.24b). To see this, we invoke an intuitive, semi-classical picture, in which we imagine the superposition of angular momenta to be a time-dependent superposition of orientations, separated by $\Delta\theta(t)$. This is shown in Fig. 7.12. Since the quantum of angular velocity is $2\omega_r$, the orientations separate at a rate $2\Delta\ell\omega_r$. This separation is reversed by the π pulse in the center of the Ramsey sequence, so that the superposition overlaps again at the time of the final $\pi/2$ pulse. At all times during this process, the decoherence rate is given instantaneously by (7.24b).

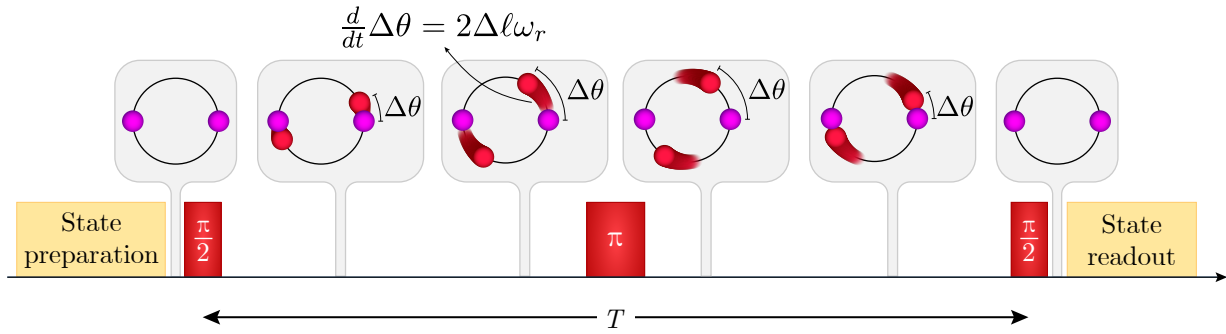


Figure 7.12: Schematic of the intuitive picture of a $\Delta\ell$ angular momentum superposition corresponding to a linearly separating superposition of orientations.

Identifying the phase contrast with the coherence, we should thus expect the contrast to be given by integrating (7.24b):

$$\begin{aligned} \ln[C(T)] &= \int_0^T -\frac{D}{\hbar^2} \sin^2[\Delta\theta(t)] dt \\ &= -\frac{D}{\hbar^2} \left[\int_0^{T/2} \sin^2(2\Delta\ell\omega_r t) dt + \int_{T/2}^T \sin^2(2\Delta\ell\omega_r T - 2\Delta\ell\omega_r t) dt \right], \end{aligned} \quad (7.26)$$

where in the first half of the integral the orientation separation $\Delta\theta$ is increasing linearly, and in the second half it is decreasing linearly. Carrying out this integral indeed gives exactly (7.25). Therefore in a sense, we may say that measuring the decoherence of angular momentum superpositions is a way of measuring the decoherence of orientation superpositions.

The functional form of (7.25) is a periodic oscillation of the decoherence rate about an underlying exponential decay. The oscillation frequency is equal to the angular separation frequency $2\Delta\ell\omega_r$, and the average exponential decay rate constant is $D/2\hbar^2$, proportional to the diffusion coefficient. It is convenient to define two rates: the rate of angular separation $\Delta\omega = 2\Delta\ell\omega_r$, and the diffusion coefficient expressed as a rate, $\tilde{D} = D/\hbar^2$. The relative values of these rates determine the shape of the contrast decay curve. This defines three regimes of interest:

1. $D/\hbar^2 \ll 2\Delta\ell\omega_r$. Here, the diffusion rate is slow compared to the rate of angular separation. The superposition is able to make many full rotations before decoherence occurs, and thus the angle-dependent decoherence rate gets averaged out, leaving the overall exponential decay as the dominant contribution:

$$C(T) \approx \exp\left(-\frac{DT}{2\hbar^2}\right). \quad (7.27)$$

2. $D/\hbar^2 \sim 2\Delta\ell\omega_r$. In this intermediate regime, the phase contrast “steps” down with a period equal to that of the angular separation $2\pi/2\Delta\ell\omega_r$, oscillating between instan-

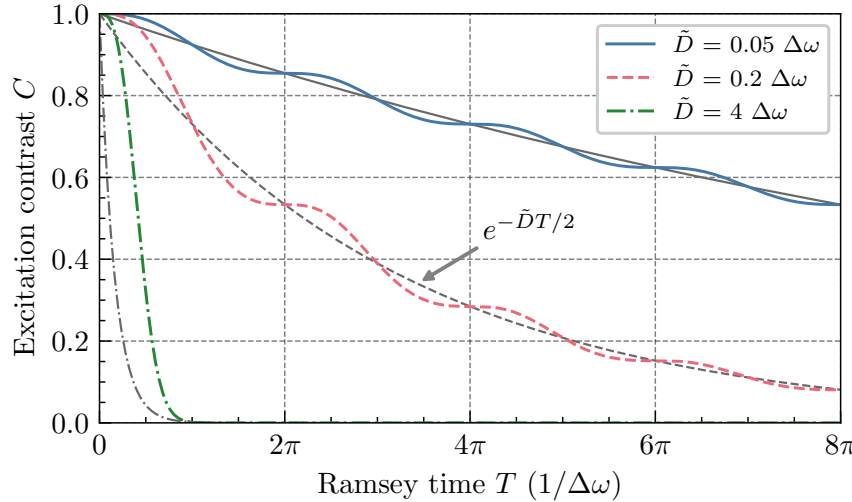


Figure 7.13: Contrast decay curves given by (7.25), showing curves roughly in the three regimes of slow diffusion, fast diffusion, and the intermediate regime. $\tilde{D} \equiv D/\hbar^2$, and $\Delta\omega \equiv 2\Delta\ell\omega_r$. Each is also shown with a corresponding reference exponential decay curve $\exp(-\tilde{D}T/2)$.

taneous decoherence rates of 0 (when the orientations overlap) and D/\hbar^2 (when the orientations are $\pi/2$ separated).

3. $D/\hbar^2 \gg 2\Delta\ell\omega_r$. Here, diffusion is fast enough that decoherence occurs well before the first oscillation in the angular separation. $\Delta\theta$ is thus restricted only to the small-angle regime, and the phase contrast is given approximately by

$$C(T) \approx \exp\left(-\frac{\omega_r^2 \Delta\ell^2 D T^3}{3\hbar^2}\right) = \exp[(-\gamma T)^3], \quad (7.28)$$

where

$$\gamma = \left(\frac{\omega_r^2 \Delta\ell^2 D}{3\hbar^2}\right)^{1/3}. \quad (7.29)$$

Because the angular separation is always small in this case, the total coherence time is longer than it would be if the system were to decohere only at the rate $D/2\hbar^2$, the average over all angles. This longer coherence can be seen in Fig. 7.13, where the decay curve for the case $\tilde{D} = 4\Delta\omega$ outlasts the exponential curve $\exp(-\tilde{D}T/2)$. This is manifested in the decoherence rate γ scaling sublinearly with the diffusion coefficient D , $\gamma \sim D^{1/3}$.

Note that from (7.25), the oscillation frequency of the contrast decay is $2\Delta\ell\omega_r$. This matches the separation frequency of the time-dependent orientations, but it is worth noting that this is in a sense a coincidence. Due to the two-fold symmetry of the rotor, the oscillation

frequency of the decoherence rate should in fact be twice the angular separation frequency. However, the spin echo pulse additionally halves this frequency, bringing the overall periodicity of the decoherence to be coincidentally equal to that of the angular separation. This is relevant in Chapter 8 for example, where we consider a long rotational Ramsey experiment without an echo pulse.

7.4.3 Measurements

In our experiments, diffusion is fast compared to the angular separation of the superpositions, so the decoherence takes place in the third regime. We therefore expect to find the contrast to decay according to (7.28). We define for our purposes the parameter γ as defined in (7.29) to be the observable *decoherence rate*. Three important observable scalings emerge from the predictions (7.28) and (7.29):

- The contrast decay profile should be an exponential decay with T^3 , which notably differs from the T or T^2 exponential decay profiles which one expects from simple models of fast or slow dephasing, respectively.
- The decoherence rate γ should scale as $\Delta\ell^{2/3}$. This differs from the dephasing mechanisms considered in Sec. 7.2, for which the decoherence rate is directly proportional to $\Delta\ell$.
- The decoherence rate γ should scale as $D^{1/3}$. This is a weaker scaling than the instantaneous decoherence rate of two separated orientations, which is directly proportional to D .

These three observable scalings are the observable manifestation of the two fundamental scalings encountered in (7.24b):

- $\dot{\rho}_{\theta_1\theta_2} \propto \sin^2(\theta_1 - \theta_2)$. The orientation difference $\Delta\theta = \theta_1 - \theta_2$ becomes $2\Delta\ell\omega_r t$ for our case of angular momentum superpositions, and in the small angle limit, $\sin^2(\Delta\theta) \approx (\Delta\theta)^2 = (2\Delta\ell\omega_r t)^2$. Integrating this over time gives us both the exponential T^3 decay profile and the $\Delta\ell^{2/3}$ scaling of the decoherence rate. These two observable scalings thus correspond directly to the sine-squared scaling of orientational decoherence (7.24b).
- $\dot{\rho}_{\theta_1\theta_2} \propto D$. This manifests in the $\gamma \sim D^{1/3}$ scaling, and is sublinear as a consequence of the small-angle regime.

Sine-squared orientation separation scaling

Fig. 7.14 shows decoherence measurements for $\Delta\ell = 1, 2$, and 3 for the same diffusion coefficient. Each is fit to a decay curve of the form $C(T) = C_0 e^{-(\gamma T)^3}$. We find that this function is a good description of the measured decay profile. As a further demonstration of this agreement, the $\Delta\ell = 1$ measurements are also shown with a fit to a Gaussian decay

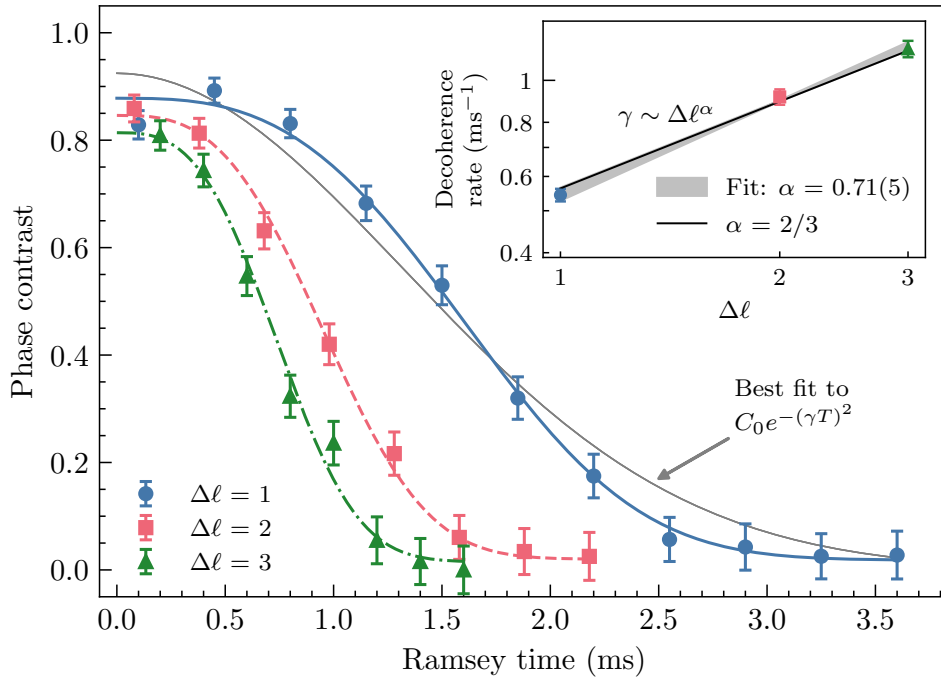


Figure 7.14: Main plot: Measured decay of phase contrast for $\Delta\ell = 1, 2$, and 3 rotational superpositions. Each is shown with a fit to a function of the form $C_0 e^{-(\gamma T)^3}$. The $\Delta\ell = 1$ data is additionally fit to a function of the form $C_0 e^{-(\gamma T)^2}$ for comparison. Inset: Fitted decoherence rates from the main plot plotted against $\Delta\ell$ on a log-log scale.

function, $C(T) = C_0 e^{-(\gamma T)^2}$. The Gaussian decay function is clearly a poor fit in comparison. This is an indication of the sine-squared decoherence rate with orientation separation in the small-angle limit with orientations that are separating at a constant rate.

The inset of Fig. 7.14 additionally shows the expected scaling of the decoherence rate with $\Delta\ell$, which in orientation space translates to the rate of angular separation. Taking the same data from the main plot, the fitted decoherence rates γ are plotted against $\Delta\ell$ on a log-log scale, and the resulting scaling is consistent with $\gamma \sim \Delta\ell^{2/3}$.

Diffusion coefficient scaling using noise injection

To see the scaling of rotational decoherence rate with diffusion, we artificially change the diffusion coefficient by injecting noise. The noise is injected only in between the two $\pi/2$ pulses so that diffusion occurs when the rotor is in superposition. We repeat the measurements shown in Fig. 7.14 for various amplitudes of injected noise to see the scaling. For each noise amplitude, we perform an independent measurement of the diffusion coefficient using the same level of noise injection. The results are shown in Fig. 7.15, where the decoherence rate is plotted against the diffusion coefficient. Noise injection allows the diffusion coefficient to be increased from $2 \hbar^2/\text{ms}$ at ambient noise levels to $1000 \hbar^2/\text{ms}$. We are able to com-

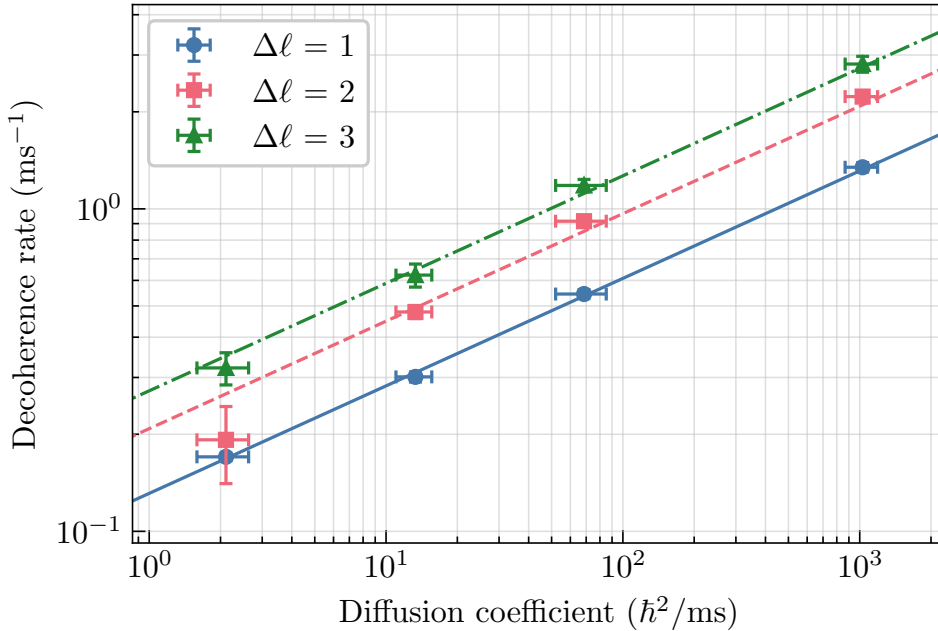


Figure 7.15: Measured decoherence rate, as fitted to (7.30), plotted against measured diffusion coefficient. The solid lines are from (7.29) for $\omega_r = 2\pi \times 13$ Hz.

pare the measured decoherence rates directly to (7.29), as all parameters are known. The corresponding curves of γ vs. D for $\Delta\ell = 1, 2$, and 3 are also shown, using the rotational constant $\omega_r = 2\pi \times 13$ Hz. We find that the data agrees with the predicted decoherence rates across the full range of parameters explored. This additionally confirms the scaling $\gamma \sim D^{1/3}$. These measurements are also presented in Ref. [45].

Unlike the measurements shown in Fig. 7.14, some of the measurements in Fig. 7.15 have long enough coherence times that they are affected by the contrast oscillation effect discussed in Sec. 7.1.2. Thus, in general, we do not fit the contrast decay profile to a function of the form (7.28), but rather to one which is also multiplied by (7.5). Explicitly,

$$C(T) = |(a + b) + (a - b) \cos(\Delta\ell^2 \omega_r T) - 1| \times \exp[-(\gamma T)^3]. \quad (7.30)$$

It was necessary to perform numerical simulations to account for the imperfect Rabi operations in the experiment and hence determine the correct values of the empirical parameters a and b to use. These were determined to be $(a, b) = (1, 0)$ for $\Delta\ell = 1$, $(0.0998, 0.012)$ for $\Delta\ell = 2$, and $(0.957, 0.174)$ for $\Delta\ell = 3$. Accounting for the contrast oscillation effect was crucial for properly extracting the decoherence rate γ from the measurements. The data shown in Fig. 7.3(b) are in fact the decay curves from the same four $\Delta\ell = 3$ data points shown in Fig. 7.15.

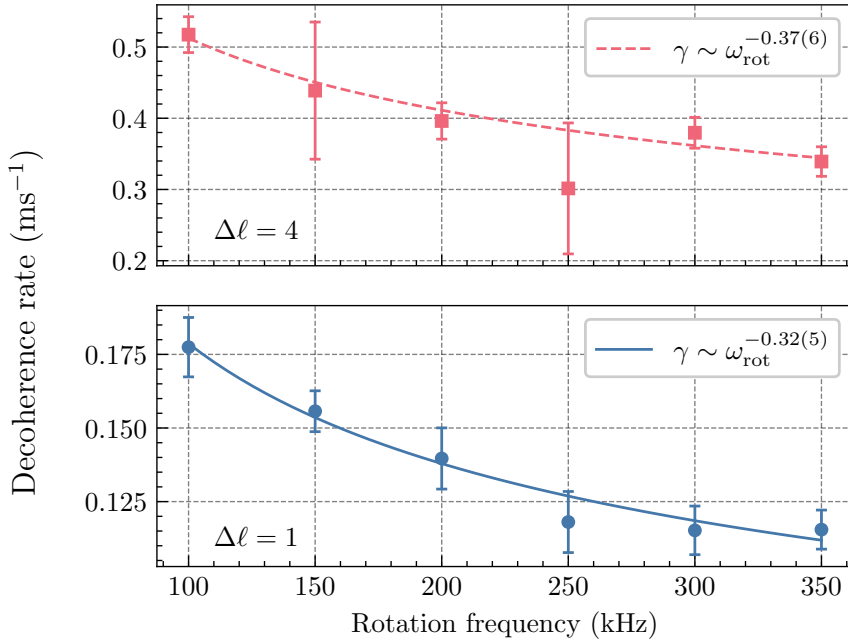


Figure 7.16: Measurements of decoherence rate as a function of rotation frequency for $\Delta\ell = 1$ and 4. Both sets of measurements are fit to a power law. Here, $\omega_r = 2\pi \times 6.4 \text{ Hz}$ (not accounting for centrifugal corrections).

Decoherence rate scaling with rotation frequency

Figure 7.16 shows measurements of the decoherence rate γ as a function of the rotation frequency. This effectively changes the frequency of electric field gradient noise that the rotor is sensitive to. The measured decoherence rates are consistent with a power law of $\gamma \sim \omega_{\text{rot}}^{-1/3}$. This scaling would be expected if the noise power spectral density has a $1/f$ frequency scaling, i.e. $S_E(\omega) \sim \omega^{-1}$, in the range between 200 kHz and 700 kHz. These measurements do not have corresponding diffusion measurements to confirm this, but it is a reasonable expectation, as a $1/f$ frequency scaling is often a good model of surface noise. In this case, the diffusion coefficient would scale as $D \sim S_E(2\omega_{\text{rot}}) \sim \omega_{\text{rot}}^{-1}$, and since the decoherence rate γ scales as $\gamma \sim D^{1/3}$, we would expect $\gamma \sim \omega_{\text{rot}}^{-1/3}$, as observed.

In these measurements, the horizontal secular frequency is relatively small, $\omega_x = 2\pi \times 0.85 \text{ MHz}$, so that centrifugal effects have some role. The ratio $(\omega_{\text{rot}}/\omega_{\text{stretch}})^2$ ranges between 0.5×10^{-2} and 5.7×10^{-2} for rotation frequencies ranging between 100 kHz and 350 kHz, so that the rotor radius differs by about 5% across these measurements. This might appear to be a confounding factor, as an increased rotor radius increases sensitivity to noise and increases the diffusion coefficient (7.21), and also lowers the rotational constant ω_r and hence also lowers the rate of angular separation in a rotational superposition. However, these two effects increase and decrease the decoherence rate, respectively, and in fact exactly cancel; this is considered more quantitatively in the following subsection.

7.4.4 Ways to improve rotational coherence

The measurements presented in this section have demonstrated that rotational coherence in our trapped-ion rotor is limited by angular momentum diffusion. Furthermore, the theoretical derivation of the effect of diffusion on rotational coherence has shown how diffusion-limited rotational decoherence scales with various parameters. This is given directly by (7.29). The scalings are

$$\gamma \sim \Delta\ell^{2/3} \omega_r^{2/3} D^{1/3}. \quad (7.31)$$

To inform how to improve rotational coherence, this is more conveniently written in terms of experimentally accessible parameters.

- The rotational constant scales with the secular trap frequency as $\omega_r \sim \omega_x^{4/3}$.
- The diffusion coefficient D scales with the rotor radius as r^4 , and directly with the power spectral density at twice the rotation frequency $S_{\mathcal{E}}(2\omega_{\text{rot}})$.
 - The rotor radius is set by the trap frequency and scales as $r \sim \omega_x^{-2/3}$.
 - If the noise power spectral density scales as $1/f$, then $S_{\mathcal{E}}(2\omega_{\text{rot}}) \sim \omega_{\text{rot}}^{-1}$.

In a remarkable coincidence, the overall scaling of the decoherence rate with trap frequency cancels: the ω_r contribution gives $\gamma \sim \omega_x^{8/9}$, and the D contribution gives $\gamma \sim \omega_x^{-8/9}$. We are left with

$$\gamma \sim \Delta\ell^{2/3} \omega_{\text{rot}}^{-1/3}. \quad (7.32)$$

This assumes that the noise which causes diffusion is surface-limited and scales with $1/f$; in general, lowering the noise amplitude or changing to a rotation frequency where the spectral density is lower will improve coherence times.

Beyond the small-angle regime

The above analysis holds only in the regime where the decoherence occurs while the separation angle of the superposition remains small. In the limit of long coherence times such that the angular dependence of the instantaneous decoherence rate averages out, the coherence decay curve approaches a simple exponential decay, as seen in Fig. 7.13. Here, the decoherence rate becomes independent of the rate of angular separation, so that there is no dependence on $\Delta\ell$ or ω_r , and becomes directly proportional to the diffusion coefficient D :

$$\gamma \sim D. \quad (7.33)$$

As above, since $D \sim r^4 S_{\mathcal{E}}(2\omega_{\text{rot}})$, translating this scaling into practical parameters, we have

$$\gamma \sim \omega_x^{-8/3} \omega_{\text{rot}}^{-1}, \quad (7.34)$$

assuming a $1/f$ noise power spectral density. In this regime, coherence time does not depend on $\Delta\ell$ since the separation angle of the superposition undergoes many full rotations.

Coherence time is improved with increasing trap frequency due to the rotor's quadrupole moment being lowered.

The more general case, including the intermediate regime which connects the limits of short and long coherence times, is considered further in Sec. 8.4.2.

Chapter 8

The trapped-ion rotational interferometer

This chapter discusses a proposal for an experiment to use the trapped-ion rotor as a rotational interferometer. In particular, we propose physically realizing a particle exchange operation. A rotational superposition can be used to create an effective superposition of orientations separated by $\Delta\theta = \pi$, where the ions' positions are superposed with their mutual particle-exchanged state. If the ions are identical, this state should produce an interferometric signal whose phase depends on the exchange symmetry, i.e. whether the ions are bosons or fermions. This would allow for observation of exchange symmetry, and the corresponding exchange phase, by way of a direct physical particle exchange. Furthermore, this would be done without ever directly overlapping the particles over each other.

8.1 Identical quantum particles and exchange symmetry

The symmetrization postulate of quantum mechanics states a system of particles is subject to a constraint which is present if and only if the particles are identical: their collective wavefunction must satisfy exchange symmetry, such that when any pair of particle indices is swapped, the wavefunction remains unchanged up to an overall phase factor $e^{i\phi_{\text{ex}}}$. In usual three-dimensional space, the exchange phase ϕ_{ex} must be only 0 or π , classifying all quantum particles as either bosons ($\phi_{\text{ex}} = 0$) or fermions ($\phi_{\text{ex}} = \pi$) [69].

The constraints placed by exchange symmetry, including the resulting quantum statistics, have manifestations which are central to common systems. Effects such as the Pauli exclusion principle explain the stability of atoms and nuclei, and manifest in many systems including the orbitals of multi-electron atoms and the Fermi sea in solid-state systems. More direct observations of exchange symmetry include experiments with ultracold quantum gases, manifesting in exotic states such as Bose-Einstein condensates and superfluids [70]. Still more direct observations include experiments with systems of only a few identical

particles, including Hong-Ou-Mandel interference experiments [71–74], experiments measuring the Hanbury Brown and Twiss effect [75–79], and experiments measuring the rotational spectra of homonuclear diatomic molecules [80]. High-precision searches for violations of the symmetrization postulate have also been performed using spectroscopic measurements [81–85].

The experiment proposed in this chapter combines two key features which makes it unique: (1) The particles remain well-separated at all times, and (2) The protocol allows for a direct measurement of the exchange phase ϕ_{ex} . Such an experiment was first proposed in Ref. [86]. Most past experiments which have aimed at direct observation of symmetrization attempt to bring the particles into the same physical location, and measure either the bunching or antibunching which results from their bosonic or fermionic quantum statistics. The exception is measurements of the rotational spectra of homonuclear diatomic molecules, whose nuclei remain separated as they rotate. However, the nuclei in these experiments are within 1 nm distance from each other, so that the molecular orbitals of the valence electrons strongly overlap. In the present experiment, on the other hand, the ions would be separated by several micrometers, and their respective valence electrons would not interact. Furthermore, no past experiment has performed a direct measurement of the exchange phase, with the recent exceptions of Refs. [87, 88]. However, these experiments involved overlapping identical photons onto a beamsplitter, and thus did not involve distant particles.

Concepts pertaining to identical particles, exchange symmetry, and indistinguishability defy intuition in several ways, and thus are often confounded with each other or otherwise confused [89]. Much of the remainder of this section is therefore devoted to precisely defining these concepts as they relate to the case of our system, in order to facilitate a careful interpretation of our proposed experiment in the context of particle symmetrization.

8.1.1 The symmetrization postulate

To aid the discussion of exchange symmetry as it pertains to our trapped-ion rotor, it is helpful to lay out explicitly what the symmetrization postulate states and what it does not. For simplicity, consideration is restricted to only two identical particles. This discussion borrows largely from lecture notes written by Prof. Robert Littlejohn [90].

Any two-particle Hamiltonian for identical particles is said to possess exchange symmetry if swapping the particle labels leaves it unchanged. For the trapped-ion rotor, this is most clearly seen in the Hamiltonian for the motion of the two ions written in terms of the individual ions' coordinates (3.9), repeated here for convenience:

$$H = \frac{p_1^2}{2m} + \frac{p_2^2}{2m} + \frac{1}{2}m\omega_x^2(x_1^2 + y_1^2 + x_2^2 + y_2^2) + \frac{1}{2}m\omega_z^2(z_1^2 + z_2^2) + \frac{e^2}{4\pi\epsilon_0|\mathbf{r}_1 - \mathbf{r}_2|}. \quad (8.1)$$

This Hamiltonian manifestly possesses exchange symmetry.

We may define an exchange operator E_{12} that swaps the particle labels 1 and 2 of the Hamiltonian. E_{12} has the property that $E_{12}^2 = 1$, the identity operation. It has two eigenvalues, ± 1 . Because the Hamiltonian possesses exchange symmetry, it commutes with the

exchange operator: $[H, E_{12}] = 0$. It is thus possible to define a simultaneous eigenbasis of H and E_{12} . In this eigenbasis, all energy eigenstates $|\psi\rangle$ may be classified by their exchange eigenvalue: either $E_{12}|\psi\rangle = |\psi\rangle$ (even under exchange), or $E_{12}|\psi\rangle = -|\psi\rangle$ (odd under exchange). We may thus define two mutually orthogonal subspaces of the Hilbert space: the subspace spanned by all the exchange-even eigenstates, and that spanned by all the exchange-odd eigenstates. All states within the even subspace are even under exchange, and all states within the odd subspace are odd under exchange. Linear combinations of states between the even and odd subspaces do not possess exchange symmetry. Time evolution under the exchange-symmetric Hamiltonian cannot map any even state into the odd subspace, nor any odd state into the even subspace.

The considerations thus far are consequences of ordinary quantum mechanics, unrelated to the symmetrization postulate. Rather, the symmetrization postulate makes an additional assertion, which cannot be derived from the above: Only one of the two exchange subspaces is physical, and states in the other subspace simply may not be occupied by a real system. Which subspace is physical depends on the particle: particles which may only occupy the even subspace are bosons, and particles which may only occupy the odd subspace are fermions. In nonrelativistic quantum mechanics this must be taken as an additional postulate, though in relativistic quantum field theory it is a direct consequence of simpler postulates. It may in fact be considered a failure of nonrelativistic quantum theory that it is even possible to define states which do not exist due to being of the wrong exchange subspace, and hence necessitating an additional postulate to exclude them. For our purposes it is most helpful to think in terms of ordinary nonrelativistic quantum mechanics, where we must remember to impose the symmetrization postulate onto the state of systems we consider. As a summary, the symmetrization postulate is a constraint only on the state of a system of identical particles, and is not a statement about its Hamiltonian.

8.1.2 Interpreting the concept of “indistinguishability”

In some contexts, it is said that all particles which are identical to each other are unconditionally indistinguishable as a result of the symmetrization postulate, because a symmetrized wavefunction prohibits any measurement which distinguishes one particle label from any other. In other contexts, it is said that identical particles must be “made” indistinguishable from one another, for example in Hong-Ou-Mandel interference experiments, where degrees of freedom such as the timing and polarization of the photons must be tuned by the experimenter in order to observe the relevant indistinguishability signal. This presents an apparent paradox: If the symmetrization postulate imposes that identical particles are fundamentally always indistinguishable, why is it ever necessary to engineer special conditions to “make” them indistinguishable? Or on the other hand, we often need not consider particle symmetrization when considering typical quantum systems; why not? What defines when we can and cannot neglect particle symmetrization?

The answer lies in the fact that real quantum systems have many degrees of freedom, and the symmetrization postulate applies only to the exchange of *all degrees of freedom simultaneously*.

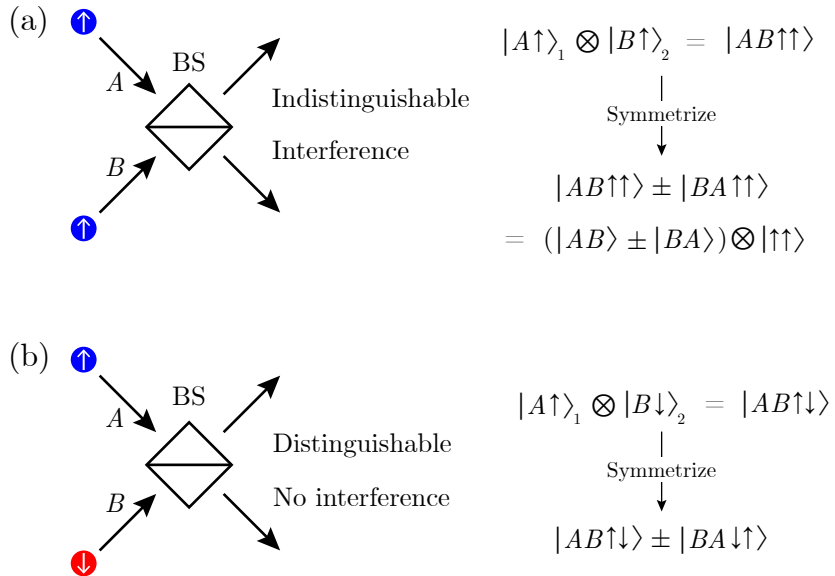


Figure 8.1: (a): Two identical particles sharing the same spin enter a beamsplitter in a Hong-Ou-Mandel-type interference experiment. At the output, the particles are indistinguishable and the probabilities at the output port may interfere due to symmetrization. (b): The particles entering the beamsplitter have different spins. They are thus distinguishable at the output, and do not exhibit interference behavior resulting from symmetrization.

neously. We typically measure only some subset of the degrees of freedom of a system, often only one. Figure 8.1 considers the example of a Hong-Ou-Mandel interference experiment, where we suppose we are interfering massive particles (to avoid requiring second quantization) undergoing an effective beamsplitter interaction. The interference of the interaction occurs in the positional degree of freedom, with the particles having input ports $|A\rangle$ and $|B\rangle$, but the particles also have an auxiliary spin degree of freedom with states $|\uparrow\rangle$ and $|\downarrow\rangle$. In Fig. 8.1(a), the particles share the same spin state. When we impose symmetrization on the input state of the two particles, we are thus able to factor out the spin degree of freedom, and the positional terms interfere. The output state involves a linear transformation of the positional degree of freedom only, and thus may result in a constructive or destructive interference of the two terms which are present due to imposing symmetrization. In Fig. 8.1(b), the particles have two different spins, and the positional terms from the symmetrization no longer factor out from the spin degree of freedom. This prevents interference of the output states, washing away any effects which would arise from particle identity.

In this example, the total wavefunction of the two particles is symmetrized in both cases, but the consequences are only observable if all degrees of freedom other than that being measured are in the same state. This highlights the relationship between *symmetrization* and *indistinguishability*: in intuitive language, if the particles have a distinguishing feature such as a different spin, then one could use the spin at the output ports to identify which particle

went in which direction. It is also the case that under these conditions, no interference occurs so that symmetrization is not observable. Only when the particles share all other degrees of freedom, so that their output state cannot be traced back to the individual input particles, does symmetrization manifest observably (as constructive or destructive interference at the output port in this example).

This example also highlights the important difference between particle *indices* (the subscripts 1 and 2) and classical particles, which correspond to localized wavefunctions (the input states $|A\rangle$ and $|B\rangle$). Classical particles are emergent observable entities, while the indices are mathematical bookkeeping tools. Many apparent paradoxes in matters of symmetrization arise from a confusion between these two distinct uses of the term “particle”. Importantly, symmetrization applies only to the indices [89]. For example, it might appear at first possible to break the exchange symmetry of a Hamiltonian, e.g. (8.1), by applying a field at the location of one particle and not the other. However, this breaks the symmetry only of the localized states; the particle *labels* can never be isolated and individually addressed. Exchange symmetry of the Hamiltonian of identical particles is thus always preserved.

In summary, the relationship between symmetrization and indistinguishability is the following: If a pair of identical particles is distinguishable in some way, then there are no observable consequences to symmetrization. If they can be made indistinguishable in some way, i.e. by interfering them on a beamsplitter and ensuring all other degrees of freedom are identical, then symmetrization may result in interference which is measurable. More generally, the other degrees of freedom need only be in a state of well-defined exchange symmetry. For our purposes, particle indistinguishability is *defined* by a measurable manifestation of particle symmetrization. While symmetrization is always present, it does not always have measurable consequences.

8.2 Making trapped ions indistinguishable in a quantum rotor

In this section, it is shown that exchange symmetry is not observable in a typical vibrational two-ion Coulomb crystal, but that it can be observed in a two-ion rotor. In other words, the ions in the vibrational crystal remain practically distinguishable, but those in the rotor can be made indistinguishable. It is also shown how one situation transitions into the other.

The strategy here for identifying how symmetrization is relevant for a system will be to identify the two subspaces of the exchange operator, and to consider the consequences of eliminating one or the other. As discussed in the previous subsection, the exchange operator shares a simultaneous eigenbasis with the Hamiltonian, so the goal is to identify the appropriate diagonalization of the Hamiltonian.

8.2.1 Symmetrization of a pinned two-ion crystal

We begin with the Hamiltonian for the ions' motion,

$$H = \frac{p_1^2}{2m} + \frac{p_2^2}{2m} + \frac{1}{2}m\omega_x^2(x_1^2 + x_2^2) + \frac{1}{2}m\omega_y^2(y_1^2 + y_2^2) + \frac{1}{2}m\omega_z^2(z_1^2 + z_2^2) + \frac{e^2}{4\pi\epsilon_0|\mathbf{r}_1 - \mathbf{r}_2|}, \quad (8.2)$$

where $\omega_x \neq \omega_y \neq \omega_z$. We define the center-of-mass and relative coordinates and momenta \mathbf{R}, \mathbf{P} and \mathbf{r}, \mathbf{p} by

$$\begin{aligned} \mathbf{R} &= \frac{\mathbf{r}_1 + \mathbf{r}_2}{2}, & \mathbf{P} &= \mathbf{p}_1 + \mathbf{p}_2 \\ \mathbf{r} &= \mathbf{r}_1 - \mathbf{r}_2, & \mathbf{p} &= \frac{\mathbf{p}_1 - \mathbf{p}_2}{2}. \end{aligned} \quad (8.3)$$

The Hamiltonian cleanly divides into two terms $H = H_{\text{COM}} + H_{\text{rel}}$, which respectively contain only center-of-mass coordinate terms and only relative coordinate terms. Any eigenfunction of the Hamiltonian may therefore be written as a product state of a state of the relative motion:

$$\Psi_{\mathbf{n}}(\mathbf{r}_1, \mathbf{r}_2) = \psi_{\mathbf{n}}^{\text{COM}}(\mathbf{R})\psi_{\mathbf{n}}^{\text{rel}}(\mathbf{r}), \quad (8.4)$$

where \mathbf{n} stands for all the quantum numbers of the particular eigenstate in question. The exchange operator E_{12} performs the operation $\mathbf{r}_1 \rightarrow \mathbf{r}_2$ and $\mathbf{r}_2 \rightarrow \mathbf{r}_1$ and similar for the momenta. In the COM and relative coordinates, we see from (8.3) that this operation is $\mathbf{R} \rightarrow \mathbf{R}$ and $\mathbf{r} \rightarrow -\mathbf{r}$. Particle exchange leaves the center-of-mass coordinate unchanged, and is equivalent to a parity operation in the relative coordinates. Thus

$$E_{12}\Psi_{\mathbf{n}}(\mathbf{r}_1, \mathbf{r}_2) = \psi_{\mathbf{n}}^{\text{COM}}(\mathbf{R})\psi_{\mathbf{n}}^{\text{rel}}(-\mathbf{r}). \quad (8.5)$$

Symmetrization thus only constrains the wavefunction of the relative coordinates, which must satisfy $\psi_{\mathbf{n}}^{\text{rel}}(-\mathbf{r}) = \pm\psi_{\mathbf{n}}^{\text{rel}}(\mathbf{r})$. The \pm sign here is fully determined by whether the ions are bosons or fermions, and the COM wavefunction plays no role in symmetrization.

We know that an eigenfunction of the relative coordinates can be broken into a product of eigenfunction of the three individual differential modes: stretch, vertical rocking, and horizontal rocking. To see how symmetrization constrains these, it is most useful to use cylindrical coordinates (ρ, θ, z) . This formulation also aids in later comparing to the case of ions in a rotor. Written this way, the stretch mode wavefunction is a function of ρ , the vertical rocking mode is a function of z , and the horizontal rocking mode is a function of θ . The relative coordinate potential is

$$\Phi_{\text{rel}} = \frac{1}{2}\mu\rho^2(\omega_x^2 \cos^2 \theta + \omega_y^2 \sin^2 \theta) + \frac{1}{2}\mu\omega_z^2 z^2 + \frac{e^2}{4\pi\epsilon_0\sqrt{\rho^2 + z^2}}, \quad (8.6)$$

where $\mu = m/2$ is the reduced mass. This potential is plotted in Fig. 8.2(a) within the xy -plane. There are two potential minima: one with $x > 0$ (ion 1 on the right), and one

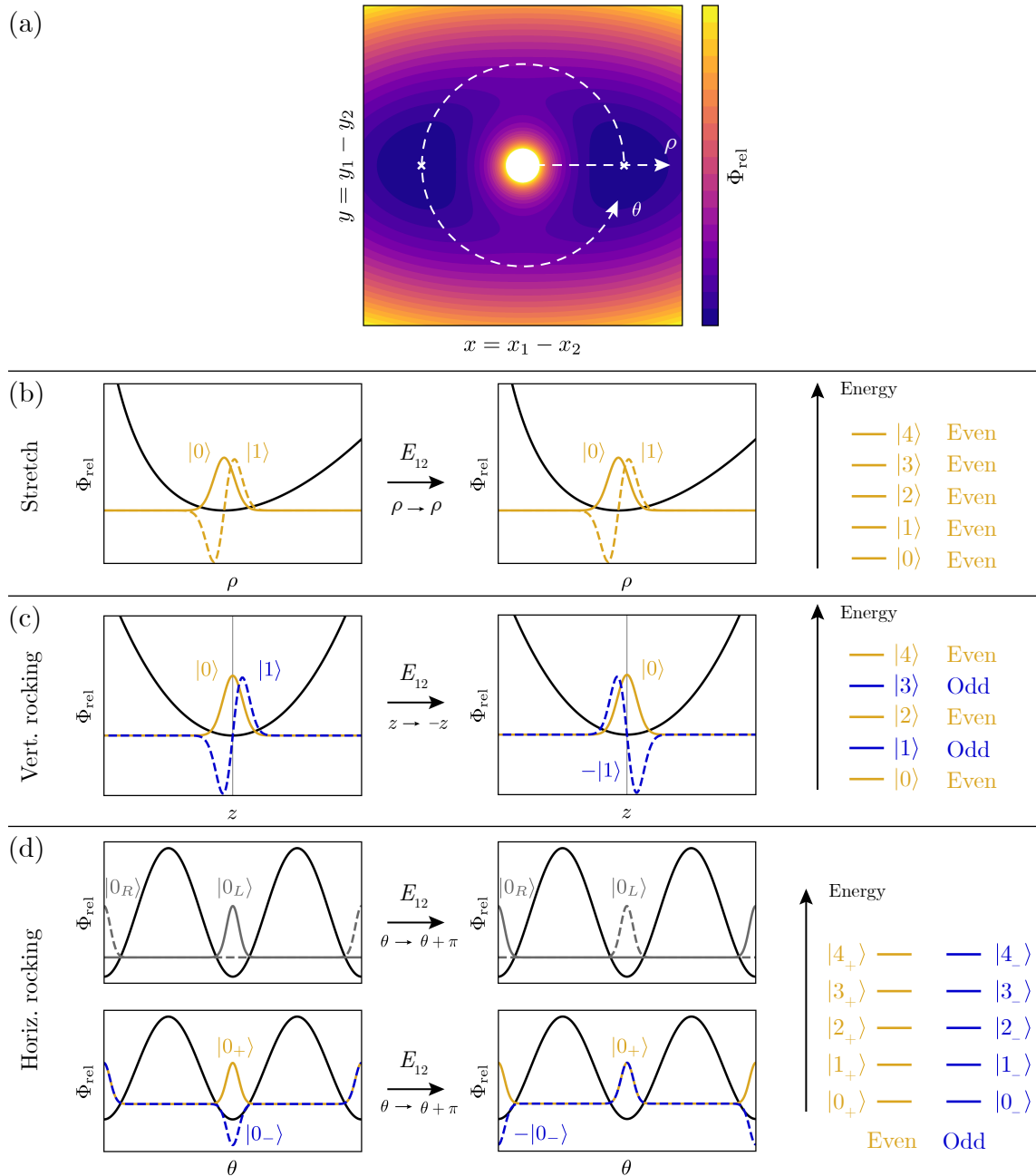


Figure 8.2: Exchange symmetry of the eigenfunctions of the relative modes of a pinned two-ion crystal. (a): The potential (8.6) in the xy plane, shown with slices along the cylindrical coordinates ρ and θ . (b-d): Potentials for the three relative modes, some example eigenfunctions, and how they transform under exchange. Exchange-even eigenfunctions are shown in gold, and exchange-odd eigenfunctions are shown in blue. (d) shows two different bases: $|0_{L,R}\rangle$ and $|0_{\pm}\rangle$, the former of which do not possess exchange symmetry. For each, an eigenspectrum is also shown, with each state color coded by its exchange symmetry.

with $x < 0$ (ion 1 on the left). As we shall see, this degeneracy is directly related to the two ions being practically distinguishable.

We can now analyze the exchange symmetry of the three relative modes. In cylindrical coordinates, the exchange operation $\mathbf{r} \rightarrow -\mathbf{r}$ performs the coordinate change

$$(\rho, \theta, z) \xrightarrow{E_{12}} (\rho, \theta + \pi, -z). \quad (8.7)$$

Figure 8.2(b-d) shows how a few example eigenfunctions of each mode transform under particle exchange, plotted along the slices shown in Fig. 8.2(a). Each subfigure also identifies which are even and which are odd under exchange.

- **Stretch mode** (Figure 8.2(b).) In cylindrical coordinates, the stretch mode is defined along the coordinate ρ , which is strictly positive. ρ is invariant under exchange symmetry, so all eigenfunctions of the stretch mode are even under exchange:

$$E_{12} |n_s\rangle = |n_s\rangle. \quad (8.8)$$

- **Vertical rocking mode** (Figure 8.2(c).) This mode is centered at $z = 0$, so the exchange operation, which performs $z \rightarrow -z$, is equivalent to a parity operation. Even-valued harmonic oscillator eigenfunctions are even under parity, and the odd-valued eigenfunctions are odd under parity. Thus the same applies to the vertical rocking mode eigenfunctions under exchange:

$$E_{12} |n_{vr}\rangle = (-1)^{n_{vr}} |n_{vr}\rangle. \quad (8.9)$$

- **Horizontal rocking mode** (Figure 8.2(d).) The two-fold degeneracy manifests in the horizontal rocking mode. The sine-squared potential has two minima, so that we may define a ground state wavefunction in either one: at $\theta = 0$ we have particle 1 on the right and particle 2 on the left, and at $\theta = \pi$ we have the reverse. We label these $|0_R\rangle$ and $|0_L\rangle$, respectively. These wavefunctions do not possess exchange symmetry; rather, they transform into each other under exchange. The appropriate basis for considering exchange symmetry is instead $|0_{\pm}\rangle = |0_L\rangle \pm |0_R\rangle$. $|0_+\rangle$ is even under exchange, and $|0_-\rangle$ is odd under exchange. The same holds for all excited states: $|n_{hr+}\rangle$ is even and $|n_{hr-}\rangle$ is odd under exchange, regardless of whether the integer n_{hr} itself is even or odd:

$$E_{12} |n_{hr\pm}\rangle = \pm |n_{hr\pm}\rangle. \quad (8.10)$$

The symmetrization postulate constrains the *overall* wavefunction to be either odd or even under exchange. Including all relative modes,

$$E_{12} |n_s, n_{vr}, n_{hr\pm}\rangle = \pm (-1)^{n_{vr}} |n_s, n_{vr}, n_{hr\pm}\rangle. \quad (8.11)$$

Since ${}^{40}\text{Ca}^+$ ions are fermions, for example, the total wavefunction must be odd under exchange, constraining $\pm(-1)^{n_{vr}} = -1$. The COM and stretch modes play no role, but the two rocking modes are relevant. If for example they are in their collective ground state, that state must be $|n_{vr}\rangle|n_{hr}\rangle = |0\rangle|0_-\rangle$. If on the other hand the vertical rocking mode is in the first excited state, then the collective state must be $|1\rangle|0_+\rangle$. If ${}^{40}\text{Ca}^+$ ions were bosons, these states would instead be $|0\rangle|0_+\rangle$ and $|1\rangle|0_-\rangle$, respectively. However, the states $|n_{hr+}\rangle$ and $|n_{hr-}\rangle$ are for all practical purposes identical to each other, with the same energy and same probability distribution¹. Thus in a sense, the consequences of symmetrization “hide” away in this degeneracy, such that the exchange-even and exchange-odd subspaces are nearly entirely identical. Because of this, symmetrization of this system is inconsequential, and thus the ions always remain practically distinguishable.

Note that in principle, using a different choice of coordinates we could have assigned the two-fold degeneracy to a different mode in the case of a pinned crystal. However, the overall result (8.11) would be the same. Assigning the degeneracy to the horizontal rocking mode is most natural when considering the transition to a free rotor.

8.2.2 Symmetrization of a two-ion rotor

We now consider the case of two ions in a rotor potential. The Hamiltonian is given by (8.1). We may again disregard the COM coordinates, and consider the relative motion in cylindrical coordinates. The corresponding potential is

$$\Phi_{\text{rel}} = \frac{1}{2}\mu\omega_x^2\rho^2 + \frac{1}{2}\mu\omega_z^2z^2 + \frac{e^2}{4\pi\epsilon_0\sqrt{\rho^2+z^2}}, \quad (8.12)$$

plotted in Fig. 8.3(a). Performing a similar analysis to the case of two pinned ions, we find the same results for the stretch and vertical rocking modes, i.e. (8.8) and (8.9). The horizontal rocking mode is now replaced by the rotational mode.

- **Rotational mode** (Figure 8.3(b).) The potential in the coordinate θ is flat, and the eigenfunctions are $e^{i\ell\theta}$. Applying the exchange operation $\theta \rightarrow \theta + \pi$, these become $e^{i\ell(\theta+\pi)} = e^{i\ell\pi}e^{i\ell\theta} = (-1)^\ell e^{i\ell\theta}$. Thus

$$E_{12}|\ell\rangle = (-1)^\ell|\ell\rangle. \quad (8.13)$$

Even angular momenta are even under exchange, and odd angular momenta are odd under exchange. Figure 8.3(b) shows the rotor eigenspectrum color coded by exchange symmetry. In contrast to the case of pinned ions seen in Fig. 8.2(d), we see that here, the even and odd eigenfunctions have distinct energies. Symmetrization therefore in principle has observable consequences: distinguishable particles, bosons, and fermions will have distinct eigenspectra from each other.

¹Strictly speaking, $|n_{hr+}\rangle$ has a very slightly lower energy than $|n_{hr-}\rangle$, but this difference is vanishingly small. In the WKB approximation, the splitting between $|0_+\rangle$ and $|0_-\rangle$ is $\sim e^{-r}\sqrt{m\Phi_{\text{pin}}^0/\hbar} \sim \exp(-10^5)$ times the energy difference between $|0_+\rangle$ and $|1_+\rangle$ [91].

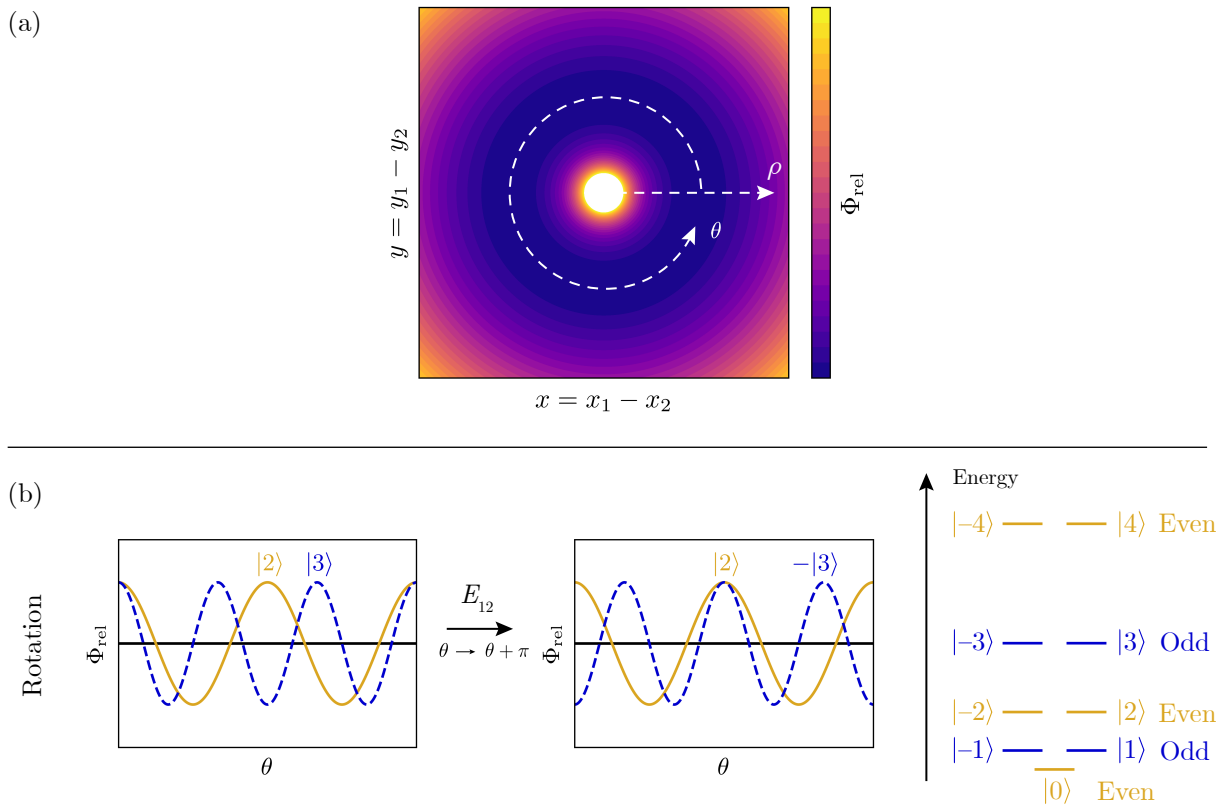


Figure 8.3: (a): The potential (8.12) in the xy -plane. (b): The potential as a function of θ along the equilibrium radius, example eigenfunctions $|\ell = 2\rangle$ and $|\ell = 3\rangle$, and how they transform under particle exchange. Only the real part of the wavefunctions is shown. At the right, an eigenspectrum of the rotational motion is shown, color coded by exchange symmetry.

Explicitly, the exchange operation of a total (relative coordinate) eigenfunction is

$$E_{12} |n_s, n_{vr}, \ell\rangle = (-1)^{n_{vr} + \ell} |n_s, n_{vr}, \ell\rangle. \quad (8.14)$$

As discussed in Sec. 8.1.2, in order for symmetrization to manifest in a particular degree of freedom, all others should have well-defined exchange symmetry. If the vertical rocking mode is in a state of well-defined exchange symmetry, then symmetrization eliminates either all rotational states with even $|\ell\rangle$ (fermions) or odd $|\ell\rangle$ (bosons). We propose to observe this via a rotational Ramsey experiment which measures revivals depending on which angular momentum states are occupied, detailed in Sec. 8.3. To make symmetrization manifest in the rotational mode, it suffices to cool the vertical rocking mode to its ground state, which is already done in our experiments.

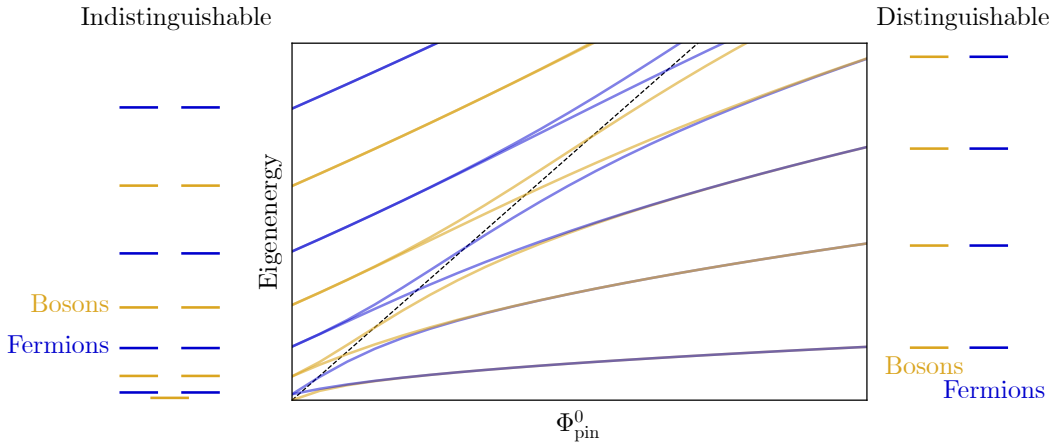


Figure 8.4: Eigenenergies in the rotor potential $\Phi_{\text{pin}}^0 \sin^2 \theta$ plotted as a function of the potential height Φ_{pin}^0 . To the left and right, in the two limits of small and large Φ_{pin}^0 , the corresponding eigenspectra are shown as energy levels. Each is color coded by exchange symmetry: even (gold) or odd (blue), which corresponds to the particles being bosons and fermions (assuming that the vertical rocking mode is in an exchange-even state; the opposite holds if it is in an exchange-odd state). The dashed line indicates where the x - and y -axes are equal.

8.2.3 The transition from distinguishable to indistinguishable

The difference between the case of a pinned and freely rotating two ion rotor is entirely in the angular coordinate θ . Comparing Figs. 8.2(d) and 8.3(b), we see that these two different potentials produce eigenspectra with qualitatively different exchange-symmetry characteristics. To understand how one transforms into the other, we may look at the eigenspectrum as a function of the potential height Φ_{pin}^0 , i.e. where the potential in the angular coordinate is $\Phi_{\text{pin}}(\theta) = \Phi_{\text{pin}}^0 \sin^2 \theta$. This is shown in Fig. 8.4. Each energy level is color coded by exchange symmetry, and we can see that on the right, the eigenspectrum matches that shown in Fig. 8.2(d), and on the left it matches that shown in Fig. 8.3(b). At large Φ_{pin}^0 , symmetrization has no observable consequence, so the ions remain distinguishable. At zero Φ_{pin}^0 , symmetrization strongly changes the energy eigenspectrum, so the ions can be indistinguishable. As the potential is lowered, the degeneracy between the harmonic oscillator states $|n_{hr\pm}\rangle$ is lifted, and they split and map onto rotational states of different angular momenta. The transition happens approximately when the potential height equals the energy of a given state. This corresponds to the point at which eigenfunctions are no longer localized.

It is interesting to note this is a way of seeing symmetrization without requiring that the particles ever occupy the same space, unlike e.g. in Hong-Ou-Mandel interference [86]. It suffices that the two ions share a potential in which their positions may exchange, but they need not actually coincide at any time.

This section has shown that the rotational energy eigenspectrum differs depending on

whether the ions are bosons or fermions. Because it is also nonlinear, the transition spectrum also differs depending on particle identity. The following section details the protocol by which we propose to measure the transition spectrum in a way that can distinguish between the three cases of unsymmetrized particles, bosons, and fermions.

8.3 The measurement protocol

The proposal is to perform a Ramsey experiment on a rotational sideband $\Delta\ell$, without a spin-echo pulse. As discussed in Sec. 6.5.1, the resulting dynamics are a dephasing of the electronic state. The position-space interpretation of this process is that the states in superposition separate from each other, and electronic state contrast is lost when they no longer overlap. If the coherence lasts long enough, the superposition will return to its initial state (in the rotating frame) after a 2π relative rotation, and a rephasing in the electronic degree of freedom should be expected. In addition, after only a π relative rotation, the two ions will have exchanged positions. Here, a rephasing should be expected if and only if the ions are indistinguishable, and the phase should depend on whether the ions are bosons or fermions. Unlike a purely mathematical exchange operation, this physical exchange operation will also come along with dynamical and geometric phases [92], which we must thus also account for.

To show this more concretely, we first consider position space to build intuition, and then show formally how the rephasing occurs.

8.3.1 The intuitive picture: position space

The position-space picture of a superposition of angular momenta which differ by $\Delta\ell$ is a time-dependent superposition of orientations, with angular separation $\Delta\theta(T)$. The separation increases linearly with time at a rate equal to the difference in angular velocity, so that $\Delta\theta(T) = 2\Delta\ell\omega_r T$. A full 2π relative rotation occurs when $\Delta\theta = 2\pi$. We define this time as the revival time T_{rev} :

$$T_{\text{rev}} = \frac{\pi}{\Delta\ell\omega_r}. \quad (8.15)$$

For typical parameters, this time is roughly 10 ms. We should thus expect a rotational superposition to rephase at time T_{rev} unconditionally (provided sufficient coherence). At time $T_{\text{rev}}/2$, $\Delta\theta = \pi$, and the ions have exchanged positions. Here we should expect an additional rephasing, which in this case is conditioned on the ions being indistinguishable. In other words, if the ions are in some sense distinct particles, then they may interfere with themselves, but not with each other.

In reality, we create a superposition of three different rotational states: $|\ell\rangle$, $|\ell + \Delta\ell\rangle$, and $|\ell + 2\Delta\ell\rangle$. Thus if we instead measure the coherence between $|\ell\rangle$ and $|\ell + 2\Delta\ell\rangle$, the unconditional revival should occur at time $T_{\text{rev}}/2$, and the revival conditioned on indistinguishability should occur at time $T_{\text{rev}}/4$. Figure 8.5 schematically shows the position-space picture at

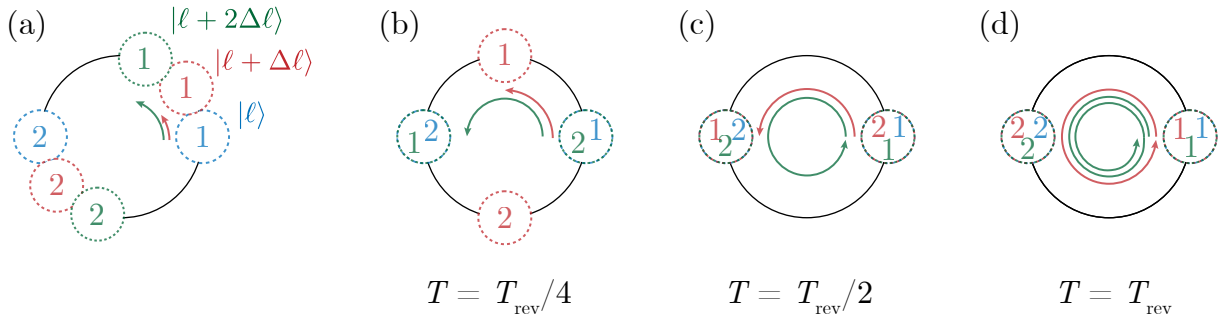


Figure 8.5: Schematic of the exchange experiment in position space, shown in a frame co-rotating with a reference angular momentum state $|\ell\rangle$, with each ion labeled 1 or 2. At different times, ions in different combinations of the three superpositions have either made a full 2π relative rotation, exchanged positions, or neither.

the three times of interest $T_{\text{rev}}/4$, $T_{\text{rev}}/2$, and T_{rev} . Each ion is given a label 1 or 2 as a guide to see when they have been exchanged and when they have not.

- At $T_{\text{rev}}/4$, the $|\ell + 2\Delta\ell\rangle$ state has rotated by π and thus the ions are exchanged relative to the $|\ell\rangle$ state. The $|\ell + \Delta\ell\rangle$ state, on the other hand, has rotated by $\pi/2$ and thus does not overlap with the others.
- At $T_{\text{rev}}/2$, the $|\ell + 2\Delta\ell\rangle$ state has rotated by 2π and is thus back at the original position, while the $|\ell + \Delta\ell\rangle$ state has rotated by π , exchanging the ions.
- At T_{rev} , the $|\ell + \Delta\ell\rangle$ state has rotated by 2π and the $|\ell + 2\Delta\ell\rangle$ state has rotated by 4π . The ions are back to their original positions in all three states, and there is no exchange.

As we shall see in Sec. 8.3.2, we choose which of the two coherences we are observing depending on the choice of observable: the excitation measures the $\Delta\ell$ coherence, and the parity measures the $2\Delta\ell$ coherence.

It should be noted that the picture of separating states with well-defined orientations is not quite correct, as the wavepacket does not stay localized in a free rotor but rather disperses. There are however revivals in the localization at the appropriate relative orientations, and the intuition afforded by this picture indeed corresponds to the results when considering the time evolution more formally.

8.3.2 The formal picture

The experimental sequence

The full measurement protocol is as follows:

1. The rotor state is prepared as usual, such that it begins in a distribution of angular momenta defined by coefficients c_ℓ : $|\psi_{\text{rot}}\rangle = \sum_\ell c_\ell |\ell\rangle$. The mean of this distribution is large enough to create resolved rotational sidebands, and the standard deviation is narrow enough to allow for high-fidelity operations on the rotational sidebands. The initial state of the electronic and rotor degrees of freedom is $\sum_\ell c_\ell |SS, \ell\rangle$. Importantly, the vertical rocking mode has also been sideband cooled to its ground state.
2. A $\pi/2$ pulse is applied on the $\Delta\ell$ sideband, which performs the operation

$$\begin{aligned} & \sum_\ell c_\ell |SS, \ell\rangle \xrightarrow{\pi/2} \\ & \frac{1}{2} \sum_\ell c_\ell [|SS, \ell\rangle - i |DS, \ell + \Delta\ell\rangle - (-1)^{\Delta\ell} i |SD, \ell + \Delta\ell\rangle - (-1)^{\Delta\ell} i |DD, \ell + 2\Delta\ell\rangle] . \end{aligned} \quad (8.16)$$

If we think of the initial state as a weighted ensemble of angular momentum states ℓ , then the $\pi/2$ pulse creates an equally-weighted superposition of the four states $|SS, \ell\rangle, |DS, \ell + \Delta\ell\rangle, |SD, \ell + \Delta\ell\rangle, |DD, \ell + 2\Delta\ell\rangle$ within each member of the ensemble. We then think of the state as an ensemble of four-dimensional manifolds.

3. The system freely evolves for a time T . During this time, each term acquires a phase:

$$\begin{aligned} |SS, \ell\rangle &\rightarrow |SS, \ell\rangle \\ |DS, \ell + \Delta\ell\rangle &\rightarrow e^{i\phi_{1,\ell}} |DS, \ell + \Delta\ell\rangle \\ |SD, \ell + \Delta\ell\rangle &\rightarrow e^{i\phi_{1,\ell}} |SD, \ell + \Delta\ell\rangle \\ |DD, \ell + 2\Delta\ell\rangle &\rightarrow e^{i\phi_{2,\ell}} |DD, \ell + 2\Delta\ell\rangle \end{aligned} \quad (8.17)$$

The phases $\phi_{1,\ell}$ and $\phi_{2,\ell}$ have been left general to allow for accounting of imperfections and geometric phases, which are considered in more detail in Sec. 8.4.

4. A final $\pi/2$ pulse is applied on the same $\Delta\ell$ sideband, with phase ϕ relative to the initial pulse.

Computation of the state probabilities

To compute the observable evolution of the system, we compute the time evolution operator for the full experimental sequence. The Hamiltonian may be broken into a term for each 4-dimensional ℓ manifold: $H = \sum_\ell H_\ell$, with H_ℓ is given by (6.26). Defining $H_\ell(\Omega_{\Delta\ell})$ as the Hamiltonian as a function of the Rabi frequency, the time-evolution operator for the experimental sequence is $U = \Pi_\ell U_\ell$, where

$$U_\ell = e^{-iH_\ell(\Omega_{\Delta\ell}e^{i\phi})t_{\pi/2}} e^{-iH_\ell(0)T} e^{-iH_\ell(\Omega_{\Delta\ell})t_{\pi/2}}. \quad (8.18)$$

$t_{\pi/2}$ is the $\pi/2$ pulse time on the $\Delta\ell$ sideband, and T is the Ramsey time. For the purpose of this computation we assume perfect operations, which in practical terms means that all detunings may be set to zero in the time-evolution operators for the $\pi/2$ pulses. Then explicitly, in the basis $\{|SS, \ell\rangle, |DS, \ell + \Delta\ell\rangle, |SD, \ell + \Delta\ell\rangle, |DD, \ell + 2\Delta\ell\rangle\}$,

$$U_\ell = \exp \left[-i \frac{\pi}{4} \begin{pmatrix} 0 & e^{-i\phi} & (-1)^{\Delta\ell} e^{-i\phi} & 0 \\ e^{i\phi} & 0 & 0 & (-1)^{\Delta\ell} e^{-i\phi} \\ (-1)^{\Delta\ell} e^{i\phi} & 0 & 0 & e^{-i\phi} \\ 0 & (-1)^{\Delta\ell} e^{i\phi} & e^{i\phi} & 0 \end{pmatrix} \right] \\ \times \exp \left[i \begin{pmatrix} 0 & 0 & 0 & 0 \\ 0 & \phi_{1,\ell} & 0 & 0 \\ 0 & 0 & \phi_{1,\ell} & 0 \\ 0 & 0 & 0 & \phi_{2,\ell} \end{pmatrix} \right] \\ \times \exp \left[-i \frac{\pi}{4} \begin{pmatrix} 0 & 1 & (-1)^{\Delta\ell} & 0 \\ 1 & 0 & 0 & (-1)^{\Delta\ell} \\ (-1)^{\Delta\ell} & 0 & 0 & 1 \\ 0 & (-1)^{\Delta\ell} & 1 & 0 \end{pmatrix} \right] \quad (8.19)$$

Having assumed perfect operations, the problem simplifies enough that this time-evolution operator may be computed analytically. Carrying through the computation for an initial state $|SS, \ell\rangle$, we find the probabilities

$$|\langle SS, \ell | U_\ell | SS, \ell \rangle|^2 = \frac{3}{8} - \frac{1}{4} \cos(\phi_{1,\ell} - \phi) - \frac{1}{4} \cos(\phi_{2,\ell} - \phi_{1,\ell} - \phi) + \frac{1}{8} \cos(\phi_{2,\ell} - 2\phi) \\ |\langle DS, \ell + \Delta\ell | U_\ell | SS, \ell \rangle|^2 = |\langle SD, \ell | U_\ell | SS, \ell \rangle|^2 = \frac{1}{4} \sin^2 \left(\frac{\phi_{2,\ell}}{2} - \phi \right) \\ |\langle DD, \ell + 2\Delta\ell | U_\ell | SS, \ell \rangle|^2 = \frac{3}{8} + \frac{1}{4} \cos(\phi_{1,\ell} - \phi) + \frac{1}{4} \cos(\phi_{2,\ell} - \phi_{1,\ell} - \phi) + \frac{1}{8} \cos(\phi_{2,\ell} - 2\phi). \quad (8.20)$$

The probability of observing a particular electronic state is the weighted average of these probabilities over the angular momentum distribution $\sum_\ell c_\ell |\ell\rangle$: $P_{SS} = \sum_\ell |c_\ell|^2 |\langle SS, \ell | U_\ell | SS, \ell \rangle|^2$, etc.

There are two observables of interest: the excitation and the parity, which are defined as

$$E = \frac{1}{2} (2P_{DD} + P_{DS} + P_{SD}) \quad (8.21)$$

$$\Pi = P_{SS} + P_{DD} - P_{DS} - P_{SD},$$

giving

$$E = \sum_\ell |c_\ell|^2 \left[\frac{1}{2} + \frac{1}{4} \cos(\phi_{1,\ell} - \phi) + \frac{1}{4} \cos(\phi_{2,\ell} - \phi_{1,\ell} - \phi) \right] \quad (8.22a)$$

$$\Pi = \sum_\ell |c_\ell|^2 \cos^2 \left(\frac{\phi_{2,\ell}}{2} - \phi \right). \quad (8.22b)$$

The excitation is a function only of the phases $\phi_{1,\ell}$ and $\phi_{2,\ell} - \phi_{1,\ell}$. $\phi_{1,\ell}$ is the relative phase between the states $|\ell\rangle$ and $|\ell + \Delta\ell\rangle$, and $\phi_{2,\ell} - \phi_{1,\ell}$ is the relative phase between the states $|\ell + \Delta\ell\rangle$ and $|\ell + 2\Delta\ell\rangle$. The excitation is therefore sensitive only to the relative phases of the $\Delta\ell$ -separated superpositions. The parity, on the other hand, is a function of only of the phase $\phi_{2,\ell}$, which is the relative phase between the states $|\ell\rangle$ and $|\ell + 2\Delta\ell\rangle$. The parity is therefore sensitive only to the relative phase of the $2\Delta\ell$ -separated superposition.

Phase contrast revivals

In the absence of imperfections, the dynamical contribution (that is, excluding geometric phases) to the free-evolution phases $\phi_{1,\ell}$ and $\phi_{2,\ell}$ after time T is (6.32)

$$\begin{aligned}\phi_{1,\ell} &= -\delta_{1,\ell}T = -T\Delta + \omega_r T(2\ell\Delta\ell + \Delta\ell^2) \\ \phi_{2,\ell} &= -(\delta_{1,\ell} + \delta_{2,\ell})T = -2T\Delta + 2\omega_r T(2\ell\Delta\ell + 2\Delta\ell^2),\end{aligned}\tag{8.23}$$

with the detunings $\delta_{\ell,1}$ and $\delta_{\ell,2}$ defined by (6.27). Note that $\phi_{2,\ell}$ is not exactly equal to $2\phi_{1,\ell}$ due to the difference in transition frequencies between the transitions $|\ell\rangle \rightarrow |\ell + \Delta\ell\rangle$ and $|\ell + \Delta\ell\rangle \rightarrow |\ell + 2\Delta\ell\rangle$. Here we choose not to write these phases in terms of an detuning from the center of the $\Delta\ell$ sideband as done in (6.34), but rather in terms of the detuning from the carrier, Δ . The former is a convenient formulation in some cases, but the latter is more precisely defined, which is appropriate for carefully considering the phases as we intend do here.

The dynamical phases depend on the angular momentum ℓ . Because the system begins in a distribution over many angular momenta, the system dephases when placed in this superposition, as discussed in Sec. 6.5.1. However, these phases across the different manifolds differ from each other by a constant (e.g. $\phi_{1,\ell+1} - \phi_{1,\ell} = 2\Delta\ell\omega_r T$), independent of ℓ . Rephasing occurs when the acquired phase differs by a multiple of 2π across all ℓ manifolds which are occupied.

Table 8.1 shows the dynamical contribution to the phases $\phi_{1,\ell}$, $\phi_{2,\ell} - \phi_{1,\ell}$, and $\phi_{2,\ell}$ at the times T_{rev} , $T_{\text{rev}}/2$, and $T_{\text{rev}}/4$. Each phase is the sum of three terms: a term proportional to the detuning from the carrier Δ , a $\Delta\ell$ -dependent shift, and a term proportional to ℓ . Only the final term differs between ℓ manifolds, so only this term is relevant is considering when a revival occurs. These terms are highlighted in Tab. 8.1. Specifically, revival occurs if the relevant phase differs by a multiple of 2π for all ℓ manifolds which are occupied. Crucially, which values of ℓ may be occupied depends on the symmetrization of the rotational degree of freedom.

- **If the rotational degree of freedom is not symmetrized**, then any integer value of ℓ may be occupied. A revival then occurs only if the difference in phase between manifolds ℓ and $\ell+1$ is a multiple of 2π . This occurs first at time T_{rev} for the excitation and at $T_{\text{rev}}/2$ for the parity. At earlier times, the phases across ℓ manifolds are not aligned and cancel each other.

Ramsey time	$\phi_{1,\ell}$	$\phi_{2,\ell} - \phi_{1,\ell}$	Revival in excitation?
T_{rev}	$-\frac{\pi\Delta}{\Delta\ell\omega_r} + \pi\Delta\ell + [2\pi\ell]$	$-\frac{\pi\Delta}{\Delta\ell\omega_r} + 3\pi\Delta\ell + [2\pi\ell]$	Yes
$T_{\text{rev}}/2$	$-\frac{\pi\Delta}{2\Delta\ell\omega_r} + [\frac{\pi}{2}\Delta\ell] + [\pi\ell]$	$-\frac{\pi\Delta}{2\Delta\ell\omega_r} + [\frac{3\pi}{2}\Delta\ell] + [\pi\ell]$	Only if indistinguishable (and $\Delta\ell$ is even)
$T_{\text{rev}}/4$	$-\frac{\pi\Delta}{4\Delta\ell\omega_r} + \frac{\pi}{4}\Delta\ell + [\frac{\pi}{2}\ell]$	$-\frac{\pi\Delta}{4\Delta\ell\omega_r} + \frac{3\pi}{4}\Delta\ell + [\frac{\pi}{2}\ell]$	No

Ramsey time	$\phi_{2,\ell}$	Revival in parity?
T_{rev}	$-\frac{2\pi\Delta}{\Delta\ell\omega_r} + 4\pi\Delta\ell + [4\pi\ell]$	Yes
$T_{\text{rev}}/2$	$-\frac{\pi\Delta}{\Delta\ell\omega_r} + 2\pi\Delta\ell + [2\pi\ell]$	Yes
$T_{\text{rev}}/4$	$-\frac{\pi\Delta}{2\Delta\ell\omega_r} + \pi\Delta\ell + [\pi\ell]$	Only if indistinguishable

Table 8.1: Free evolution phases at Ramsey times of interest, and whether or not they result in a phase contrast revival for excitation (top) and parity (bottom). Unconditional revivals are indicated by green highlighting, revivals conditioned on indistinguishability are indicated by yellow highlighting, and non-revivals are indicated by red highlighting. Only ideal dynamical phases (8.23) are included.

- If the rotational degree of freedom is symmetrized, then only even values or only odd values of ℓ will be occupied. We then need only for the difference in phase between manifolds ℓ and $\ell + 2$ to be a multiple of 2π for a revival to occur. This first occurs at half the Ramsey time at which is occurs in the unsymmetrized case: $T_{\text{rev}}/2$ for the excitation, and $T_{\text{rev}}/4$ for the parity.

When considering the excitation, an additional constraint is present: revival at $T_{\text{rev}}/2$ only occurs if $\Delta\ell$ is also even. This comes from the discrepancy between the phases $\phi_{1,\ell}$ and $\phi_{2,\ell} - \phi_{1,\ell}$, highlighted in grey in Tab. 8.1. If $\Delta\ell$ is even then the discrepancy is a multiple of 2π , and the $\phi_{1,\ell}$ and $\phi_{2,\ell} - \phi_{1,\ell}$ terms of (8.22a) constructively interfere. If on the other hand $\Delta\ell$ is odd, then the discrepancy is an odd multiple of π , and the two corresponding terms of (8.22a) destructively interfere. This is the same contrast oscillation effect considered in 7.1.2, defined by a profile in the excitation phase contrast given by (7.4), which is still valid even in the absence of a spin-echo pulse. If $\Delta\ell$ is odd, then $T_{\text{rev}}/2$ coincides with a node of the contrast oscillation profile, so no revival is seen. It can be shown that T_{rev} always coincides with an antinode of the contrast oscillation profile, regardless of $\Delta\ell$.

The interference signal, computed from (8.22), is plotted in Fig. 8.6. The final pulse phase is kept constant, and a detuning from the center of the rotational sideband is added in order to see interference fringes. The angular momentum distribution is taken to be Gaussian. The revivals are indeed seen at the times indicated in Tab. 8.1. The width of the interference signal in time is given by $1/\gamma_{\Delta\ell}$, the reciprocal of the linewidth of the $\Delta\ell$ sideband. This linewidth is proportional to the width of the angular momentum distribution, so that the narrower the angular momentum spread, the wider the interference signal in time.

Discussion

The results from this section corroborate the expectations from Sec. 8.3.1, shown in Fig. 8.5: Unconditional revivals occur when the ions have made a full 2π relative rotation, and revivals conditioned on indistinguishability occur when the ions have exchanged positions². This demonstrates the correspondence between state symmetrization and the observable manifestation of indistinguishability: The condition for making the ions indistinguishable is to make the symmetrization manifest in the rotational mode. As shown in Sec. 8.2.2, to do this, it suffices in this experiment to cool the vertical rocking mode to its ground state.

At the indistinguishability-conditioned revival time, which is $T_{\text{rev}}/2$ for the excitation and $T_{\text{rev}}/4$ for the parity, the ℓ -dependent term of the relevant phase is $\pi\ell$. The corresponding phase factor, $e^{i\pi\ell}$, is therefore -1 if all ℓ are odd, and $+1$ if all ℓ are even. This term is therefore precisely the exchange phase ϕ_{ex} : the particle identity, bosons or fermions, manifests in the phase of the $\Delta\theta = \pi$ revival. It is interesting to note that the exchange phase only matches the particle identity if the vertical rocking mode is placed into a state of

²For the excitation at $T_{\text{rev}}/2$, which we have seen is additionally conditioned on $\Delta\ell$ being even, consider Fig. 8.5(c). Here, the $|\ell + \Delta\ell\rangle$ state is exchanged with both the $|\ell\rangle$ state and the $|\ell + 2\Delta\ell\rangle$ state. The phases of these two exchanges must line up in order for revival to occur.

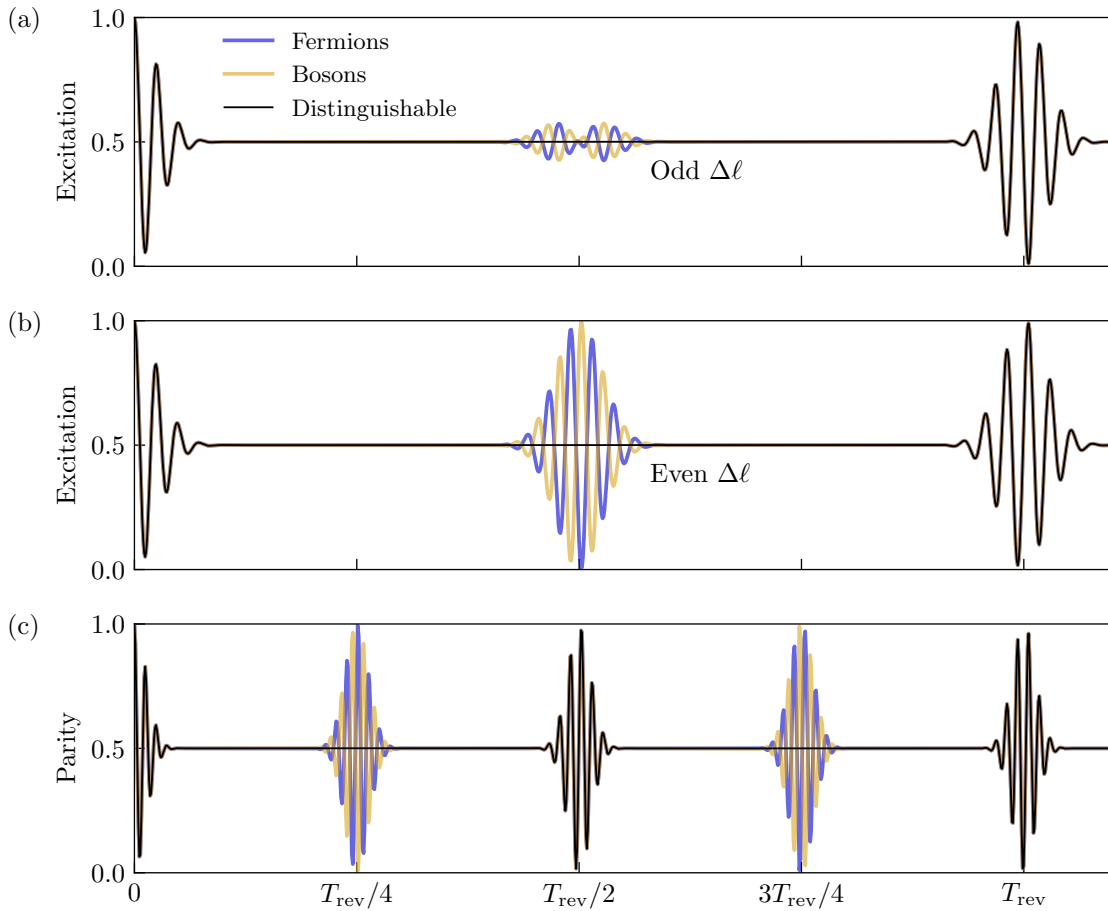


Figure 8.6: Expected signals for the 2-ion rotor interference experiment, computed from (8.22) and (8.23) with a detuning applied, for (a) excitation when $\Delta\ell$ is odd, (b) excitation when $\Delta\ell$ is even, and (c) parity. A Gaussian distribution of angular momentum states is assumed.

even exchange symmetry, e.g. the ground state. By instead placing it in the $|n_{vr} = 1\rangle$ Fock state, for example, one may modify the exchange phase of the rotational revival, which now becomes π for bosons and 0 for fermions.

It is also noteworthy that unlike many other experiments which depend strongly on quantum statistics, e.g. creation of a Bose-Einstein condensate, the outcome of this experiment is not qualitatively different depending on whether the particles are bosons or fermions. Rather, here the particle identity only determines the phase of the reinterference. This can be related to the fact that this experiment does not overlap the particles, and thus does not involve bunching or antibunching. While the two particles do become superposed onto each others' positions, they importantly remain distant throughout the entire experiment in the sense that if a position measurement is performed at any time during the experiment, the two particles are always found to be on opposite ends of the rotor.

Measuring the exchange phase presents a significant challenge. The following section outlines experimental requirements and considerations for doing so.

8.4 Experimental considerations

We can break the requirements for performing the rotational interference experiment into three steps, each of which has additional requirements on top of the last: (1) observing the $\Delta\theta = 2\pi$ full rotation revival, (2) observing the $\Delta\theta = \pi$ exchange revival, and (3) measuring the exchange phase. Observing the full rotation revival requires sufficient phase contrast at the revival time and requires that the spacing in $\ell \rightarrow \ell + \Delta\ell$ transition frequencies be commensurate. Observing the exchange revival additionally requires that the rotational degree of freedom is symmetrized. Finally, measuring the exchange phase additionally requires calculation and/or calibration of all dynamical and geometric phases to an absolute uncertainty within π . This section considers each of these steps one at a time. We identify and quantify effects which may hinder these steps, propose ways to mitigate them, and consider the tradeoffs therein.

Some of the effects considered in this section are shifts to the rotational energy eigen-spectrum, which in turn shift the transition frequencies. We will find it useful to organize each shift into terms which are constant, linear, and higher-order in ℓ . These three terms have different effects which are relevant to different steps of the experiment, so effects which shift the transition frequency are relevant to all three steps of the experiment. We thus begin with an overview of effects which cause rotational transition frequency shifts, before subsequently considering more quantitatively how both transition frequency shifts and other imperfections affect each of the three steps of the experiment. Finally, we conclude with some considerations relevant to using more than two ions for this experiment.

The considerations presented here are not complete; rather, they intend to offer a starting point for more carefully considering the requirements and error budget associated with performing this measurement.

8.4.1 Effects which shift rotational transition frequencies

In an ideal planar rotor, the transition frequency between the state $|\ell\rangle$ and $|\ell + \Delta\ell\rangle$ is

$$\omega_{\ell,\ell+\Delta\ell} = \frac{E_{\ell+\Delta\ell} - E_\ell}{\hbar} = \omega_{r0}(2\ell\Delta\ell + \Delta\ell^2), \quad (8.24)$$

where ω_{r0} is the rotational constant in the absence of any shifts. We write a shift to this transition frequency as $\delta\omega_{\ell,\ell+\Delta\ell}$. The shifts considered in this subsection all take the form

$$\delta\omega_{\ell,\ell+\Delta\ell,(i)} \approx [a_i + b_i\ell + c_i(\ell - \bar{\ell})^2 + \mathcal{O}((\ell - \bar{\ell})^3)] \Delta\ell, \quad (8.25)$$

in the neighborhood of $\ell \sim \bar{\ell}$, where i indexes the particular mechanism causing a shift, of which there may be multiple. Since the angular momentum distribution is localized, $\bar{\ell} \gg \ell - \bar{\ell}$

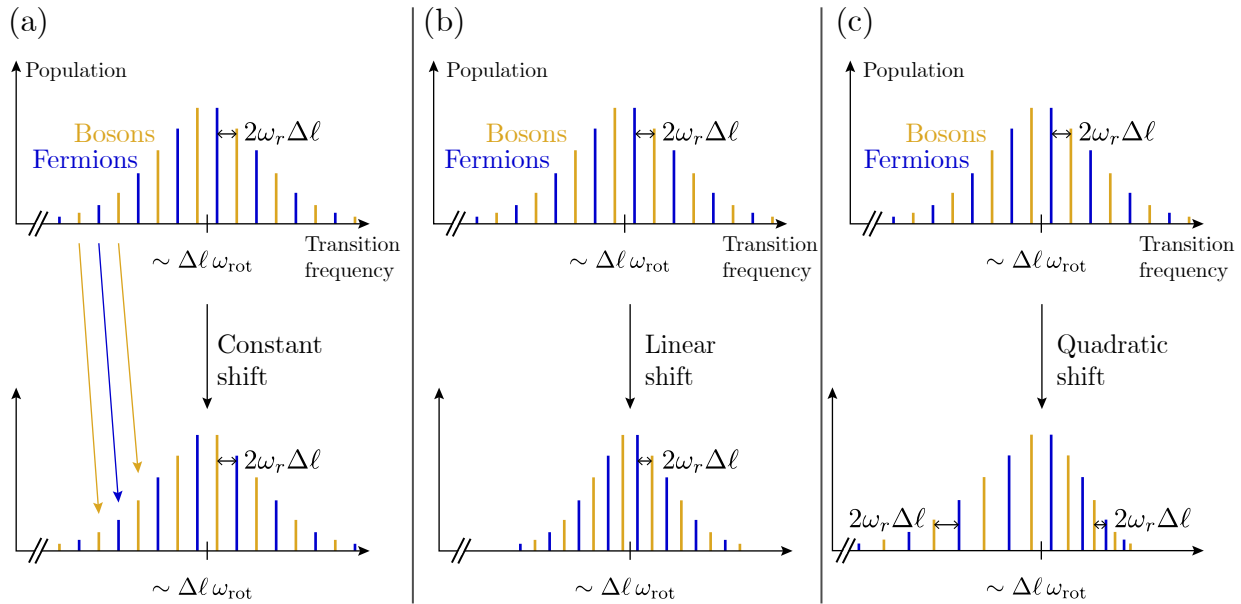


Figure 8.7: Illustration of shifts to the rotational transition frequency, which are (a) independent of ℓ , (b) linear in ℓ , and (c) quadratic in ℓ . The top spectrum of each subfigure is the transition frequency spectrum of the $\Delta\ell$ sideband for the ideal rotor, (8.24). The individual underlying $\ell \rightarrow \ell + \Delta\ell$ transitions within the $\Delta\ell$ sideband, centered at approximately $\Delta\ell\omega_{\text{rot}}$, are shown. Each is color coded by whether they are odd or even, so that if the particles are bosons then only the gold transitions occur, if they are fermions then only the blue transitions occur, and if they are distinguishable then all transitions occur. The example constant shift shown in (a) is exactly $2\omega_r\Delta\ell$. Linear shifts (b) change the effective rotational constant ω_r . For quadratic shifts (c), the effective rotational constant becomes dependent on ℓ .

for all values of ℓ which are occupied. We write the linear term in terms of ℓ rather than $\ell - \bar{\ell}$ for reasons which become apparent in Sec. 8.4.4. We ignore terms which are cubic and higher-order in $\ell - \bar{\ell}$. The transition frequency, including all shifts, is

$$\omega_{\ell,\ell+\Delta\ell} = [(\omega_{r0}\Delta\ell + a) + (2\omega_{r0} + b)\ell + c(\ell - \bar{\ell})^2] \Delta\ell, \quad (8.26)$$

where $a = \sum_i a_i$, $b = \sum_i b_i$, $c = \sum_i c_i$.

The effects of these three terms are as follows: a shifts the transition frequency independent of ℓ , contributing accumulated phase over the duration of the experiment. It is thus relevant to consider when considering extraction of the exchange phase itself. b shifts the spacing between transitions of neighboring ℓ manifolds, shifting the revival time to

$$T_{\text{rev}} = \frac{2\pi}{\Delta\ell(2\omega_{r0} + b)}. \quad (8.27)$$

c makes the spacing between these transition frequencies nonlinear, so that the phase contrast of the revival is imperfect. These three effects are illustrated in Fig. 8.7.

The remainder of this subsection lists a few effects which contribute transition frequency shifts. We do not estimate the magnitude of the terms of the shifts here, but instead do so in the following subsections within the context of each of the three steps of the experiment.

Centrifugal distortion

This effect is considered in detail in Sec. 3.5. To first order in the expansion parameter ϵ_ℓ , the eigenenergy is shifted by $\delta E_\ell = -\hbar D \ell^4$, where $D = 4\omega_{r0}^3/3\omega_x^2$ is the centrifugal distortion constant, where ω_{r0} is the rotational constant in the absence of centrifugal distortion. The leading term of the resulting shift to the transition frequency is

$$\delta\omega_{\ell,\ell+\Delta\ell} \approx -4D\ell^3\Delta\ell. \quad (8.28)$$

Expanding this about $\bar{\ell}$,

$$\begin{aligned} \delta\omega_{\ell,\ell+\Delta\ell} &\approx -4D [\bar{\ell}^3 + 3\bar{\ell}^2(\ell - \bar{\ell}) + 3\bar{\ell}(\ell - \bar{\ell})^2 + \mathcal{O}((\ell - \bar{\ell})^3)] \Delta\ell \\ &\approx [8D\bar{\ell}^3 - 12D\bar{\ell}^2\ell - 12D\bar{\ell}(\ell - \bar{\ell})^2] \Delta\ell. \end{aligned} \quad (8.29)$$

Section 3.5 defined ϵ_ℓ as the fractional change in rotor radius due to centrifugal distortion, which is $10^{-3} - 10^{-2}$ for typical parameters and is equal to $D\ell^2/\omega_{r0}$. It is convenient to write the non-rigid transition frequency shift in terms of the distortion factor at the center of the distribution, $\epsilon_{\bar{\ell}} = D\bar{\ell}^2/\omega_{r0} = \omega_{\text{rot}}^2/3\omega_x^2$:

$$\begin{aligned} \delta\omega_{\ell,\ell+\Delta\ell} &\approx \left[4\epsilon_{\bar{\ell}}\omega_{\text{rot}} - 12\epsilon_{\bar{\ell}}\omega_{r0}\ell - \frac{24\epsilon_{\bar{\ell}}\omega_{r0}^2}{\omega_{\text{rot}}}(\ell - \bar{\ell})^2 \right] \Delta\ell \\ &\approx \left[\frac{4\omega_{\text{rot}}^3}{3\omega_x^2} - \frac{4\omega_{\text{rot}}^2\omega_{r0}}{\omega_x^2}\ell - \frac{8\omega_{\text{rot}}\omega_{r0}^2}{\omega_x^2}(\ell - \bar{\ell})^2 \right] \Delta\ell. \end{aligned} \quad (8.30)$$

Here we have used $\omega_{\text{rot}} = 2\omega_{r0}\bar{\ell}$, which does not hold exactly in the presence of the imperfections considered in this subsection, but we apply it here for the purpose of estimating the magnitude of these effects.

Residual quadrupole fields

A residual static quadrupole potential shifts the transition frequencies by (7.10)

$$\delta\omega_{\ell,\ell+\Delta\ell} = \frac{\omega_{hr,\text{resid}}^4}{512\omega_{r0}^3\ell^3}\Delta\ell, \quad (8.31)$$

where $\omega_{hr,\text{resid}}$ is the horizontal rocking mode frequency left by the residual quadrupole potential. Expanding about $\bar{\ell} - \ell$,

$$\delta\omega_{\ell,\ell+\Delta\ell} \approx \frac{\omega_{hr,\text{resid}}^4}{32\omega_{\text{rot}}^3} \left[2 - \frac{3\omega_{r0}}{\omega_{\text{rot}}}\ell + \frac{12\omega_{r0}^2}{\omega_{\text{rot}}^2}(\ell - \bar{\ell})^2 \right] \Delta\ell. \quad (8.32)$$

Finite temperature of other modes

From (7.12),

$$\delta\omega_{\ell,\ell+\Delta\ell} \approx 4\omega_{r0}^2 \left(\frac{n_s}{\omega_s} + \frac{n_{vr}}{\omega_{vr}} \right) \ell \Delta\ell. \quad (8.33)$$

Here we have only a term linear in ℓ .

Aharonov-Bohm phase

A local magnetic field is present at the location of the ions in order to provide Zeeman splitting. As the ions are charged particles enclosing an area of space, the Aharonov-Bohm effect will produce a geometric phase in their free evolution. The Aharonov-Bohm effect shifts the rotor's Hamiltonian from $\hbar\omega_{r0}L_z^2$ to

$$H = \hbar\omega_{r0}(L_z - 2erA_\phi)^2, \quad (8.34)$$

where A_ϕ is the angular component of the magnetic vector potential, e is the ions' charge, and r is the rotor radius. The eigenenergies of this Hamiltonian are

$$E_\ell = \hbar\omega_{r0} \left(\ell - \frac{e\Phi_B}{\pi\hbar} \right)^2 \quad (8.35)$$

where Φ_B is the magnetic flux through the rotor. This effect therefore shifts the transition frequencies by

$$\delta\omega_{\ell,\ell+\Delta\ell} = -\omega_{r0} \frac{2e\Phi_B}{\pi\hbar} \Delta\ell. \quad (8.36)$$

This shift is a constant independent of ℓ , since the area swept out by the two different terms of the superposition is a function only of their relative rotation rate.

8.4.2 Observing the $\Delta\theta = 2\pi$ revival

Requirements for observing the revival signal when the rotational superposition has undergone a relative rotation of 2π are unrelated to symmetrization. We can break the requirements into three categories:

- The coherence of the superposition must last longer than the time it takes for the 2π relative rotation to occur. This has thus far constituted the main experimental challenge. This subsection primarily considers how to optimize rotational coherence relative to revival time.
- The phase contrast due to the initial superposition created must also be sufficient, as it places an upper limit on the phase contrast of any subsequent revival.
- The spacing in $\ell \rightarrow \ell + \Delta\ell$ transition frequencies must be sufficiently linear across the distribution of occupied angular momentum states, as a nonlinearity in this spacing will limit the visibility of the revival.

Rotational decoherence from angular momentum diffusion

The primary hindrance to performing the rotational interferometer experiment has thus far been poor rotational coherence, limited by angular momentum diffusion. Here, the contribution of diffusion to decoherence differs slightly from that considered in Sec. 7.4.2, as there is no spin-echo to reverse the angular separation. The corresponding decoherence envelopes for the phase contrast of the excitation and parity in the presence of angular momentum diffusion are instead

$$C_{\text{exc}}(T) = \exp \left(-\frac{DT}{2\hbar^2} [1 - \text{sinc}(4\Delta\ell\omega_r T)] \right), \quad (8.37\text{a})$$

$$C_{\text{par}}(T) = \exp \left(-\frac{DT}{2\hbar^2} [1 - \text{sinc}(8\Delta\ell\omega_r T)] \right). \quad (8.37\text{b})$$

The excitation contrast envelope differs from (7.25) by a factor of 2 in the oscillation frequency because in the absence of the echo pulse, it takes half the time for the rotor's quadrupole moment to return to its initial orientation (in the co-rotating frame). The parity contrast oscillates at a factor of 2 faster still, because the $|\ell\rangle + |\ell + 2\Delta\ell\rangle$ superposition separates twice as quickly as the $|\ell\rangle + |\ell + \Delta\ell\rangle$ superposition.

We require that the rotational coherence lasts at least as long as the time it takes for the superpositions to undergo a 2π relative rotation. This is $T_{\text{rev}} = \pi/\Delta\ell\omega_r$ if measuring the excitation and is $T_{\text{rev}}/2 = \pi/2\Delta\ell\omega_r$ is measuring the parity. If we define the rate of angular separation as $\Delta\omega = 2\omega_r\Delta\ell$ for the excitation and $\Delta\omega = 4\omega_r\Delta\ell$ for the parity, then in both cases we require that the coherence lasts longer than $2\pi/\Delta\omega$. We may define a general decoherence rate $\gamma = 1/T_{\text{coh}}$, where the coherence time T_{coh} is the time it takes for the phase contrast to reduce by a factor of e : $C(T_{\text{coh}}) = e^{-1}$. If we scale both the decoherence rate γ and the diffusion rate D/\hbar^2 by $\Delta\omega/2\pi$, we find a universal relation which implicitly defines the scaled decoherence rate in terms of the scaled diffusion coefficient:

$$\exp \left(-\frac{D^*}{2\gamma^*} \left[1 - \text{sinc} \left(\frac{4\pi}{\gamma^*} \right) \right] \right) = e^{-1}. \quad (8.38)$$

The dimensionless diffusion coefficient is defined as $D^* = 2\pi D/\hbar^2\Delta\omega$ and the dimensionless decoherence rate is defined as $\gamma^* = 2\pi\gamma/\Delta\omega$. Eq. (8.38) is valid for both the excitation and the parity, since the latter has both double the angular separation rate and double the instantaneous decoherence rate. In the limit of large diffusion this relation yields the $\gamma \sim D^{1/3}$ scaling found in Sec. 7.4.2, but here we leave the relation more general. Figure 8.8 plots the scaled decoherence rate against the scaled diffusion coefficient. For reference, the curve corresponding to the case of including a spin-echo pulse included, (7.25), is also plotted, along with the measurements from Fig. 7.15. For the interferometer experiment, we require $\gamma^* < 1$. The scaling becomes more favorable as we approach the target regime. The data points corresponding to no injected noise serve as a reference point for the diffusion due to intrinsic noise in our system.

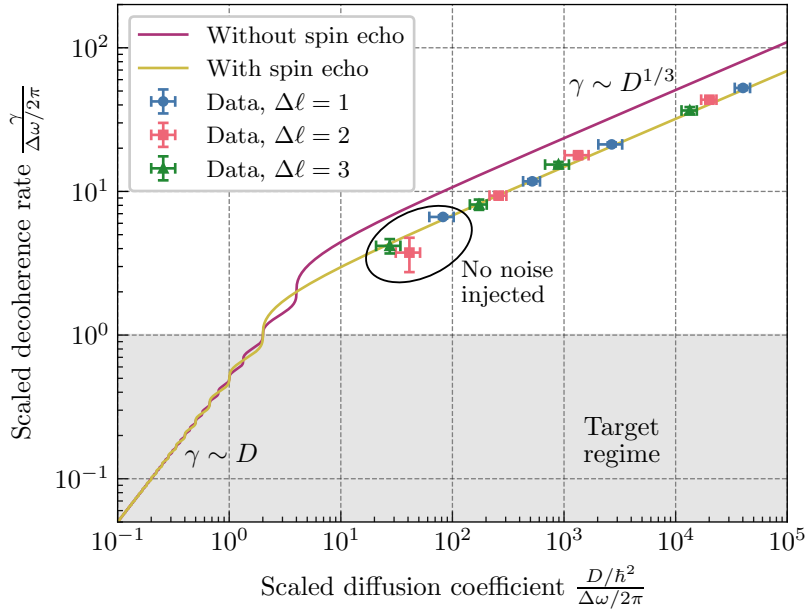


Figure 8.8: Scaled decoherence rate versus scaled diffusion coefficient. The target regime is where the scaled decoherence rate is less than 1.

We can translate this relation to be more practical, in terms of experimental parameters of our system. Section 7.4.4 considers how to improve the absolute rotational coherence time in these terms. For the interferometer experiment, the figure of merit is instead the ratio of the coherence time to the revival time, where the revival time scales as

$$T_{\text{rev}} \sim \Delta\ell^{-1} \omega_r^{-1} \sim \Delta\ell \omega_x^{-4/3}. \quad (8.39)$$

Thus in general, the ratio of the coherence time to the revival time scales as

$$\frac{T_{\text{coh}}}{T_{\text{rev}}} = \frac{1}{\gamma T_{\text{rev}}} \sim \Delta\ell \omega_x^{4/3} \gamma^{-1}. \quad (8.40)$$

The scaling of γ with the relevant parameters depends on the regime, defined by the scaled diffusion coefficient D^* , i.e. the rate of diffusion relative to the rate of angular separation of the superposition. In the limit of fast diffusion where $D^* \gg 1$, (8.40) becomes

$$\frac{T_{\text{coh}}}{T_{\text{rev}}} \sim \Delta\ell^{1/3} \omega_x^{4/3} \omega_{\text{rot}}^{1/3} \quad (8.41a)$$

when also limited by $1/f$ noise, from (7.32). In opposite limit $D^* \ll 1$, when the diffusion is slow compared to the relative rotation frequency, $\gamma \sim D \sim \omega_x^{-8/3} \omega_{\text{rot}}^{-1}$ (7.34), so that

$$\frac{T_{\text{coh}}}{T_{\text{rev}}} \sim \Delta\ell \omega_x^4 \omega_{\text{rot}}. \quad (8.41b)$$

We may improve this ratio by using higher-order superpositions, higher trap frequency, or a faster rotation frequency.

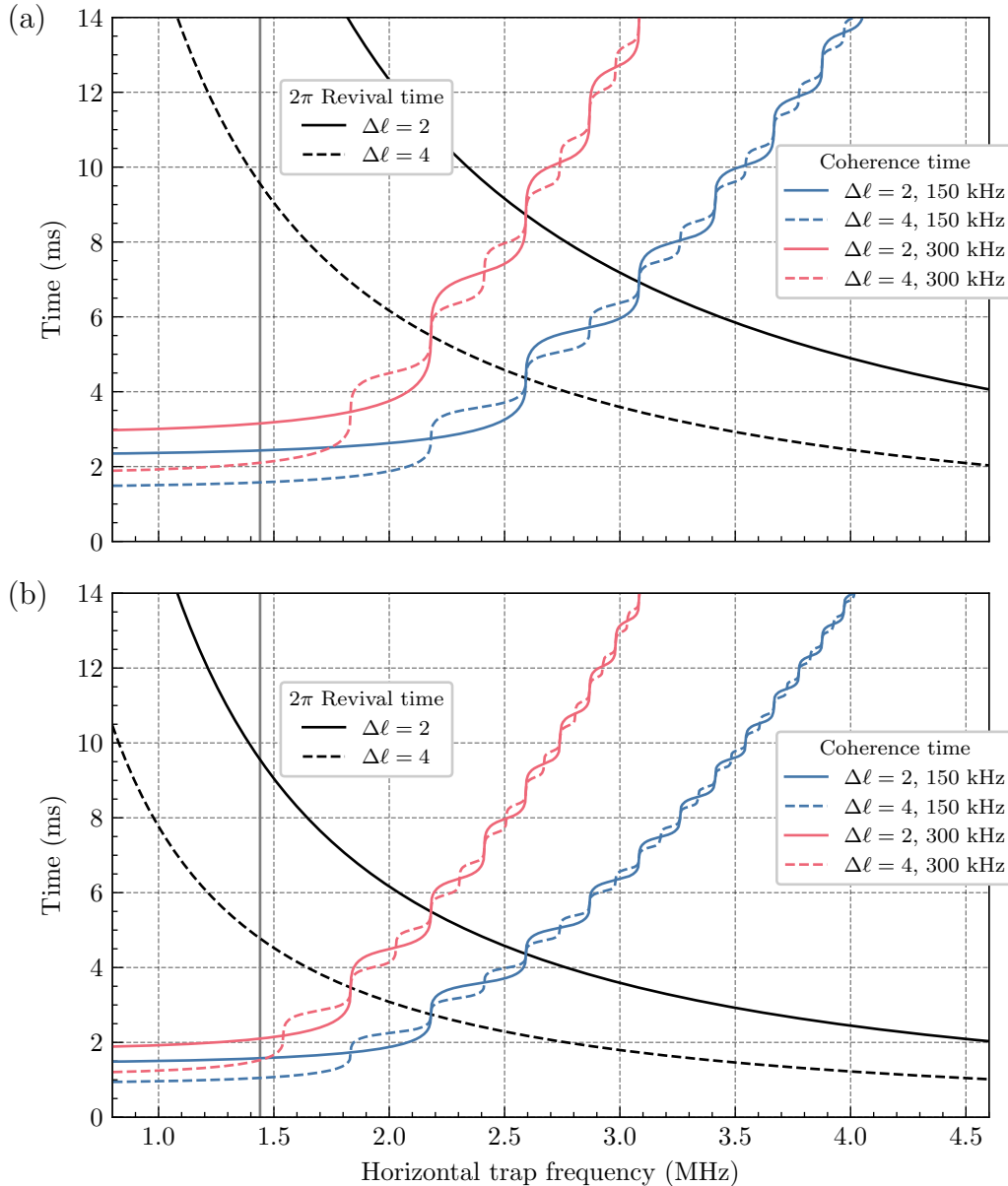


Figure 8.9: 2π revival time and diffusion-limited rotational coherence time plotted against trap frequency, for various combinations of $\Delta\ell$ and rotation frequency, for (a) excitation and (b) parity. For the excitation, the 2π revival time is equal to T_{rev} as defined by (8.15), and for the parity, the 2π revival time is equal to $T_{\text{rev}}/2$. The dependence on rotation frequency assumes $1/f$ noise. The vertical line is at 1.44 MHz, where rotational coherence was measured.

- Higher-order superpositions exchange faster. They also decohere faster in the fast-diffusion limit, but not in the slow-diffusion limit.
- Higher trap frequency increases the rotational constant ω_r , thus speeding up the relative rotation rate for a given $\Delta\ell$ -order superposition, exchanging faster. It also makes the rotor smaller than thus significantly less sensitive to noise. This benefit is cancelled by the faster decoherence rate in the fast-diffusion limit, but not in the slow-diffusion limit.
- Higher rotation frequency makes the rotor sensitive to noise at a higher frequency, which will have a lower spectral density if the noise scales as $1/f$.

Of these scalings, the trap frequency scales the strongest. The easiest way to improve the ratio of the coherence time to the revival time is thus to increase the horizontal trap frequency. Figure 8.9 plots both the coherence time and revival time against the trap frequency for a few values of rotation frequency and $\Delta\ell$. The vertical line is at 1.44 MHz trap frequency, the trap frequency used for the data presented in Chapter 7. These data serve as a reference point for the noise level to set the coherence times³.

Some considerations for adjusting experimental parameters so that the coherence time exceeds the revival time are follows:

- **Increasing the trap frequency.** This can be done by either applying a higher amplitude RF drive to the trap's RF electrodes to increase the horizontal and vertical trap frequencies proportionally, by applying a DC bias to one of the RF electrodes to increase the horizontal trap frequency at the cost of the vertical trap frequency, or a combination of the two. Increasing the RF amplitude could be done by using a resonator with a higher Q-factor, or by using an RF amplifier. The latter could compromise trap frequency stability, another source of rotational decoherence, if not used along with active stabilization. Figure 8.10 shows how a DC bias can change the trap frequency when the unbiased horizontal trap frequency is 2.5 MHz using a numerical simulation of the ring trap. A DC bias voltage of 10 V can increase the horizontal trap frequency from 2.5 MHz to 3.3 MHz without further increasing the RF drive amplitude. The vertical trap frequency must be kept larger than the horizontal for the crystal to form a rotor in the xy -plane. Furthermore, lowering the ratio of the vertical to the horizontal trap frequency lowers the vertical rocking mode frequency $\omega_{vr} = \sqrt{\omega_z^2 - \omega_x^2}$, which can increase its contribution to rotational transition frequency shifts (8.33) and can increase its heating rate, thus lowering the visibility of the $\Delta\theta = \pi$ exchange revival (Sec. 8.4.3). However, both of these effects are likely to be small.

³Note that the coherence times shown in Fig. 8.9 are also scaled from the reference measurements to infer coherence times without a spin-echo pulse given measurements using a spin-echo pulse. For example, the actual measured coherence time for $\Delta\ell = 2$ at 150 kHz rotation and 1.44 MHz trap frequency is $\sqrt[3]{4}$ times longer than what is shown in Fig. 8.9.

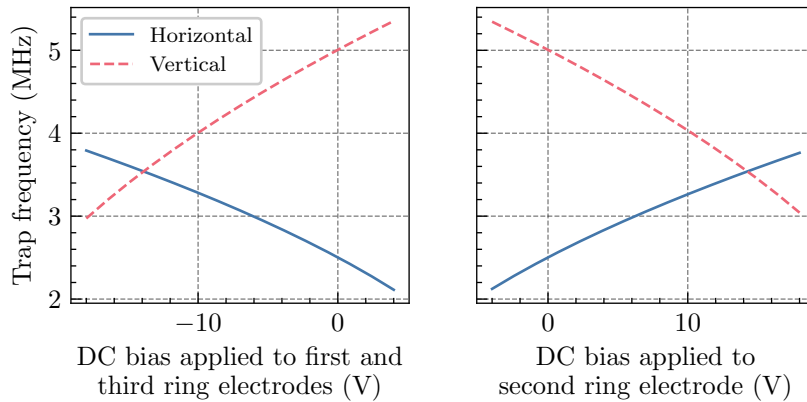


Figure 8.10: Secular trap frequencies of the ring trap as a function of DC bias from numerical simulations. 172 V amplitude RF is applied at 21.3 MHz, giving an unbiased horizontal trap frequency of 2.5 MHz.

- **Creating higher-order superpositions.** As the horizontal trap frequency is increased, the rotor radius is reduced, thus reducing the dimensionless parameter $\zeta = 2\pi r/k_{\parallel}$. Achieving an acceptable Rabi frequency on a higher-order sideband, $\Omega_{\Delta\ell} = \Omega J_{\Delta\ell}(\zeta)$, then requires a deeper tilt of the vertical 729 nm beam, or more laser power overall (Sec. 6.3). Also, preparing higher-order superpositions is more challenging since the linewidth of the $\Delta\ell$ sideband is proportional to $\Delta\ell$, hurting the achievable initial phase contrast. This can be mitigated by finding a way to prepare a narrower initial angular momentum distribution. A few advanced techniques, which have not been tested experimentally, could also aid in the preparation in higher-order superpositions:
 - *Light with orbital angular momentum.* Rather than a tilted vertical plane wave, one may use a vertical 729 nm beam in an orbital angular momentum (OAM) mode to impart transverse angular momentum. OAM light has been used to impart angular momentum onto microscopic particles [93, 94] and has even been used to excite the transverse vibrational motion of a trapped ion’s vibrational motion [95]. For our rotor, OAM light would yield different coupling strengths to $\Delta\ell$ sidebands than a plane wave, which may enhance the coupling strength of a desired high-order $\Delta\ell$ sideband. However, it is not yet known how the rotational sideband coupling strengths would be modified, and it may depend on the size of the OAM beam relative to the rotor [96].
 - *Concatenated ladder pulses.* Ref. [97] demonstrates the creation of high-order superpositions of Fock states with the form $|0\rangle + |n\rangle$, with n up to 100, using the vibrational motion of one trapped ion. This is done addressing only low-order sidebands, first applying a blue-sideband $\pi/2$ pulse and then applying alternating red- and blue-sideband π pulses to bring the initial superposition state up the number state “ladder”. The same technique could be used in our trapped-ion

rotor to create high-order rotational superpositions without needing to address a high-order $\Delta\ell$ sideband. The experiment may in fact be simplified when applied to a rotor, since the coupling strengths of the rotational sidebands do not change as ℓ changes, simplifying calibration.

- **Increasing the rotation frequency.** In principle, increasing the rotation frequency is simply a matter of choosing a higher target rotation frequency during rotational state preparation. However, we have seen that rotational state preparation is not consistently reliable, and have not succeeded in preparing the rotor at a rotation frequency faster than 350 kHz for unknown reasons. Using a faster rotation frequency also worsens effects from centrifugal distortion, though this is mitigated by using a higher horizontal trap frequency which stiffens the rotor.

Rotational decoherence from trap frequency instability

From (7.15), the coherence time due to trap frequency instability is

$$T_{\Delta\ell}^{\text{coh}} = \frac{3\omega_x}{4\omega_{\text{rot}}\Delta\ell} T_x^{\text{coh}} \quad (8.42)$$

where T_x^{coh} is the coherence time of the horizontal trap frequency, which may be measured using a $|0\rangle + |1\rangle$ state of the horizontal COM vibrational mode. Increasing the rotation frequency reduces the coherence time because the rotational superposition has a larger transition frequency. If the vibrational coherence stays constant as the trap frequency is improved, then increasing the trap frequency also improves rotational coherence times. However, it is more likely that the relative vibrational stability will remain approximately constant as the trap frequency is increased, so that $\omega_x T_x^{\text{coh}}$ remains constant.

Unlike Sec. 7.2.4, here the relevant vibrational coherence time is unechoed. Slowly drifting trap frequency fluctuations will therefore contribute to decoherence in the interferometer experiment, whereas they are cancelled by the echo pulse in the measurements shown in Fig. 7.5. The unechoed vibrational coherence time has not been measured recently, but was found to be approximately 6.5 ms at $\omega_x = 2\pi \times 1.6$ MHz in December 2020, which was prior to the construction of the Faraday cage. This is a fractional instability of $[1/(6.5 \text{ ms})]/(2\pi \times 1.6 \text{ MHz}) \approx 1.5 \times 10^{-5}$. Assuming this fractional stability to be constant as the horizontal trap frequency is raised to 3 MHz, a $\Delta\ell = 4$ superposition rotating at 300 kHz will have a trap-frequency-stability-limited coherence time of 6.6 ms, compared to a revival time of 3.7 ms. Note that the decoherence rate due to trap frequency instability always scales linearly with $\Delta\ell$, while that due to diffusion always scales sublinearly with $\Delta\ell$. Thus a choice of $\Delta\ell$ which is too large may make trap frequency stability the limiting decoherence source.

Electronic coherence

The spin-echo pulse used in electronic coherence measurements presented in Fig. 7.4 also significantly aids the electronic coherence. In the absence of this echo pulse, even using line triggering, the electronic coherence is poor, lasting about 1 ms. This problem may be solved in the rotational interferometer experiment by applying spin-echo pulses on the carrier only, thus echoing the electronic state without affecting the rotational motion. An even number of carrier echo pulses must be used to restore the electronic state before the final $\pi/2$ rotational sideband pulse. The optimal spacing of the pulses will depend on the nature of the slow magnetic field or laser frequency fluctuations which otherwise cause electronic decoherence [98].

Initial phase contrast

The visibility of the revival interference fringes will also be limited by the fidelity of the initial rotational sideband $\pi/2$ pulse, which sets the initial phase contrast. The choice of $\Delta\ell$ cannot be too high to preclude sufficient fidelity rotational operations, though a narrower angular momentum distribution of the use of OAM light can help.

Commensurate spacings in rotational transition frequencies

The ideal dynamical phases given in (8.23) allow for a phase contrast revival because the phase difference of all neighboring ℓ -manifolds, e.g. $\phi_{1,\ell+1} - \phi_{1,\ell}$ (or $\phi_{1,\ell+2} - \phi_{1,\ell}$ for indistinguishable particles), is a constant which is independent of ℓ . Revival occurs when this constant difference is a multiple of 2π . This constant phase difference results from a linear spacing between neighboring transition frequencies $\omega_{\ell,\ell+\Delta\ell}$ and $\omega_{\ell+1,\ell+\Delta\ell+1}$, whose difference is $2\Delta\ell\omega_r$. The linear spacing of transition frequencies in turn arises from the quadratic energy spectrum $E_\ell = \hbar\omega_r\ell^2$. Imperfections which shift the eigenspectrum nonuniformly, so that the spectrum is no longer quadratic, therefore reduce the visibility of the phase contrast revival by creating nonuniformly spaced rotational transition frequencies. This is the effect illustrated in Fig. 8.7(c).

The effects which contribute to this mechanism of reduced revival visibility are those whose corresponding transition frequency shifts $\delta\omega_{\ell,\ell+\Delta\ell}$ include a term which is nonlinear in ℓ . From (8.26),

$$\frac{d\omega_{\ell,\ell+\Delta\ell}}{d\ell} = [(2\omega_{r0} + b) + 2c(\ell - \bar{\ell})] \Delta\ell. \quad (8.43)$$

The c term changes the spacing of the transition frequency across the angular momentum distribution, which spans from $\ell = \bar{\ell} + \sigma_\ell$ to $\ell = \bar{\ell} - \sigma_\ell$. At the revival time T_{rev} , the phase difference between manifolds is approximately

$$\phi_{1,\ell+1} - \phi_{1,\ell} \approx \frac{d\omega_{\ell,\ell+\Delta\ell}}{d\ell} T_{\text{rev}} \approx 2\pi \left[1 + \frac{c(\ell - \bar{\ell})}{\omega_{r0}} \right]. \quad (8.44)$$

Across the angular momentum distribution, the fractional difference in the revival phase is thus $2c\sigma_\ell/\omega_{r0}$.

Of the effects considered in Sec. 8.4.1, only centrifugal distortion and residual quadrupole shifts have a nonlinear transition frequency shift term.

- **Centrifugal distortion.** From (8.30),

$$c_i = -\frac{8\omega_{\text{rot}}\omega_{r0}^2}{\omega_x^2} \implies \frac{2c_i\sigma_\ell}{\omega_{r0}} = -\frac{16\omega_{\text{rot}}\omega_{r0}\sigma_\ell}{\omega_x^2}. \quad (8.45)$$

Conservatively assuming unfavorable parameters of $\omega_{\text{rot}} = 2\pi \times 300 \text{ kHz}$, $\omega_x = 2\pi \times 1.5 \text{ MHz}$, $\omega_{r0} = 2\pi \times 14 \text{ Hz}$, and $\sigma_\ell = 100$, the fractional difference in the revival phase across the distribution is 3×10^{-3} .

- **Residual quadrupoles.** From (8.32),

$$c_i = \frac{3\omega_{hr,\text{resid}}^4\omega_{r0}^2}{8\omega_{\text{rot}}^5} \implies \frac{2c_i\sigma_\ell}{\omega_{r0}} = \frac{3\omega_{hr,\text{resid}}^4\omega_{r0}\sigma_\ell}{4\omega_{\text{rot}}^5}. \quad (8.46)$$

Conservatively assuming unfavorable parameters of $\omega_{hr,\text{resid}} = 2\pi \times 40 \text{ kHz}$, $\omega_{\text{rot}} = 2\pi \times 100 \text{ kHz}$, $\omega_{r0} = 2\pi \times 50 \text{ Hz}$, and $\sigma_\ell = 100$, the fractional difference in the revival phase across the distribution is 1×10^{-3} .

Both of these effects are therefore likely to be negligible in reducing the revival contrast visibility.

8.4.3 Observing the $\Delta\theta = \pi$ exchange revival

The only requirement for observing the $\Delta\theta = \pi$ exchange revival beyond those for observing the $\Delta\theta = 2\pi$ full rotation revival is for the rotational degree of freedom to be symmetrized. As shown in Sec. 8.2, for this it suffices to cool the vertical rocking mode to its ground state. Residual population in the $|n_{vr} = 1\rangle$ state, for example, will contribute population in the rotational degree of freedom of the “wrong” exchange symmetry, limiting the contrast visibility of the exchange revival, but not of the full rotation revival. It is straightforward to sideband cool the vertical rocking mode so that > 90% of the population is in the ground state.

Heating of the vertical rocking mode

We may worry that heating of the vertical rocking mode during the experiment will move population from the $|n_{vr} = 0\rangle$ ground state to the $|n_{vr} = 1\rangle$ state. The nature of the heating mechanism when the ions freely rotate is different from when the ions are pinned to well-defined equilibrium positions, but the order of magnitude of the heating rate is the same.

To see this, we consider the Hamiltonian for the two-ion rotor interacting with electric-field gradient noise, given in (7.17). The relevant terms are those which contain the vertical

rocking mode ladder operators, a_{vr} , a_{vr}^\dagger . Using (7.18), we find that the relevant terms in (7.17) are the xz and yz terms. These terms of the Hamiltonian give

$$H_{E,vr}(t) = r \sqrt{\frac{\hbar}{m\omega_{vr}}} (a_{vr} + a_{vr}^\dagger) [\mathcal{E}_{\rho z}(t)L_+ + \mathcal{E}_{\rho z}(t)^*L_-], \quad (8.47)$$

where $\mathcal{E}_{\rho z} = \partial_z E_x - i\partial_z E_y$ is a complex-valued electric field gradient. These field gradients couple the vertical rocking motion to the rotational motion at their sum and difference frequencies. Unlike a pinned two-ion crystal, the vertical rocking motion in the rotor cannot heat without coupling to another mode. There are also terms by which the same gradients couple the vertical rocking, stretch, and rotational motion all together, but these are suppressed by a factor of $\sqrt{\hbar/m\omega_s}/r$ relative to (8.47) and are thus negligible. Thus the dominant mechanism by which the vertical rocking mode heats in the rotating ion crystal is by exchanging quanta with the rotational motion. Note that this interaction preserves the *overall* exchange symmetry, as must be the case since the Hamiltonian itself is exchange-symmetric⁴.

The quadrupole moment for the heating rate of the vertical rocking mode in the rotating ion crystal is $er\sqrt{\hbar/m\omega_{vr}}$, the ion-ion distance times the vertical rocking ground state wavefunction size. This is the same as the case of a pinned ion crystal. The heating rate itself is therefore of the same order. The heating rate of a differential mode of motion is slow compared to a comparable center-of-mass mode, as discussed in Sec. 5.1.1. We thus expect heating of the vertical rocking mode to be negligible.

8.4.4 Measuring the exchange phase

With the phase conventions defined in (8.23), the phases $\phi_{1,\ell}$ and $\phi_{2,\ell}$ are the difference between two terms: one proportional to the laser detuning from the carrier, and one equal to the dynamical phase from the rotation. This difference is small (zero if Δ is exactly on resonance with the $\ell \rightarrow \ell + \Delta\ell$ transition), but each of the terms is large.

To identify the exchange phase, it is most convenient to organize the total phase into two categories: terms which are proportional to ℓ , and terms which are constant with ℓ , as is done in Tab. 8.1⁵. Those which are proportional to ℓ become $\pi\ell$ at half the revival time, which together reduce to the exchange phase as shown in Sec. 8.3.2. However, we measure only the *total* phase, $\phi_{1,\ell}$ (for excitation) or $\phi_{2,\ell}$ (for parity) (8.22). It is thus necessary to know the terms which remain after collapsing the exchange phase down to 0 or π . These terms are comprised of all dynamical and geometric phases, and must be known to an absolute uncertainty within π in order to extract the exchange phase from the measured

⁴Note also that, when the vertical rocking mode heats in a pinned two-ion crystal, exchange symmetry is still preserved even though only the rocking mode changes its quantum number. This is possible via the extra degeneracy due to the pinning (Sec. 8.2.1).

⁵Here we neglect terms which are quadratic and higher-order in ℓ , which do not enter directly into these considerations as long as these terms have been expanded about the center of the distribution $\bar{\ell}$, as done in Sec. 8.4.1. Sec. 8.4.2 has shown that these contributions are negligible.

total phase. Since $\ell \sim 10^3$, the remaining constant term will similarly be of order $10^3 \times 2\pi$, and thus requires very precise calibration.

As an example, let us consider the exchange revival in the excitation, so that we consider the phase $\phi_{1,\ell}$ at time $T_{\text{rev}}/2$, for now ignoring any shifts due to imperfections. This can be seen in Tab. 8.1. We also suppose $\Delta\ell = 4$, so that the $\frac{\pi}{2}\Delta\ell$ term becomes $2\pi \rightarrow 0$ for simplicity. We are left with the constant phase $-\pi\Delta/2\Delta\ell\omega_r$ plus the exchange phase, where Δ is the detuning from the carrier. To interpret this leftover constant phase, we can write $\Delta = \Delta\ell\omega_{\text{rot}} + \delta$, defining δ as the detuning from the rotational sideband being addressed. Then the leftover phase is

$$-\frac{\pi\Delta}{2\Delta\ell\omega_r} = -\pi \left(\frac{\omega_{\text{rot}}}{2\omega_r} + \frac{\delta}{2\Delta\ell\omega_r} \right). \quad (8.48)$$

The first of these terms is the dynamical phase: in the time it takes the rotational superposition to undergo a π relative rotation, the crystal makes $\omega_{\text{rot}}/4\Delta\ell\omega_r$ full rotations, and acquires a phase equal to $2\pi\Delta\ell$ times this number. The second term is additional phase acquired due to the detuning. The dynamical phase is of order $\sim 10^3 \times 2\pi$, but should be known to within π to identify the exchange phase. Shifts due to imperfections will also contribute to the dynamical phase, and geometric phases will contribute as well. These large dynamical and geometric phases are likely to be the main challenge of measuring the exchange phase.

We may also think of the precision required to measure the exchange phase in terms of transition frequencies. Knowing the exchange phase is equivalent to knowing whether the $\ell \rightarrow \Delta\ell$ transitions being driven on the $\Delta\ell$ sideband are from odd or even ℓ . Referring to Fig. 8.7(a), a shift in transition frequency of only $2\omega_r\Delta\ell$ swaps transition frequencies of odd and even ℓ . This is equivalent to a π phase shift in the dynamical and geometric phases. These shifts therefore need to be known to within $2\omega_r\Delta\ell$ in order to be able to identify the exchange phase. All shifts considered here are proportional to $\Delta\ell$, so that using higher $\Delta\ell$ reduces the revival time but proportionally increases the shift. Ignoring the $\Delta\ell$ factor then, all shifts must be known to within $2\omega_r < 100$ Hz in order to know the exchange phase with an uncertainty of less than π (see also (8.52)).

Some information may be gained by measuring the phase at the revival time, $\phi_1(T_{\text{rev}})$. This is the same regardless of particle identity, and thus does not depend on exchange phase. Ignoring slow magnetic field drifts during the experiment, the phase at the exchange time must be either $\phi_1(T_{\text{rev}}/2) = \phi_1(T_{\text{rev}})/2$ or $\phi_1(T_{\text{rev}}/2) = \phi_1(T_{\text{rev}})/2 + \pi$. However, this does not disambiguate which of the two possibilities belongs to bosons and which to fermions.

Importantly, while the magnitude of some of the shifts considered here are dependent on the center of the angular momentum distribution $\bar{\ell}$ via the rotation frequency, it is not necessary to know $\bar{\ell}$ or the shape of the distribution itself very precisely to calibrate them. By organizing the ℓ -dependent phases into a term which becomes the exchange phase, we need only know the detuning of the laser pulse from the carrier frequency, rather than the detuning from the center of the rotational sideband being addressed.

Shifts to the revival time

The dynamical and geometric phases will depend on the Ramsey time at which the measurement is made. Effects which shift the revival time therefore also shift these phases. In practice, the revival time may be directly measured. Still, here we estimate the magnitude of some effects which cause this shift.

As discussed in Sec. 8.4.1, the revival time is defined by the time at which the phases from all ℓ manifolds line up to differ by a multiple of 2π . Thus the term of the transition frequency shift which is proportional to ℓ , termed b_i in Sec. 8.4.1, is responsible for shifting the revival time (8.27). This term changes the spacing between neighboring transition frequencies $\ell \rightarrow \ell + \Delta\ell$ and $\ell + 1 \rightarrow \ell + \Delta\ell + 1$. The fractional shift in the revival time is $2\omega_{r0}/\sum_i b_i$. Assuming parameters of $\omega_{\text{rot}} = 2\pi \times 200 \text{ kHz}$, $\omega_x = 2\pi \times 3 \text{ MHz} \implies \omega_{r0} = 2\pi \times 35 \text{ Hz}$, the effects considered in Sec. 8.4.1 shift the transition frequency spacing as follows:

- Centrifugal distortion.

$$b_i = -\frac{4\omega_{\text{rot}}^2 \omega_{r0}}{\omega_x^2} = -2\pi \times 0.6 \text{ Hz}. \quad (8.49)$$

- Residual quadrupole fields.

$$b_i = -\frac{3\omega_{hr,\text{resid}}^4 \omega_{r0}}{32\omega_{\text{rot}}^4} = -2\pi \times 8 \times 10^{-4} \text{ Hz} \quad (8.50)$$

assuming a horizontal rocking frequency due to residual quadrupoles of $\omega_{hr,\text{resid}} = 25 \text{ kHz}$.

- Finite temperature of other modes

$$b_i = 4\omega_{r0}^2 \left(\frac{n_s}{\omega_s} + \frac{n_{vr}}{\omega_{vr}} \right) = 2\pi \times 0.02 \text{ Hz} \quad (8.51)$$

assuming $n_{vr} = 0$ and $n_s = 20$ on average.

Centrifugal distortion is the only one of these effects likely to result in a measurable shift in the revival time. For $\Delta\ell = 2$, T_{rev} shifts from 7.14 ms to 7.27 ms, a change of about 2%, due to centrifugal distortion using these parameters.

Dynamical and geometric phases

Here we consider dynamical and geometric contributions to the revival phase itself from the effects considered in Sec. 8.4.1. These arise from the constant shifts in transition frequency, i.e. the a_i terms as defined in (8.32). These phases at the exchange time $T_{\text{rev}}/2$ are $a_i \Delta\ell T_{\text{rev}}/2$. For simplicity we estimate the magnitude of these phases ignoring the small

shifts to the transition frequency spacing b_i , so that the effective rotational constant is simply $\omega_r = \omega_{r0}$, and $T_{\text{rev}} = \pi/\Delta\omega_r$. The phase contribution at the exchange time is then

$$\phi_{\text{shift},i} = 2\pi \times \frac{a_i}{4\omega_r}. \quad (8.52)$$

We assume the same parameters of $\omega_{\text{rot}} = 2\pi \times 200 \text{ kHz}$, $\omega_x = 2\pi \times 3 \text{ MHz} \implies \omega_r = 2\pi \times 35 \text{ Hz}$.

- **Centrifugal distortion.**

$$\begin{aligned} a_i &= \frac{4\omega_{\text{rot}}^3}{3\omega_x^2} = 2\pi \times 1.19 \text{ kHz} \\ \phi_{\text{shift},i} &= 2\pi \times \frac{a_i}{4\omega_r} = 2\pi \times \frac{1.19 \text{ kHz}}{140 \text{ Hz}} = 2\pi \times 8.5. \end{aligned} \quad (8.53)$$

- **Residual quadrupole fields.**

$$\begin{aligned} a_i &= \frac{\omega_{hr,\text{resid}}^4}{16\omega_{\text{rot}}^3} = 2\pi \times 3 \text{ Hz} \\ \phi_{\text{shift},i} &= 2\pi \times \frac{a_i}{4\omega_r} = 2\pi \times \frac{3 \text{ Hz}}{140 \text{ Hz}} = 2\pi \times 0.02. \end{aligned} \quad (8.54)$$

assuming $\omega_{hr,\text{resid}} = 2\pi \times 25 \text{ kHz}$.

- **Aharanov-Bohm phase**

$$\begin{aligned} a_i &= -\frac{2e\Phi_B\omega_{r0}}{\pi\hbar} = -2\pi \times 55 \text{ Hz} \\ \phi_{\text{shift},i} &= 2\pi \times \frac{a_i}{4\omega_r} = -2\pi \times \frac{55 \text{ Hz}}{140 \text{ Hz}} = -2\pi \times 0.4. \end{aligned} \quad (8.55)$$

Here we have used $\Phi_B = B_{\parallel} \times \pi r^2$ and assumed a magnetic field of 4 G tilted 45° relative to the rotor plane, and have used that $\omega_r = 2\pi \times 35 \text{ Hz}$ corresponds to a rotor radius of $r = 1.35 \mu\text{m}$.

- **Magnetic field drifts.** Over the timescale of several milliseconds, the local magnetic field tends to drift, shifting the $|S\rangle \leftrightarrow |D\rangle$ electronic transition frequency on the order of kHz. This drift is typically matched to the 60 Hz AC wall power and thus can be made constant over experimental repetitions by line triggering. The Zeeman shift will contribute to the acquired phases $\phi_{1,\ell}$ and $\phi_{2,\ell}$ during the Ramsey experiment. This contribution is independent of ℓ , but in general will not accumulate at a constant rate. These drifts can be calibrated with a Ramsey measurement on the carrier transition.

All of these effects are likely to be considerable, with the exception of shifts due to residual quadrupole fields. It is likely straightforward to measure the local magnetic field to estimate the Aharonov-Bohm phase, as well as to directly measure phase drifts of the carrier transition. Effects of centrifugal distortion, however, may require careful measurement, and may possibly even require estimating the shift to second order, (i.e. beyond what is considered in Sec. 3.5) to resolve it to within the 100 Hz level. Rotating at 300 kHz rather than 200 kHz would increase the dynamical phase contribution (as estimated here to first order only) of centrifugal distortion from $2\pi \times 8.5$ to $2\pi \times 28.6$ radians.

The previous subsection estimates the shift in the revival time due to imperfections, estimating the shift to be about 2%. This changes the acquired dynamical and geometric phases by the same fraction. The dynamical phase contribution from centrifugal distortion may then be an appreciable fraction of 2π , necessitating accounting for this shift in revival time. In practice, rather than assuming $T_{\text{rev}} = \pi/\Delta\ell\omega_{r0}$, the revival time can be carefully measured directly. This is especially important when considering how shifts to the revival time change the phase contribution of the Δ term in Tab. 8.1. This phase contribution is more generally expressed as $-\Delta T_{\text{rev}}/2$. Because this phase is large $\sim 10^3 \times 2\pi$, T_{rev} should be carefully measured.

Summary

Measuring the exchange phase requires knowledge of all dynamical and geometric phases to within π . This is equivalent to knowing all relevant frequencies to within $\sim 2\omega_r$, the splitting between transition frequencies of neighboring ℓ . This is about $2\pi \times 100$ Hz or smaller, and depends on the choice of trap frequency. This information allows one to resolve whether transitions from odd or even ℓ are being addressed, from which it can be inferred that only odd or even ℓ were occupied to begin with. The frequencies to be known include the detuning from the carrier Δ as seen in Tab. 8.1, but also include shifts due to other effects. The former is of order hundreds of kHz, contributing phase of order $\sim 10^3 \times 2\pi$, and thus requires precise knowledge of the carrier frequency and the revival time, which itself also shifts from imperfections. Centrifugal distortion will contribute a smaller but still-substantial phase $\sim 10^1 \times 2\pi$ and thus should also be carefully accounted for. The geometric Aharonov-Bohm phase due to the rotor enclosing a finite magnetic field may also contribute a phase shift which is near 2π .

8.4.5 On using more than two ions

In principle, it is also possible to perform the interferometer experiment using a crystal of more than two ions. The main motivation for doing so would be to improve diffusion-limited rotational coherence. More ions would give the crystal a higher degree of rotational symmetry, making it insensitive to higher multipole orders of electric field noise. However, many of the considerations explored in this chapter change if more than two ions are used. A few of these differences are noted in this subsection.

Many of the differences noted depend on the degree of rotational symmetry, rather than directly on the number of ions in the crystal. Numerical simulations suggest that N ions in a planar rotor equilibrate along a single concentric ring up to $N = 5$. With $N = 6$, one ion sits at the center, so that the crystal still has only 5-fold rotational symmetry.

Rotational state preparation

A Coulomb crystal with three-fold or higher rotational symmetry is insensitive to quadrupole fields. While this helps with angular momentum diffusion, it complicates rotational state preparation. The eight outer DC electrodes of the ring trap provide enough degrees of freedom to produce an arbitrarily oriented potential with only up to two potential wells. They can create an octupole field, but its orientation is fixed.

If using three or more ions, a sufficiently strong pinning potential can break the crystal's rotational symmetry so that the crystal acquires an induced quadrupole moment. This pinning can then be used for rotational state preparation in the same way that has been done in this work. The height of the pinning potential due to the induced quadrupole would be weak compared to the case of two ions, which may complicate cooling of the pinned librational mode which maps onto the rotational mode. Compensating for this would likely require amplification of the voltage from the AWG used to provide the pinning potential, which is otherwise limited to $\pm 10\text{ V}$.

Rotational decoherence

An ion crystal with N -fold rotational symmetry is insensitive to electric field multipole orders up to $N - 1$. Thus, a crystal of three or more ions would not be affected by the noisy quadrupole electric fields that currently limit the electronic coherence. The dominant multipole for resonant electric field interactions is the $(N - 1)$ th-order gradient of the electric field, and the corresponding multipole moment of the crystal is proportional to r^N . The diffusion coefficient thus scales as

$$D \propto r^{2N} S_{\nabla^{N-1}\mathcal{E}}(N\omega_{\text{rot}}). \quad (8.56)$$

For each increment in multipole order, this diffusion coefficient is suppressed by a factor of about $(h/r)^2 \sim 10^3$, where $h = 181\text{ }\mu\text{m}$ is the distance of the ion crystal to the trap surface. The diffusion coefficient also scales more strongly with the radius and thus also more strongly with the horizontal trap frequency.

Observing phase contrast revivals

With two ions, a $\pi/2$ pulse on a rotational sideband creates a superposition of four states for each ℓ manifold. Similarly, there are eight such states with three ions: $|SSS, \ell\rangle$, $|DSS, \ell + \Delta\ell\rangle$, ..., $|DDD, \ell + 3\Delta\ell\rangle$. There are four different rotational states within each manifold ($\ell, \ell + \Delta\ell, \ell + 2\Delta\ell, \ell + 3\Delta\ell$), and thus more combinations of relative phases which could constructively or destructively interfere at exchange times.

Making the ions indistinguishable

An N -ion crystal has a total of $3N$ motional modes. More ions thus means more degrees of freedom which could contain distinguishing information about the ions' particle identity, whereas the only such mode in a 2-ion rotor is the vertical rocking mode. All of the additional modes which contain distinguishing information would also need to be cooled to their ground state, and would need to be maintained at this temperature throughout the experiment.

Measuring the exchange phase

The exchange phase is measurable with a two-ion crystal under the proposed experimental protocol because a relative rotation of π is equivalent to an exchange of the particles. With N ions, a relative rotation is more generally a cyclic permutation, which can be expressed as some combination of exchange operations. If N is odd, then the cyclic permutation is always equivalent to an even number of exchanges, thus making the total exchange phase 0 regardless of particle identity. For example, a 3-ion crystal in superposition undergoing a $2\pi/3$ relative rotation performs the permutation $\{1, 2, 3\} \rightarrow \{2, 3, 1\}$, which is equivalent to two exchange operations: $1 \leftrightarrow 2$ followed by $1 \leftrightarrow 3$. A measurement of the exchange phase may thus require the use of an even number of ions.

Chapter 9

Summary and outlook

This work has demonstrated the creation of non-classical states of the rotational motion of a trapped-ion Coulomb crystal, using a unique surface ion trap. This rotational motion features many characteristics which differ from the usual vibrational motion of Paul-trapped ion crystals. We have shown in Chapter 6 that the spacing of rotational sidebands of a coherent electronic transition can be set by choosing the rotation frequency of the crystal. We have also found agreement in the rotational sideband coupling strength as a function of sideband order $\Delta\ell$ with the theory established in Chapter 3. We have shown how to prepare the rotational state in such a way that addressing rotational sidebands results in clean coherent Rabi oscillations, which we have used to create superpositions of angular momentum states with reasonably high fidelity. Finally, with careful measurements and an application of fairly new theory to our system, we have studied the decoherence of these rotational superpositions and shown that it is limited by interaction with resonant electric-field gradient noise in Chapter 7. This is the first experimental study of decoherence of a quantum rotor through angular momentum diffusion, and agrees closely with theory.

For some time, the functionality of this experiment had been limited by electric field noise normal to the trap, which had been causing resonant heating of the vertical center-of-mass motion of the ions and preventing ground-state cooling of this motion. This in turn prevented clean addressing of the ion crystal's rotational motion. Following a long hiatus due to the COVID-19 pandemic in 2020, this noise was newly measured in early 2021. As discussed in Chapter 5, efforts were made to mitigate this noise, but were not successful until the construction of the Faraday cage in mid 2022. It is interesting to note that during this time, the heating rate in the direction parallel to the trap surface remained low, indicating that the electric field noise was strongly directed normal to the trap surface. It may be the case that this trap is particularly susceptible to such highly directed noise due to its high degree of circular symmetry. It may also be the case that surface-ion traps always exhibit their largest component of electric-field noise in the direction normal to the surface simply because the electrode which is physically closest to the ion crystal is the one directly underneath it. Nearly all other trapped-ion experiments which use surface traps do not address motion normal to the surface and thus would be insensitive to this noise if it were

present.

Coherently addressing the rotational motion of the Coulomb crystal crucially relies on a clean preparation of the rotational state. However, the success of the spin-up-and-release procedure established and studied in Chapter 6 is highly sensitive to many factors, many of which are not well-understood. It is difficult to predict under what conditions it will be successful and what conditions it will not be, and successful rotational state preparation has often been a matter of luck. In continuing this work, this lack of reliability may prove to be a significant limitation. Overcoming it may require a deeper understanding of what limits the reliability via careful theoretical and/or experimental study.

Having arrived at a detailed understanding of the mechanisms limiting the rotational coherence in our system, we have been able to establish how to overcome the decoherence by straightforward changes to experimental parameters, primarily by increasing the transverse trap frequency. This can be done without needing to lower the diffusion-causing electric-field gradient noise itself, which may in fact already be surface-noise limited. The experiment is thus in a favorable position for attempting the rotational interferometer experiment. Being able to observe phase coherence revivals appears to be fairly straightforward, while extracting the exchange phase from the revival signal is likely to be fairly challenging, requiring careful calibrations and calculations of dynamical and geometric phases.

Beyond the rotational interferometer experiment, the ring trap is likely to provide a platform for several other experiments which take advantage of its unique symmetry. The ability to carefully resolve and measure rotational sideband coupling strengths could provide a tool for studying the local angular momentum density of light carrying orbital angular momentum, which remains in some sense ambiguous and has not been measured before [96]. Also, quantum rotors in general feature a rich array of physical phenomena which are not present in harmonic oscillators. Further developing the control over the quantum state of the rotational degree of freedom could open the door to other rotor-based quantum experiments that are able to take advantage of the precision of trapped ions, such as a kicked quantum rotor to study quantum chaos [99]. Finally, the ring trap has in the past also been used to create a large (90 μm diameter), highly symmetric toroidal potential with many ions [15]. This is akin to a linear ion crystal, but with the special property of having intrinsic periodic boundary conditions. This modality of the ring trap may provide a platform for quantum simulations of phenomena which display unique behavior under periodic boundary conditions, such as the Kibble-Zurek mechanism [100] and quantum friction [101].

Bibliography

- [1] D. J. Wineland, R. E. Drullinger, and F. L. Walls. “Radiation-Pressure Cooling of Bound Resonant Absorbers”. In: *Physical Review Letters* 40.25 (June 1978), pp. 1639–1642. ISSN: 0031-9007. DOI: [10.1103/PhysRevLett.40.1639](https://doi.org/10.1103/PhysRevLett.40.1639).
- [2] W. Neuhauser et al. “Optical-Sideband Cooling of Visible Atom Cloud Confined in Parabolic Well”. In: *Physical Review Letters* 41.4 (July 1978), pp. 233–236. ISSN: 0031-9007. DOI: [10.1103/PhysRevLett.41.233](https://doi.org/10.1103/PhysRevLett.41.233).
- [3] D. J. Wineland and Wayne M. Itano. “Spectroscopy of a Single Mg+ Ion”. In: *Physics Letters A* 82.2 (Mar. 1981), pp. 75–78. ISSN: 0375-9601. DOI: [10.1016/0375-9601\(81\)90942-7](https://doi.org/10.1016/0375-9601(81)90942-7).
- [4] Pradip K. Ghosh. *Ion Traps*. Oxford University Press, Nov. 1995. ISBN: 978-1-383-02679-5. DOI: [10.1093/oso/9780198539957.001.0001](https://doi.org/10.1093/oso/9780198539957.001.0001).
- [5] F. M. Penning. “Die Glimmentladung Bei Niedrigem Druck Zwischen Koaxialen Zylindern in Einem Axialen Magnetfeld”. In: *Physica* 3.9 (Nov. 1936), pp. 873–894. ISSN: 0031-8914. DOI: [10.1016/S0031-8914\(36\)80313-9](https://doi.org/10.1016/S0031-8914(36)80313-9).
- [6] Wolfgang Paul and Helmut Steinwedel. “Notizen: Ein Neues Massenspektrometer Ohne Magnetfeld”. In: *Zeitschrift für Naturforschung A* 8.7 (July 1953), pp. 448–450. ISSN: 1865-7109. DOI: [10.1515/zna-1953-0710](https://doi.org/10.1515/zna-1953-0710).
- [7] H. Paul and O. Graf. *Zur Frage der Unfälle im Bergbau*. Wiesbaden: VS Verlag für Sozialwissenschaften, 1956. ISBN: 978-3-663-04161-0. DOI: [10.1007/978-3-663-05607-2](https://doi.org/10.1007/978-3-663-05607-2).
- [8] R. F. Wuerker, H. Shelton, and R. V. Langmuir. “Electrodynamic Containment of Charged Particles”. In: *Journal of Applied Physics* 30.3 (1959), pp. 342–349. ISSN: 0021-8979. DOI: [10.1063/1.1735165](https://doi.org/10.1063/1.1735165).
- [9] D. Leibfried et al. “Quantum Dynamics of Single Trapped Ions”. In: *Reviews of Modern Physics* 75.1 (Mar. 2003), pp. 281–324. DOI: [10.1103/RevModPhys.75.281](https://doi.org/10.1103/RevModPhys.75.281).
- [10] Fouad G. Major, Victoria N. Gheorghe, and Günther Werth. *Charged Particle Traps*. Vol. 37. Springer Series on Atomic, Optical, and Plasma Physics. Berlin/Heidelberg: Springer-Verlag, 2005. ISBN: 978-3-540-22043-5. DOI: [10.1007/b137836](https://doi.org/10.1007/b137836).

- [11] Wolfgang Paul. “Electromagnetic Traps for Charged and Neutral Particles”. In: *Reviews of Modern Physics* 62.3 (July 1990), pp. 531–540. ISSN: 0034-6861, 1539-0756. DOI: 10.1103/RevModPhys.62.531.
- [12] C. E. Pearson et al. “Experimental Investigation of Planar Ion Traps”. In: *Physical Review A* 73.3 (Mar. 2006), p. 032307. ISSN: 1050-2947, 1094-1622. DOI: 10.1103/PhysRevA.73.032307.
- [13] S. Seidelin et al. “Microfabricated Surface-Electrode Ion Trap for Scalable Quantum Information Processing”. In: *Physical Review Letters* 96.25 (June 2006), p. 253003. ISSN: 0031-9007, 1079-7114. DOI: 10.1103/PhysRevLett.96.253003.
- [14] C. Henkel and M. Wilkens. “Heating of Trapped Atoms near Thermal Surfaces”. In: *Europhysics Letters* 47.4 (Aug. 1999), p. 414. ISSN: 0295-5075. DOI: 10.1209/epl/i1999-00404-8.
- [15] Hao-Kun Li et al. “Realization of Translational Symmetry in Trapped Cold Ion Rings”. In: *Physical Review Letters* 118.5 (Jan. 2017), p. 053001. ISSN: 0031-9007, 1079-7114. DOI: 10.1103/PhysRevLett.118.053001.
- [16] Erik Urban. “Implementation of a Rotationally Symmetric Ring Ion Trap and Coherent Control of Rotational States”. PhD thesis. University of California, Berkeley, 2019.
- [17] D. J. Berkeland et al. “Minimization of Ion Micromotion in a Paul Trap”. In: *Journal of Applied Physics* 83.10 (May 1998), pp. 5025–5033. ISSN: 0021-8979. DOI: 10.1063/1.367318.
- [18] Janus H Wesenberg. “Electrostatics of Surface-Electrode Ion Traps”. In: (2008). DOI: 10.1103/PhysRevA.78.063410.
- [19] Robert J. Clark. “Ideal Multipole Ion Traps from Planar Ring Electrodes”. In: *Applied Physics B* 113.2 (Nov. 2013), pp. 171–178. ISSN: 1432-0649. DOI: 10.1007/s00340-013-5451-0.
- [20] Robert G. Littlejohn. *Hydrogen and Hydrogen-Like Atoms*. <https://bohr.physics.berkeley.edu/classes/221/notes/hydrogen.pdf>. 2021.
- [21] C. J. Foot. *Atomic Physics*. OUP Oxford, Nov. 2004. ISBN: 978-0-19-103707-8.
- [22] Robert G. Littlejohn. *Emission and Absorption of Radiation*. <https://bohr.physics.berkeley.edu/classes/221/notes/radnmatt.pdf>. 2021.
- [23] D.F.V. James. “Quantum Dynamics of Cold Trapped Ions with Application to Quantum Computation”. In: *Applied Physics B* 66.2 (Feb. 1998), pp. 181–190. ISSN: 1432-0649. DOI: 10.1007/s003400050373.
- [24] Sönke Alexander Möller. “How to Couple Trapped Ions to Superconducting Resonators : Towards Hybrid Quantum Devices”. PhD thesis. 2016.
- [25] F. Diedrich et al. “Laser Cooling to the Zero-Point Energy of Motion”. In: *Physical Review Letters* 62.4 (Jan. 1989), pp. 403–406. DOI: 10.1103/PhysRevLett.62.403.

- [26] Jürgen Eschner et al. "Laser Cooling of Trapped Ions". In: *JOSA B* 20.5 (May 2003), pp. 1003–1015. ISSN: 1520-8540. DOI: [10.1364/JOSAB.20.001003](https://doi.org/10.1364/JOSAB.20.001003).
- [27] Anders Sørensen and Klaus Mølmer. "Quantum Computation with Ions in Thermal Motion". In: *Physical Review Letters* 82.9 (Mar. 1999), pp. 1971–1974. ISSN: 0031-9007, 1079-7114. DOI: [10.1103/PhysRevLett.82.1971](https://doi.org/10.1103/PhysRevLett.82.1971).
- [28] J P Home et al. "Normal Modes of Trapped Ions in the Presence of Anharmonic Trap Potentials". In: *New Journal of Physics* 13.7 (July 2011), p. 073026. ISSN: 1367-2630. DOI: [10.1088/1367-2630/13/7/073026](https://doi.org/10.1088/1367-2630/13/7/073026).
- [29] J. Michael Hollas. *Modern Spectroscopy*. John Wiley & Sons, Apr. 2013. ISBN: 978-1-118-68160-2.
- [30] Thaned Pruttivarasin. "Spectroscopy, Fundamental Symmetry Tests and Quantum Simulation with Trapped Ions". PhD thesis. 2014.
- [31] Markus Ansmann. "Benchmarking the Superconducting Josephson Phase Qubit: The Violation of Bell's Inequality". PhD thesis. University of California, Santa Barbara, 2009.
- [32] M. Brownnutt et al. "Ion-Trap Measurements of Electric-Field Noise near Surfaces". In: *Reviews of Modern Physics* 87.4 (Dec. 2015), pp. 1419–1482. ISSN: 0034-6861, 1539-0756. DOI: [10.1103/RevModPhys.87.1419](https://doi.org/10.1103/RevModPhys.87.1419).
- [33] M. A. Rowe et al. *Transport of Quantum States and Separation of Ions in a Dual RF Ion Trap*. May 2002. arXiv: [quant-ph/0205094](https://arxiv.org/abs/quant-ph/0205094).
- [34] A. J. Rasmussen et al. "Optimized Pulsed Sideband Cooling and Enhanced Thermometry of Trapped Ions". In: *Physical Review A* 104.4 (Oct. 2021), p. 043108. DOI: [10.1103/PhysRevA.104.043108](https://doi.org/10.1103/PhysRevA.104.043108).
- [35] Colin D. Bruzewicz et al. "Trapped-Ion Quantum Computing: Progress and Challenges". In: *Applied Physics Reviews* 6.2 (June 2019), p. 021314. ISSN: 1931-9401. DOI: [10.1063/1.5088164](https://doi.org/10.1063/1.5088164).
- [36] N. Daniilidis et al. "Fabrication and Heating Rate Study of Microscopic Surface Electrode Ion Traps". In: *New Journal of Physics* 13.1 (Jan. 2011), p. 013032. ISSN: 1367-2630. DOI: [10.1088/1367-2630/13/1/013032](https://doi.org/10.1088/1367-2630/13/1/013032).
- [37] C Monroe et al. "A "Schrödinger Cat" Superposition State of an Atom". In: *Science* 272.5265 (1996), pp. 1131–1136. ISSN: 00368075. DOI: [10.1126/science.272.5265.1131](https://doi.org/10.1126/science.272.5265.1131).
- [38] D. M. Meekhof et al. "Generation of Nonclassical Motional States of a Trapped Atom". In: *Physical Review Letters* 76.11 (Mar. 1996), pp. 1796–1799. ISSN: 0031-9007, 1079-7114. DOI: [10.1103/PhysRevLett.76.1796](https://doi.org/10.1103/PhysRevLett.76.1796).
- [39] Junhua Zhang et al. "NOON States of Nine Quantized Vibrations in Two Radial Modes of a Trapped Ion". In: *Physical Review Letters* 121.16 (Oct. 2018), p. 160502. ISSN: 0031-9007, 1079-7114. DOI: [10.1103/PhysRevLett.121.160502](https://doi.org/10.1103/PhysRevLett.121.160502).

- [40] S. C. Burd et al. *Experimental Speedup of Quantum Dynamics through Squeezing*. Apr. 2023. arXiv: 2304.05529 [physics, physics:quant-ph].
- [41] Erik Urban et al. “Coherent Control of the Rotational Degree of Freedom of a Two-Ion Coulomb Crystal”. In: *Physical Review Letters* 123.13 (Sept. 2019), p. 133202. DOI: 10.1103/PhysRevLett.123.133202.
- [42] Benjamin A. Stickler, Birthe Papendell, and Klaus Hornberger. “Spatio-Orientational Decoherence of Nanoparticles”. In: *Physical Review A* 94.3 (Sept. 2016), p. 033828. ISSN: 2469-9926, 2469-9934. DOI: 10.1103/PhysRevA.94.033828.
- [43] Birthe Papendell, Benjamin A. Stickler, and Klaus Hornberger. “Quantum Angular Momentum Diffusion of Rigid Bodies”. In: *New Journal of Physics* 19.12 (Dec. 2017), p. 122001. ISSN: 1367-2630. DOI: 10.1088/1367-2630/aa99d1.
- [44] Benjamin A. Stickler, Björn Schrinski, and Klaus Hornberger. “Rotational Friction and Diffusion of Quantum Rotors”. In: *Physical Review Letters* 121.4 (July 2018), p. 040401. DOI: 10.1103/PhysRevLett.121.040401.
- [45] Neil Glikin et al. *Systematic Study of Rotational Decoherence with a Trapped-Ion Planar Rotor*. Oct. 2023. DOI: 10.48550/arXiv.2310.13293. arXiv: 2310.13293 [physics, physics:quant-ph].
- [46] Timo Fischer. “Decoherence of the Orientation State”. PhD thesis. University of Duisburg-Essen, 2014.
- [47] Changchun Zhong and F Robicheaux. “Decoherence of Rotational Degrees of Freedom”. In: *Physical Review A* 94.5 (2016), p. 52109. ISSN: 24699934. DOI: 10.1103/PhysRevA.94.052109.
- [48] G. S. Agarwal. “Master Equations in Phase-Space Formulation of Quantum Optics”. In: *Physical Review* 178.5 (Feb. 1969), pp. 2025–2035. ISSN: 0031-899X. DOI: 10.1103/PhysRev.178.2025.
- [49] D.F. Walls and G.J Milburn. “Influence of Dissipation on Quantum Coherence”. In: *Physical Review A* 31.4 (1985), pp. 2403–2408. ISSN: 00319007. DOI: 10.1103/PhysRevLett.49.1545.
- [50] M Brune et al. “Observing the Progressive Decoherence of the “Meter” in a Quantum Measurement”. In: *Physical Review Letters* 77.24 (1996), pp. 4887–4890. ISSN: 10797114. DOI: 10.1103/PhysRevLett.77.4887.
- [51] C J Myatt et al. “Decoherence of Quantum Superpositions through Coupling to Engineered Reservoirs”. In: *Nature* 403.6767 (2000), pp. 269–273. ISSN: 00280836. DOI: 10.1038/35002001.
- [52] Q A Turchette et al. “Decoherence and Decay of Motional Quantum States of a Trapped Atom Coupled to Engineered Reservoirs”. In: *Physical Review A* 62.5 (2000), pp. 053807–053801. ISSN: 10502947. DOI: 10.1103/PhysRevA.62.053807.

- [53] T. Vieillard et al. “Field-Free Molecular Alignment of CO₂ Mixtures in Presence of Collisional Relaxation”. In: *Journal of Raman Spectroscopy* 39.6 (2008), pp. 694–699. ISSN: 1097-4555. DOI: 10.1002/jrs.1976.
- [54] Alexander A. Milner et al. “Effects of Ultrafast Molecular Rotation on Collisional Decoherence”. In: *Physical Review Letters* 113.4 (July 2014), p. 043005. ISSN: 0031-9007, 1079-7114. DOI: 10.1103/PhysRevLett.113.043005.
- [55] Ian F Tenney et al. “Collisional Decoherence and Rotational Quasirevivals in Asymmetric-Top Molecules”. In: *Physical Review A* 93.1 (2016), p. 13421. ISSN: 24699934. DOI: 10.1103/PhysRevA.93.013421.
- [56] B. Neyenhuis et al. “Anisotropic Polarizability of Ultracold Polar 40K87Rb Molecules”. In: *Physical Review Letters* 109.23 (Dec. 2012), p. 230403. DOI: 10.1103/PhysRevLett.109.230403.
- [57] Bo Yan et al. “Observation of Dipolar Spin-Exchange Interactions with Lattice-Confining Polar Molecules”. In: *Nature* 501.7468 (Sept. 2013), pp. 521–525. ISSN: 1476-4687. DOI: 10.1038/nature12483.
- [58] Sean Burchesky et al. “Rotational Coherence Times of Polar Molecules in Optical Tweezers”. In: *Physical Review Letters* 127.12 (Sept. 2021), p. 123202. ISSN: 0031-9007, 1079-7114. DOI: 10.1103/PhysRevLett.127.123202.
- [59] Bhuvanesh Sundar et al. “Strings of Ultracold Molecules in a Synthetic Dimension”. In: *Physical Review A* 99.1 (Jan. 2019), p. 013624. ISSN: 2469-9926, 2469-9934. DOI: 10.1103/PhysRevA.99.013624.
- [60] Yicheng Bao et al. “Dipolar Spin-Exchange and Entanglement between Molecules in an Optical Tweezer Array”. In: *Science* 382.6675 (Dec. 2023), pp. 1138–1143. DOI: 10.1126/science.adf8999.
- [61] Lysander Christakis et al. “Probing Site-Resolved Correlations in a Spin System of Ultracold Molecules”. In: *Nature* 614.7946 (Feb. 2023), pp. 64–69. ISSN: 1476-4687. DOI: 10.1038/s41586-022-05558-4.
- [62] Jun-Ru Li et al. “Tunable Itinerant Spin Dynamics with Polar Molecules”. In: *Nature* 614.7946 (Feb. 2023), pp. 70–74. ISSN: 1476-4687. DOI: 10.1038/s41586-022-05479-2.
- [63] Arne L. Grimsmo, Joshua Combes, and Ben Q. Baragiola. “Quantum Computing with Rotation-Symmetric Bosonic Codes”. In: *Physical Review X* 10.1 (Mar. 2020), p. 011058. ISSN: 2160-3308. DOI: 10.1103/PhysRevX.10.011058.
- [64] Victor V. Albert, Jacob P. Covey, and John Preskill. “Robust Encoding of a Qubit in a Molecule”. In: *Physical Review X* 10.3 (Sept. 2020), p. 031050. ISSN: 2160-3308. DOI: 10.1103/PhysRevX.10.031050.

- [65] Thai M. Hoang et al. “Torsional Optomechanics of a Levitated Nonspherical Nanoparticle”. In: *Physical Review Letters* 117.12 (Sept. 2016), p. 123604. ISSN: 0031-9007, 1079-7114. DOI: 10.1103/PhysRevLett.117.123604.
- [66] Fons van der Laan et al. “Sub-Kelvin Feedback Cooling and Heating Dynamics of an Optically Levitated Librator”. In: *Physical Review Letters* 127.12 (Sept. 2021), p. 123605. DOI: 10.1103/PhysRevLett.127.123605.
- [67] A. Pontin et al. “Simultaneous Cavity Cooling of All Six Degrees of Freedom of a Levitated Nanoparticle”. In: *Nature Physics* 19.7 (July 2023), pp. 1003–1008. ISSN: 1745-2481. DOI: 10.1038/s41567-023-02006-6.
- [68] H Shi and M Bhattacharya. “Optomechanics Based on Angular Momentum Exchange between Light and Matter”. In: *Journal of Physics B: Atomic, Molecular and Optical Physics* 49.15 (2016), p. 153001. ISSN: 0953-4075. DOI: 10.1088/0953-4075/49/15/153001.
- [69] Catalina Curceanu, J. D. Gillaspy, and Robert C. Hilborn. “Resource Letter SS–1: The Spin-Statistics Connection”. In: *American Journal of Physics* 80.7 (July 2012), pp. 561–577. ISSN: 0002-9505. DOI: 10.1119/1.4704899.
- [70] Kathryn Levin et al. *Ultracold Bosonic and Fermionic Gases*. Elsevier, July 2012. ISBN: 978-0-444-53857-4.
- [71] C. K. Hong, Z. Y. Ou, and L. Mandel. “Measurement of Subpicosecond Time Intervals between Two Photons by Interference”. In: *Physical Review Letters* 59.18 (Nov. 1987), pp. 2044–2046. ISSN: 0031-9007. DOI: 10.1103/PhysRevLett.59.2044.
- [72] E. Bocquillon et al. “Coherence and Indistinguishability of Single Electrons Emitted by Independent Sources”. In: *Science* 339.6123 (Mar. 2013), pp. 1054–1057. DOI: 10.1126/science.1232572.
- [73] A. M. Kaufman et al. “Two-Particle Quantum Interference in Tunnel-Coupled Optical Tweezers”. In: *Science* 345.6194 (July 2014), pp. 306–309. DOI: 10.1126/science.1250057.
- [74] R. Lopes et al. “Atomic Hong–Ou–Mandel Experiment”. In: *Nature* 520.7545 (Apr. 2015), pp. 66–68. ISSN: 1476-4687. DOI: 10.1038/nature14331.
- [75] R. Hanbury Brown and R. Q. Twiss. “Correlation between Photons in Two Coherent Beams of Light”. In: *Nature* 177.4497 (Jan. 1956), pp. 27–29. ISSN: 1476-4687. DOI: 10.1038/177027a0.
- [76] M. Henny et al. “The Fermionic Hanbury Brown and Twiss Experiment”. In: *Science* 284.5412 (Apr. 1999), pp. 296–298. ISSN: 0036-8075, 1095-9203. DOI: 10.1126/science.284.5412.296.
- [77] William D. Oliver et al. “Hanbury Brown and Twiss-Type Experiment with Electrons”. In: *Science* 284.5412 (Apr. 1999), pp. 299–301. ISSN: 0036-8075, 1095-9203. DOI: 10.1126/science.284.5412.299.

- [78] Simon Fölling et al. “Spatial Quantum Noise Interferometry in Expanding Ultracold Atom Clouds”. In: *Nature* 434.7032 (Mar. 2005), pp. 481–484. ISSN: 1476-4687. DOI: 10.1038/nature03500.
- [79] M. Schellekens et al. “Hanbury Brown Twiss Effect for Ultracold Quantum Gases”. In: *Science* 310.5748 (Oct. 2005), pp. 648–651. ISSN: 0036-8075, 1095-9203. DOI: 10.1126/science.1118024.
- [80] F. Rasetti. “On the Raman Effect in Diatomic Gases”. In: *Proceedings of the National Academy of Sciences* 15.3 (Mar. 1929), pp. 234–237. ISSN: 0027-8424, 1091-6490. DOI: 10.1073/pnas.15.3.234.
- [81] D. Kekez, A. Ljubicić, and B. A. Logan. “An Upper Limit to Violations of the Pauli Exclusion Principle”. In: *Nature* 348.6298 (Nov. 1990), pp. 224–224. ISSN: 1476-4687. DOI: 10.1038/348224a0.
- [82] M. de Angelis et al. “Test of the Symmetrization Postulate for Spin-0 Particles”. In: *Physical Review Letters* 76.16 (Apr. 1996), pp. 2840–2843. DOI: 10.1103/PhysRevLett.76.2840.
- [83] Robert C. Hilborn and Candice L. Yuca. “Spectroscopic Test of the Symmetrization Postulate for Spin-0 Nuclei”. In: *Physical Review Letters* 76.16 (Apr. 1996), pp. 2844–2847. DOI: 10.1103/PhysRevLett.76.2844.
- [84] G. Modugno, M. Inguscio, and G. M. Tino. “Search for Small Violations of the Symmetrization Postulate for Spin-0 Particles”. In: *Physical Review Letters* 81.22 (Nov. 1998), pp. 4790–4793. DOI: 10.1103/PhysRevLett.81.4790.
- [85] P. Cancio Pastor et al. “Testing the Validity of Bose-Einstein Statistics in Molecules”. In: *Physical Review A* 92.6 (Dec. 2015), p. 063820. DOI: 10.1103/PhysRevA.92.063820.
- [86] C. F. Roos et al. “Revealing Quantum Statistics with a Pair of Distant Atoms”. In: *Physical Review Letters* 119.16 (Oct. 2017), p. 160401. DOI: 10.1103/PhysRevLett.119.160401.
- [87] Konrad Tschernig et al. “Direct Observation of the Particle Exchange Phase of Photons”. In: *Nature Photonics* 15.9 (Sept. 2021), pp. 671–675. ISSN: 1749-4893. DOI: 10.1038/s41566-021-00818-7.
- [88] Zhi-Feng Liu et al. “Hong-Ou-Mandel Interference between Two Hyperentangled Photons Enables Observation of Symmetric and Antisymmetric Particle Exchange Phases”. In: *Physical Review Letters* 129.26 (Dec. 2022), p. 263602. ISSN: 0031-9007, 1079-7114. DOI: 10.1103/PhysRevLett.129.263602.
- [89] Dennis Dieks and Andrea Lubberdink. “How Classical Particles Emerge From the Quantum World”. In: *Foundations of Physics* 41.6 (June 2011), pp. 1051–1064. ISSN: 1572-9516. DOI: 10.1007/s10701-010-9515-2.

- [90] Robert G. Littlejohn. *Identical Particles*. <https://bohr.physics.berkeley.edu/classes/221/notes/identpart.pdf>. 2021.
- [91] H. Dekker. “Fractal Analysis of Chaotic Tunneling of Squeezed States in a Double-Well Potential”. In: *Physical Review A* 35.4 (Feb. 1987), pp. 1825–1837. ISSN: 0556-2791. DOI: 10.1103/PhysRevA.35.1825.
- [92] S. J. van Enk. *Exchanging Identical Particles and Topological Quantum Computing*. Feb. 2019. doi: 10.48550/arXiv.1810.05208. arXiv: 1810.05208 [quant-ph].
- [93] H. He et al. “Direct Observation of Transfer of Angular Momentum to Absorptive Particles from a Laser Beam with a Phase Singularity”. In: *Physical Review Letters* 75.5 (July 1995), pp. 826–829. ISSN: 0031-9007, 1079-7114. DOI: 10.1103/PhysRevLett.75.826.
- [94] V. Garcés-Chávez et al. “Observation of the Transfer of the Local Angular Momentum Density of a Multiringed Light Beam to an Optically Trapped Particle”. In: *Physical Review Letters* 91.9 (Aug. 2003), p. 093602. ISSN: 0031-9007, 1079-7114. DOI: 10.1103/PhysRevLett.91.093602.
- [95] Felix Stopp et al. “Coherent Transfer of Transverse Optical Momentum to the Motion of a Single Trapped Ion”. In: *Physical Review Letters* 129.26 (Dec. 2022), p. 263603. ISSN: 0031-9007, 1079-7114. DOI: 10.1103/PhysRevLett.129.263603.
- [96] Andrei Afanasev, Carl E. Carlson, and Asmita Mukherjee. “Superkicks and the Photon Angular and Linear Momentum Density”. In: *Physical Review A* 105.6 (June 2022), p. L061503. ISSN: 2469-9926, 2469-9934. DOI: 10.1103/PhysRevA.105.L061503.
- [97] Katherine C. McCormick et al. “Quantum-Enhanced Sensing of a Single-Ion Mechanical Oscillator”. In: *Nature* 572.7767 (Aug. 2019), pp. 86–90. ISSN: 1476-4687. DOI: 10.1038/s41586-019-1421-y.
- [98] Alexandre M. Souza, Gonzalo A. Álvarez, and Dieter Suter. “Robust Dynamical Decoupling”. In: *Philosophical Transactions of the Royal Society A: Mathematical, Physical and Engineering Sciences* 370.1976 (Oct. 2012), pp. 4748–4769. DOI: 10.1098/rsta.2011.0355.
- [99] M.S. Santhanam, Sanku Paul, and J. Bharathi Kannan. “Quantum Kicked Rotor and Its Variants: Chaos, Localization and Beyond”. In: *Physics Reports* 956 (Apr. 2022), pp. 1–87. ISSN: 03701573. DOI: 10.1016/j.physrep.2022.01.002.
- [100] K. Pyka et al. “Topological Defect Formation and Spontaneous Symmetry Breaking in Ion Coulomb Crystals”. In: *Nature Communications* 4.1 (Aug. 2013), p. 2291. ISSN: 2041-1723. DOI: 10.1038/ncomms3291.
- [101] Alexei Bylinskii, Dorian Gangloff, and Vladan Vuletić. “Tuning Friction Atom-by-Atom in an Ion-Crystal Simulator”. In: *Science* 348.6239 (June 2015), pp. 1115–1118. ISSN: 0036-8075, 1095-9203. DOI: 10.1126/science.1261422.